

Ozonation and Photodegradation of Oil Compounds by Surface Level Ozone and Engineered Catalysts in Marine Ecosystem

by

Haodong Ji

A dissertation submitted to the Graduate Faculty of
Auburn University
in partial fulfillment of the
requirements for the Degree of
Doctor of Philosophy

Auburn, Alabama
December 15, 2018

Keywords: Ozonation, Oil Compounds, Photodegradation,
Photocatalyst, Oil spill, Oil dispersant

Copyright 2018 by Haodong Ji

Approved by

Dongye Zhao, Huff Professor of Environmental Engineering (Major advisor)
Prabhakar Clement, Harold Vince Groome Jr. Professor of Environmental Engineering
Yucheng Feng, Professor of Crop, Soil and Environmental Sciences
Clifford Lange, Associate Professor of Environmental Engineering
Xinyu Zhang, Associate Professor of Chemical Engineering

Abstract

Marine oil spill has been an environmental challenge for many decades. As the use of oil dispersants has become one of the main approaches to clean up spilled oil, the environmental behavior of dispersed oil remains poorly understood.

Specifically, Oil degradation by surface-level atmospheric ozone has been largely ignored in the field. To address this knowledge gap, this study in Chapter 2 investigated the ozonation rate and extent of typical petroleum compounds by simulated surface-level ozone, including total petroleum hydrocarbons (TPHs), *n*-alkanes, and polycyclic aromatic hydrocarbons (PAHs). Moreover, the work explored the effect of a prototype oil dispersant, Corexit EC9500A, on the ozonation rate. Rapid oxidation of TPHs, *n*-alkanes and PAHs was observed at various gaseous ozone concentrations (i.e. 86, 200 and 300 ppbv). Generally, the presence of the oil dispersant enhanced ozonation of the oil compounds. The addition of humic acid inhibited the reaction, while increasing salinity accelerated the degradation. Both direct ozonation by molecular ozone and indirect oxidation by ozone-induced radicals play important roles in the degradation process. The findings indicate that ozonation should be taken into account in assessing environmental fate and weathering of spilled oil. Meanwhile, little is known on the removal of dispersed oil from marine water using conventional adsorbents. This study in Chapter 3 investigated the effectiveness of three model activated charcoals (ACs) of different particle sizes (4-12, 12-20 and 100 mesh, i.e., GAC4×12, GAC12×20, PAC100) for removal of oil dispersed in marine water by two prototype oil dispersants (Corexit EC9500A and Corexit EC9527A). Sorption kinetic data revealed that all

three ACs can efficiently adsorb dispersant Corexit EC9500A and two dispersed oil (DWA0-I and DWA0-II) following the same trend: PAC100 > GAC12×20 > GAC4×12. PAC100 showed much faster and more effective adsorption rate than the GACs, with a pseudo second-order rate constant k_2 (g/(mg·h)) value of 8.94, 7.62 and 0.51 for Corexit EC9500A, DWA0-I, and DWA0-II, respectively, and equilibrium uptake 5.23, 31.65, and 29.52 mg/g. Sorption isotherms confirmed PAC100 showed the highest adsorption capacity for dispersed oil in DWA0-I with a Freundlich K_F value of 10.90 mg/g·(L/mg)^{1/n} ($n = 1.38$). In addition, PAC100 also showed the highest sorption of *n*-alkanes and PAHs. The various characterization results showed PAC100 have the higher measured BET surface area as 889 m²/g and total pore volume as 0.95 cm³/g (pH_{PZC} = 6.1). Furthermore, the presence of additional dispersant Corexit EC9500A showed two contrasting effects on the oil sorption, i.e., adsolubilization effect and solubilization effect. Meanwhile, the solution pH only modestly affected the sorption of dispersed oil, i.e. the oil uptake decreased by <8% when increasing the solution pH from 6.0 to 9.0. However, salinity presents the inhibitive effect for the sorption uptake of oil hydrocarbons. This information is important for understanding roles of oil dispersant on the sorption of dispersed oil by activated charcoals from the dispersant-seawater-oil system. The results also indicate that the sorption of dispersed oil by activated charcoal is a low-cost and efficient way for the oil and dispersed oil cleanup process.

In addition, we prepared various silica aerogel supported TiO₂ (TiO₂/SiO₂) composite materials through initial sol-gel method and subsequent calcination, and tested the materials for removal of a model of PAHs, i.e., phenanthrene, through adsorption and photocatalysis as shown in Chapter 4. Anatase was formed at calcination temperature of 400 and 600 °C, while mixed crystal phases of anatase and rutile were found at 800 °C. All the TiO₂/SiO₂ composite materials were able to rapidly adsorb phenanthrene, with equilibrium being reached within 180 min. Higher

calcination temperature resulted in better crystallinity of TiO_2 , higher photocatalytic activity, and reduced the adsorption affinity of the material toward phenanthrene. $\text{TiO}_2/\text{SiO}_2$ -800 showed minimal phenanthrene uptake (only 5.2% of total phenanthrene) but the strongest photocatalytic activity, and it was able to completely degrade phenanthrene within 3 h without any residual in the solid phase. For $\text{TiO}_2/\text{SiO}_2$ -800, TiO_2 acts as the primary photocatalyst and silica serves as the support for nano- TiO_2 , which can facilitate accumulation and subsequent photodegradation of phenanthrene at the surface of the material by acting as a weak adsorbent as well as a medium. The material can be repeatedly used in multiple cycles of operations without significant loss in its photocatalytic activity. Meanwhile, we proposed and tested a composite material, activated charcoal supported titanate nanotubes (TNTs@AC), for efficient adsorption and photodegradation of oil components from (dispersed water accommodated oil) DWAO. TNTs@AC was prepared through a one-step hydrothermal method, and is composed of an activated charcoal core and a shell of carbon-coated titanate nanotubes. TNTs@AC held great potential to substantially advance current practices in treating spilled oil from water/seawater. >99.5% of TPHs, *n*-alkanes and PAHs could be adsorbed at 1.25 g/L TNTs@AC within 24 h, and the adsorption mainly occurred in the first 4 h. In the following photocatalysis process, 98.0%, 94.8% and 98.4% of the pre-concentrated (through adsorption) TPHs, *n*-alkanes and PAHs could be degraded within 4 h. >97% of TPHs could be further removed by photo-regenerated TNTs@AC.

Acknowledgments

It is so glad to write the acknowledgments, which means I am close enough to my graduation. At this moment, I have to express my gratitude to so many people who support and help me during the period of pursuing my doctorate degree in Auburn.

First, I would like to give my greatest acknowledge to my dissertation advisor Dr. Dongye Zhao for his excellent guidance, patience, and help. His outstanding knowledge and unstoppable passion for science enrich and inspire me how to be a researcher.

I sincerely acknowledge the helpful and insightful guidance from my committee members Drs. Prabhakar Clement, Clifford Lange, Yucheng Feng and Xinyu Zhang, and my dissertation University Reader Dr. Brendan Higgins for their encouraging words, and the time and attention they have devoted to me in their busy schedules. I feel fortunate that I can meet them and have an opportunity to learn from them.

I would like to thank Jinling Zhuang, Dr. Eduardus Duin and Dr. Michael Bozack for their analytical and technical assistance. I also enjoy the moment and daily life with my fellow students for their support during the research. Special thanks to Dr. Wen Liu for all the support and research advice. It would have been a lonely life, especially in holiday and uncreative research without them.

Finally, I would also like to express my gratitude and love to my wife and parents for their infinite support, endurance and encouragement during the last five years. I have experienced both

happiness and loneliness during the long march towards my Ph.D. and I could not have achieved through without my wife's companionship, sympathy and support.

Table of Contents

Abstract.....	ii
Acknowledgments.....	v
List of Tables	xii
List of Figures.....	xiv
List of Abbreviations	xviii
Chapter 1. General Introduction.....	1
1.1 Chemical dispersion of oil spill.....	1
1.2 Oxidation of oil spill by atmospheric ozone	5
1.3 Removal of spilled oil by various sorbents	6
1.4 Enhanced adsorption and photodegradation using engineered catalysts	7
1.5 Objectives.....	9
1.6 Organization	10
Chapter 2. Degradation of petroleum hydrocarbons in seawater by simulated surface-level atmospheric ozone: Reaction kinetics and effect of oil dispersant	12
2.1 Introduction.....	12
2.2 Materials and Methods	16
2.2.1 Materials	16
2.2.2 Experimental set-up	20
2.2.3 Ozonation of dispersed oil and effects of dispersant	21

2.2.4 Effects of gaseous ozone concentration and solution chemistry on ozonation of petroleum hydrocarbons in DWAO.....	23
2.2.5 Analytical methods	23
2.3 Results and Discussion.....	27
2.3.1 Effects of oil dispersant on volatilization and ozonation of petroleum hydrocarbons in seawater.....	27
2.3.2 Degradation of oil hydrocarbons in DWAO at various atmospheric ozone concentrations	40
2.3.3 Effect of dispersant concentration on ozonation of petroleum hydrocarbons in DWAO	43
2.3.4 Effects of pH	49
2.3.5 Effects of humic acid	53
2.3.6 Effects of salinity	57
2.3.7 Ozonation mechanisms	62
2.4 Conclusions	70
Chapter 3. Sorption of dispersed petroleum hydrocarbons by activated charcoals: Kinetics, isotherms and roles of oil dispersants	72
3.1 Introduction	72
3.2 Materials and Methods	75
3.2.1. Chemicals and Materials.....	75
3.2.2 Seawater and oil samples	79

3.2.3 Effects of dispersant on sorption of oil hydrocarbons	80
3.2.4 Effects of solution chemistry on sorption of dispersed oil	82
3.2.5 Analytical methods	82
3.2.6 Material characterization	83
3.3 Results and Discussion.....	84
3.3.1 Characterization of Activated charcoal.....	84
3.3.2 Sorption of dispersed oil by various model sorbents	90
3.3.3 Sorption kinetics of dispersed oil by AC	91
3.3.4 Sorption isotherms of dispersed oil by ACs	95
3.3.5 Effects of dispersant on sorption of dispersed oil by ACs.....	97
3.3.6 Effect of pH.....	111
3.3.7 Effect of salinity.....	113
3.4 Conclusions	115
Chapter 4. Silica aerogel supported titanium dioxide (TiO₂/SiO₂) composites for adsorption and efficient visible light photocatalytic degradation of PAHs	118
4.1 Introduction	118
4.2 Materials and Methods	120
4.2.1 Chemicals.....	120
4.2.2 Synthesis of TiO ₂ /SiO ₂	121
4.2.3 Material characterizations	121
4.2.4 Experimental methods: adsorption and photocatalysis.....	122

5.3.2 Distribution of oil components in DWAO during adsorption by TNTs@AC	169
5.3.3 Adsorption isotherms of oil components in DWAO by TNTs@AC	173
5.3.4 Photodegradation of adsorbed oil components by TNTs@AC	178
5.4 Conclusion.....	181
Chapter 6. Conclusions and Suggestions for Future Research.....	182
6.1 Summary and Conclusions.....	182
6.2 Suggestions for Future Work	186
References	188
Appendix.....	203

List of Tables

Table 2-1. Target PAHs compounds and quantification ions (QIs).....	17
Table 2-2. Chemical constituents of dispersant Corexit EC9500A.....	18
Table 2-3. First-order ozonation rate constants for TPHs, <i>n</i> -alkanes and total PAHs in WAO and DWAO.....	30
Table 2-4. Pseudo first-order ozonation rate constants for parent and alkylated PAHs in WAO and DWAO.....	37
Table 2-5. First-order ozonation rate constants for TPHs, <i>n</i> -alkanes and TPAHs in DWAO at various concentrations of simulated atmospheric ozone.....	42
Table 2-6. First-order ozonation rate constants for TPHs in DWAO in the presence of various concentrations of humic acid.....	54
Table 2-7. First-order ozonation rate constants for TPHs, <i>n</i> -alkanes and total PAHs in DWAO.....	66
Table 3-1. Chemical constituents of dispersants Corexit EC9500A and Corexit EC9527A.....	77
Table 3-2. Atomic compositions of GAC12×20.....	86
Table 3-3. Atomic percent of different compositions of C 1s and O 1s.....	86
Table 3-4. Key physicochemical properties of three model activated charcoals.....	89
Table 3-5. Kinetic model parameters for sorption of dispersed oil from DWAO-I by three model activated charcoals.....	93
Table 3-6. Kinetic model parameters for sorption of dispersed oil from DWAO-II by three model activated charcoals.....	93
Table 3-7. Kinetic model parameters for sorption of dispersed oil from DWAO-II by three model activated charcoals.....	96
Table 3-8. Kinetic model parameters for sorption of dispersed oil from DWAO-II by three model activated charcoals.....	99
Table 4-1. Parameters of Pseudo-first-order and Pseudo-second-order kinetic models for phenanthrene adsorption onto various TiO ₂ /SiO ₂ materials.....	130

Table 4-2. Parameters of isotherm models for phenanthrene adsorption onto various TiO ₂ /SiO ₂ materials.....	132
Table 4-3. Phenanthrene removal efficiency (<i>R</i>) by TiO ₂ /SiO ₂ -800 over 5 cycles of consecutive runs.....	152
Table 4-4. First order ozone oxidation rate constants for TPHs, <i>n</i> -alkanes and TPAHs in DWAO for different reactions.....	157
Table 5-1. Kinetic parameters for adsorption of TPHs, <i>n</i> -alkanes and PAHs in DWAO by TNTs@AC.....	130
Table 5-2. Isotherm parameters for adsorption of TPHs, <i>n</i> -alkanes and PAHs in DWAO by TNTs@AC.....	132
Table 5-3. Parameters of first-order kinetic model for photocatalytic degradation of TPHs, <i>n</i> -alkanes and PAHs by TNTs@AC.....	152

List of Figures

Figure 2-1. Schematic of the experimental set-up for ozonation of dispersed oil under simulated atmospheric ozone.	21
Figure 2-2. UV-Vis absorbance of aqueous ozone in DWAO.....	26
Figure 2-3. Volatilization and ozonation kinetics of: (a) TPHs, (b) <i>n</i> -alkanes and (c) total PAHs in WAO and DWAO (Corexit EC9500A) solutions.....	29
Figure 2-4. Distributions of <i>n</i> -alkanes in WAO (a) and DWAO (b) before and after 48 h exposure to gaseous ozone.	33
Figure 2-5. Distributions of parent and alkylated PAHs in WAO (a) and DWAO (b) before and after 24 hours ozonation.....	35
Figure 2-6. Distributions of parent and alkylated PAHs in WAO (a) and DWAO (b) before and after 24 hours ozonation.....	36
Figure 2-7. Ozonation of parent PAHs (a) and alkylated PAHs (b) in DWAO (with Corexit EC9500A) under 86 ppbv simulated atmospheric ozone.	39
Figure 2-8. Ozonation kinetics of (a) TPHs, (b) <i>n</i> -alkanes and (c) total PAHs in DWAO at various gaseous ozone concentrations.	42
Figure 2-9. Remaining concentrations of TPHs, <i>n</i> -alkanes and total PAHs (a), and parent PAHs and alkylated PAHs (b) in DWAO after 24 h ozonation in the presence of various concentrations of the dispersant, and distributions of <i>n</i> -alkanes (c) and PAHs (d) in DWAO after 24 h ozonation.	46
Figure 2-10. Oxidation of <i>p</i> CBAs (normalized to initial concentration) during ozonation with or without 18 or 24 mg/L of Corexit EC9500A in seawater.....	48
Figure 2-11. Remaining concentrations of TPHs, <i>n</i> -alkanes and total PAHs in DWAO after 24 h ozonation at various initial pH levels.....	50
Figure 2-12. Effect of pH on ozonation of parent and alkylated PAHs in DWAO by simulated atmospheric ozone.	51
Figure 2-13. Distributions of remaining <i>n</i> -alkanes (a) and PAHs (b) in DWAO after 24 h ozonation at various pH levels.....	52

Figure 2-14. Effect of HA on ozonation of TPHs in DWAO.	54
Figure 2-15. Distributions of <i>n</i> -alkanes (a) and PAHs (b) in DWAO after 24 h ozonation in the presence of various concentrations of humic acid.	56
Figure 2-16. Remaining concentrations of: (a) TPHs, (b) <i>n</i> -alkanes and (c) PAHs in DWAO after 24-h ozonation at various salinity levels.....	58
Figure 2-17. Distributions of remaining <i>n</i> -alkanes (a) and PAHs (b) in DWAO after 24h ozonation at various salinity.	60
Figure 2-18. Transformation of (a) TPHs, (b) <i>n</i> -alkanes and (c) total PAHs by molecular ozone and hydroxyl radicals during ozonation of DWAO.....	65
Figure 2-19. Distributions of remaining <i>n</i> -alkanes (a) and PAHs (b) after 24h ozonation (overall versus direct ozonation).	68
Figure 3-1. SEM images (a) and EDS spectra (b) of GAC12×20.	85
Figure 3-2. XRD patterns of GAC12×20.....	86
Figure 3-3. FTIR spectra of GAC12×20.....	87
Figure 3-4. (a) Pore size distributions of three activated charcoals tested in this work, and (b) Zeta potential of three ACs as a function of solution pH.....	89
Figure 3-5. Percentage removal of dispersed oil prepared in DWAO-I (Corexit EC9500A) by selected commercial sorbents..	90
Figure 3-6. Sorption kinetics dispersed oil by three activated charcoals in DWAO-I (a) and DWAO-II (b).	92
Figure 3-7. Sorption isotherms of dispersed oil in DWAO-I by three activated charcoals.	96
Figure 3-8. Sorption kinetics (a) and isotherms (b) of Corexit EC9500A by three model activated charcoals.	99
Figure 3-9. Uptake of dispersed oil by three model activated charcoals as a function of additional dispersant (Corexit EC9500A) added in DWAO-I.....	103
Figure 3-10. The schematic for sorption of dispersed oil in the dispersant-oil-seawater-activated charcoal system.....	105
Figure 3-11. Aqueous <i>n</i> -alkanes distributions in DWAO-I (a) and DWAO-II (b) before and after 8 hour's sorption by three model activated charcoals, and aqueous <i>n</i> -alkanes distributions in DWAO-I in the absence or presence of additional 15 mg/L Corexit EC9500A (c).....	108
Figure 3-11. Aqueous PAHs distributions in DWAO-I (a) and DWAO-II (b) before and after 8 hour's sorption by three model activated charcoals.....	111

Figure 3-11. Equilibrium uptakes of dispersed oil by three model ACs as a function of solution pH (a) and salinity (b).	113
Figure 4-1. Schematic of the experimental set-up for photocatalytic reaction.	124
Figure 4-2. TEM and HRTEM images of uncalcined TiO ₂ /SiO ₂ (a, b, c, d), TiO ₂ /SiO ₂ -600 (e, f) and TiO ₂ /SiO ₂ -800 (g, h).	126
Figure 4-3. XRD patterns of various TiO ₂ /SiO ₂ composites.	128
Figure 4-4. Adsorption kinetics of phenanthrene by various TiO ₂ /SiO ₂ composite materials. ..	130
Figure 4-5. Adsorption isotherms of phenanthrene by various TiO ₂ /SiO ₂ composite materials.	132
Figure 4-6. Total phenanthrene (a), dissolved phenanthrene (b), and adsorbed phenanthrene (c) in the adsorption-photocatalysis system in the presence of various TiO ₂ /SiO ₂ composite materials.	136
Figure 4-7. Removal of phenanthrene by TiO ₂ /SiO ₂ -800 with and without pre-adsorption.	138
Figure 4-8. PL spectra of various Ti-based materials under solar illumination.	139
Figure 4-9. EPR spectra for various TiO ₂ /SiO ₂ composites materials.	141
Figure 4-10. Schematic illustration of enhanced photocatalytic activity of TiO ₂ /SiO ₂ -800.	143
Figure 4-11. Proposed degradation pathway of phenanthrene by TiO ₂ /SiO ₂ -800 under solar light.	145
Figure 4-12. Total ion chromatograms of phenanthrene and degradation intermediates at (a) 0, (b) 1, (c) 3, and (d) 6 h of photocatalysis using TiO ₂ /SiO ₂ -800.	147
Figure 4-13. Mass spectra of phenanthrene and degradation intermediates in the photocatalysis process by TiO ₂ /SiO ₂ -800.	150
Figure 4-14. PL spectra of various Ti-based materials under solar illumination.	151
Figure 4-15. Removal of (a) TPHs, (b) <i>n</i> -alkanes and (c) Total PAHs in DWAO (Corexit EC9500A) solution by combined ozonation and photodegradation.	156
Figure 5-1. Adsorption kinetics of TPHs, <i>n</i> -alkanes and PAHs in DWAO by TNTs@AC (a) with a material dosage of 0.625 g/L, and (b) 1.25 g/L.	141
Figure 5-2. Distribution of <i>n</i> -alkanes in DWAO during adsorption by TNTs@AC.	143
Figure 5-3. Distribution of PAHs in DWAO during adsorption by TNTs@AC.	145
Figure 5-4. Adsorption isotherms of: (a) TPHs, (b) <i>n</i> -alkanes and (c) PAHs in DWAO by TNTs@AC.	147

Figure 5-5. Photodegradation kinetics of oil components (a) Photodegradation of various oil components, and (b) various PAHs pre-concentrated on TNTs@AC.....	150
Figure A-1. Preparation of water accommodated oil (WAO) and dispersant-enhanced WAO..	145
Figure A-2. A simulated photodegradation system.	147
Figure A-3. Stainless steel jacket with a Teflon reactor for titanate nanotubes synthesis.....	150

List of Abbreviations

AC	Activated charcoal
BET	Brunauer–Emmett–Teller
BOEM	Bureau of Ocean Energy Management
CMC	Critical Micelle Concentration
DCM	Dichloromethane
DI	Deionized water
DLS	Dynamic Light Scattering
DOM	Dissolved Organic Matter
DPnB	Di(propylene glycol) Butyl Ether
DWAO	Dispersant-facilitated Water Accommodated Oil
<i>DwH</i>	Deepwater Horizon
EDS	Energy-dispersive X-ray Spectroscopy
EPA	Environmental Protect Agency
FTIR	Fourier Transform Infrared Spectroscopy
GAC	Granular Activated Carbon
GC-FID	Gas Chromatograph with a Flame Ionization Detector
GC-MS	Gas Chromatography-Mass Spectrometry
GOM	Gulf of Mexico
HA	Humic Acid

HLB	Hydrophile-Lipophile Balance
HOC	Hydrophobic Organic Compounds
HPLC	High Performance Liquid Chromatography
IS	Ionic Strength
LSC	Louisiana Sweet Crude
MOS	Marine Oil Snow
MSR	Molar Solubilization Ratio
NAAQS	National Ambient Air Quality Standards
PAC	Powder Activated Charcoal
PAHs	Polycyclic Aromatic Hydrocarbons
<i>p</i> CBA	<i>para</i> -Chlorobenzoic Acid
PTFE	Polytetrafluoroethylene
QIs	Quantification Ions
SDS	Sodium Dodecyl Sulfate
SDSS	Sodium Dioctyl Sulfosuccinate
SEM	Scanning Electron Microscope
TEM	Transmission Electron Microscope
TBOT	Tetrabutyl Titanate
TNTs	Titanate Nanotubes
TOC	Total Organic Carbon
TPHs	Total Petroleum Hydrocarbons
TPAHs	Total Polycyclic Aromatic Hydrocarbons

VOCs	Volatile Organic Compounds
WAO	Water Accommodated Oil
XPS	X-ray Photoelectron Spectroscopy
XRD	X-ray Diffractometer

Chapter 1. General Introduction

1.1 Chemical dispersion of oil spill

Oil spill has been a major marine pollution concern in the modern time. For instance, the 1989 *Exxon Valdez* in Alaska spilled at least 43,000m³ (~11 million gallons) of crude oil, and affected marine ecosystems, i.e. growth suppression, embryotoxicity to fish, persistence on beaches and other indirect effects (Short, 2017); the *Mega Borg* shipboard explosion in Texas discharge 17,100m³ (~4.5 million gallons) of crude oil (Smultea and Würsig, 1995); and the 1996 North Cape discharged ~3000m³ (~0.8 million gallons) of No. 2 fuel oil just offshore of Rhode Island (Ho et al., 1999). The 2010 Deepwater Horizon (*DwH*) oil spill released more than 795 million liters of Louisiana Sweet Crude (LSC) oil into the Gulf of Mexico (Camilli et al., 2010; Reddy et al., 2012; Sammarco et al., 2013). As a result, high concentrations of oil compounds in the water column were detected following the spill. For instance, Camilli et al. (2010) reported that the concentration of mono-aromatic petroleum hydrocarbons in the affected seawater exceeded 50 mg/L, and Reddy et al. (2012) observed that the light aromatic hydrocarbons (benzene, toluene, ethylbenzene, and total xylenes) reached up to 78 mg/L. Typically, crude oil contains saturated *n*-alkanes, polycyclic aromatic hydrocarbons (PAHs) and their alkylated homologues. For instance, the *DwH* oil contained ~3.9 wt.% of PAHs ($\sim 2.1 \times 10^7$ kg), ~1.5 wt.% of their alkylated PAHs ($\sim 7.9 \times 10^6$ kg) and ~15.3 wt.% of *n*-alkanes ($\sim 8.1 \times 10^7$ kg) (Reddy et al., 2012).

As an emergency mitigation measure, two chemical dispersants, Corexit EC9500A (6.8 million liters) and Corexit EC9527A (1.1 million liters) were applied at the wellhead and on the

seawater surface to disperse the oil slicks into the water column (Kujawinski et al., 2011). As a result, it was estimated that 16% of the spilled oil was dispersed by chemical dispersants (Ramseur, 2010). While several recent studies have reported that oil dispersant enhanced degradation of oil, particularly *n*-alkanes, under conditions relevant to the northern Gulf of Mexico, a thorough understanding of the process and mechanisms is needed (Bacosa, 2015; Liu et al., 2016).

The use of oil dispersants has become one of major emergency response measures to cope with oil spills and to mitigate the environmental impacts. According to the U.S. Environmental Protection Agency's National Contingency Plan Subpart J Product Schedule, there are currently 22 oil dispersants that are available and authorized to use during an oil spill. During the 2010 *DwH* oil spill, BP applied ca. 6.8 million liters of Corexit EC9500A and 1.1 million liters Corexit EC9527A at the sea surface and the wellhead (Bianchi et al., 2014; Kujawinski et al., 2011). As a result, it was estimated that ~16% of the spilled oil was dispersed by the dispersants (Ramseur, 2010).

Oil dispersants are complex mixtures of anionic, nonionic surfactants, and solvents (Board and Council, 1989; Gong et al., 2014). Corexit EC9500A consists of three nonionic surfactants including ethoxylated sorbitan mono- and trioleates and sobitan monooleate (commercially known as Tween 80, Tween 85, and Span 80) and an anionic surfactant, namely, sodium dioctyl sulfosuccinate (SDSS) and solvents as a mixture of di(propylene glycol) butyl ether (DPnB), propylene glycol, and hydro-treated light distillates (petroleum) (Cai et al., 2016; Place et al., 2010; Scelfo and Tjeerdema, 1991). Numerous studies have investigated the impacts of surfactants on sorption and desorption of hydrophobic organic compounds (HOC). There are two contrasting effects: On one hand, surfactant can increase the solubility of HOC, by portioning them into the hydrophobic cores of surfactant micelles, which reduces sorption, and facilitates desorption of

HOC. On the other hand, the sorption of surfactant itself to the solid matrix may enhance the HOC sorption by partitioning HOC into immobile adsorbed surfactant.

While oil dispersants are aimed to enhance the aqueous apparent solubility and bioavailability of crude oil (Mendoza et al., 2013; Zhou and Guo, 2012; Zhou et al., 2013), our knowledge on their roles in altering the environmental fate and transport of spilled oil in the aquatic environment (including marine ecosystems) has been limited. Fu et al. (2014) observed that the dispersant Corexit EC9500A facilitated the formation of marine oil snow (MOS), leading to vertical transport (rising or sinking) of dispersed oil. In addition, they observed that the dispersant not only enhanced dissolution of *n*-alkanes (C9–C40) from oil slicks into the aqueous phase, but facilitated sorption of more oil components onto MOS. Gong et al. (2014) studied that the effect of oil dispersant (Corexit EC9500A) on sorption/desorption of phenanthrene with two marine sediments, indicating that the presence of the dispersant (18 mg/L) can not only enhance the uptake of phenanthrene by up to 7% but reduce the desorption of phenanthrene by up to 5%. In addition, Zhao et al. (2015) investigated three dispersants (Corexit EC500A, Corexit EC9527A and SPC 1000) in the simulated marine system. They found that additional dispersant Corexit EC9500A (18 mg/L) can increase the uptake of 2-3 ring PAHs on sediment, whereas higher dispersant dosages will reduce the uptake.

The past use of chemical dispersants in response to oil spills in the U.S. has been limited primarily to offshore marine waters (typically ≥ 3 miles from the shoreline). As the use of dispersants is becoming more accepted, there is an growing interest in their use in nearer shore (Herndon, 2010). However, near-shore application of oil dispersants may generate larger amounts of wastewater containing high concentrations 0.5–50 mg/L (McAuliffe, 1989) of dispersed oil (i.e., dispersed oil droplets with dispersant molecules). It was reported that dispersed

oil can be more toxic or pose more acute toxicity to marine life or aquatic communities than the oil slicks (Anderson et al., 2009; Bejarano and Barron, 2014; Mitchell and Holdway, 2000; Singer et al., 1998; Singer et al., 1991). As such, invasion of the wastewater into coastal sensitive areas pose a serious threat to the health of coastal ecosystems and human health. Moreover, as dispersants are often used in combination with other clean-up methods (e.g., skimmers, booms, and/or burning) and used to clean or remove oil from wildlife or from beach areas, larger amounts of wastewater with dispersed oil are generated. For instance, during the DwH oil spill, estimated 20 millions of gallons of oil-laden wastewater were produced near shore, which demanded costly further handling or treatment (Beyer et al., 2016; Fakhru'l-Razi et al., 2009; Lee and Neff, 2011; Short, 2017).

A number of physical, chemical and biological processes can affect the fate and transport of spilled oil, including spreading, drifting, evaporation and dissolution (Liu et al., 2012; 2017; Ryerson et al., 2011), dispersion of oil droplets into the water column (Conmy et al., 2014; Kleindienst et al., 2015), interactions of dissolved and dispersed oil compounds with suspended particulate matter and sediment particles (Fu et al., 2014; Gong et al., 2014; Zhao et al., 2015; Zhao et al., 2016), sorption (Gong et al., 2014; Zhao et al., 2015; Zhao et al., 2016), bioaccumulation and biodegradation (Baumard et al., 1998), and photodegradation (Gong et al., 2015; Zhao et al., 2016). Another potentially significant oil weathering process is oxidation by atmospheric ozone (O_3). However, ozonation has been completely ignored in estimating oil budget and in assessing the fate and weathering of spilled oil despite the known high reactivity and fairly high concentrations of atmospheric ozone at the ground or sea level. This research is described in detail in Chapter 2, 3 and 5.

1.2 Oxidation of oil spill by atmospheric ozone

Typically, surface-level ozone is formed through photochemical reactions involving volatile organic compounds (VOCs) and nitrogen oxides (Haagen-Smit et al., 1953). High levels of ozone have been widely detected at the ground level along the Gulf of Mexico coast. For instance, based on 2002-2013 monitoring data, the 8-hour average ozone in Alabama air ranged from 60 to 92 ppbv (ADEM, 2016). Nationally, the average of the fourth highest daily maximum 8-h ozone level had consistently exceeded the then National Ambient Air Quality Standards (NAAQS) of 75 ppbv from 1986 through 2016 (EPA, 2017). It is noted that the ozone levels over an oil slick may be much higher than in the bulk air due to the extensive evaporation of volatile hydrocarbons from the oil slick (Ryerson et al., 2011).

Ozone is a well-known strong oxidant ($E^0 = +2.07$ V) and relatively strong electrophile (Yu et al., 2007). In engineered processes, ozone has been widely used to degrade various organic compounds, including PAHs (Chelme-Ayala et al., 2011; Lin et al., 2014; von Gunten, 2003) and *n*-alkanes (Masten and Davies, 1994; von Gunten, 2003; Yu et al., 2007). In general, ozonation of organic compounds (e.g., *n*-alkanes and PAHs) can take place in the following fashions: 1) direct attack by molecular O₃ on the σ -bond between C and H atoms via 1,3-dipolar insertion for alkanes or via cycloaddition or electrophilic reactions for PAHs (Hellman and Hamilton, 1974); and 2) indirect attack by free radicals (primarily hydroxyl radicals, •OH) (Masten and Davies, 1994; Zhao et al., 2004, 2011). Therefore, it is reasonable to postulate that oxidation under atmospheric ozone is an important natural weathering process for petroleum hydrocarbons.

Ozonation of organic contaminants can be affected by surfactants, and the effect depends on the type of the surfactants (anionic, nonionic and cationic). Pryor and Wu (1992) reported that the ozonation of methyl oleate was increased by 1.2 times when an anionic surfactant, sodium

dodecyl sulfate (SDS), was increased from 0.02 M to 0.5 M. Chiu et al. (2007) observed that the presence of a nonionic surfactant Brij 30 decreased the gas–liquid mass transfer rates of both naphthalene and ozone, resulting in reduced removal efficiency of naphthalene. Chu et al. (2006) reported that ozonation of atrazine was enhanced by 17% by adding a nonionic surfactant, Brij 35, and the researchers stated that the surfactant played dual roles in the ozonation of atrazine: 1) it increased dissolution of ozone, and 2) it served as a radical booster and hydrogen source. Therefore, oil dispersants may also affect oil ozonation. Gong and Zhao (2017) observed that the presence of 18 and 180 mg/L of Corexit 9500A inhibited the ozonation rate of phenanthrene by 32%-80%, and that for pyrene by 51%-85%, due to competition for the reactive ozone and free radicals. They also reported that in the presence of 18 mg/L of the dispersant, the pyrene degradation rate decreased with increasing solution pH and temperature. However, information has been lacking on the effects of oil dispersants on the ozonation of petroleum hydrocarbons (e.g. TPHs, *n*-alkanes and PAHs). Moreover, the influences of ozone concentration, pH, DOM and salinity on ozonation of petroleum hydrocarbons in the presence of oil dispersants have not yet been explored. This research is reported in Chapter 2.

1.3 Removal of spilled oil by various sorbents

Since dispersants are designed to disperse oil slicks into water column, the high salinity and high concentration of dispersed oil in the resulting wastewater impede effective separation or degradation of the petroleum hydrocarbons through conventional municipal wastewater treatment processes. To facilitate oil removal from water, researchers have studied various types of sorbents, such as activated charcoal/carbon (AC) (Ahmad et al., 2005; Ayotamuno et al., 2006; Pollard et al., 1992), biochar (Nguyen and Pignatello, 2013), synthetic nanocomposites (Chu and Pan, 2012),

aerogel (Chin et al., 2014), fibers (Zhu et al., 2011), exfoliated graphite (Toyoda and Inagaki, 2003; Wang et al., 2010), peat-based materials (Cojocaru et al., 2011), sponge or foam (Calcagnile et al., 2012; He et al., 2013; Liu et al., 2013), natural materials (Kumagai et al., 2007) and other types of sorbents (Adebajo et al., 2003; Guix et al., 2012; Yu et al., 2012). However, the knowledge on the effects of oil dispersants on the sorption of dispersed petroleum hydrocarbons by activated charcoal has been very limited. In addition, the influences of other factors such as pH and salinity on the sorption of oil hydrocarbons in the presence of oil dispersants have not yet been explored. This research is reported in Chapter 3.

1.4 Enhanced adsorption and photodegradation using engineered catalysts

Heterogeneous photocatalysis using TiO_2 under UV-irradiation and/or solar light has shown great potential (Grover et al., 2014; Nakata and Fujishima, 2012) and drawn great interest in recent years (Chen and Burda, 2008; Chen and Mao, 2007a; Liu et al., 2013; Pelaez et al., 2012; Tan et al., 2014) for the photocatalytic decomposition and adsorption of organic contaminants due to their low-cost, environmental friendly and high photocatalytic activity (PCA). TiO_2 is a typical *n*-type semiconductor with relatively large band gaps (Pelaez et al., 2012), which can limit its optical absorption in the solar spectrum consisting of UV, visible and infrared (IR) radiations with a relative energy distribution of ~5%, 43% and 55%, respectively (Chen et al., 2015; Shankar et al., 2015). Therefore, a great deal of effort has been devoted to improving the visible light absorption of TiO_2 . Zhao et al. (2016) prepared a new type of photocatalyst, referred to as cobalt-doped titanate nanotubes for catalyzing photodegradation of phenanthrene under solar light, which was about 10 times higher removal efficiency than the original TiO_2 photocatalysts. Pal et al. (Grover et al., 2017) developed the $\text{SiO}_2@ \text{TiO}_2$ nanocomposites for adsorption and photocatalytic

degradation of naphthalene and anthracene. The results indicated that the PCA in the presence of SiO₂ was improved.

However, lower specific surface areas of TiO₂, fewer reacting molecules can adsorb on the surface, which indicates the disadvantage of its PCA. Based on this content, surface modification of TiO₂ through depositing, coating and other ways with inert compounds, especially SiO₂, has elicited numerous research interest (Chen and Mao, 2007b; Grover et al., 2017; Haghightzadeh et al., 2017; Nussbaum and Paz, 2012). Silica aerogel is an effective adsorbent for oil hydrocarbons (Adebajo et al., 2003; Standeker et al., 2007; Wang et al., 2012), and it can float on water due to its mesoporous structure and low density. Considering the excellent photocatalytic activity of TiO₂ and good adsorptive performance of silica aerogel, depositing nano-TiO₂ onto silica aerogel may result in a highly efficient supported photocatalyst that can remove TPHs through initial adsorption and subsequent photocatalysis. In this study, a series of new composite materials, namely, silica aerogel supported TiO₂ (denoted as TiO₂/SiO₂), were synthesized through a sol-gel method, and these novel materials were found highly efficient for removing phenanthrene (and possibly other PAHs) via simultaneous adsorption and photocatalysis. Moreover, the synthetic materials can float on the water, which offer great convenience for *in-situ* oil removal from contaminated water. This research is reported in Chapter 4.

It is well known that the morphology of TiO₂ has a great effect on its photocatalytic activity. Of various modifications, one-dimensional titanate nanotubes (TNTs) synthesized by hydrothermal treatment of TiO₂ have gained significant attention in recent years (He et al., 2013; Liu et al., 2013a; Liu et al., 2013b). We therefore expect that the synthesis of titanium nanotubes (TNTs) and hybridize with active charcoal to improve the adsorption and photocatalytic activity.

Taking advantage of the high adsorption capacity of AC and photocatalytic activity of TNTs, we conceived a novel composite material, referred to as TNTs@AC, by depositing TNTs onto a common activated charcoal. This research is reported in Chapter 5.

1.5 Objectives

The overall objectives of this proposed research are to demonstrate and evaluate the performance of atmospheric ozone *in situ* strategy to oxidation of dispersed hydrocarbons in seawater and to determine effects of oil dispersants on ozonation process and sorption behavior using activated charcoals of oil components in the Gulf marine ecosystems. And to develop the catalyst as a “green” (environmental friendly) and cost-effective technology that can rapidly and completely degrade oil components or organic compounds by enhancing the natural weathering processes. The specific objectives are to:

- Determine the role of surface-level ozone oxidation in weathering of oil components (i.e. TPHs, *n*-alkanes, and PAHs) in seawater, and examine how dispersants affect the reactions; Understand the roles of a model dispersant (Corexit 9500A) in the ozonation process.
- Investigate the effects of oil dispersant on the sorption of dispersed oil using activated charcoal, and understand the roles of oil dispersant in the sorption process. The specific objectives were to: 1) determine the kinetics rates and isotherm of dispersed oil in two different DWAO by activated charcoal, 2) investigate the effects of a model dispersant (Corexit EC9500A and Corexit EC9527A) on the sorption process; and 3) elucidate the sorption mechanisms.

- Develop a new technology for enhancing the natural photodegradation of spilled oil by developing a new class of low-cost and ‘green’ photocatalysts. Test the effectiveness of the catalyst for oil components adsorption and photodegradation.

1.6 Organization

This dissertation consists of six chapters and is formatted in the style specified by the journal *Water Research* except for Chapter 1 (General Introduction) and Chapter 6 (Conclusions and Suggestions for Future Research). Chapter 1 introduces the background and objectives of this dissertation. Chapter 2 investigates the ozonation rate and extent of dispersed oil in dispersant-oil-seawater systems that are exposed to relatively high surface-level atmospheric ozone, and understand the roles of a model dispersant (Corexit 9500A) in the ozonation process. Various effects (i.e. dispersant, pH, humic acid, salinity) for the ozonation of oil components in dispersant-oil-seawater systems were tested. This chapter is based on a paper previously published in the journal *Marine Pollution Bulletin* (Ji et al., 2018). Chapter 3 presents the effects of oil dispersant on the sorption of dispersed oil using activated charcoal and the explanation for the sorption mechanism based on the characterization of activated charcoal, including BET, XRD, FTIR and Zeta potential. Chapter 4 develops and tests a new type of silica aerogel supported TiO₂ (TiO₂/SiO₂) composite materials for efficient removal of phenanthrene (as a model of PAHs) under solar light. Meanwhile, elucidate the mechanisms for adsorption and photocatalysis by characterizing the morphology, crystal phases and compositions of TiO₂/SiO₂. In addition, we test the synergistic effect between ozonation and photodegradation using TiO₂/SiO₂ for remove the oil hydrocarbons in DWAO. Chapter 5 reports a novel bi-functional material, i.e. activated charcoal supported titanate nanotubes (TNTs@AC) that offers both high adsorption capacity and efficient

photodegradation/regeneration for rapid and complete removal of oil components in seawater. Chapter 6 summarizes the major conclusions of this research and makes suggestions for future work. Appendix contains other related figures with the major parts, like synthesized materials, prepared samples, equipment and so on.

Chapter 2. Degradation of petroleum hydrocarbons in seawater by simulated surface-level atmospheric ozone: Reaction kinetics and effect of oil dispersant

This chapter introduces the ozonation rate and extent of typical petroleum compounds by simulated surface-level ozone, including total petroleum hydrocarbons (TPHs), *n*-alkanes, and polycyclic aromatic hydrocarbons (PAHs). Moreover, the work explored the effect of a prototype oil dispersant, Corexit EC9500A, on the ozonation rate. Effects of various water chemistry on ozonation of petroleum hydrocarbons in DWAO (i.e. pH, humic acid, salinity) were evaluated.

2.1 Introduction

The 2010 Deepwater Horizon (*DwH*) oil spill released more than 795 million liters of Louisiana Sweet Crude (LSC) oil into the Gulf of Mexico (Camilli et al., 2010; Reddy et al., 2012; Sammarco et al., 2013). As a result, high concentrations of oil compounds in the water column were detected following the spill. For instance, Camilli et al. (2010) reported that the concentration of mono-aromatic petroleum hydrocarbons in the affected seawater exceeded 50 mg/L, and Reddy et al. (2012) observed that the light aromatic hydrocarbons (benzene, toluene, ethylbenzene, and total xylenes) reached up to 78 mg/L. The *DwH* oil contained ~3.9% total polycyclic aromatic hydrocarbons (TPAHs), ~1.5% alkylated PAHs, and ~15.3% *n*-alkanes by weight; as such, the incident released approximately $\sim 2.1 \times 10^7$ kg of TPAHs, $\sim 7.9 \times 10^6$ kg of alkylated PAHs, and $\sim 8.1 \times 10^7$ kg of *n*-alkanes into the Gulf of Mexico (Reddy et al., 2012).

As an emergency mitigation measure, two chemical dispersants, Corexit EC9500A (6.8 million liters) and Corexit EC9527A (1.1 million liters) were applied at the wellhead and on the

seawater surface to disperse the oil slicks into the water column (Kujawinski et al., 2011). As a result, it was estimated that 16% of the spilled oil was dispersed by chemical dispersants (Ramseur, 2010). While several recent studies have reported that oil dispersant enhanced degradation of oil, particularly *n*-alkanes, under conditions relevant to the northern Gulf of Mexico, a thorough understanding of the process and mechanisms is needed (Bacosa, 2015; Liu et al., 2016).

A number of physical, chemical and biological processes can affect the fate and transport of spilled oil, including spreading, drifting, evaporation and dissolution (Liu et al., 2012; 2017; Ryerson et al., 2011), dispersion of oil droplets into the water column (Conmy et al., 2014; Kleindienst et al., 2015), interactions of dissolved and dispersed oil compounds with suspended particulate matter and sediment particles (Fu et al., 2014; Gong et al., 2014; Zhao et al., 2015; Zhao et al., 2016), sorption (Gong et al., 2014; Zhao et al., 2015; Zhao et al., 2016), bioaccumulation and biodegradation (Baumard et al., 1998), and photodegradation (Gong et al., 2015; Zhao et al., 2016). Another potentially significant oil weathering process is oxidation by atmospheric ozone (O₃). However, ozonation has been completely ignored in estimating oil budget and in assessing the fate and weathering of spilled oil despite the known high reactivity and fairly high concentrations of atmospheric ozone at the ground or sea level.

Typically, surface-level ozone is formed through photochemical reactions involving volatile organic compounds (VOCs) and nitrogen oxides (Haagen-Smit et al., 1953). High levels of ozone have been widely detected at the ground level along the Gulf of Mexico coast. For instance, based on 2002-2013 monitoring data, the 8-hour average ozone in Alabama air ranged from 60 to 92 ppbv (ADEM, 2016). Nationally, the average of the fourth highest daily maximum 8-h ozone level had consistently exceeded the then National Ambient Air Quality Standards (NAAQS) of 75 ppbv from 1986 through 2016 (EPA, 2017). It is noted that the ozone levels over

an oil slick may be much higher than in the bulk air due to the extensive evaporation of volatile hydrocarbons from the oil slick (Ryerson et al., 2011).

Ozone is a well-known strong oxidant ($E^0 = +2.07$ V) and relatively strong electrophile (Yu et al., 2007). In engineered processes, ozone has been widely used to degrade various organic compounds, including PAHs (Chelme-Ayala et al., 2011; Lin et al., 2014; von Gunten, 2003) and *n*-alkanes (Masten and Davies, 1994; von Gunten, 2003; Yu et al., 2007). In general, ozonation of organic compounds (e.g., *n*-alkanes and PAHs) can take place in the following fashions: 1) direct attack by molecular O₃ on the σ -bond between C and H atoms via 1,3-dipolar insertion for alkanes or via cycloaddition or electrophilic reactions for PAHs (Hellman and Hamilton, 1974); and 2) indirect attack by free radicals (primarily hydroxyl radicals, •OH) (Masten and Davies, 1994; Zhao et al., 2004, 2011). Therefore, it is reasonable to postulate that oxidation under atmospheric ozone is an important natural weathering process for petroleum hydrocarbons.

Oil dispersants are complex mixtures of anionic, nonionic surfactants, and solvents (Board and Council, 1989; Gong et al., 2014). Corexit EC9500A consists of three nonionic surfactants including ethoxylated sorbitan mono- and trioleates and sobitan monooleate (commercially known as Tween 80, Tween 85, and Span 80) and an anionic surfactant, namely, sodium dioctyl sulfosuccinate (SDSS) and solvents as a mixture of di(propylene glycol) butyl ether (DPnB), propylene glycol, and hydro-treated light distillates (petroleum) (Cai et al., 2016; Place et al., 2010; Scelfo and Tjeerdema, 1991).

Ozonation of organic contaminants can be affected by surfactants, and the effect depends on the type of the surfactants (anionic, nonionic and cationic). Pryor and Wu (1992) reported that the ozonation of methyl oleate was increased by 1.2 times when an anionic surfactant, sodium dodecyl sulfate (SDS), was increased from 0.02 M to 0.5 M. Chiu et al. (2007) observed that the

presence of a nonionic surfactant Brij 30 decreased the gas–liquid mass transfer rates of both naphthalene and ozone, resulting in reduced removal efficiency of naphthalene. Chu et al. (2006) reported that ozonation of atrazine was enhanced by 17% by adding a nonionic surfactant, Brij 35, and the researchers stated that the surfactant played dual roles in the ozonation of atrazine: 1) it increased dissolution of ozone, and 2) it served as a radical booster and hydrogen source. Therefore, oil dispersants may also affect oil ozonation. Gong and Zhao (2017) observed that the presence of 18 and 180 mg/L of Corexit 9500A inhibited the ozonation rate of phenanthrene by 32%-80%, and that for pyrene by 51%-85%, due to competition for the reactive ozone and free radicals. They also reported that in the presence of 18 mg/L of the dispersant, the pyrene degradation rate decreased with increasing solution pH and temperature. However, information has been lacking on the effects of oil dispersants on the ozonation of petroleum hydrocarbons (e.g. TPHs, *n*-alkanes and PAHs). Moreover, the influences of ozone concentration, pH, DOM and salinity on ozonation of petroleum hydrocarbons in the presence of oil dispersants have not yet been explored.

The overall goal of this study was to investigate the ozonation rate and extent of dispersed oil in dispersant-oil-seawater systems that are exposed to relatively high surface-level atmospheric ozone, and understand the roles of a model dispersant (Corexit 9500A) in the ozonation process. The specific objectives were to: 1) determine the ozonation rate and extent of various key petroleum components (TPHs, *n*-alkanes and PAHs) under simulated surface-level atmospheric ozone, 2) investigate effect of Corexit 9500A on the ozone oxidation; and 3) elucidate the ozonation mechanisms. The findings will improve our understanding of the role of atmospheric ozone in the weathering of spilled oil.

2.2 Materials and Methods

2.2.1 Materials

All chemicals used in this study were of analytical grade or higher unless indicated otherwise. Methanol and 1,4-benzoquinone were purchased from Alfa Aesar (Ward Hill, MA, USA). Chromatographic hexane, dichloromethane (DCM), NaOH and NaCl were obtained from Fisher Scientific (Fair lawn, NJ, USA). HCl was acquired from BDH Aristar (West Chester, PA, USA). 4-chlorobenzoic acid (*p*CBA) was procured from Acros Organics (Morris Plains, NJ, USA). A standard leonardite humic acid (LHA, IHSS 1S104H, 64% as total organic carbon (TOC)) was purchased from the International Humic Substances Society. The following standard reagents were purchased from Supelco (Bellefonte, PA, USA): a standard of *n*-alkanes mixtures (C9–C40), a standard for the 16 USEPA listed PAHs (**Table 2-1**), two internal standards (5 α -androstande for *n*-alkanes and fluorene-d₁₀ for PAHs), and a surrogate standard of naphthalene-d₈, acenaphthene-d₁₀, phenanthrene-d₁₀, and benzo(a)pyrene-d₁₂. Corexit EC9500A was obtained by courtesy of Nalco Company (Naperville, IL, USA). **Table 2-2** gives the formulations of Corexit EC9500A.

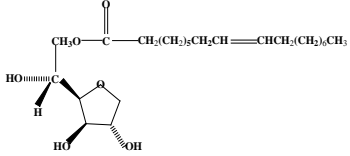
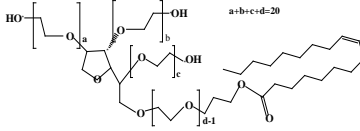
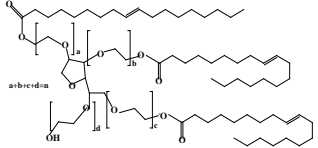
Table 2-1. Target PAHs compounds and quantification ions (QIs).

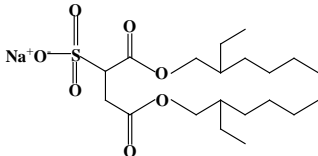
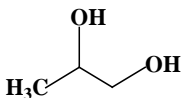
Abbr ^a	Compounds	QIs ^b	Abbr	Compounds	QIs
	Parent PAHs			Alkylated PAHs	
	2-Ring			2-Ring	
Naph	Naphthalene	128	C1-Naph	C1-Naphthalenes	142
			C2-Naph	C2-Naphthalenes	156
			C3-Naph	C3-Naphthalenes	170
			C4-Naph	C4-Naphthalenes	184
	3-Ring			3-Ring	
AcI	Acenaphthylene	152			
Ace	Acenaphthene	154			
Fluo	Fluorene	166			
Phen	Phenanthrene	178	C1-Fluo	C1-Fluorenes	180
An	Anthracene	178	C2-Fluo	C2-Fluorenes	194
			C3-Fluo	C3-Fluorenes	208
			C1-PhenAn	C1-Phenanthrenes/anthracenes	192
Fl	Fluoranthene	202	C2-PhenAn	C2-Phenanthrenes/anthracenes	206
Py	Pyrene	202	C3-PhenAn	C3-Phenanthrenes/anthracenes	220
BaA	Benz(a)anthracene	228	C4-PhenAn	C4-Phenanthrenes/anthracenes	234
Chry	Chrysene	228			
	4-Ring			4-Ring	
			C1-FIPy	C1-Fluoranthrenes/pyrenes	216
BbF	Benzo(b)fluoranthene	252	C2-FIPy	C2-Fluoranthrenes/pyrenes	230
BkF	Benzo(k)fluoranthene	252	C3-FIPy	C3-Fluoranthrenes/pyrenes	244
BaP	Benzo(a)pyrene	252	C1-ChryBa	C1-Chrysenes/benz(a)anthracene	242
IP	Indeno(1,2,3-cd)pyrene	276	C2-ChryBa	C2-Chrysenes/benz(a)anthracene	256
DA	Dibenz(a,h)anthracene	278	C3-ChryBa	C3-Chrysenes/benz(a)anthracene	270
BgP	Benzo(ghi)perylene	276			

^a Abbr: Abbreviation

^b QIs: quantification ions

Table 2-2. Chemical constituents of dispersant Corexit EC9500A^a.

Name	CAS number	Ionic property	Synonym	Molecular formula	Average		CMC (mg/L)	Chemical structure
					MW (g/mol)	HLB		
Span 80	1338-43-8	Neutral surfactant	Sorbitan, mono-(9Z)-9-octadecenoate	C ₂₄ H ₄₄ O ₆	428.61	4.3	N/A	
Tween 80	9005-65-6	Neutral surfactant	Sorbitan, mono-(9Z)-9-octadecenoate, poly(oxy-1,2-ethanediyl) derivs.	C ₆₄ H ₁₂₄ O ₂₆	1310	15	14	
Tween 85	9005-70-3	Neutral surfactant	Sorbitan, tri-(9Z)-9-octadecenoate, poly(oxy-1,2-ethanediyl) derivs	C ₆₀ H ₁₀₈ O ₈ (C ₂ H ₄ O) _n	1838.57	11	23	

DOSS	577-11-7	Anionic surfactant	Butanedioic acid, 2-sulfo-, 1,4-bis(2-ethylhexyl) ester, sodium salt (1:1)	$C_{20}H_{37}SO_7Na$	444.57	10.9	578	
DPnB	29911-28-2	Solvent	Propanol, 1-(2-butoxy-1-methylethoxy)	$C_{10}H_{22}O_3$	190		N\A	$H_3C-CH_2-CH_2-CH_2-OC_3H_6OC_3H_6OH$
PG	57-55-6	Solvent	Propylene Glycol, 1,2-dihydroxypropane	$CH_3CHOHCH_2OH$	76.1		N\A	
Distillates	64742-47-8	Solvent	Distillates (petroleum), hydrotreated light	N\A	N\A		N\A	N\A

^aThe above information is summarized based on several studies (Zhao et al. 2015, Gong et al. 2014, Glover et al. 2014, Kover et al. 2014, Omotosho et al. 1989, Nadarajah et al. 2002, Koos et al. 2012).

Seawater was collected from the top 30 cm of the water column from Grand Bay, AL, USA (N30.37926/W88.30684). Before use, the sample was first passed through 0.45 μm membrane filters to remove suspended solids, and then sterilized at 121 $^{\circ}\text{C}$ for 35 min via autoclaving. Salient properties of the seawater sample are: pH = 8.1, DOM = 2.2 mg/L as TOC, salinity = 2 wt.%, Cl^- = 18.55 g/L, NO_3^- = 2.55 g/L, SO_4^{2-} = 4.25 g/L, and ionic strength (IS) = 0.7 M.

A surrogate LSC oil was obtained through courtesy of BP (Houston, TX, USA). According to the supplier, the physical, chemical and toxicological properties of the surrogate oil are analogous to those of the Macondo Well crude oil of Mississippi Canyon Block 252. Before use, the crude oil was artificially weathered according to the evaporation method by Sorial et al. (2004). Briefly, 1.0 L of the crude oil was purged in the dark through a glass tube from the bottom of a flask at a constant air flowrate of ~ 2 L/min to remove the lighter compounds. After 10 days of the weathering process, the oil mass diminished from 807.1 to 608.5 g (by 24.6 wt.%), and the density increased from 0.807 to 0.834 g/cm^3 . This procedure simulates the loss of the volatile oil compounds at sea surface shortly following an oil spill (Li et al., 2009).

2.2.2 Experimental set-up

Fig. 2-1 displays the schematic of the ozonation experiment set-up. The experiments were carried out in a glass cylinder batch reactor ($\text{H} \times \text{D} = 5 \text{ cm} \times 8 \text{ cm}$) with a thin quartz cover. The two ports connected with Teflon tubes were for gas flow and the other two ports sealed by ground glass joints were used for sample collection. Ozone was generated from medical grade oxygen using an A2Z Ozone Generator (Model HB5735B, A2Z Ozone Inc., Louisville, Kentucky, USA), which is able to generate a maximum of 1 g ozone h^{-1} . The gas ($\text{O}_2 + \text{O}_3$) flow rate into the reactor was 4

mL/min controlled by an Aalborg mass flow controller (Model GFC17, Orangeburg, New York, USA). The inlet ozone-laden gas was gently passed through the surface of the reaction solution. The inlet gas-phase ozone concentration was kept at 86 ppbv, which was analyzed by a M106-L Ozone Monitor (2B Technologies, Inc., Boulder, CO, USA) through measuring the UV absorbance at 254 nm. In the outlet gas-phase, the excess ozone was passed into a gas absorption bottle containing 300 mL of a 2 wt.% KI solution. All connecting tubes were Teflon-made.

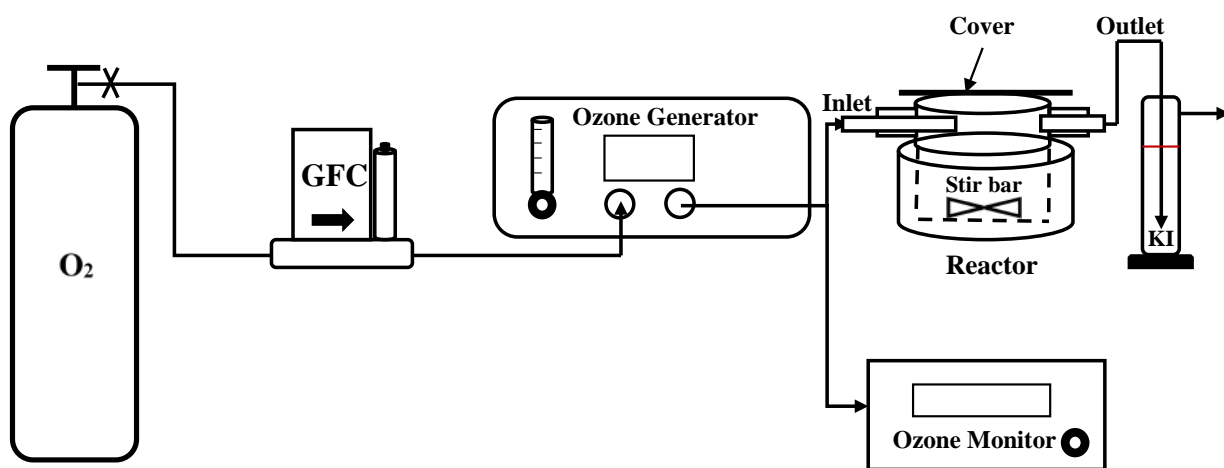


Figure 2-1. Schematic of the experimental set-up for ozonation of dispersed oil under simulated atmospheric ozone. Note: GFC: gas flow controller.

2.2.3 Ozonation of dispersed oil and effects of dispersant

Water accommodated oil (WAO) and dispersant-facilitated water accommodated oil (DWAO) were prepared with the surrogate oil following a slightly modified protocol by Singer et al. (2000). Briefly, WAO was prepared in a 2200 mL glass aspirator bottle containing a hose bib fitted with silicon tubing and a clamp at the bottom of the vessel. About 1760 mL of the seawater

was added into the bottle, leaving a ~20% headspace. Afterwards, 8.8 mL of the weathered LSC oil was added to the seawater by a glass syringe (i.e., oil-to-seawater volume ratio = 1:200). Then, the mixture was sealed and magnetically stirred for 18 h in the dark. The stirring rate was adjusted so as to obtain a vortex of ~25% of the total volume of seawater. After gravity-settling for 6 h, the WAO fraction was collected in glass vials with Teflon-lined caps from the bottom without disturbing the surface oil slicks, allowing for no headspace in the vials. The dispersed oil was prepared in the form of DWAO following the same protocol except that a dispersant solution of Corexit EC9500A was added at a dispersant-to-oil volume ratio of 1:20 (Gong et al., 2014; Zhao et al., 2016).

Batch ozonation kinetic tests were conducted in the glass cylinder reactor. For each test, the reactor was filled with 250 mL of a WAO or DWAO solution, and stirred gently (400 rpm) with a magnetic stirrer to simulate ocean wave action, which is expected to enhance the ozonation due to increased gas-water interface and mass transfer rates. The ozone-laden gas stream was then gently passed through the surface of the solution (i.e., the headspace of the reactor). At pre-determined times, each 80 mL of the solution was sampled and then analyzed for the remaining petroleum hydrocarbons (including *n*-alkanes, parent PAHs and their alkylated homologs). Control tests were carried out with nitrogen gas (no O₃) at the same gas flowrate to determine the loss of TPHs in WAO and DWAO due to volatilization. All experiments were conducted in duplicate.

To investigate effects of the dispersant, additional Corexit EC9500A (18 or 24 mg/L) was added into the as-prepared DWAO solution in selected cases, and the ozonation rates were then tested following the same kinetic experiments.

To examine the relative contributions of direct ozone oxidation and indirect oxidation (by •OH), the ozonation kinetic tests were carried out in the presence of 3 μM of *para*-chlorobenzoic

acid (*p*CBA), which has been known to be very slow in direct reaction with ozone but fast with •OH ($k_{\text{OH}, p\text{CBA}} = 5 \times 10^9 \text{ M}^{-1}\text{s}^{-1}$, $k_{\text{O}_3, p\text{CBA}} \leq 0.5 \text{ M}^{-1}\text{s}^{-1}$) (Elovitz and von Gunten, 1999).

As a control, dispersant solutions without oil were prepared under otherwise identical conditions and then analyzed for the non-petroleum hydrocarbons (i.e., hydrocarbons from the dispersant) following the procedure described in Section 2.2.5. The chromatographic peak areas associated with the non-petroleum hydrocarbons were deducted from those for DWAO in quantifying the petroleum hydrocarbons following the approach by Hemmer et al. (2011).

2.2.4 Effects of gaseous ozone concentration and solution chemistry on ozonation of petroleum hydrocarbons in DWAO

Effects of gaseous ozone concentration, pH, DOM and salinity on ozonation of petroleum hydrocarbons in DWAO were examined through the same kinetic tests as described above. To investigate the ozone concentration effect, the gaseous ozone concentration was varied from 86 to 300 ppbv, which corresponded to an aqueous ozone concentration ranging from 0.05 to 0.12 mg/L. To study the pH effect, the initial DWAO solution pH was adjusted to 6, 7, and 9 using dilute HCl (0.1 M) or NaOH (0.1 M). To examine the effect of DOM, standard leonardite humic acid was added in DWAO at 0.5, 1.0, and 5.0 mg/L as TOC. To test the effect of salinity, the initial solution salinity was varied from 2 to 8 wt.% by adding a NaCl stock solution (25 wt.%).

2.2.5 Analytical methods

Oil concentrations in WAO or DWAO were quantified based on analysis of TPHs, *n*-alkanes, and PAHs. During the kinetic tests, each 80 mL of the solution sample was extracted with dichloromethane (DCM) in three consecutive steps (5 mL DCM in each step) according to EPA

Method 3510C (EPA, 1996), and then the extracts were combined and filtered through a glass column (L×D = 3×1 cm) packed with 5 g of anhydrous sodium sulfate to remove moisture, and then concentrated to 4 mL under a gentle nitrogen flow. Then, the concentrated samples were filtered through a polytetrafluoroethylene (PTFE) membrane (0.22 μm) filter, and split into two even subsamples in two amber glass vials (2 mL each and labeled as B1 and B2). Then, the B1 fraction was analyzed for *n*-alkanes and PAHs by gas chromatography/mass spectrometry (GC-MS) (Agilent 7890A GC coupled with the 5975C Series mass spectrometry, Agilent Technologies Inc., Santa Clara, CA, USA) equipped with a DB-EUPAH column (30 m × 0.18 mm, 0.14 μm film thickness) following the method described as below. Sixteen parent PAHs (**Table 2-1**) (specified in EPA Method 610 (EPA, 1984)) and *n*-alkanes (C9–C40) were targeted. The B2 subsample was analyzed for TPHs following the method described below using gas chromatograph with a flame ionization detector (GC-FID, Agilent 6890 GC-FID) equipped with a DB5 column.

The B1 samples were analyzed for *n*-alkanes (C9-C40) using GC-FID (Agilent 6890 GC-FID system) equipped with a DB5 column (30 m × 0.25 mm, 0.25 μm film thickness). The injection volume was 1 μL with a split ratio of 20. The column temperature was programmed to ramp from 40 to 280 °C at 8 °C min⁻¹ and then held at 280 °C for 60 min (Fu et al., 2014; Liu et al., 2012). GC-MS (Agilent Gas Chromatography 7890A coupled with the 5975C Series Mass Spectrometry) was also used in the total ion mode to identify the non-petroleum hydrocarbons based on the NIST library and the peaks due to the dispersant hydrocarbons. The *n*-alkenes were quantified based on the internal standard of 5-androstane and external standards of *n*-alkenes (C9-C40).

PAHs in B1 were analyzed using the GC-MS system. A total of 16 parent PAHs (specified in EPA Method 610) and 17 alkylated homologues were targeted. The analytical method was

optimized and the selected ion monitoring (SIM) mode was set up based on the previous reports and the National Institute of Standards and Technology (NIST) library (Wang et al., 2007; Liu et al., 2012). A DB-EUPAH column (30 m×0.18 mm, 0.14 μm film thickness) was used to separate the analytes. The inlet temperature was set at 250 °C. The GC oven temperature was programmed as follows: 40 °C (1 min hold) ramped to 280 °C at 8 °C/min and held for 40 min. The sample injection volume was 2 μL. Standard curves were developed for each PAH following EPA Method 610 and the alkylated homologues were estimated according to a semi-quantitative method following the relative response approach (Wang et al., 2007; Yin et al., 2015). The recoveries of the internal surrogate naphthalene-*d*₈, acenaphthene-*d*₁₀, phenanthrene-*d*₁₀ and benzo(a)pyrene-*d*₁₂ were 78 ± 4.2%, 84 ± 4.2%, 96 ± 5.6% and 95.5 ± 6.3%, respectively. **Table 2-1** lists the selected characteristic ions used for each PAH.

For TPHs in B2, we adopted the definition that TPHs refer to the sum of all GC-resolved and unresolved hydrocarbons (Wang and Fingas, 1997). The resolvable TPHs appear as peaks and the unresolved complex mixture (UCM) appears as a “hump” in the chromatograms. The TPHs, which include both peaks and humps on the chromatograms of GC-FID (programmed in the same way as for *n*-alkanes), was quantified using the baseline corrected total area and calculated based on the average response of the *n*-alkenes standards (Faksness et al., 2008).

The *p*CBA concentration in the aqueous phase was analyzed via high performance liquid chromatography (HPLC, Agilent Technologies, 1260 Infinity, DE, USA) with a UV detector and at a wavelength of 240 nm. A Poroshell 120 EC-C18 column (50×4.6 mm, 2.7 μm) was used, with the oven temperature held constant at 30 °C. An eluent consisting of 60%:40% (v:v) of methanol:H₂O (adjusted to pH 2 using H₃PO₄) was used as the mobile phase and the flowrate was 1 mL min⁻¹ (Rosenfeldt et al., 2006).

Dissolved ozone concentration was measured within 1 min after sampling on a UV-vis spectrophotometer (SpectraMax M2, Molecular Devices, CA, USA) at a wavelength of 258 nm shown in **Fig. 2-2** (Bader and Hoigné, 1981; Fujita et al., 2004), which gives a detection limit of 0.01 mg/L.

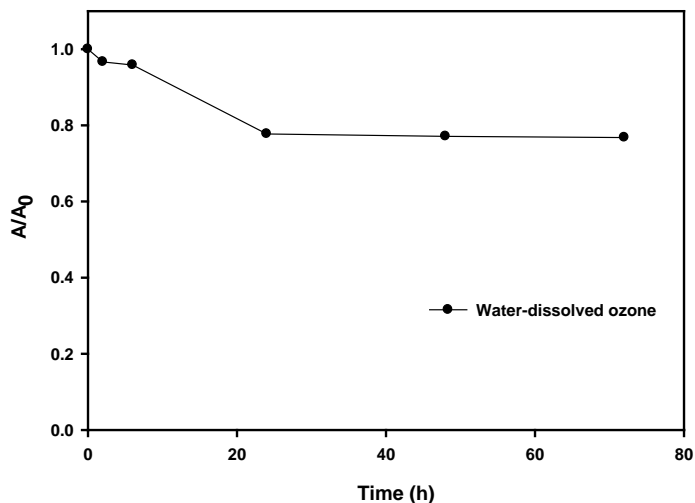


Figure 2-2. UV-Vis absorbance of aqueous ozone in DWAO. Experimental condition: initial TPHs in DWAO = 149.7mg/L, gas flow rate = 4 mL/min, inlet ozone concentration = 86 ppbv, temperature = 22 ± 1 °C, pH = 8.1, salinity = 2 wt.% and initial DOM = 2.2 mg/L as TOC, wavelength = 258 nm.

2.3 Results and Discussion

2.3.1 Effects of oil dispersant on volatilization and ozonation of petroleum hydrocarbons in seawater

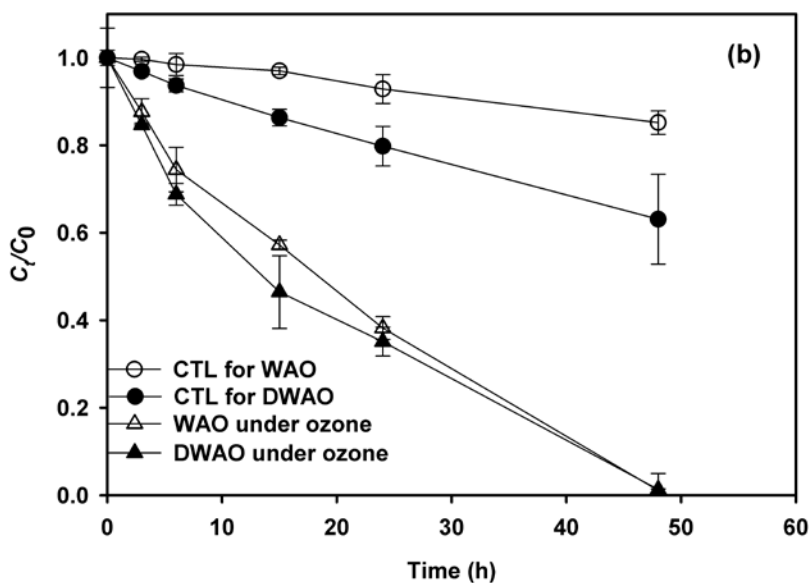
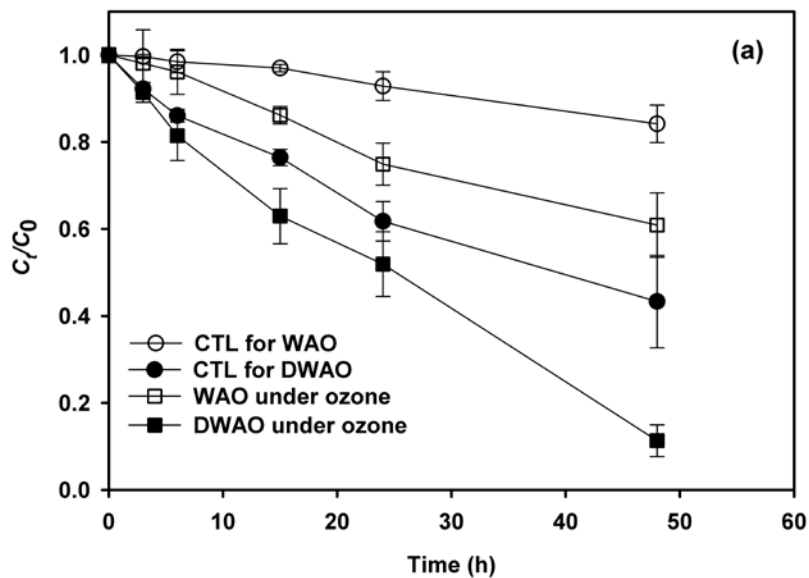
Volatilization is a parallel process along with the ozonation reactions of various oil components. Therefore, an integrated pseudo first-order kinetic model was employed to interpret the overall dissipation rates of TPHs, *n*-alkanes and total PAHs (Lin et al., 2014; Ning et al., 2015):

$$\ln(C_t/C_0) = -kt = -(k_v + k_o)t \quad (2-1)$$

where C_0 (mg/L) and C_t (mg/L) are the reactant concentrations at time $t = 0$ and t (h), respectively; k (h^{-1}) and k_v (h^{-1}) are the pseudo first-order rate constants of overall depletion and volatilization, respectively; and k_o (h^{-1}) is the ozonation rate constant. The values of k and k_v were obtained by fitting Eqn. (2-1) to the corresponding experimental kinetic data (ozonation and volatilization control tests), and k_o was then calculated from the difference.

Fig. 2-3 shows the volatilization and ozonation kinetics of TPHs (**Fig. 2-3a**), *n*-alkanes (**Fig. 2-3b**) and PAHs (**Fig. 2-3c**) under a simulated atmospheric ozone level of 86 ppbv. The initial concentration of TPHs, *n*-alkanes and total PAHs were 0.79, 0.12 and 0.52 mg/L, respectively, in WAO, which were raised to 149.7, 79.1 and 6.2 mg/L in DWAO. Evidently, the presence the dispersant (238 mg/L) increased the concentrations of TPHs by 189 times, *n*-alkanes by 648 times and total PAHs by 12 times compared to those in WAO, which also indicates that the dispersant is more effective for dispersing *n*-alkanes than PAHs. Control tests with nitrogen gas indicated that volatilization losses of TPHs, *n*-alkanes, and total PAHs were 15.8%, 14.8% and 20.5% in WAO in 48 hours, respectively, and the percentiles rose to 56.7%, 36.9% and 52.1% in DWAO, indicating that a larger fraction of the dispersed oil components is volatile than the truly

dissolve counterparts. When exposed to the gaseous ozone, the overall depletion of TPHs, *n*-alkanes, and total PAHs were 56.7%, 98.9% and 81.0% in WAO, and 88.7%, 98.7% and 89.6% in DWAO, respectively, indicating that the ozonation was very reactive in degrading high concentrations of oil hydrocarbons in the dispersant solution.



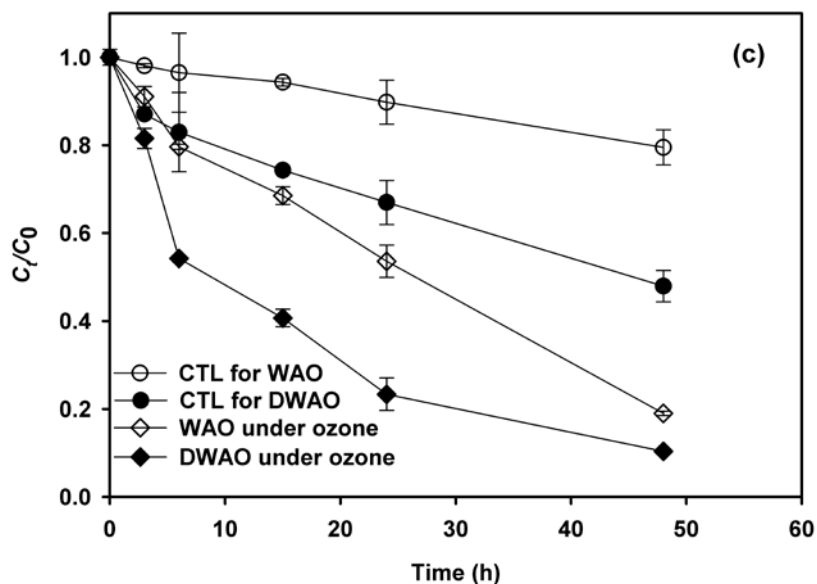


Figure 2-3. Volatilization and ozonation kinetics of: (a) TPHs, (b) n-alkanes and (c) total PAHs in WAO and DWAO (Corexit EC9500A) solutions. Experimental conditions: For WAO, initial TPHs = 0.79 mg/L, n-alkanes = 0.12 mg/L and PAHs = 0.52 mg/L; For DWAO, initial TPHs = 149.70 mg/L, n-alkanes = 79.30 mg/L, PAHs = 6.21 mg/L, and Corexit EC9500A = 238 mg/L; ozone concentration = 86 ppbv, gas flow rate = 4 mL/min, temperature = 22±1 °C, solution volume = 250 mL, pH = 8.1±1, salinity = 2 wt.%, and DOM = 2.2 mg/L as TOC. Symbols: experimental data plotted as mean of duplicates and error bars refer to deviation from the mean to indicate data reproducibility.

Table 2-3 gives the model-fitted kinetic parameters for volatilization and ozonation of TPHs, *n*-alkanes and total PAHs in WAO and DWAO. Both volatilization and overall dissipation of TPHs, *n*-alkanes and total PAHs can be adequately interpreted by the pseudo first-order kinetic model ($R^2 > 0.96$). For WAO, the k_v values of TPHs, *n*-alkanes and total PAHs were determined to be 0.004, 0.003 and 0.005 h⁻¹, respectively, whereas the k_o values were 0.007, 0.041 and 0.025 h⁻¹, when exposed to 86 ppbv of ozone. For DWAO, the k_v values of TPHs, *n*-alkanes and total PAHs

were elevated to 0.018, 0.009 and 0.015 h⁻¹, while the k_o values reached 0.016, 0.042 and 0.048 h⁻¹, respectively. Noting that the total oil mass in DWAO far exceeded that in WAO, the ozonation rate in DWAO was 2.2 times higher than in WAO for TPHs and PAHs, while comparable for *n*-alkanes. The elevated ozonation rates are attributed to the higher concentration, the type of dispersed hydrocarbons and the dispersant effect, as illustrated later in this section and in Section 2.3.3). The data revealed that the dispersed oil components are quite prone to ozonation, and thus, atmospheric ozonation can play a significant role in natural weathering of oil hydrocarbons.

Table 2-3. First-order ozonation rate constants for TPHs, *n*-alkanes and total PAHs in WAO and DWAO.

Type		Volatilization		Overall dissipation		Ozonation
		k_v (h ⁻¹)	R^2	k (h ⁻¹)	R^2	k_o (h ⁻¹)
TPHs	WAO	0.004	0.981	0.011	0.990	0.007
	DWAO	0.018	0.992	0.034	0.975	0.016
<i>n</i> -alkanes	WAO	0.003	0.986	0.045	0.974	0.041
	DWAO	0.009	0.999	0.051	0.984	0.042
Total PAHs	WAO	0.005	0.992	0.029	0.981	0.025
	DWAO	0.015	0.964	0.063	0.966	0.048

$$R^2 = 1 - \frac{\sum_i (y_i - y_{i(predict)})^2}{\sum_i (y_i - \bar{y})^2}$$

Note: R^2 : coefficient of determination, where y_i and $y_{i(predict)}$ are observed data and model values, respectively, and \bar{y} is the mean of the observed data.

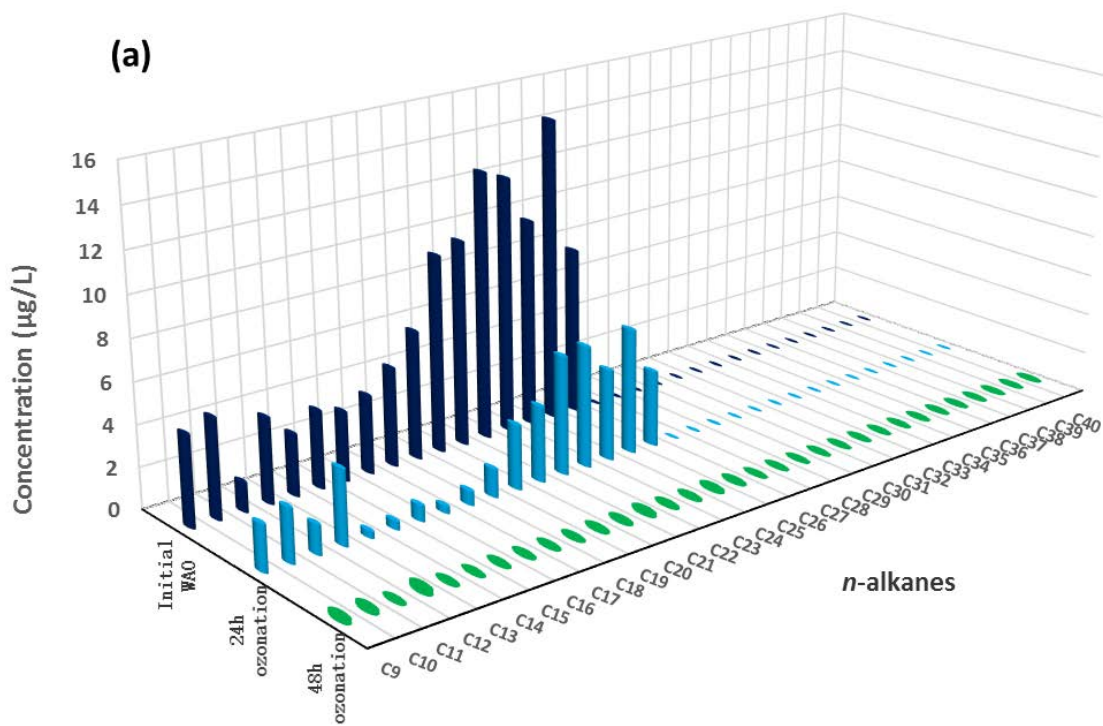
Several factors can affect the ozonation rate of *n*-alkanes. First, the molecular weight or the molecular size can affect dispersibility, volatility and ozone reactivity of *n*-alkanes. In general, smaller molecules are more volatile and more vulnerable to degradation (Yin et al., 2015). In the absence of the dispersant (WAO), the oil components are truly dissolved with C19-C26 being the most abundant *n*-alkanes (**Fig. 2-4a**), and thus the volatilization rate was less than that in DWAO. While the C14-C19 fraction appeared to be more preferentially degraded in WAO, virtually all *n*-

alkanes dissipated from the solution after 40 hours of ozone exposure. This observation indicates that: 1) all dissolved *n*-alkanes are prone to ozonation, and 2) the high molecular weight *n*-alkanes were completely degraded without accumulation of smaller *n*-alkanes.

Second, alkyl radicals can be produced during reaction of ozonation with olefins (Hellman and Hamilton, 1974). The alkyl radicals may attack PAHs to form alkylated PAHs, also known as alkylation, resulting in decreased concentration of *n*-alkanes.

Third, the dispersant may have a profound effect on the ozonation process. In the presence of the dispersant, much more oil is dispersed, and the component distribution in DWAO appeared quite similar to that of WAO as well as in the crude oil (Zhao et al., 2016). However, dispersed *n*-alkanes were more volatile than the dissolved *n*-alkanes (**Fig. 2-3**). As the dispersion of *n*-alkanes involves π - π interactions and/or hydrophobic interactions between *n*-alkanes and the dispersant aggregates and/or micelles, the medium-molecular-weight (e.g., C24-C30) fraction of *n*-alkanes is preferably dispersed (in this study, the C24-C30 fraction accounted for 61.1% of the total *n*-alkanes) (**Fig. 2-4b**). The higher concentration and higher volatility of the dispersed *n*-alkanes are more conducive to both direct and indirect ozonation, where larger *n*-alkanes are transformed to the smaller homologs and then mineralized (Vikhorev et al., 1978). On the other hand, the mass transfer rate of larger *n*-alkanes is slower than that of smaller *n*-alkanes, which can be further slowed down due to the attachment of the dispersant molecules, resulting in slower degradation for larger *n*-alkanes. Moreover, the dispersant can increase soluble ozone concentration and enhance the radical generation, especially superoxide radicals (Gong and Zhao, 2017); on the other hand, the dispersant may also compete for the reactive species. As the dispersant lowers the surface tension of water, it reduces the ozone mass transfer resistance at the ozone-water interface, which may increase both direct ozonation and generation of radicals in the aqueous phase (Chu et al.,

2006; Gong and Zhao, 2017). Lastly, the dispersant (mainly Span 80) can facilitate accumulation of more hydrophobic hydrocarbons to the upper layer of the water column in the reactor, promoting the exposure to the gaseous ozone, and thus the ozonation reactions (Fu et al., 2017).



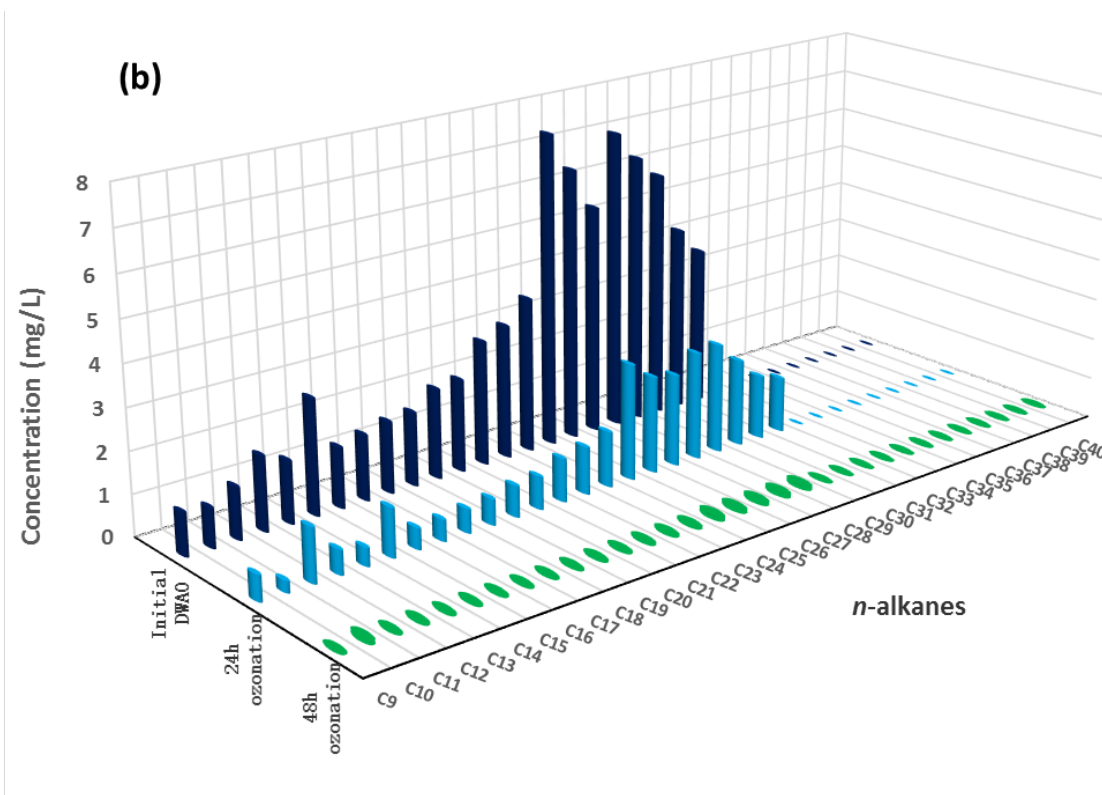
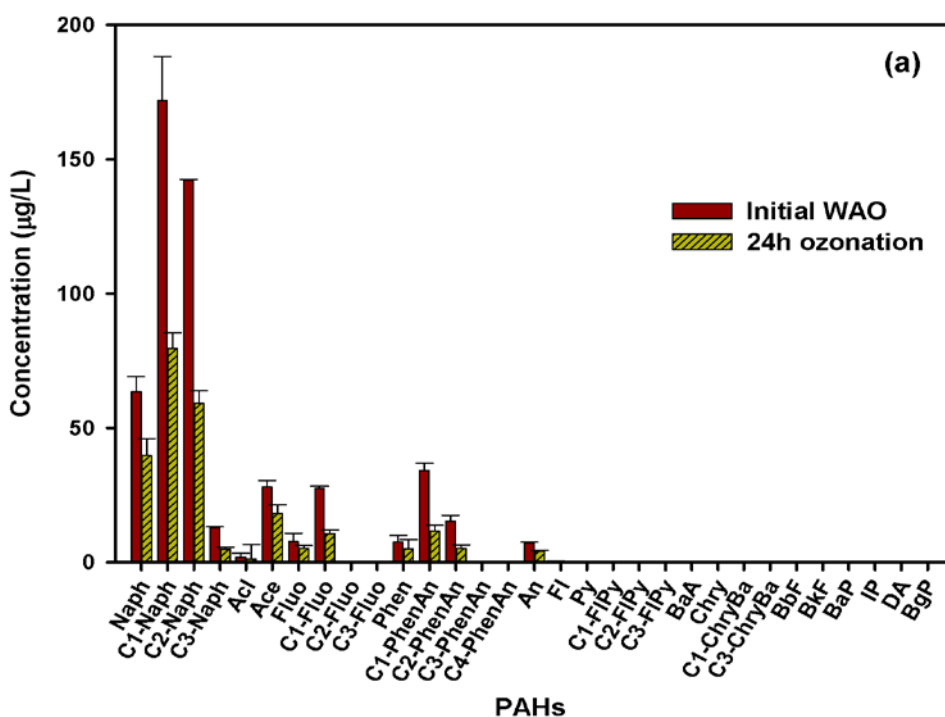


Figure 2-4. Distributions of *n*-alkanes in WAO (a) and DWAO (b) before and after 48 h exposure to gaseous ozone. Experimental conditions are the same as in Fig. 2-3.

Compared to *n*-alkanes, the dispersant was much less effective in dispersing PAHs. **Fig. 2-5** displays the distributions of PAHs in WAO and DWAO before and after ozonation. The initial concentrations of parent PAHs and alkylated PAHs were 0.12 and 0.41 mg/L in WAO, which were raised to 1.34 and 4.82 mg/L in DWAO, respectively. Notably, the 2-ring and 3-ring PAHs and their alkylated PAHs (e.g., C1-naphthalene, C2-naphthalene, C3-naphthalene, C1-phenanthrene and C2-phenanthrene) were preferably dispersed in DWAO. Phenanthrene (Phen) is the most abundant parent PAH, accounting for 11.3% of the total PAHs, followed by fluorene (Fluo) (4.5%), naphthalene (3.4%) and acenaphthene (Ace) (2.3%). The 3-ring PAHs make up 22.3% of

the total PAHs. The concentration of total alkylated PAHs was 3.6 times higher than total parent PAHs, which is consistent with other studies (Yin et al., 2015; Zhao et al., 2016).

The ozonation rates for both parent and alkylated PAHs in DWAO were much faster than in WAO, especially for the 2-ring (naphthalene), 3-ring (acenaphthylene, fluorene and phenanthrene) and 4-ring (fluoranthene and pyrene) PAHs and their alkylated homologs (**Fig. 2-5, Fig. 2-6 and Table 2-4**).



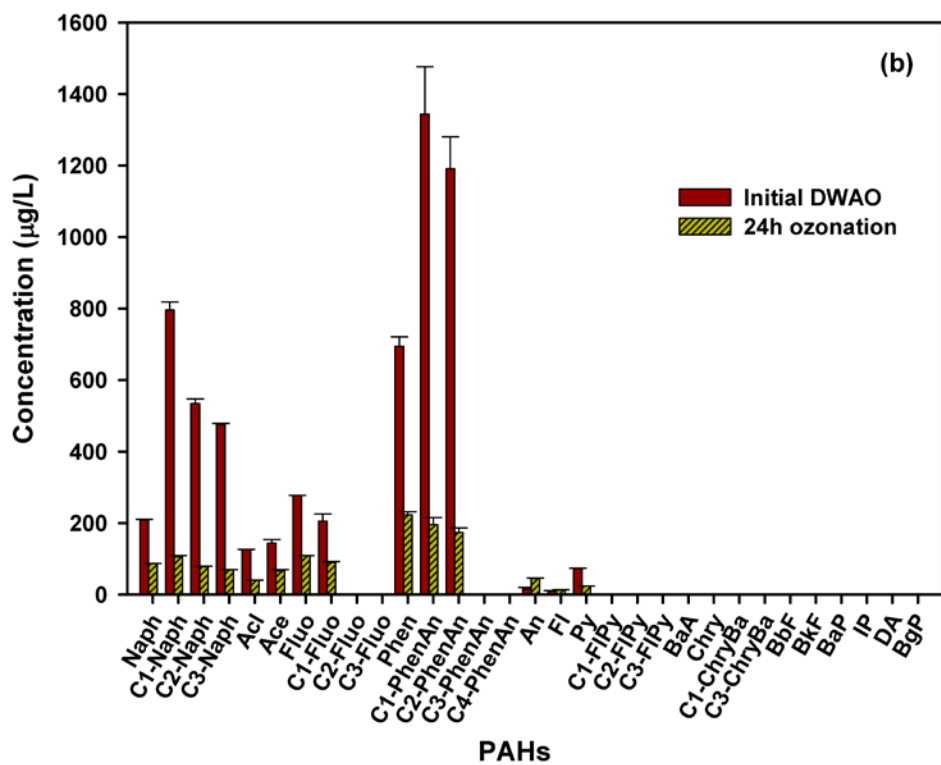


Figure 2-5. Distributions of parent and alkylated PAHs in WAO (a) and DWAO (b) before and after 24 hours ozonation. Experimental conditions are the same as in Fig. 2-3.

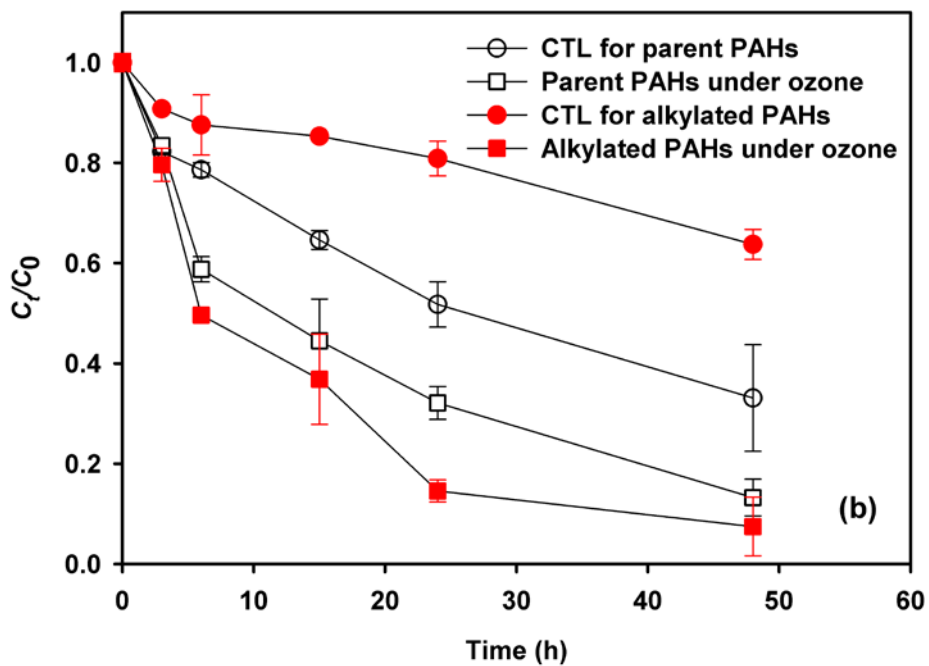
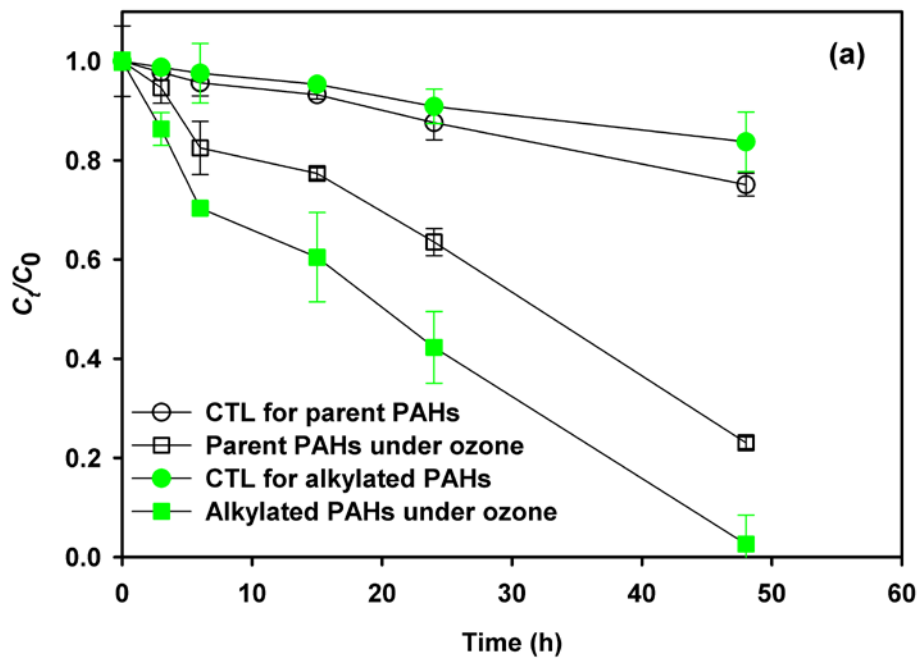


Figure 2-6. Distributions of parent and alkylated PAHs in WAO (a) and DWAO (b) before and after 24 hours ozonation. Experimental conditions are the same as in Fig. 2-3.

Table 2-4. Pseudo first-order ozonation rate constants for parent and alkylated PAHs in WAO and DWAO.

Type		Volatilization		Overall dissipation		Ozonation
		k_v (h ⁻¹)	R^2	k (h ⁻¹)	R^2	k_o (h ⁻¹)
Parent PAHs	WAO	0.006	0.990	0.024	0.949	0.018
	DWAO	0.024	0.970	0.050	0.963	0.026
Alkylated PAHs	WAO	0.004	0.995	0.041	0.958	0.037
	DWAO	0.008	0.940	0.078	0.968	0.042
Total PAHs	WAO	0.005	0.992	0.029	0.981	0.025
	DWAO	0.015	0.964	0.063	0.966	0.048

For instance, the 24-h degradation of Naph, C1-Naph, C2-Naph, and C3-Naph reached 37.3%, 53.7%, 58.4%, and 62.1%, respectively in WAO, which was elevated to 58.3%, 86.7%, 85.4%, and 85.4% in DWAO. Moreover, the alkylated PAHs were more effectively degraded than their parent homologs in both WAO and DWAO; and the most degradation was observed for alkylated naphthalenes (85.4%-86.7%), alkylated phenanthrenes/anthracenes (84.5%), and alkylated fluoranthrenes/pyrenes (100%) in DWAO.

Bacosa et al. (2015) studied photodegradation of dispersed oil hydrocarbons, and they observed some similar degradation patterns. For instance, they found that 3-ring PAHs were more sensitive to photooxidation than 4- to 5-ring PAHs, and that except for phenanthrene, 3-ring PAHs were degraded faster than naphthalene. Moreover, they observed that alkylated pyrenes were photodegraded faster than alkylated phenanthrenes, while alkylated naphthalenes were degraded faster than alkylated phenanthrenes; and alkylated PAHs were photodegraded faster than their parent homologs. These similarities suggest that ozonation and photodegradation of dispersed oil

hydrocarbons may share some common reaction mechanisms such as degradation facilitated by radicals.

Moreover, the volatilization rates of parent and alkylated PAHs in DWAO were 4 and 2 times higher than in WAO. This can be attributed to the much higher concentration of the 2-ring PAHs in DWAO, which are known to be more volatile (Liu et al. 2012). At 48 h, the volatilization loss of parent PAHs in WAO and DWAO was 24.9% and 66.9%, respectively, compared to 6.3% and 36.3% for alkylated PAHs, indicating that like *n*-alkanes, dispersed PAHs are more volatile than the dissolved counterparts. The overall depletion was 77.0% and 86.7% for the parent PAHs in WAO and DWAO, respectively, and 97.4% and 92.5% for alkylated PAHs, indicating that alkylated PAHs are more vulnerable to ozonation than the parent PAHs and that dispersed PAHs are more prone to ozonation than the dissolved counterparts. Mechanistically, the dissolution/dispersion and ozonation of PAHs can be affected by the following factors: First, the lower abundance of PAHs in oil hydrocarbons may result in the lower dispersion of PAHs than *n*-alkanes by the dispersant (Zhao et al., 2016). Second, the hydrophile-lipophile balance (HLB) values of the different surfactants in Corexit EC9500A range from 4.3 to 15 (**Table 2-2**); as such, the dispersant is more favorable towards *n*-alkanes than PAHs (Couillard et al., 2005; Diallo et al., 1994). Third, more hydrophobic PAHs (i.e. larger PAHs) tend to resist the dispersing and ozonation processes (Walter et al., 2000). Fourth, the presence of ozone may cause alkylation of the parent PAHs, resulting in a rise in alkylated PAHs (Lima et al. 2005; Ringuet et al., 2012 Zhao et al., 2016). This assertion is supported by **Fig. 2-7**, which shows a faster removal rate of parent PAHs than alkylated PAHs in the early stage (<15 hours). After 15 hours, or upon completion of the initial alkylation of the parent PAHs, the ozonation rate increased sharply, indicating alkylated PAHs are more ozone-reactive than the corresponding parent PAHs.

The dispersant effects on the ozonation of PAHs followed a similar manner as for *n*-alkanes, although the extents differed due to their different molecular characteristics.

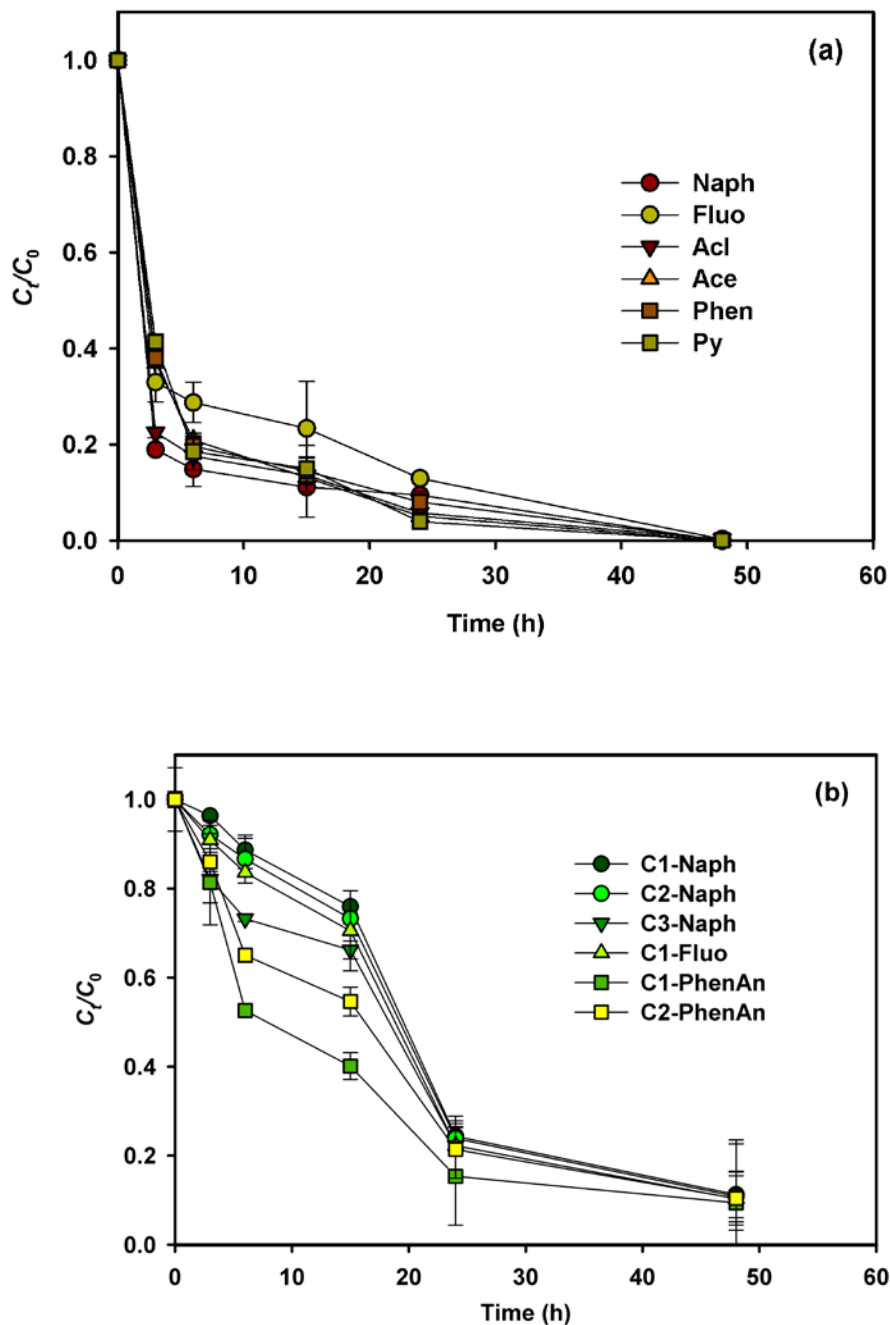
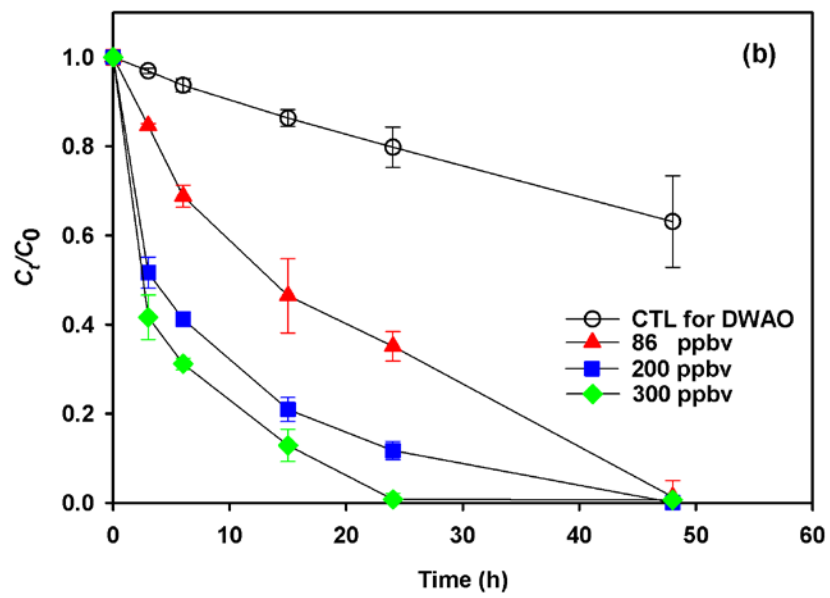
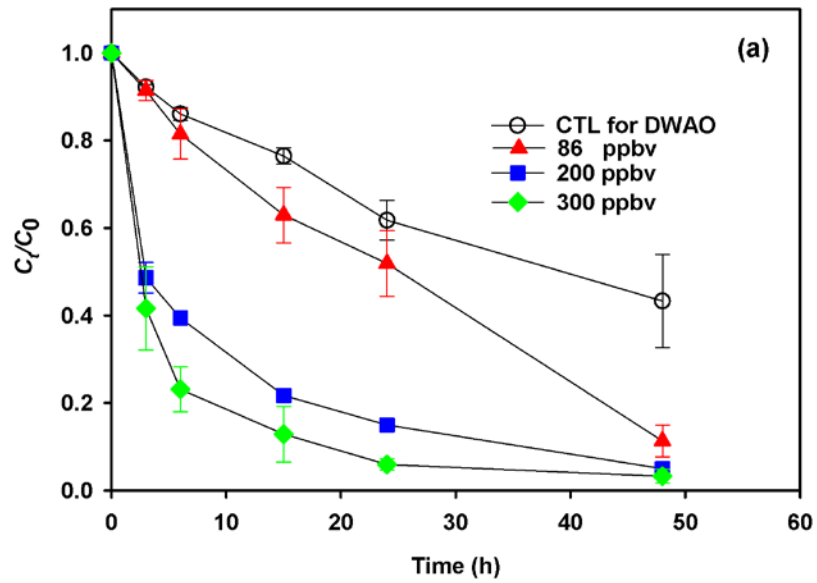


Figure 2-7. Ozonation of parent PAHs (a) and alkylated PAHs (b) in DWAO (with Corexit EC9500A) under 86 ppbv simulated atmospheric ozone. Initial TPHs = 149.70 mg/L, *n*-alkanes

= 79.30 mg/L, PAHs = 6.21 mg/L, Corexit EC9500A = 238 mg/L, gas flow rate = 4 mL/min, temperature = 22±1 °C, solution volume = 250 mL, pH = 8.1±1, salinity = 2 wt.%, and DOM = 2.2 mg/L TOC. Symbols: experimental data plotted as mean of duplicates and error bars refer to deviation from the mean to indicate data reproducibility.

2.3.2 Degradation of oil hydrocarbons in DWAO at various atmospheric ozone concentrations

Fig. 2-8 shows ozonation kinetics of TPHs (**Fig. 2-8a**), *n*-alkanes (**Fig. 2-8b**) and PAHs (**Fig. 2-8c**) in DWAO when exposed to various gaseous ozone concentrations but at a fixed gas flowrate 4 mL/min. The overall removal rate of the oil components increased with increasing ozone concentration. As the ozone concentration increased from 86 to 300 ppbv, the rate constant k_o was boosted from 0.016 to 0.237 h⁻¹ for TPHs (by 14.8 times), from 0.042 to 0.210 h⁻¹ for *n*-alkanes (by 5.1 times) and from 0.048 to 0.302 h⁻¹ for total PAHs (by 6.3 times) (**Table 2-5**). According to the Henry's law, the higher gaseous ozone concentration results in higher soluble ozone in the aqueous phase, leading to more accessible molecule ozone and free radicals. However, the effect of ozone concentration became less profound at O₃>200 ppbv, suggesting that mass transfer became more important at elevated O₃ concentration. In addition, the ozone-facilitated alkylation rate may also be enhanced at higher ozone concentrations.



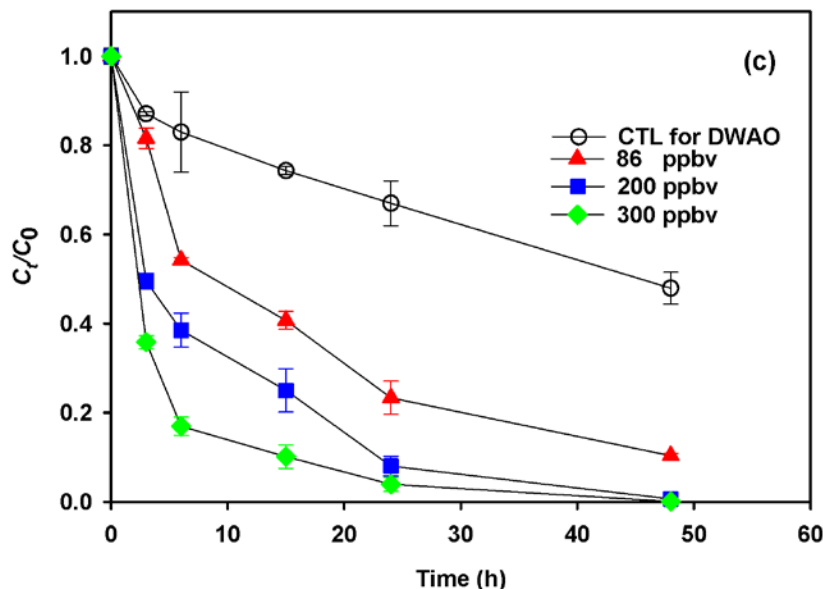


Figure 2-8. Ozonation kinetics of (a) TPHs, (b) *n*-alkanes and (c) total PAHs in DWAO at various gaseous ozone concentrations. Experimental conditions: Initial TPHs = 149.70 mg/L, *n*-alkanes = 79.30 mg/L, PAHs = 6.21 mg/L, Corexit EC9500A = 238 mg/L, gas flow rate = 4 mL/min, temperature = 22±1 °C, solution volume = 250 mL, pH = 8.1±1, salinity = 2 wt.%, and DOM = 2.2 mg/L TOC. Symbols: experimental data plotted as mean of duplicates and error bars refer to deviation from the mean to indicate data reproducibility.

Table 2-5. First-order ozonation rate constants for TPHs, *n*-alkanes and TPAHs in DWAO at various concentrations of simulated atmospheric ozone.

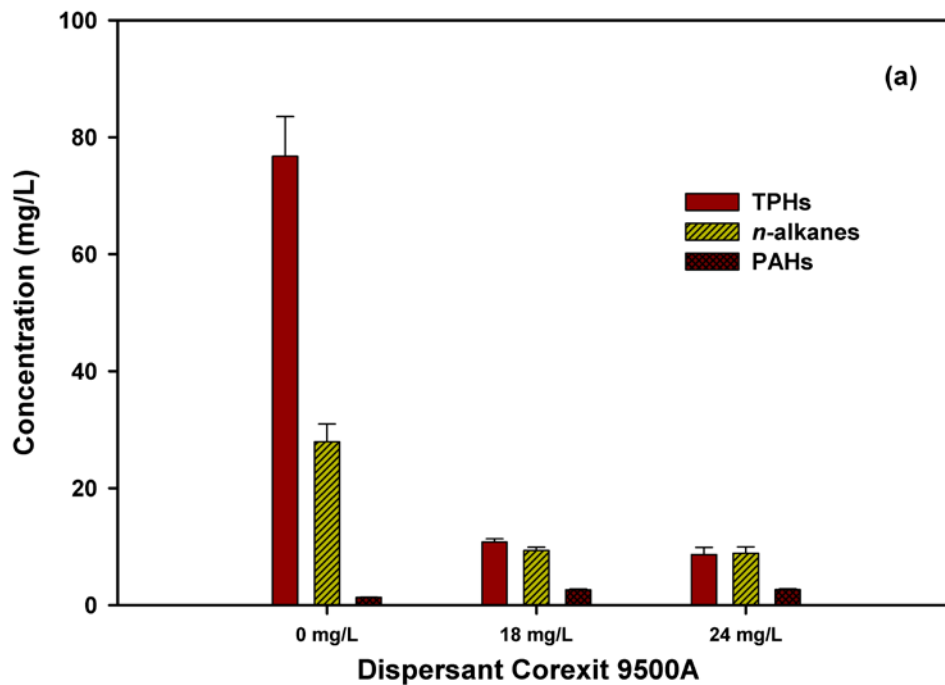
Type	Ozone	Volatilization		Overall dissipation		Ozonation
	(ppbv)	k_v (h ⁻¹)	R^2	k (h ⁻¹)	R^2	k_o (h ⁻¹)
TPHs	86	0.018	0.992	0.034	0.975	0.016
	200	0.018	0.992	0.136	0.919	0.118

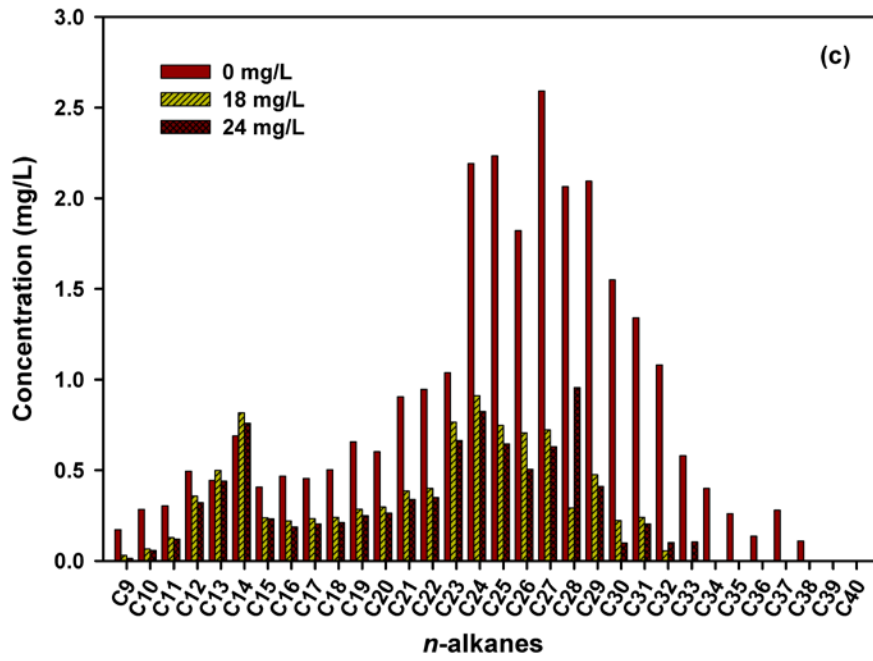
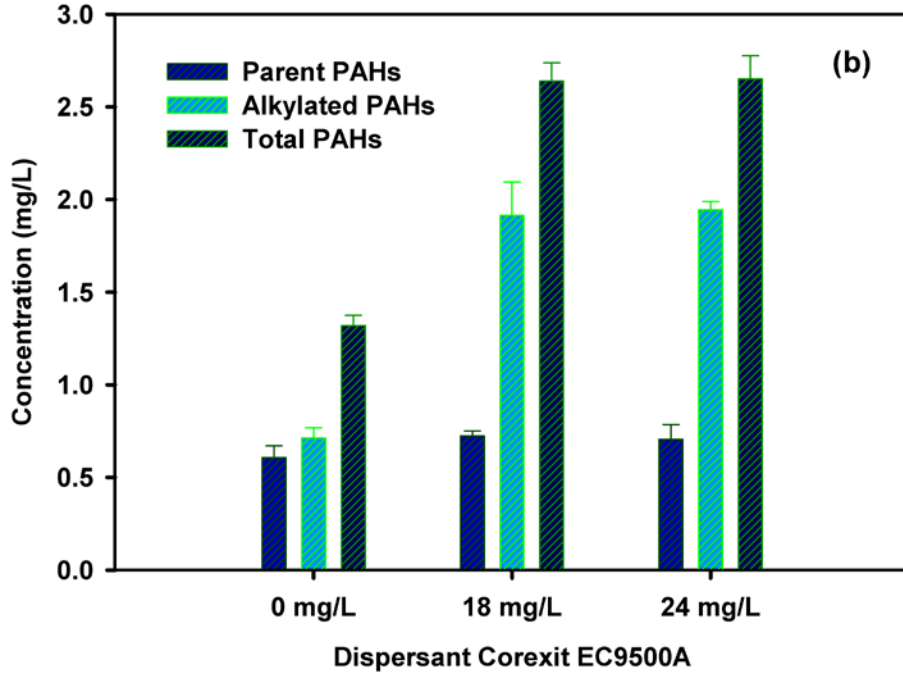
	300	0.018	0.992	0.254	0.973	0.237
	86	0.009	0.999	0.051	0.984	0.042
<i>n</i> -alkanes	200	0.009	0.999	0.134	0.954	0.124
	300	0.009	0.999	0.220	0.972	0.210
Total	86	0.015	0.964	0.063	0.966	0.048
PAHs	200	0.015	0.964	0.138	0.939	0.124
	300	0.015	0.964	0.316	0.984	0.302

2.3.3 Effect of dispersant concentration on ozonation of petroleum hydrocarbons in DWAO

Fig. 2-9 shows the remaining concentrations of TPHs, *n*-alkanes and PAHs in DWAO after 24 h of ozonation when additional 18 or 24 mg/L of Corexit EC9500A was added to the DWAO. **Fig. 2-9a** shows that the addition of the dispersant resulted in much lower concentrations of TPHs and *n*-alkanes, and the addition of 18 and 24 mg/L of the dispersant gave comparable results. The findings indicate that the addition of excess dispersant enhances ozonation of TPHs and *n*-alkanes. However, there exists a threshold concentration, above which the dispersant effect becomes less significant. **Fig. 2-9c** shows that the dispersant promotes ozonation of >C₂₀ *n*-alkanes to a greater extent. The favorable effects of the dispersant on TPHs and *n*-alkanes are attributed to the mechanisms discussed in Section 2.3.1. However, the degradation for PAHs was inhibited at the elevated dispersant concentrations (**Figs. 2-9a** and **2-9b**). After 24 hours of ozonation, the final concentrations of parent PAHs were 0.61, 0.72 and 0.71 mg/L when 0, 18, and 24 mg/L of the dispersant were added, respectively; and the final concentrations of alkylated PAHs were 0.71, 1.91 and 1.94 mg/L. Increasing the dispersant concentration from 0 to 18 mg/L decreased the

degradation of total PAHs from 78.6% to 57.0%, parent PAHs from 54.8% to 47.4%, and alkylated PAHs from 85.2% to 59.6%. Further increasing the dispersant addition to 24 mg/L had insignificant further effect. **Fig. 2-9d** shows that such inhibitive effects at elevated dispersant concentrations occurred mainly to the 2-ring and 3-ring alkylated PAHs.





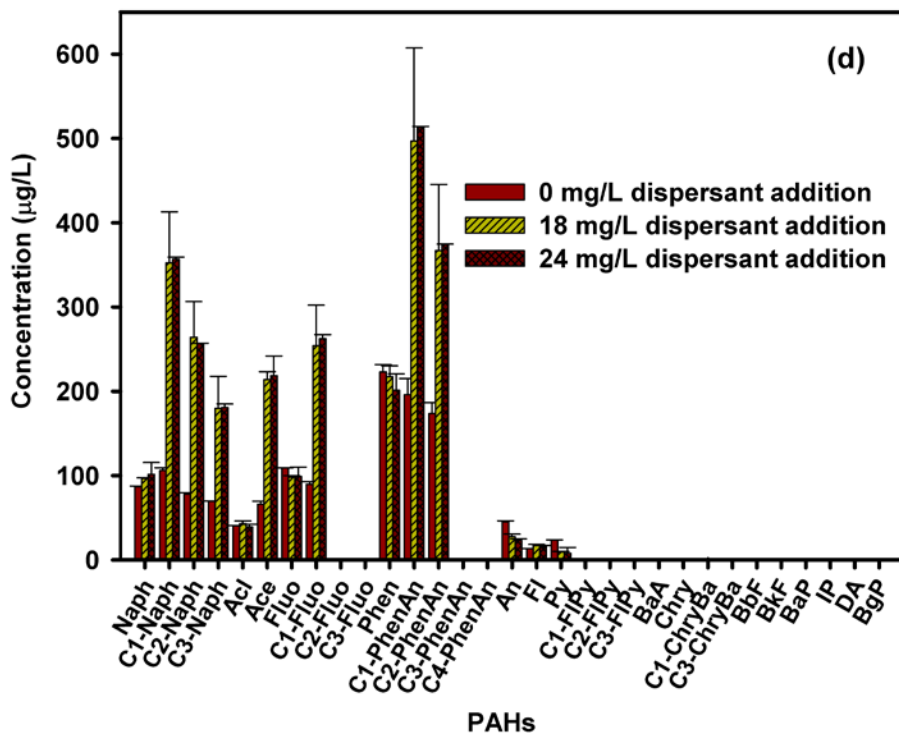


Figure 2-9. Remaining concentrations of TPHs, *n*-alkanes and total PAHs (a), and parent PAHs and alkylated PAHs (b) in DWAO after 24 h ozonation in the presence of various concentrations of the dispersant, and distributions of *n*-alkanes (c) and PAHs (d) in DWAO after 24 h ozonation. Experimental conditions: Initial TPHs = 149.70 mg/L, *n*-alkanes = 79.30 mg/L and total PAHs = 6.21 mg/L, Corexit EC9500A = 238 mg/L, gas flow rate = 4 mL/min, gaseous ozone = 86 ppbv, temperature = 22±1 °C, solution volume = 250 mL, solution pH = 8.1±1, salinity = 2 wt.%, and DOM = 2.2 mg/L as TOC. Symbols: experimental data plotted as mean of duplicates and error bars refer to deviation from the mean to indicate data reproducibility.

The critical micelle concentration (CMC) of Corexit EC9500A was reported to be 22.5 mg/L (Gong et al., 2014). Our results suggest that both *n*-alkanes and PAHs can interact with the dispersant molecules strongly even below the CMC. PAHs are intrinsically more stable due to the π electrons delocalized over the aromatic rings than *n*-alkanes (Rubio-Clemente et al., 2014). The

3-rings PAHs are the dominant components for both parent and alkylated PAHs. These relatively smaller aromatic compounds may undergo the “caging effect”, i.e., partitioning into the surfactant (e.g., Span 80) aggregates/micelles, which retards the encountering between ozone molecules/radicals and PAHs. (Fu et al., 2017; Zhang et al., 2011). The effect is less significant for *n*-alkanes due to their chain-like structures. In addition, the rise in alkylated PAHs at elevated dispersant concentrations can also be due to the fact that while elevated dispersant concentration facilitates alkylation of parent PAHs due to generation of more alkyl radicals, the high dispersant concentration can also inhibit the subsequent degradation of the alkylated PAHs due to the caging effect.

To determine the effect of the dispersant on production of •OH radicals, *p*CBA was used as a probe chemical and an •OH scavenger to measure the •OH radicals (Details are described in **Section 2.3.7**). **Fig. 2-10** shows ozone-oxidation of *p*CBA during ozonation with or without the dispersant. It is evident that the presence of 18 mg/L of the dispersant significantly enhanced the degradation of *p*CBA ($P = 0.003$ at the 0.05 level of significance), indicating enhanced generation of hydroxyl radicals. However, further increasing the dispersant to 24 mg/L (higher than the CMC value) resulted in less ozonation of *p*CBA, or a statistically insignificant change in the reaction rate ($P = 0.852$) compared to that without dispersant. This inhibitive effect at 24 mg/L of the dispersant may be attributed to: 1) the formation of micelles may exert the caging effect, which retards the decomposition of soluble ozone (Margareta Eriksson, 2005), and 2) elevated competition of the dispersant for the free radicals at higher dispersant concentrations.

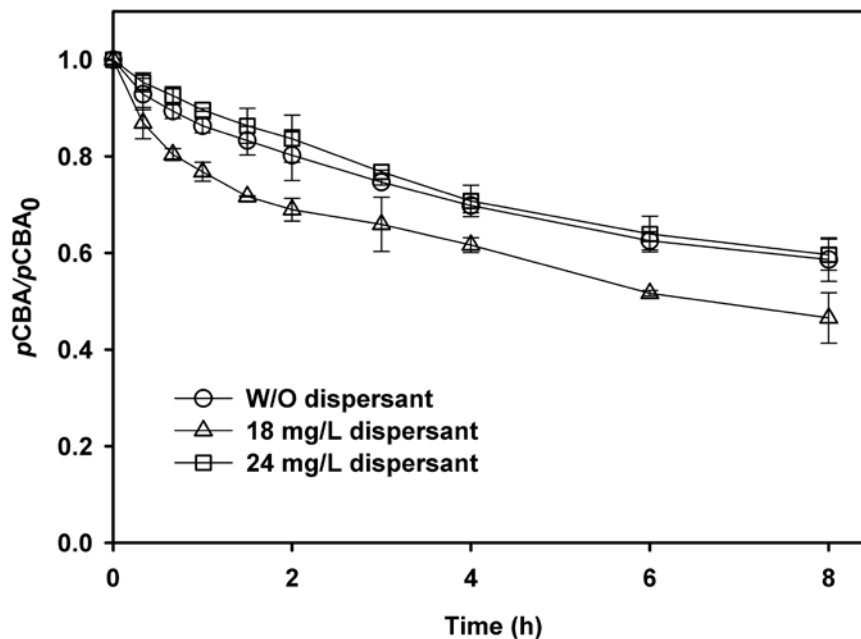
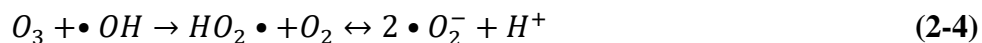


Figure 2-10. Oxidation of *p*CBA (normalized to initial concentration) during ozonation with or without 18 or 24 mg/L of Corexit EC9500A in seawater. Experimental conditions: Gas flow rate = 4 mL/min, gaseous ozone = 86 ppbv, initial *p*CBA concentration = 3 μ M, temperature = 22 ± 1 °C, solution volume = 250 mL, salinity = 2 wt.%, and DOM = 2.2 mg/L as TOC. Symbols: experimental data plotted as mean of duplicates and error bars refer to deviation from the mean to indicate data reproducibility.

2.3.4 Effects of pH

Fig. 2-11 shows the concentrations of TPHs, *n*-alkanes and total PAHs in DWAO at various pH levels (6.0, 7.0, 8.0, and 9.0) after 24 hours of exposure to 86 ppbv of gaseous ozone. The overall dissipation rate of TPHs, *n*-alkanes and PAHs decreased from 59.7% to 46.2% ($P = 0.003$ at the 0.05 level of significance), from 66.3% to 61.5% ($P = 0.078$) (**Fig. 2-13**) and from 87.8% to 86.9% ($P = 0.551$) (**Figs. 2-12** and **2-13**), respectively, when the solution pH was increased from 6.0 to 9.0, indicating an inhibitive effect at higher pH in the tested pH range. It has been well known that solution pH can affect both direct and indirect ozonation reactions (Zhao et al., 2011). As pH increases, the aqueous ozone decomposes via the reactions as shown in Eqns. (2-2 to 2-6) (Kasprzyk-Hordern et al., 2003):



Alkaline conditions favor aqueous ozone decomposition to form more free radicals including hydroxyl radicals and superoxide radicals (Eqns. 3–4), and thus enhances the indirect ozonation. However, direct ozonation is compromised due to consumption of molecular ozone. Because direct ozonation is the predominant process for oxidation of TPHs (Direct ozonation accounted for 53% of the overall ozonation), the lessened direct ozonation resulted in the observed inhibitive effect at higher pH. However, depending on the different ozonation mechanisms, such pH effects can vary. For instance, Beltran et al. (1995) reported that the ozone oxidation rate of fluorene increased with increasing pH; however, Gong and Zhao (2017) observed that ozonation

of pyrene in the presence of the same dispersant decreased with increasing pH. They claimed that this discordance may result from the dispersant effect, which can compete for the radicals more intensely than for the ozone molecules, thus inhibiting indirect ozonation.

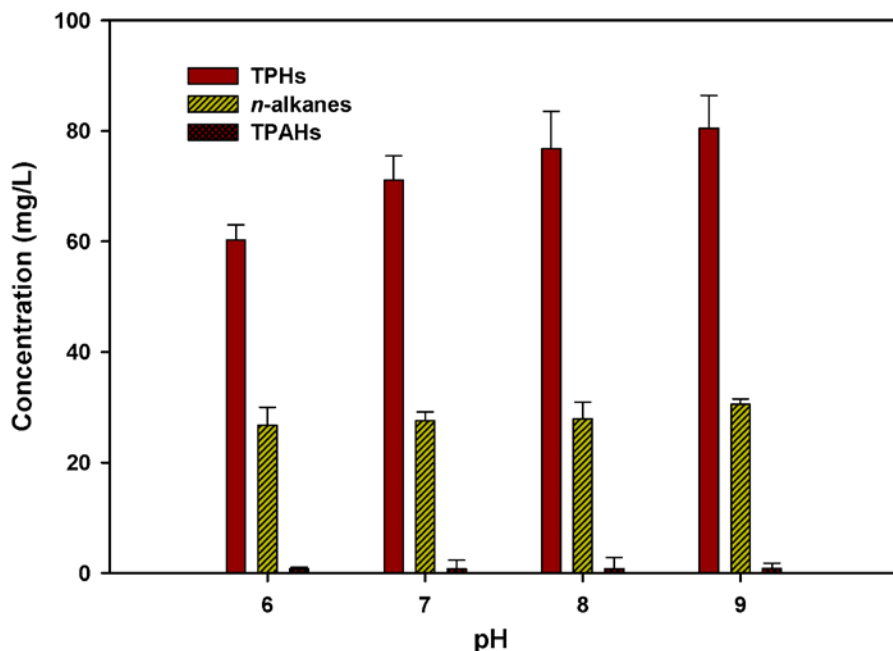


Figure 2-11. Remaining concentrations of TPHs, *n*-alkanes and total PAHs in DWAO after 24 h ozonation at various initial pH levels. Experimental conditions: Initial TPHs = 149.70 mg/L, *n*-alkanes = 79.30 mg/L and total PAHs = 6.21 mg/L, Corexit EC9500A = 238 mg/L, gas flow rate = 4 mL/min, gaseous ozone = 86 ppbv, temperature = 22±1 °C, solution volume = 250 mL, salinity = 2 wt.%, and DOM = 2.2 mg/L as TOC. Symbols: experimental data plotted as mean of duplicates and error bars refer to deviation from the mean to indicate data reproducibility.

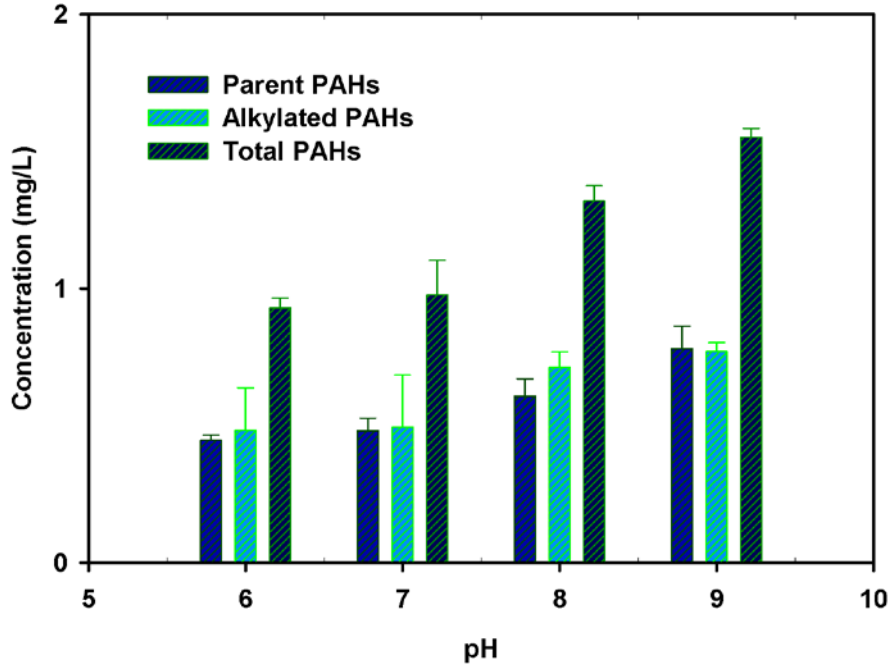
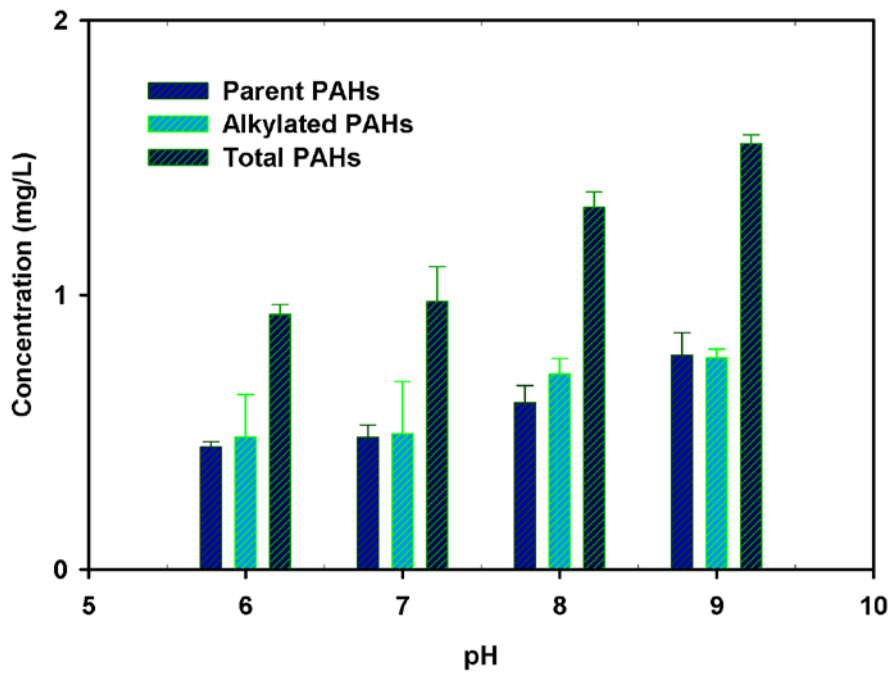


Figure 2-12. Effect of pH on ozonation of parent and alkylated PAHs in DWAO by simulated atmospheric ozone. Experimental conditions are the same as in Fig. 2-11.



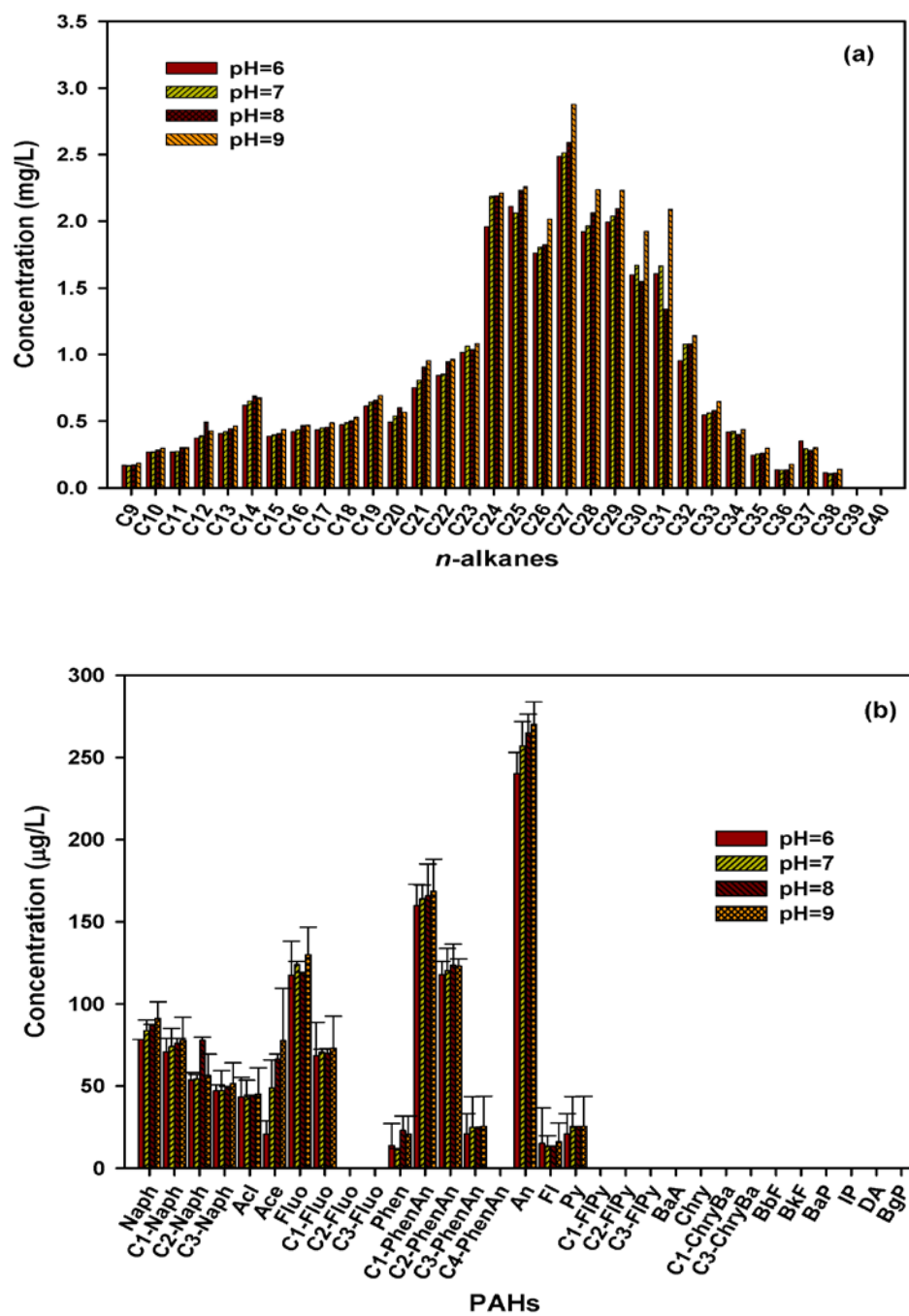


Figure 2-13. Distributions of remaining *n*-alkanes (a) and PAHs (b) in DWAO after 24 h ozonation at various pH levels. Experimental conditions are the same as in Fig. 8.

2.3.5 Effects of humic acid

Fig. 2-14 shows ozonation kinetics of TPHs in DWAO with 0.5, 1.0 or 5.0 mg/L as TOC of humic acid added and at a gaseous ozone concentration of 200 ppbv. After 24 h of exposure to the nitrogen gas flow, the volatilization loss of TPHs in DWAO was 38.2% in all cases, whereas the overall depletion of TPHs was 93.4%, 89.9% and 74.6%, respectively, in the presence of 0.5, 1.0 and 5.0 mg/L humic acid and when exposed to the gaseous ozone. **Table 2-6** presents the respective rate constants for overall depletion, volatilization and ozonation. When 5.0 mg/L of humic acid was added, the overall dissipation rate constant (k) was decreased from 0.136 to 0.051 h^{-1} , and the ozonation rate constant (k_o) from 0.118 h^{-1} to 0.032 h^{-1} (**Table 2-6**). The distribution of different segments of n -alkanes after 24 hours of ozonation (**Fig. 2-15a**) indicates that the inhibitive effect of humic acid was more evident on the larger n -alkanes, in particular the C24–C30 fraction; and the higher the TOC concentration, the less these larger n -alkanes were degraded. **Fig. 2-15b** shows the distributions of PAHs after 24 h of ozonation at various humic acid concentrations. The remaining concentrations of parent PAHs were 3.0, 8.9, 17.0 and 18.4 mg/L, respectively, when 0.5, 1.0, 5.0, and 10 mg/L as TOC of humic acid were added. Evidently, more 3-ring PAHs (acenaphthene, fluorene and phenanthrene) remained after the ozonation at higher humic acid concentrations (5.0 or 10 mg/L), indicating degradation of these PAHs were inhibited to a greater extent. The inhibitive effect on 2-ring PAHs (naphthalene) was much less, and there was virtually no effect on the 2-ring alkyl homologues (C1-naphthalene, C2-naphthalene and C3-naphthalene).

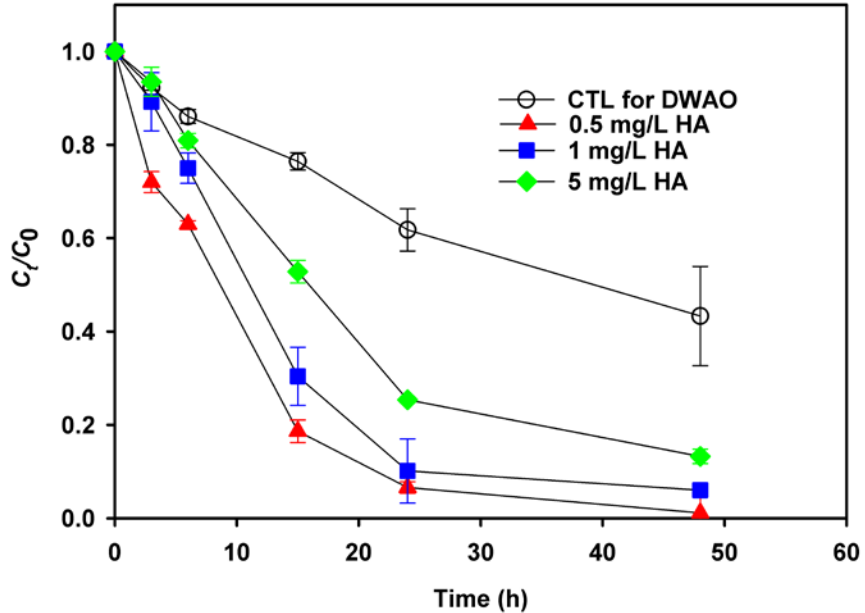


Figure 2-14. Effect of HA on ozonation of TPHs in DWAO. Experimental conditions: Initial TPHs = 149.7 mg/L, *n*-alkanes = 79.3 mg/L and total PAHs = 6.21 mg/L (in DWAO with Corexit EC9500A), gas flow rate = 4 mL/min, ozone concentration = 200 ppbv, temperature = 22±1 °C, volume of solution = 250 mL, solution pH = 8.1±1, salinity = 2.0 wt.%, and DOM = 2.2 mg/L as TOC. Symbols: experimental data plotted as mean of duplicates and error bars refer to deviation from the mean to indicate data reproducibility.

Table 2-6. First-order ozonation rate constants for TPHs in DWAO in the presence of various concentrations of humic acid.

HA concentration	Volatilization		Overall dissipation		Ozonation
	k_v (h ⁻¹)	R^2	k (h ⁻¹)	R^2	k_o (h ⁻¹)
0 mg/L	0.018	0.992	0.136	0.919	0.118
0.5 mg/L	0.018	0.992	0.100	0.985	0.082
1 mg/L	0.018	0.992	0.077	0.970	0.059

5 mg/L

0.018

0.992

0.050

0.976

0.032

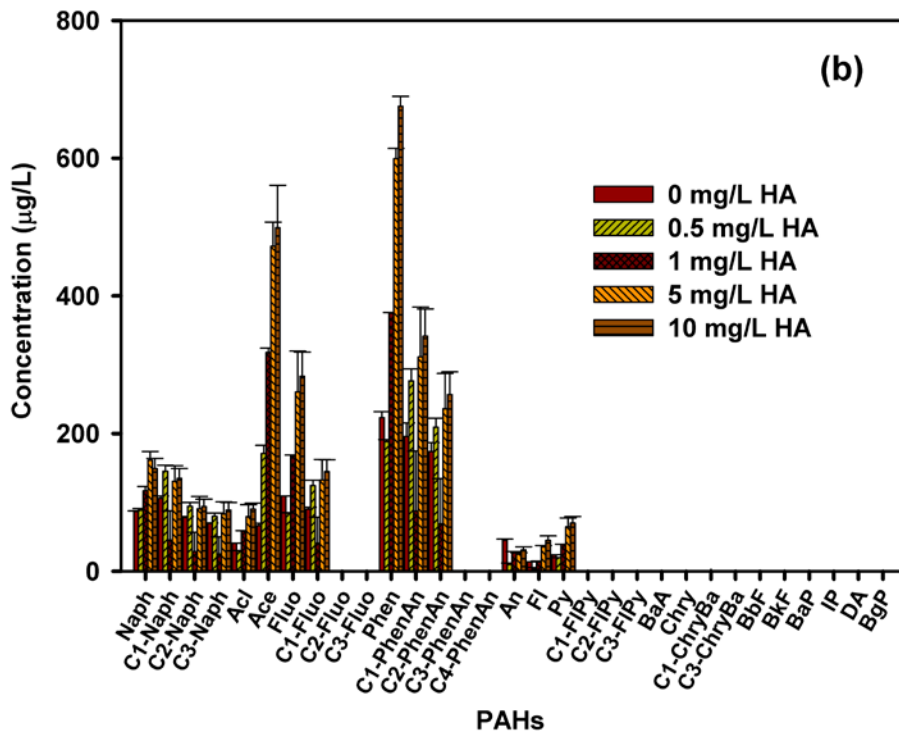
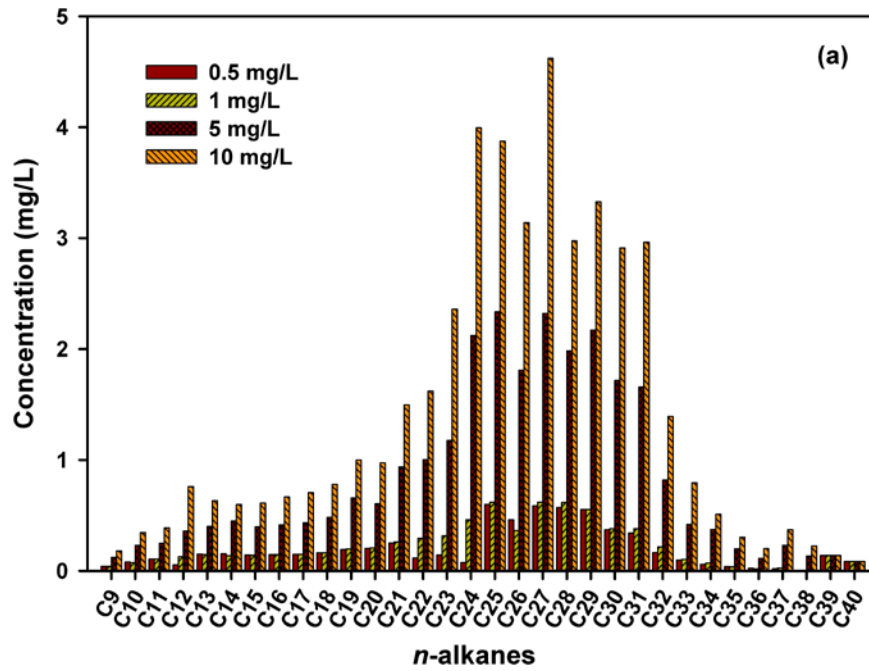
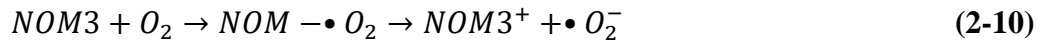


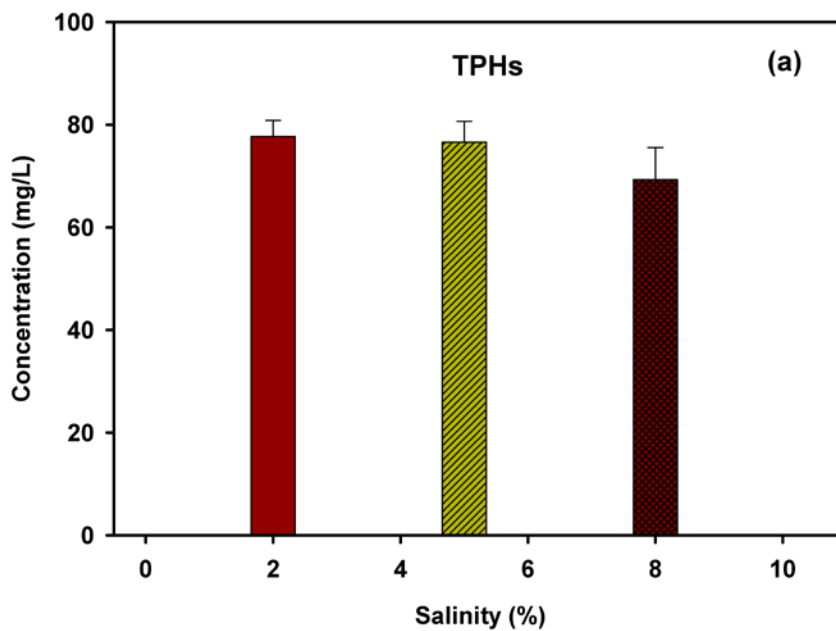
Figure 2-15. Distributions of *n*-alkanes (a) and PAHs (b) in DWAO after 24 h ozonation in the presence of various concentrations of humic acid. Experimental conditions are the same as in Fig. 2-14.

DOM can affect soluble ozone stability in three ways: 1) directly react with soluble ozone (Eqns. 2-7 and 2-8) (von Gunten, 2003) and therefore compete for molecular ozone with the target hydrocarbons; 2) acting as a promoter to convert the nonselective hydroxyl radicals into superoxide radicals (Eqns. 9 and 10) (Staelin and Hoigne, 1985; von Gunten, 2003), resulting in a net loss in the indirect ozonation because the oxidation power of superoxide radicals is lower than that of hydroxyl radicals (Litter and Quici, 2010); and 3) sorption of some oil components (e.g., PAHs) within the complex HA matrix may shield it from the molecular ozone and free radicals (Simpson et al., 2004).



2.3.6 Effects of salinity

Fig. 2-16 shows the effects of salinity on ozonation of TPHs, *n*-alkanes and total PAHs in DWAO. The overall dissipation of all the oil components after 24 h of ozonation was increased when the solution salinity was increased from 2.0% to 8.0%, namely, from 48.1% to 53.7% for TPHs ($P = 0.058$), from 64.8 to 74.2% for *n*-alkanes ($P = 0.022$), and from 78.8% to 84% for total PAHs ($P = 0.065$). **Fig. 2-17** shows the distributions of *n*-alkanes and PAHs in DWAO after 24-h ozonation and at various salinity levels. Evidently, the most salinity effects occurred to the <C14 or >C24 *n*-alkanes.



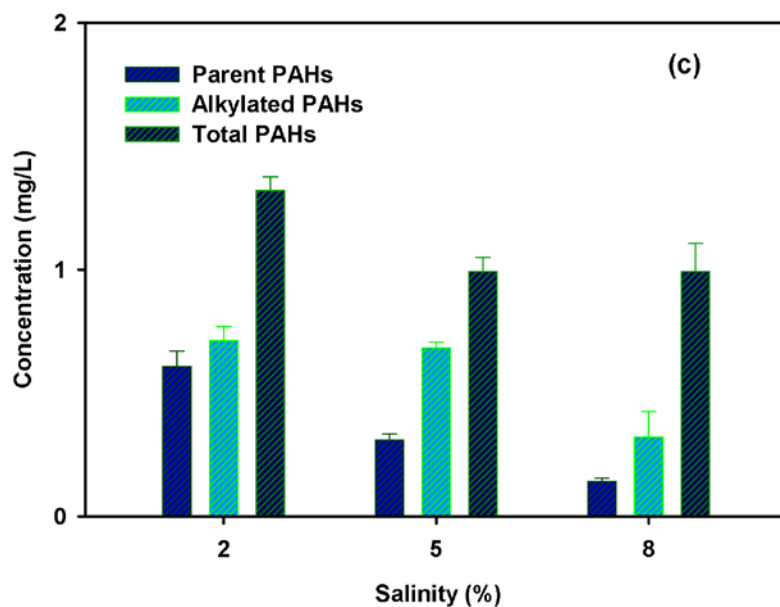
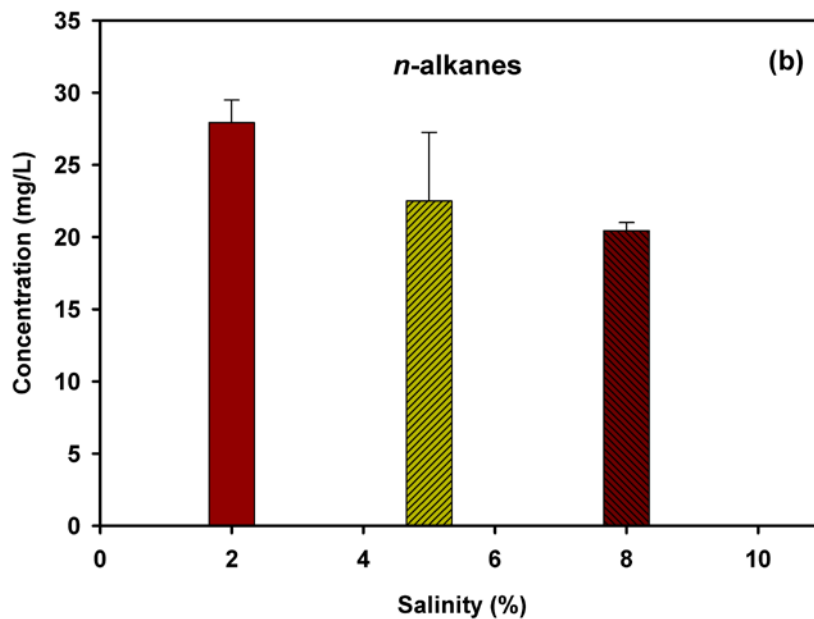
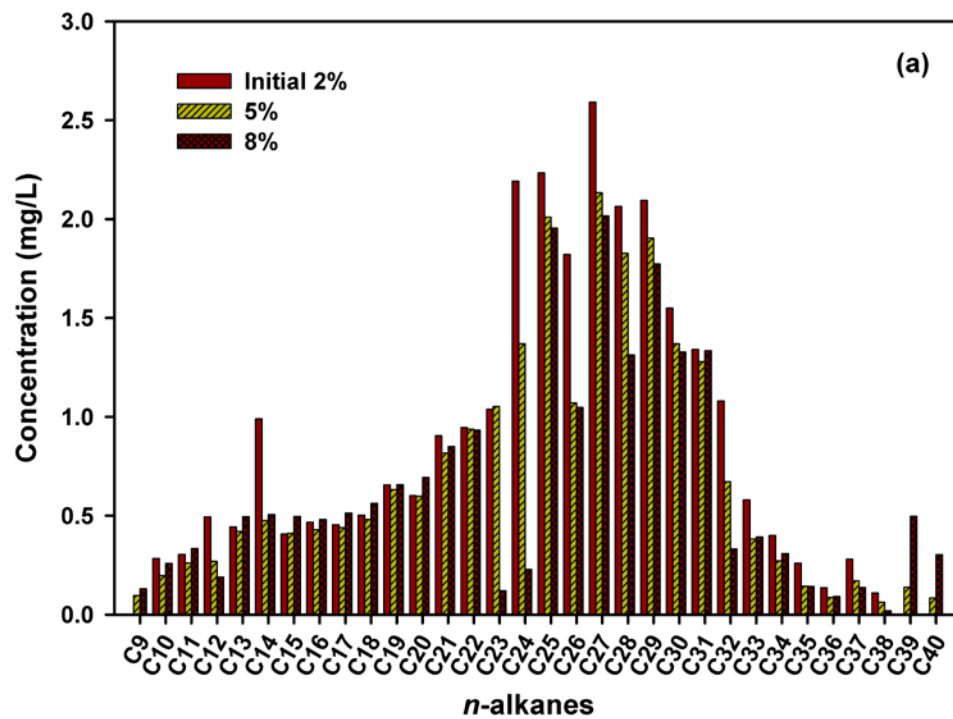


Figure 2-16. Remaining concentrations of: (a) TPHs, (b) *n*-alkanes and (c) PAHs in DWAO after 24-h ozonation at various salinity levels. Experimental conditions: Initial TPHs = 149.7 mg/L, *n*-alkanes = 79.3 mg/L and total PAHs = 6.2 mg/L (in DWAO with Corexit EC9500A), gas flow rate = 4 mL/min, ozone concentration = 86 ppbv, temperature = 22±1 °C, volume of solution = 250 mL, solution pH = 8.1±1, and DOM = 2.2 mg/L as TOC. Symbols: experimental data plotted

as mean of duplicates and error bars refer to deviation from the mean to indicate data reproducibility.



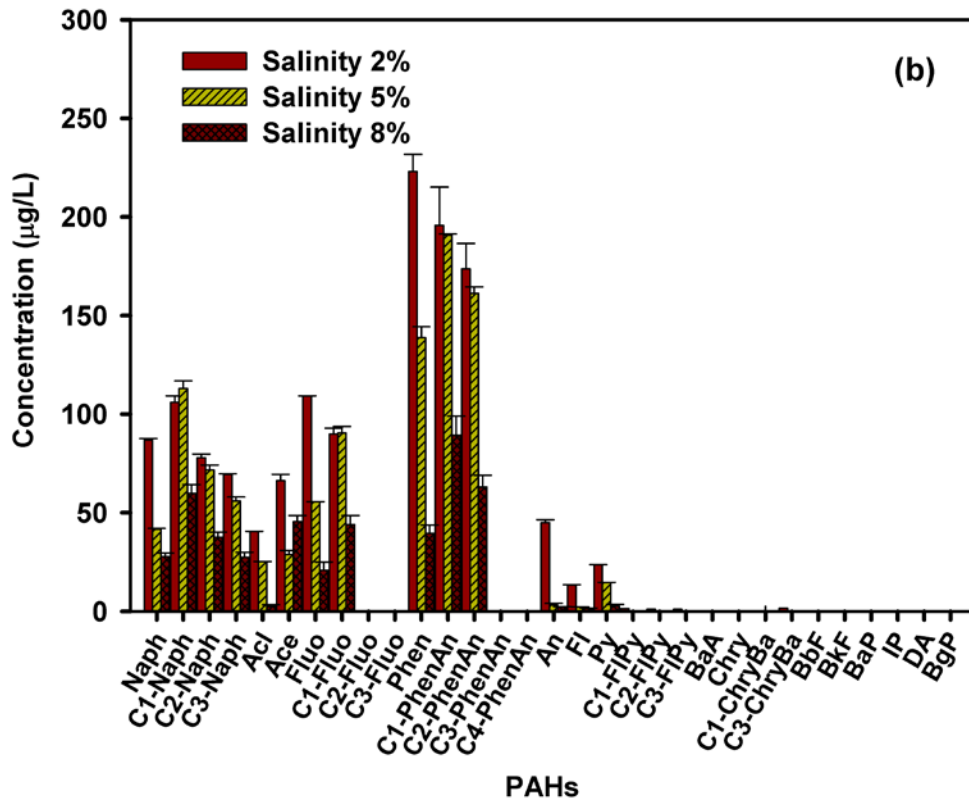


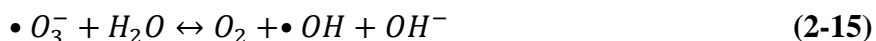
Figure 2-17. Distributions of remaining *n*-alkanes (a) and PAHs (b) in DWAO after 24h ozonation at various salinity. Experimental conditions are the same as in Fig. 2-16.

Salinity can affect ozone oxidation of oil components in the dispersant solutions in some contrasting ways (Gong and Zhao, 2017). First, NaCl can compete for dissolved ozone and radicals. As such, high salinity results in more inhibition of the ozonation on oil hydrocarbons (Muthukumar and Selvakumar, 2004). Second, elevated IS can increase the interfacial concentration of oil hydrocarbons at the ozone-solution interface due to the “salting out effect”, which enhances degradation of oil hydrocarbons. However, in the presence of the dispersant, the “salting out” effect is partially offset due to lowered surface tension and enhanced solubilization of the hydrophobic oil compounds. Third, in the presence of the dispersant, some of the lighter and

less-soluble components in the dispersant (e.g., Span 80) may entrain more oil hydrocarbons to the top layer of the water column, which is conducive to the contact and reactions with gaseous ozone in the headspace. Fourth, elevated IS may push more oil compounds to the dispersant/solvent cages, inhibiting ozonation.

2.3.7 Ozonation mechanisms

Typically, the radicals are formed through the following reactions (Forni et al., 1982; von Gunten, 2003; Zhao et al., 2004).



It is worth noting that the oxidation power of superoxide, ozonide and hydroperoxyl radicals is lower than that of hydroxyl radicals ($E^0 = +2.86$ V) (Litter and Quici, 2010).

To quantify the relative contributions of direct and indirect ozonation mechanisms, ozonation kinetics of TPHs, *n*-alkanes and total PAHs were measured with *p*CBA as an $\bullet OH$ scavenger and with or without the dispersant. Equations (2-16) and (2-17) illustrates reactions of *p*CBA with $\bullet OH$, and the second-order rate constant has been reported to be $k_{\bullet OH, pCBA} = 5.2 \times 10^9$ M⁻¹ s⁻¹ (Elovitz et al., 2000). The steady-state concentration of $\bullet OH$ ($[\bullet OH]_{ss}$) is calculated based on the depletion rate of *p*CBA according to Eqn. (2-18) (von Gunten, 2003; Zhang et al., 2013):



$$-\frac{d[pCBA]}{dt} = k_{\bullet OH, pCBA}[pCBA][\bullet OH]_{ss} \quad (2-17)$$

$$k_{\bullet OH, pCBA}[\bullet OH]_{ss} = k_{obs, pCBA} \quad (2-18)$$

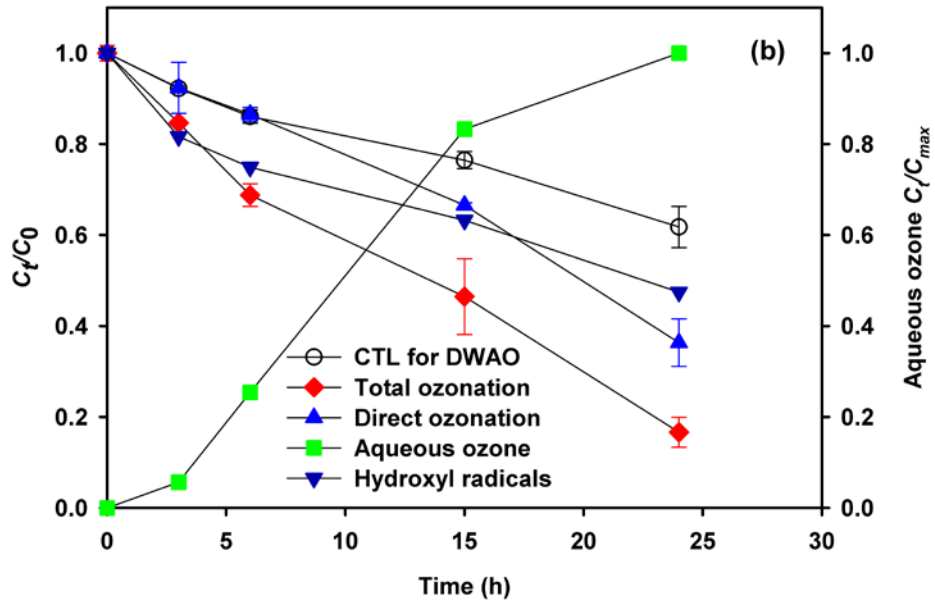
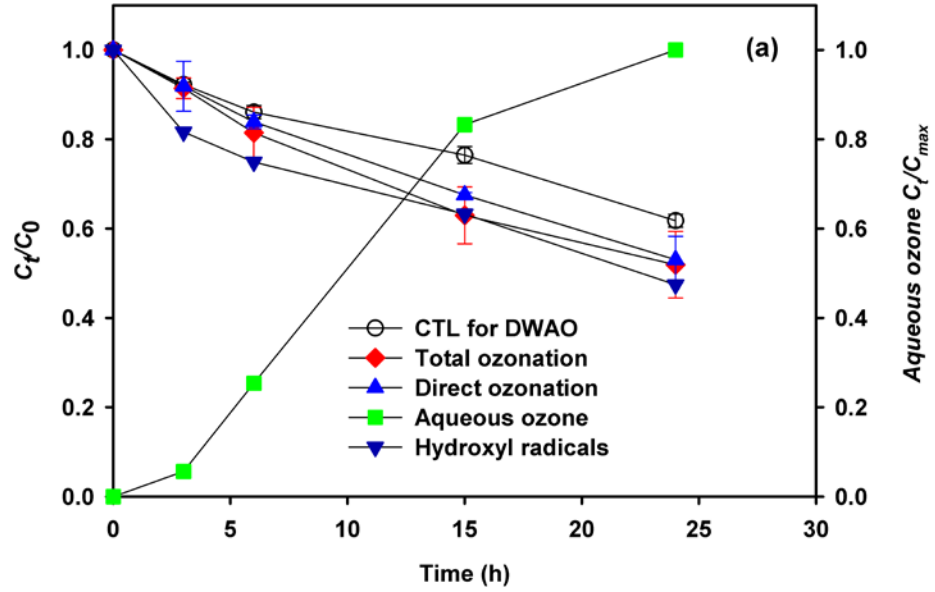
where the $k_{obs, pCBA}$ is the pseudo-first-order rate constant of *p*CBA degradation, which is 0.029 h⁻¹ (Eqn. 2-1 was employed to fit the experimental data in Fig. 2-18).

The overall TPHs depletion, involving volatilization, direct ozone oxidation and indirect radical oxidation, can be described by:

$$\frac{dC}{dt} = (k_v + k_D + k_R)C \quad (2-19)$$

where C is the reactant concentration ($\mu\text{g/L}$) at time t (h); and k_v , k_D and k_R refer to the rate constants (h^{-1}) of volatilization, direct ozonation and indirect ozonation.

Fig. 2-18 compares the overall ozonation and direct ozonation rates of TPHs (**Fig. 2-18a**), n -alkanes (**Fig. 2-18b**), and total PAHs (**Fig. 2-18c**), and **Table 2-7** gives the respective rate constants due to volatilization and different ozonation mechanisms. In the absence of $p\text{CBA}$, the overall ozonation rate constant of TPHs was 0.016 h^{-1} ; in the presence of the $p\text{CBA}$, the ozonation (direct ozonation) rate constant of TPHs was reduced to 0.009 h^{-1} , indicating that direct ozonation accounted for 56% of the overall ozonation based on the pseudo first-order rate constant. **Fig. 2-18b** shows the volatilization, total ozonation and direct ozonation of n -alkanes in DWAO. In the absence of the $p\text{CBA}$, the total ozonation rate of n -alkanes was 0.033 h^{-1} ; in the presence of $p\text{CBA}$, the ozonation rate was reduced to 0.018 h^{-1} , namely, 55% of the overall ozonation was attributed to direct ozonation, indicating that direct ozonation played a more important role than the indirect ozonation for degradation of n -alkanes. In addition, **Fig. 2-19a** shows that after 24 h of ozonation, 67.5% (by mass) of n -alkanes was degraded due to direct ozonation. **Fig. 2-18c** shows the volatilization, total ozonation and direct ozonation of PAHs under the same gas flow rate with or without $p\text{CBA}$. In the absence of $p\text{CBA}$, the ozonation rate constant of total PAHs was 0.048 h^{-1} ; in the presence of $p\text{CBA}$, the ozonation rate constant was lowered to 0.022 h^{-1} , indicating that direct ozonation contributed 45.8% to the total ozonation of total PAHs. In addition, the parent and alkylated PAHs were degraded by 37.5% and 39.9% due to direct ozonation, respectively (**Fig. 2-19b**).



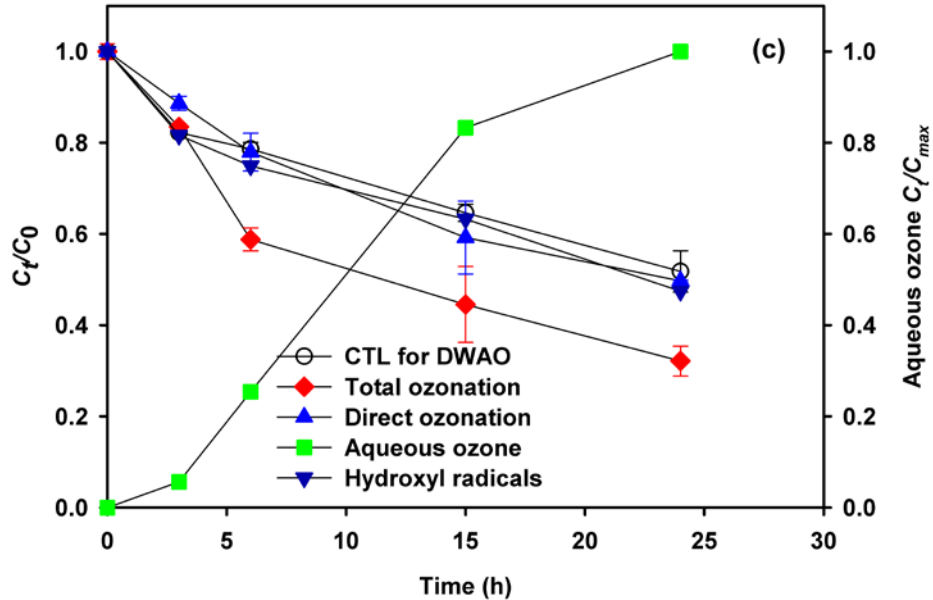
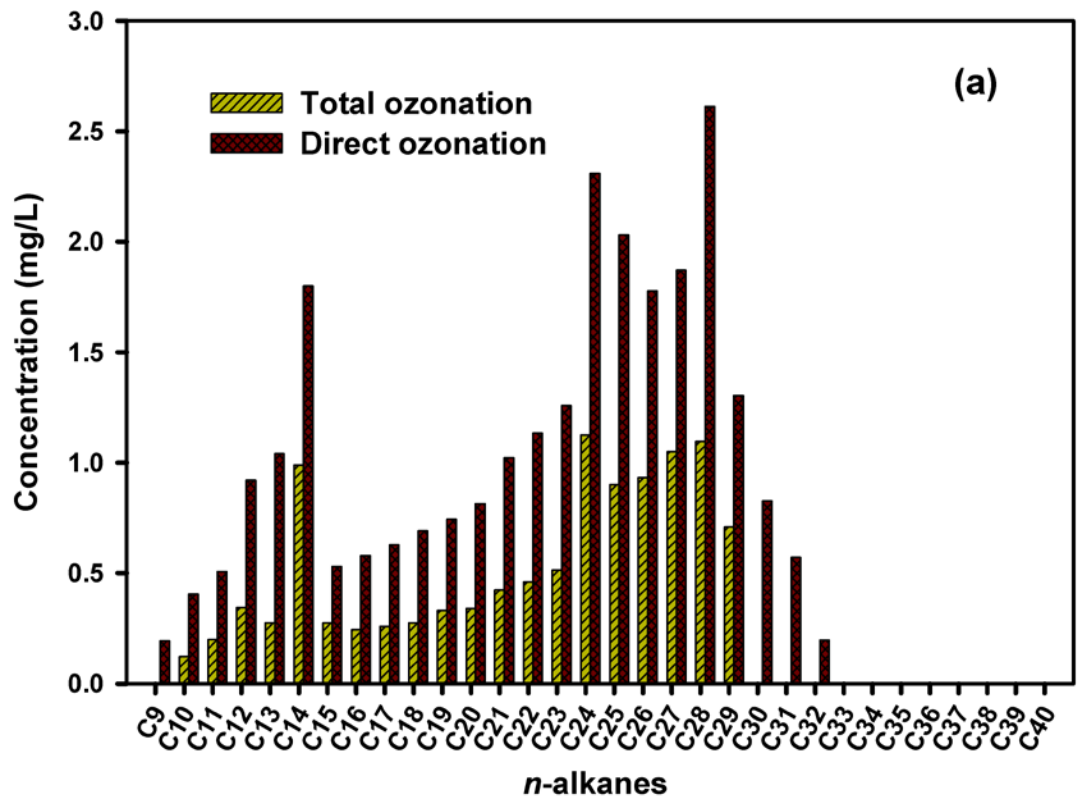


Figure 2-18. Transformation of (a) TPHs, (b) *n*-alkanes and (c) total PAHs by molecular ozone and hydroxyl radicals during ozonation of DWAO. Experimental conditions: Initial TPHs = 149.7 mg/L, *n*-alkanes = 79.3 mg/L and total PAHs = 6.2 mg/L (in DWAO with Corexit EC9500A), gas flow rate = 4 mL/min, ozone concentration = 86 ppbv, temperature = 22±1 °C, volume of solution = 250 mL, solution pH = 8.1±1, salinity = 2.0 wt.% and DOM = 2.2 mg/L as TOC.

Table 2-7. First-order ozonation rate constants for TPHs, n-alkanes and total PAHs in DWAO.

Type		Volatilization		Overall dissipation		Ozonation		
		k_v (h ⁻¹)	R^2	k (h ⁻¹)	R^2	k_o (h ⁻¹)	k_R (h ⁻¹)	k_D (h ⁻¹)
TPHs	Total ozonation	0.018	0.992	0.034	0.975	0.016	0.008	-
	Direct ozonation	0.018	0.992	0.026	0.999	0.009	-	0.009
<i>n</i> -alkanes	Total ozonation	0.009	0.999	0.051	0.984	0.042	0.033	
	Direct ozonation	0.009	0.999	0.026	0.956	0.018	-	0.018
Total PAHs	Total ozonation	0.015	0.964	0.063	0.966	0.048	0.026	
	Direct ozonation	0.015	0.964	0.036	0.956	0.022	-	0.022



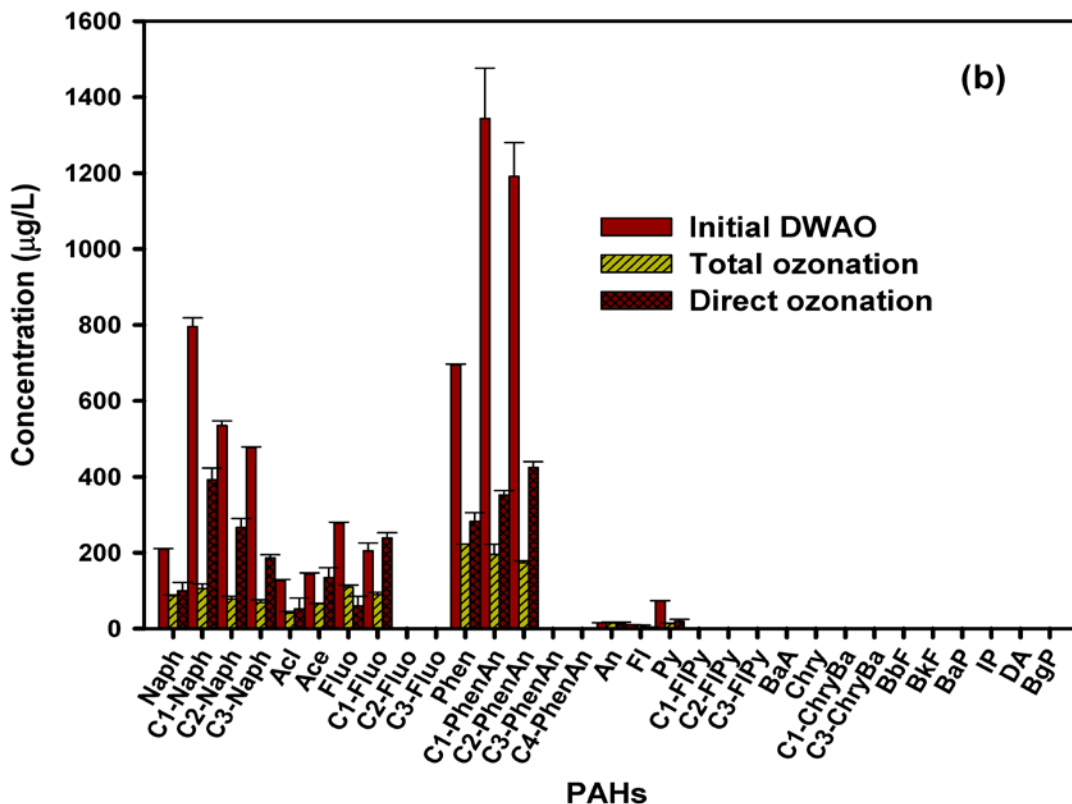
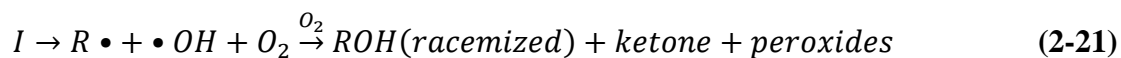


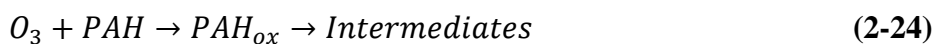
Figure 2-19. Distributions of remaining *n*-alkanes (a) and PAHs (b) after 24h ozonation (overall versus direct ozonation). Experimental conditions are the same as in Fig. 2-18.

Ozone molecules can directly react with the C-H bonds in alkanes. The initial attack of ozone on alkanes is centered on the σ -bonding between C and H atoms, which includes 1,3-dipolar insertion, and subsequent transformation to isomers of ketones, racemized alcohols and peroxides, as illustrated by the following reactions (Hamilton et al., 1968):



where *I* and *II* are the transition states (or solvent caged intermediates) given by the initial attacking of alkanes by ozone (*I* is for $[R\bullet HO\bullet \bullet O-O\bullet]$ and *II* is for $[R\bullet \bullet OOOH]$).

Direct reaction between PAHs and ozone lead to ring cleavage by electrophilic mechanisms (Bailey et al., 1968; Razumovskii, 2005), resulting in the formation of intermediates, such as quinones, hydroxylated and carboxylate benzenes, and oxygen derivatives of aliphatic compounds (Miller and Olejnik, 2004) (Eqn. 24). The intermediates may compete with the PAHs for both direct and indirect ozonation (Rubio-Clemente et al., 2014).



Ozonation of PAHs in DWAO solution can be attributed to several factors. On the one hand, the dispersant may promote the ozonation due to: 1) the dispersant-enhanced solubilization of molecular ozone can increase the formation of intermediates due to ring cleavage through direct oxidation and generation of free radicals (especially superoxide radicals), and 2) the ozone-facilitated alkylation not only promotes degradation of parent PAHs, but also leads to formation of more alkylated PAHs, which are known to be more ozone-reactive than the parent PAHs (Rubio-Clemente et al., 2014; von Gunten, 2003). On the other hand, the dispersant may inhibit the reaction due to: 1) the competition of intermediates with parent compounds for both molecular ozone and radicals, and 2) the competition of dispersant components, for instance, solvent propylene glycol can undergo both direct and indirect ozonolysis (Chou et al., 2006). The overall effect depends on the extent of these contrasting factors. In this work, the promoting effects for PAHs outran the inhibitive effects, and indirect ozonation attributed more than direct ozonation.

2.4 Conclusions

This study investigated the volatilization, direct ozonation and indirect ozonation of dispersed petroleum hydrocarbons in dispersant-oil-seawater systems under simulated atmospheric ozone. The primary findings are summarized as follows:

- 1) Corexit EC9500A accelerates ozonation of TPHs, *n*-alkanes and PAHs in DWAO. In the presence of 238 mg/L of Corexit EC9500A and at a gaseous ozone concentration of 86 ppbv, the pseudo first-order ozonation rate constants of TPHs, *n*-alkanes and total PAHs were 2.2, 1.01 and 1.96 times higher than those in WAO. Alkylated PAHs were more prone to ozonation than parent PAHs in both WAO and DWAO.
- 2) Corexit EC9500A increased the concentrations of TPHs, *n*-alkanes and PAHs in DWAO by 189, 648 and 12 times, respectively, than in WAO. The dispersant is more effective for *n*-alkanes than PAHs.
- 3) The ozonation rates for all the oil compounds increased with increasing ozone concentration. The ozonation rates of TPHs, *n*-alkanes and total PAHs were increased by 14.8, 5.1 and 6.3 times when the gaseous ozone concentration was increased from 86 to 300 ppbv. PAHs, especially naphthalene and C1-phenanthrene, were more sensitive to the ozone concentration than *n*-alkanes in DWAO.
- 4) Increasing pH slightly inhibited ozonation, especially for the 2-, 3- and 4-ring PAHs and their homologues in DWAO due to the major loss in the direct ozonation. Elevated humic acid concentrations also inhibited the ozonation reactions, and the inhibitive effect of humic acid is more evident on larger *n*-alkanes, in particular the C24–C30 fraction. Higher salinity enhanced the ozonation of all the dispersed oil components due to reduced solvent cage effect and the salting-out effect of hydrophobic compounds. Meanwhile, addition of 18 mg/L or 24 mg/L of

the dispersant to DWAO accelerated the ozonation of TPHs and *n*-alkanes, but inhibited the ozonation of PAHs due to ozone-facilitated alkylation process and dispersant cage effect.

- 5) Direct ozonation accounted for 56%, 54% and 45.8% of the overall ozonation of TPHs, *n*-alkanes and PAHs, respectively. For *n*-alkanes, the direct ozonation played a more important role. In contrast, for PAHs, the indirect ozonation was more important, respectively, especially for the 2-ring PAHs (naphthalene and its homologues, acenaphthylene and acenaphthene) and 3-ring PAHs (phenanthrene and its homologues). In addition, the parent and alkylated PAHs were degraded by 37.5% and 39.9% due to direct ozonation.
- 6) The dispersant can increase soluble ozone concentration and enhance the hydroxyl radical generation, but may also compete with oil hydrocarbons for both molecular ozone and free radicals. These contrasting effects result in the different reaction rates for various oil compounds.

This work is the first systematic investigation on oil weathering under simulated atmospheric ozone, and on the effects of a model oil dispersant on the ozonation rates of various oil components. The results indicate that ozonation may play an important role in oil weathering, and thus should be taken into account in the oil budget estimation and in the related impact assessment.

Chapter 3. Sorption of dispersed petroleum hydrocarbons by activated charcoals:

Kinetics, isotherms and roles of oil dispersants

This study investigated the effectiveness of three model activated charcoals (ACs) of different particle sizes (4-12, 12-20 and 100 mesh) for removal of oil dispersed in marine water by two prototype oil dispersants (Corexit EC9500A and Corexit EC9527A). Sorption kinetics and isotherms were conducted. To elucidate the sorption mechanism, various characterizations of ACs were investigated. Furthermore, the effects of presence of additional dispersant Corexit EC9500A, pH and salinity were also determined. This information is important for understanding roles of oil dispersant on the sorption of dispersed oil by activated charcoals from the dispersant-seawater-oil system.

3.1 Introduction

Oil spill has been a major marine pollution concern in the modern time. For instance, the 1989 *Exxon Valdez* in Alaska spilled at least 43,000m³ (~11 million gallons) of crude oil, and affected marine ecosystems, i.e. growth suppression, embryotoxicity to fish, persistence on beaches and other indirect effects (Short, 2017); the *Mega Borg* shipboard explosion in Texas discharge 17,100m³ (~4.5 million gallons) of crude oil (Smultea and Würsig, 1995); and the 1996 North Cape discharged ~3000m³ (~0.8 million gallons) of No. 2 fuel oil just offshore of Rhode Island (Ho et al., 1999). During the Deepwater Horizon (*DwH*) oil spill in 2010, more than 4.4 million barrels (6.4 million liters) of Louisiana Sweet Crude (LSC) oil were released into the Gulf

of Mexico (GOM) (Camilli et al., 2010; Reddy et al., 2012; Sammarco et al., 2013). Typically, crude oil contains saturated *n*-alkanes, polycyclic aromatic hydrocarbons (PAHs) and their alkylated homologues (Ryerson et al., 2012). For instance, the *DwH* oil contained ~3.9 wt.% of PAHs ($\sim 2.1 \times 10^7$ kg), ~1.5 wt.% of their alkylated PAHs ($\sim 7.9 \times 10^6$ kg) and ~15.3 wt.% of *n*-alkanes ($\sim 8.1 \times 10^7$ kg).

The use of oil dispersants has become one of major emergency response measures to cope with oil spills and to mitigate the environmental impacts. According to the U.S. Environmental Protection Agency's National Contingency Plan Subpart J Product Schedule, there are currently 22 oil dispersants that are available and authorized to use during an oil spill. During the 2010 *DwH* oil spill, BP applied ca. 6.8 million liters of Corexit EC9500A and 1.1 million liters Corexit EC9527A at the sea surface and the wellhead (Bianchi et al., 2014; Kujawinski et al., 2011). As a result, it was estimated that ~16% of the spilled oil was dispersed by the dispersants (Ramseur, 2010).

While oil dispersants are aimed to enhance the aqueous apparent solubility and bioavailability of crude oil (Mendoza et al., 2013; Zhou and Guo, 2012; Zhou et al., 2013), our knowledge on their roles in altering the environmental fate and transport of spilled oil in the aquatic environmental (including marine ecosystems) has been limited. Fu et al. (2014) observed that the dispersant Corexit EC9500A facilitated the formation of marine oil snow (MOS), leading to vertical transport (rising or sinking) of dispersed oil. In addition, they observed that the dispersant not only enhanced dissolution of *n*-alkanes (C9–C40) from oil slicks into the aqueous phase, but facilitated sorption of more oil components onto MOS. Gong et al. (2014) studied that the effect of oil dispersant (Corexit EC9500A) on sorption/desorption of phenanthrene with two marine sediments, indicating that the presence of the dispersant (18 mg/L) can not only enhance the uptake

of phenanthrene by up to 7% but reduce the desorption of phenanthrene by up to 5%. In addition, Zhao et al. (2015) investigated three dispersants (Corexit EC500A, Corexit EC9527A and SPC 1000) in the simulated marine system. They found that additional dispersant Corexit EC9500A (18 mg/L) can increase the uptake of 2-3 ring PAHs on sediment, whereas higher dispersant dosages will reduce the uptake.

The past use of chemical dispersants in response to oil spills in the U.S. has been limited primarily to offshore marine waters (typically ≥ 3 miles from the shoreline). As the use of dispersants is becoming more accepted, there is an growing interest in their use in nearer shore (Herndon, 2010). However, near-shore application of oil dispersants may generate larger amounts of wastewater containing high concentrations 0.5–50 mg/L (McAuliffe, 1989) of dispersed oil (i.e., dispersed oil droplets with dispersant molecules). It was reported that dispersed oil can be more toxic or pose more acute toxicity to marine life or aquatic communities than the oil slicks (Anderson et al., 2009; Bejarano and Barron, 2014; Mitchell and Holdway, 2000; Singer et al., 1998; Singer et al., 1991). As such, invasion of the wastewater into costal sensitive areas pose a serious threat to the health of coastal ecosystems and human health. Moreover, as dispersants are often used in combination with other clean-up methods (e.g., skimmers, booms, and/or burning) and used to clean or remove oil from wildlife or from beach areas, larger amounts of wastewater with dispersed oil are generated. For instance, during the DwH oil spill, estimated 20 millions of gallons of oil-laden wastewater were produced near shore, which demanded costly further handling or treatment (Beyer et al., 2016; Fakhru'l-Razi et al., 2009; Lee and Neff, 2011; Short, 2017).

Since dispersants are designed to disperse oil slicks into water column, the high salinity and high concentration of dispersed oil in the resulting wastewater impede effective separation or

degradation of the petroleum hydrocarbons through conventional municipal wastewater treatment processes. To facilitate oil removal from water, researchers have studied various types of sorbents, such as activated charcoal/carbon (AC) (Ahmad et al., 2005; Ayotamuno et al., 2006; Pollard et al., 1992), biochar (Nguyen and Pignatello, 2013), synthetic nanocomposites (Chu and Pan, 2012), aerogel (Chin et al., 2014), fibers (Zhu et al., 2011), exfoliated graphite (Toyoda and Inagaki, 2003; Wang et al., 2010), peat-based materials (Cojocararu et al., 2011), sponge or foam (Calcagnile et al., 2012; He et al., 2013; Liu et al., 2013), natural materials (Kumagai et al., 2007) and other types of sorbents (Adebajo et al., 2003; Guix et al., 2012; Yu et al., 2012). However, the knowledge on the effects of oil dispersants on the sorption of dispersed petroleum hydrocarbons by activated charcoal has been very limited. In addition, the influences of other factors such as pH and salinity on the sorption of oil hydrocarbons in the presence of oil dispersants have not yet been explored.

The overall goal of this study was to investigate the effects of oil dispersant on the sorption of dispersed oil using activated charcoal, and understand the roles of oil dispersant in the sorption process. The specific objectives were to: 1) determine the kinetics rates and isotherm of dispersed oil in two different DWAO by activated charcoal, 2) investigate the effects of a model dispersant (Corexit EC9500A and Corexit EC9527A) on the sorption process; and 3) elucidate the sorption mechanisms.

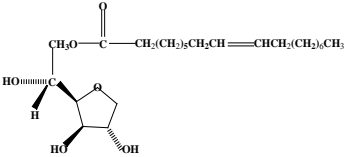
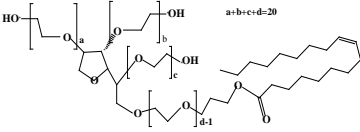
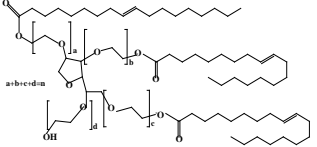
3.2 Materials and Methods

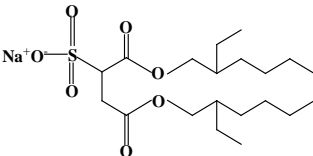
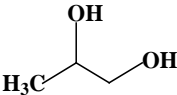
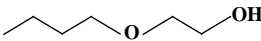
3.2.1. Chemicals and Materials

All chemicals used in this study were analytical grade or higher. Methanol was purchased from Alfa Aesar (Ward Hill, MA, USA). Chromatographic grade dichloromethane (DCM), hexane, NaOH, NaCl and Sodium azide (NaN_3) were obtained from Fisher Scientific (Fair lawn,

NJ, USA). HCl was acquired from BDH Aristar (West Chester, PA, USA). Corexit EC9500A and Corexit EC9527A, which were used during the *DwH* oil spill, were obtained by the courtesy of Nalco Company (Naperville, IL, USA). The critical micelle concentration (CMC) of Corexit EC9500A and Corexit EC9527A was reported to be 22.50 mg/L (Gong et al., 2014) and 20.11 mg/L (Fu et al., 2015), respectively. **Table 3-1** gives specific information about the formulations of the two model dispersants.

Table 3-1. Chemical constituents of dispersants Corexit EC9500A^a and Corexit EC9527A.

Name	CAS number	Ionic property	Synonym	Molecular formula	Average MW (g/mol)	HLB	CMC (mg/L)	Chemical structure
Span 80	1338-43-8	Neutral surfactant	Sorbitan, mono-(9Z)-9-octadecenoate	C ₂₄ H ₄₄ O ₆	428.61	4.3	N/A	
Tween 80	9005-65-6	Neutral surfactant	Sorbitan, mono-(9Z)-9-octadecenoate, poly(oxy-1,2-ethanediyl) derivs.	C ₆₄ H ₁₂₄ O ₂₆	1310	15	14	
Tween 85	9005-70-3	Neutral surfactant	Sorbitan, tri-(9Z)-9-octadecenoate, poly(oxy-1,2-ethanediyl) derivs	C ₆₀ H ₁₀₈ O ₈ (C ₂ H ₄ O) _n	1838.57	11	23	

SDSS	577-11-7	Anionic surfactant	Butanedioic acid, 2-sulfo-, 1,4-bis(2-ethylhexyl) ester, sodium salt (1:1)	$C_{20}H_{37}SO_7Na$	444.57	10.9	578	
DPnB	29911-28-2	Solvent	Propanol, 1-(2-butoxy-1-methylethoxy)	$C_{10}H_{22}O_3$	190		N/A	$H_3C-CH_2-CH_2-OC_2H_4OC_2H_4OH$
PG	57-55-6	Solvent	Propylene Glycol, 1,2-dihydroxypropane	$CH_3CHOHCH_2OH$	76.1		N/A	
Distillates	64742-47-8	Solvent	Distillates (petroleum), hydrotreated light	N/A	N/A		N/A	N/A
Ethanol, 2-butoxy ^b	111-76-2	Solvent	2-Butoxyethanol	$C_6H_{14}O_2$	118.17		N/A	

^aThe above information is summarized based on several studies (Glover et al. 2014, Gong et al. 2014, Ji et al. 2018, Kover et al. 2014, Koos et al. 2012, Nadarajah et al. 2002, Omotosho et al. 1989, Zhao et al. 2015).

^bThis chemical component is not included in Corexit 9500A.

Three commercially available activated charcoals were tested in a series of batch sorption equilibrium and kinetic experiments, including two granular activated charcoals (GAC) from Sigma-Aldrich (St. Louis, MO, USA), namely, with a mesh size 4-12 (GAC4×12) and 12-20 (GAC12×20), and a powder AC with a 100 mesh size (PAC100). For comparison, a coarse biochar purchased from Charcoal Green (Crawford, NE, USA) and a polypropylene fiber (Bon Tool Co., Gibsonia, PA, USA) were also tested. The biochar, and ACs were first acid-washed to remove inorganic carbon or other impurities by mixing 10 g of a sorbent with 100 mL of 1 M HCl for 2 hours. Then, the sorbents were rinsed five times with deionized water, and dried at 85 °C for 24 hours. To compare, the fiber was also pre-treated as the above procedure.

3.2.2 Seawater and oil samples

Seawater was collected from the top 30 cm of the water column from Grand Bay, AL, USA (N30.37926/W88.30684). Seawater sample was stored in sealed containers at 4 °C in the refrigerator. The sample was first filtered through 0.22 µm sterile membrane filters (mixed cellulose ester) to remove suspended solids, and then sterilized by autoclaving at 121 °C for 35 min. Salient properties of the treated seawater sample were: pH = 8.3, dissolved organic matter (DOM) = 2.2 mg/L as TOC, salinity = 2 wt.%, Cl⁻ = 18.55 g/L, NO₃⁻ = 2.55 g/L, SO₄²⁻ = 4.25 g/L, and ionic strength (IS) = 0.7 M. The treated seawater was free of *n*-alkanes and PAHs.

A surrogate LSC oil was acquired through courtesy of BP (Houston, TX, USA). According to the supplier, the physical, chemical and toxicological properties of the surrogate oil are similar to those of the Macondo Well crude oil of Mississippi Canyon Block 252. To simulate the natural loss of the volatile oil compounds at sea surface following an oil spill, the crude oil was artificially weathered according to the method by Sorial et al. (2004). In brief, 1.0 L of the oil sample was

purged by air through a glass tube from the bottom of a flask in dark at a constant air flowrate of ~2 L/min for 10 days to eliminate the lighter compounds. Upon the weathering process, the oil mass diminished from 807.1 to 608.5 g (by 24.6 wt.%), and the density increased from 0.807 to 0.834 g/cm³.

3.2.3 Effects of dispersant on sorption of oil hydrocarbons

Water accommodated oil (WAO) and dispersant-facilitated water accommodated oil (DWAO) were prepared with the surrogate oil following a slightly modified protocol by Singer et al. (2000). The preparation details were described by Ji et al. (2018). In this paper, DWAO also refers to dispersed oil. For typographical convenience, DWAO prepared with Corexit EC9500A and Corexit EC9527A is referred to as DWAO-I and DWAO-II, respectively.

The oil sorption kinetic tests were conducted by adding 0.1 g of an adsorbent into 43 mL amber glass vials with Teflon-lined caps containing 40 mL of DWAO, and then mixing them on an end-to-end rotator at 60 rpm and at room temperature (22±1 °C). At predetermined times, selected vials were centrifuged at 3000 rpm for 5 minutes, and then each 20 mL of the solution sample was extracted with DCM in three consecutive steps (5 mL DCM in each step) according to EPA Method 3510C (EPA, 1996), and then the extracts were combined and filtered through a glass column (L×D = 3×1 cm) packed with 5 g of anhydrous sodium sulfate to remove moisture, and then concentrated to 4 mL under a gentle nitrogen flow. Then, the concentrated samples were filtered through a polytetrafluoroethylene (PTFE) membrane (0.22 μm) filter to remove residual sodium sulfate, and then filtrates were analyzed for oil content and/or PAHs, *n*-alkanes followed the analytic method described in Section 3.2.5.

The sorption isotherm tests were carried out following similar procedures as for the kinetic tests and by equilibrating the sorption for 24 h. The sorption was initiated by adding 0.005–0.5 g of an adsorbent into 40 mL of DWAO-I in 43 mL amber glass vials with Teflon-lined caps. Upon equilibrium, the vials were centrifuged, and the samples were extracted and analyzed in the same manner as in the kinetic tests. Control tests were carried in the absence of AC, and the results indicated that the loss of TOCs in DWAO-I and DWAO-II was less than 1% in all cases. All experiments were conducted in duplicate, and data reported as mean of duplicates with errors calculated as relative deviation from the means.

The equilibrium oil uptake (q_e , mg/g) and removal efficiency (E , %) are calculated via:

$$q_e = \frac{(C_0 - C_e)V}{m} \quad (3-1)$$

$$E = \frac{(C_0 - C_e)}{C_0} \times 100\% \quad (3-2)$$

where C_0 and C_e are the initial and equilibrium oil concentrations (mg/L) in the aqueous phase, respectively, V is the solution volume (L), and m is the mass of the sorbents.

To investigate effects of oil dispersants on oil sorption, equilibrium batch sorption tests were conducted by adding various amounts of Corexit EC9500A in the DWAO-I. In brief, a dispersant stock solution was first prepared by adding 0.1 g of Corexit EC9500A into 100 mL of seawater under magnetic stirring. Then, various volumes of the dispersant solution (0.2, 0.4, 0.6, 0.8 and 1 mL) were added into 40 mL of DWAO-I in 43 mL amber glass vials, and mixed for 10 minutes, resulting in the additional Corexit EC9500A concentration of 5, 10, 15, 20 and 25 mg/L. The sorption tests were then conducted by equilibrating the systems for 24 h following the same experimental equilibrium isotherm procedures as described above. To acquire further insights into the mechanisms underlying the dispersant effects, the sorption behaviors of Corexit EC9500A by the ACs were investigated through batch sorption kinetic tests. To this end, a dispersant solution

of 50 mg/L was prepared using the seawater sample. The kinetic tests were initiated by adding 0.1 g of an AC into 40 mL of the dispersant solution in amber glass vials with Teflon-lined caps. The sorption rates were then followed by monitoring the change in the dispersant concentration in the solution phase, which was measured as total organic carbon (TOC). The sorption isotherm tests of Corexit EC9500A were carried out following similar procedures as for the kinetic tests and by equilibrating the sorption for 24 h. The sorption was initiated by adding 0.1 g of an adsorbent into 40 mL of seawater in 43 mL amber glass vials with Teflon-lined caps in the presence of 15.1, 42.3, 84.6, 169.3, 423.3, 846.5 and 1693.7 mg/L as TOC of Corexit EC9500A. After equilibrium, the vials were centrifuged (3000 rpm for 10 min), and the samples were obtained and analyzed in the same manner as in the kinetic tests.

3.2.4 Effects of solution chemistry on sorption of dispersed oil

Effects of aqueous pH and salinity on sorption of dispersed oil in DWAO were tested through the sorption isotherm tests as described in **Section 3.2.3**. To study pH effect, the initial DWAO solution pH was adjusted to 6, 7 and 9 using dilute HCl (0.1 M) or NaOH (0.1 M). To test effect of salinity, the initial DWAO solution salinity was varied from 2 wt.% to 8 wt.% by adding a NaCl stock solution (25 wt.%).

3.2.5 Analytical methods

Oil concentrations in DWAO were determined based on analyses of total petroleum hydrocarbons (TPHs), *n*-alkanes, and PAHs. TPHs in the DCM extracts were analyzed following the method described in Section S1 of SM using a Gas Chromatograph system with a flame ionization detector (GC-FID, Agilent 6890 GC-FID) equipped with a DB5 column (30 m × 0.25

mm, 0.25 μm film thickness). In addition, *n*-alkanes and PAHs in the extracts were analyzed by a GC-MS system (Agilent 7890A GC coupled with the 5975C Series mass spectrometry, Agilent Technologies Inc., Santa Clara, CA, USA) equipped with a DB-EUPAH column (30 m \times 0.18 mm, 0.14 μm film thickness) following the method described in **Section 2.2.5**. Sixteen PAHs (**Table 2-1** in **Section 2.2.1**) specified in EPA Method 610 (EPA, 1984) and *n*-alkanes (C9–C40) were targeted. TOC was analyzed using a Tekmar Dohrmann Pheonix 8000 UV-Persulfate TOC analyzer (Mason, OH, USA) with a detection limit of 0.1 mg/L. Zeta potential of ACs was measured using Dynamic Light Scattering (DLS) (Nano-ZS90 Zetasizer, Malvern Instruments, UK).

3.2.6 Material characterization

The BET surface area of the sorbents was acquired using an ASAP 2010 BET surface area analyzer (Micromeritics, USA) in the relative pressure (P/P_0) range of 0.06–0.20. Meanwhile, pore size distribution was obtained following the Barret-Joyner-Halender method, where the nitrogen adsorption at the relative pressure of 0.99 was used to determine the pore volume and the average pore diameter. The surface elemental compositions and oxidation states of the sorbent were analyzed using an AXIS-Ultra X-ray photoelectron spectroscopy (XPS) (Kratos Analytical Ltd.), which was operated under the monochromatic Al $K\alpha$ radiation (225W, 15 kV, 15 mA). All the peaks were calibrated using the C 1s hydrocarbon peak at 284.80 eV in order to compensate for the static charge effects. The surface morphology of the sorbent was imaged using a scanning electron microscope (SEM) (FEI XL30F, Philips, USA) operated at 20 kV, and further analyzed via energy-dispersive X-ray spectroscopy (EDS). The crystal phases of the samples were analyzed using an X-ray diffractometer (XRD) (D/max-2400, Rigaku, Japan) at 100 kV and 40 mA with the

Cu $K\alpha$ radiation ($\lambda = 1.542 \text{ \AA}$) and a scanning rate of $2^\circ/\text{min}$. Fourier transform infrared spectroscopy (FTIR) (Tensor 27, Bruker, Germany) analysis was carried out to analyze the surface functional groups, and it was operated with a scanning range of $4000\text{--}400 \text{ cm}^{-1}$ and a resolution of 4 cm^{-1} through the KBr pellet method.

3.3 Results and Discussion

3.3.1 Characterization of Activated charcoal

Fig. 3-1 displays the SEM images of neat GAC12 \times 20. The surface of the virgin AC appeared bulky, flat and smooth (**Fig. 3-1a**). The EDS data revealed two major elements (C, O) on the surface (**Fig. 3-1b**). **Fig. 3-2** presents the XRD patterns of the AC. The two peaks at 26° and 43° are attributed to the diffractions of crystal planes of graphite (002) and (100), respectively (Liu et al., 2016; Quiñones et al., 2014). **Tables 3-2** and **3-3** list the atomic compositions according to the XPS spectra of the AC (not shown). The presence of atomic percentile of C associated with the $\pi\text{--}\pi$ bond (9.9 %) is attributed to adsorption of organic compounds through $\pi\text{--}\pi$ interactions. **Fig. 3-3** shows the FTIR spectra, where the peak at 1091 cm^{-1} belongs to the C–OH groups; the weak peak at 3437 cm^{-1} , 1574 cm^{-1} and 789 cm^{-1} assigned to the O–H groups, C=C or C=O groups and C–H groups, respectively. (Przepiórski, 2006; Tan et al., 2007; Terzyk, 2001).

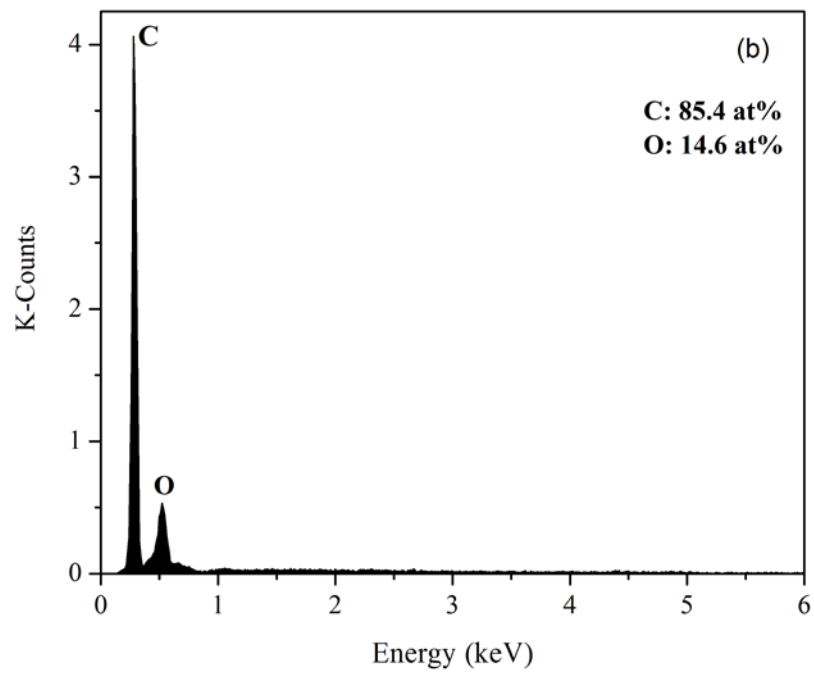
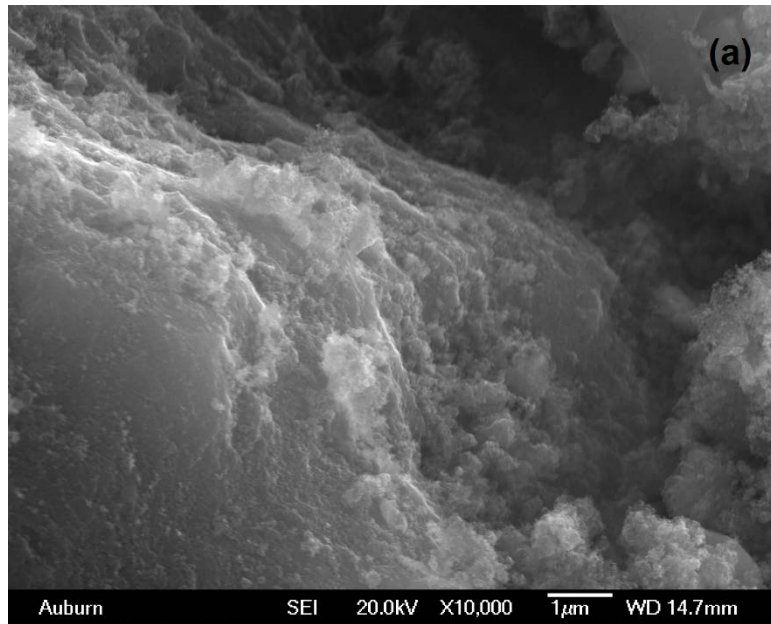


Figure 3-1. SEM images (a) and EDS spectra (b) of GAC12×20.

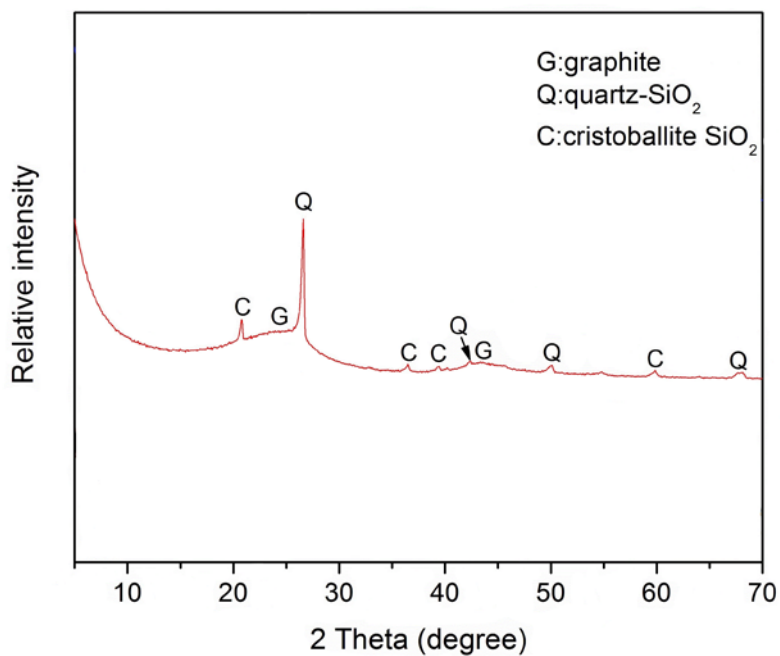


Figure 3-2. XRD patterns of GAC12×20.

Table 3-2. Atomic compositions of GAC12×20.

Material	Element atomic percent (%)			
	C	O	Na	Si
GAC12×20	82.1	12.7	0.2	5.0

Table 3-3. Atomic percent of different compositions of C 1s and O 1s.

Material	Element atomic percent (%)			
	C	O	Na	Si
GAC12×20	82.1	12.7	0.2	5.0

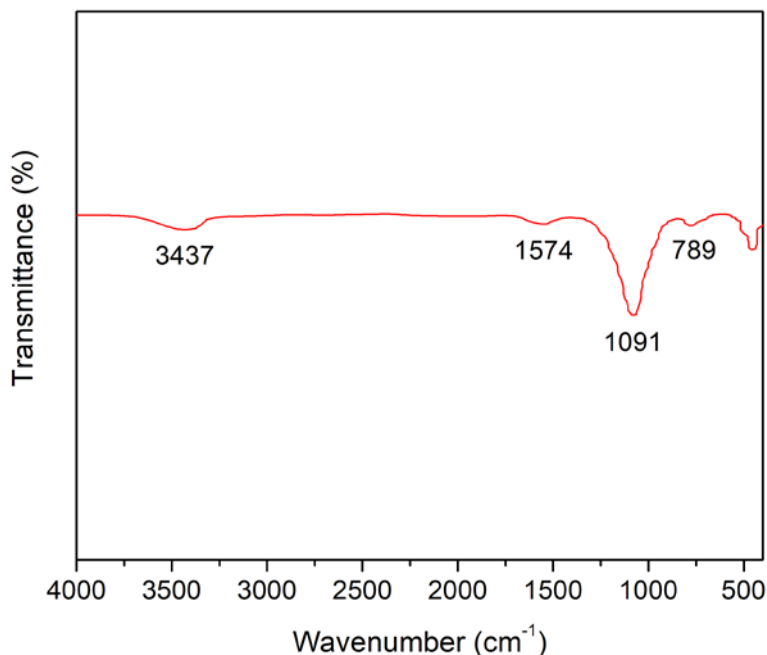
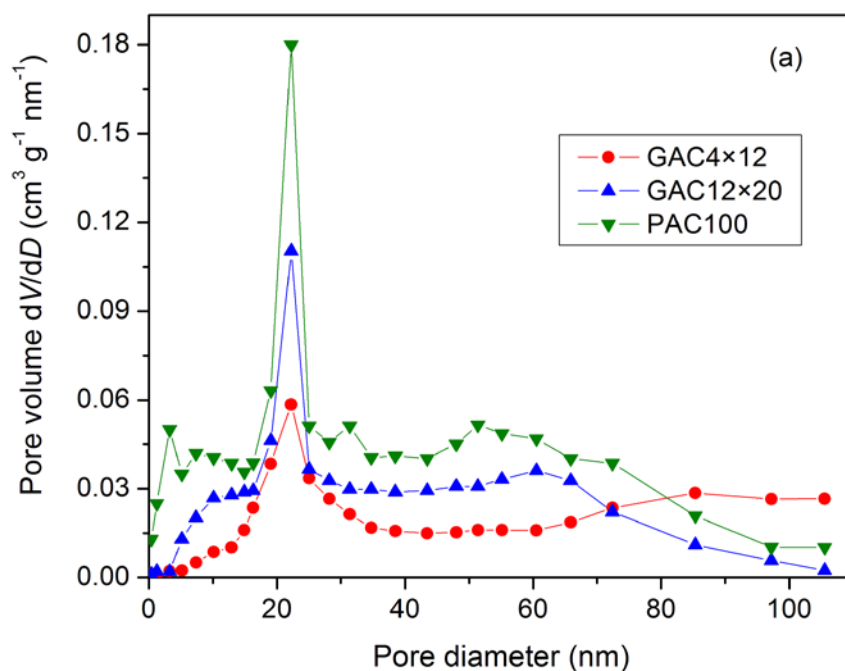


Figure 3-3. FTIR spectra of GAC12×20.

Fig. 3-4a presents the pore size distributions of the three ACs. As the particle size of AC increases, the BET surface area and total pore volume decreased. For instance, the BET surface area and total pore volume of PAC100 (889 m²/g, 0.95 cm³/g) were 71.0% and 75.9% higher, respectively, than those of GAC4×12 (520 m²/g, 0.54 cm³/g), and 65.9% and 39.7% higher than those of GAC12×20 (536 m²/g, 0.68 cm³/g) (**Table 3-4**). These values are consistent with those reported values by Ahn et al. (2008). The peak positions on the pore size distributions were centered around 22 nm for all three ACs, which are expected because the ACs were manufactured from similar raw material and following the same activating procedure. However, the peak height decreased and the width increased with increasing particle size, indicating the smaller ACs have

more smaller pores at around 2 nm and narrower size distribution. The results are consistent with Ahn et al. (2007), who reported that GAC4×12 contained 37.2% macropores (>50 nm), 22.5% mesopores (2-50 nm), and 40.3% micropores (<2 nm); whereas GAC12×20 had 45.6% macropores, 21.9% mesopores, and 32.5% micropores. Moreover, PAC100 contained 43.4% macropores, 21.9% mesopores, and 32.5% micropores. Morevoer, PAC100 contained 43.4% mesopores and 40.6% micropores, and smaller pores (<15 nm). **Fig. 3-4b** shows the zeta potential of ACs as a function of pH, from which the point-of-zero-charge pH (pH_{PZC}) values were derived to be 7.3, 6.8 and 6.1 for GAC4×12, GAC12×20 and PAC100, respectively (**Table 3-4**).



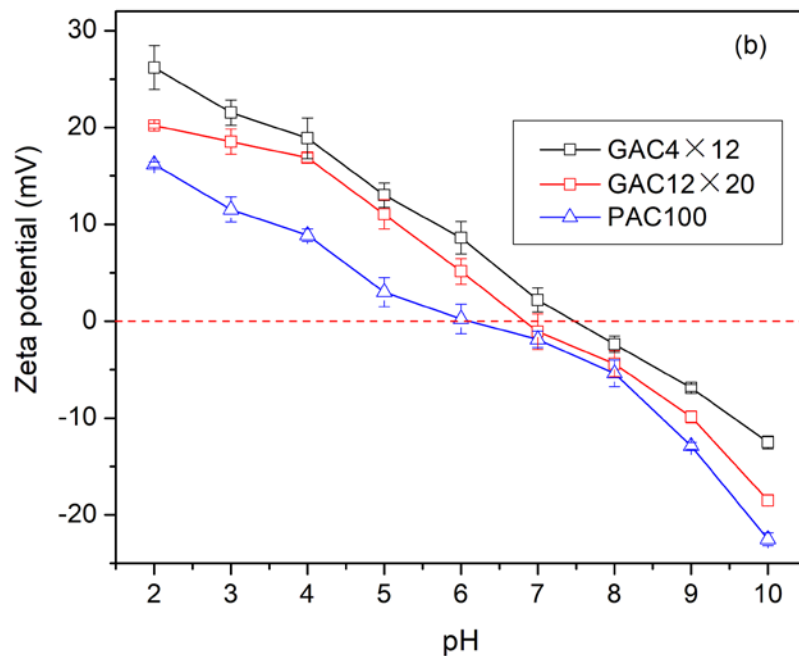


Figure 3-4. (a) Pore size distributions of three activated charcoals tested in this work, and (b) Zeta potential of three ACs as a function of solution pH.

Table 3-4. Key physicochemical properties of three model activated charcoals.

Activated charcoal	BET surface area (m ² /g)	Single point total pore volume (cm ³ /g)	Point of zero charge (pH _{PzC})
GAC4×12	520 ^a	0.54 ^a	7.3 or 6.9 ^a
GAC12×20	536.1 or 539 ^a	0.60 or 0.70 ^a	6.8
PAC100	889	0.95	6.1

^a From Ahn et al., 2007

3.3.2 Sorption of dispersed oil by various model sorbents

Fig. 3-5 compares the equilibrium (24 h) removals of dispersed oil in DWAO-I by the five adsorbents. On an equal mass basis, the removal efficiency followed the sequence of: PAC100 (99.3%) > GAC12×20 (97.5%) > GAC4×12 (91.4%) > Biochar (31.4%) > polypropylene fiber (22.4%). Evidently, all ACs displayed much greater oil sorption capacity, and thus, were further tested in the subsequent sorption studies. Of the three ACs, the larger ACs removed less oil, which is also consistent with the BET surface area and pore volume.

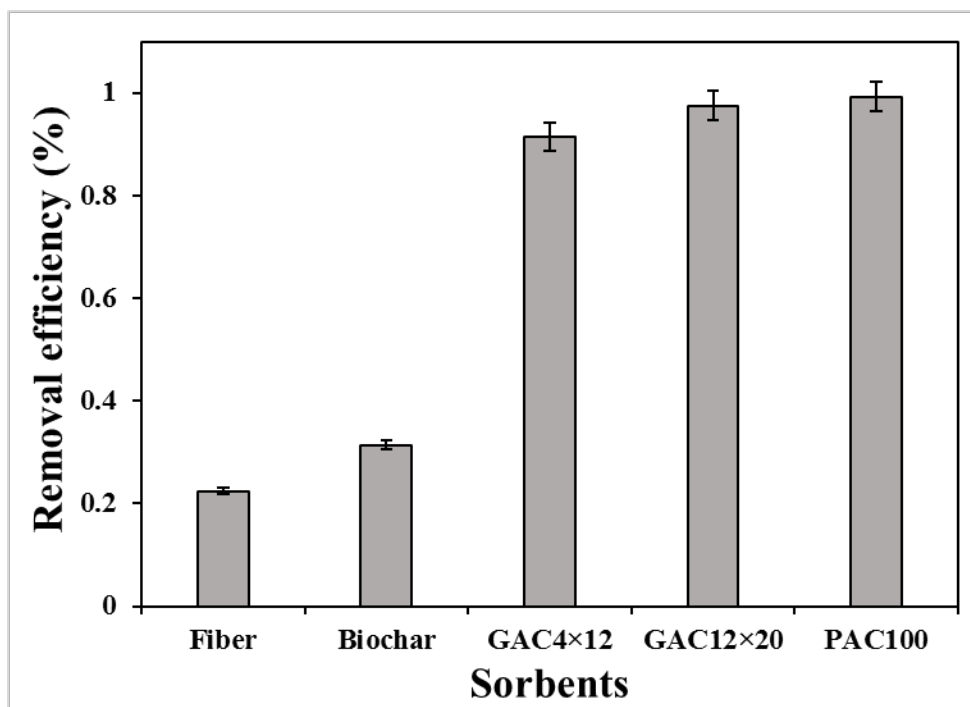


Figure 3-5. Percentage removal of dispersed oil prepared in DWAO-I (Corexit EC9500A) by selected commercial sorbents. Experimental conditions: Initial oil content = 79.3 mg/L, volume of solution = 40 mL, mass of sorbent = 0.1 g, equilibrium time = 24 hours, temperature = 22 ± 1 °C, pH = 8.3 ± 0.1 , salinity = 2%, and dissolved organic matter (DOM) = 2.2 mg/L as TOC.

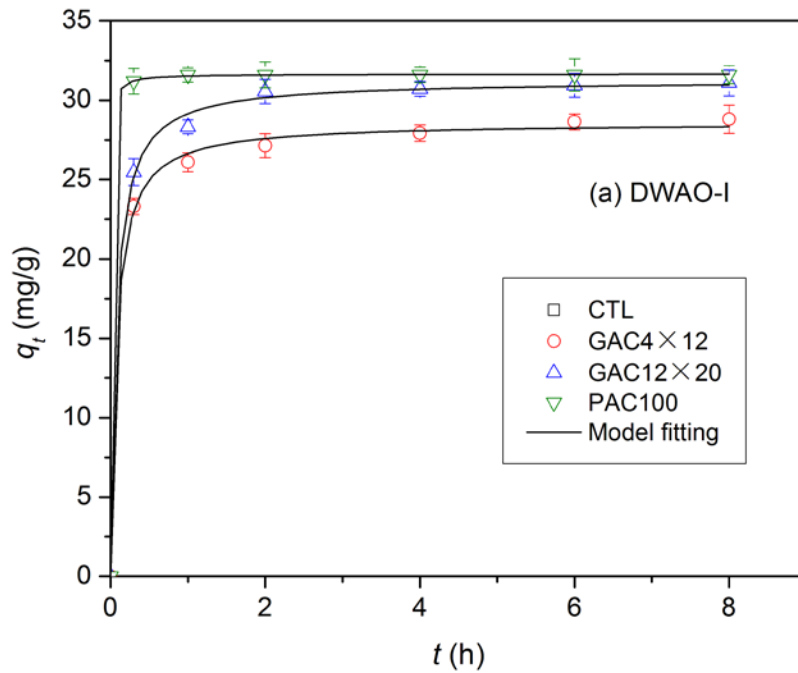
3.3.3 Sorption kinetics of dispersed oil by AC

Fig. 3-6 shows sorption kinetics of the three ACs during sorption of dispersed oil in DWAO-I and DWAO-II. The following pseudo-first-order and pseudo-second-order were tested to fit the sorption kinetics: (Ho and McKay, 1998; Liu et al., 2016):

$$\text{Pseudo-first-order model: } q_t = q_e - q_e \exp(-k_1 t) \quad (3-3)$$

$$\text{Pseudo-second-order model: } \frac{t}{q_t} = \frac{1}{k_2 q_e^2} + \frac{t}{q_e} \quad (4-4)$$

where q_t and q_e are the dispersed oil uptakes (mg/g) at time t (h) and equilibrium, respectively; k_1 (h^{-1}) and k_2 ($\text{g}/(\text{mg}\cdot\text{h})$) are the respective rate constants.



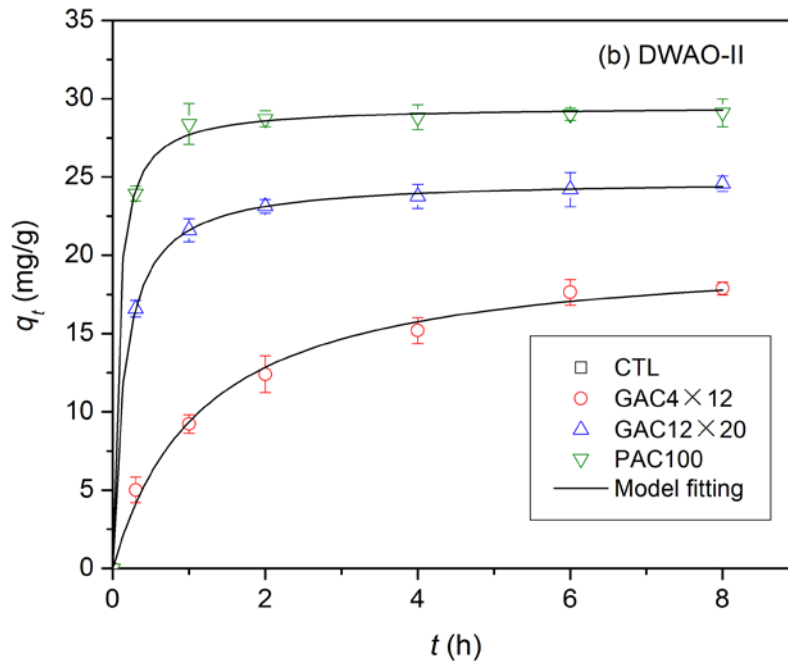


Figure 3-6. Sorption kinetics dispersed oil by three activated charcoals in DWAO-I (a) and DWAO-II (b). Experimental conditions: Initial oil content = 79.3 mg/L, volume of solution = 40 mL, mass of sorbent = 0.1 g, equilibrium time = 24 hours, temperature = 22 ± 1 °C, pH = 8.3 ± 0.1 , salinity = 2%, and dissolved organic matter (DOM) = 2.2 mg/L as TOC.

In all cases, the initial dispersed oil concentration was identical (79.3 mg/L). It is noteworthy that the oil adsorption rate and extent were much faster for DWAO-I than for DWAO-II. And in both cases, PAC100 offered fastest removal rate and amount, with an equilibrium time of <1 h in DWAO-I and ~6 h in DWAO-II. **Tables 3-5** and **3-6** in SM list the best-fitted parameters for the kinetic models. For instance, the k_2 (g/(mg·h)) values of GAC4×12, GAC12×20, and PAC100 were, respectively, 0.48, 0.52 and 7.62 in DWAO-I, but only 0.04, 0.27, and 0.51 in

DWAO-II. Both models were able to adequately fit the experimental data for all the adsorbents, though the second-order model appeared slightly better ($R^2 \geq 0.995$).

Table 3-5. Kinetic model parameters for sorption of dispersed oil from DWAO-I by three model activated charcoals.

Models	Parameters	Materials		
		GAC4×12	GAC12×20	PAC100
Pseudo-first-order model	$q_{e,cal}^a$ (mg/g)	27.75	30.36	31.60
	k_1 (h ⁻¹)	6.05	6.09	14.54
	R^2	0.992	0.994	0.999
Pseudo-second-order model	$q_{e,cal}^a$ (mg/g)	28.58	31.24	31.65
	k_2 (g/(mg·h))	0.48	0.52	7.62
	R^2	0.998	0.999	1.000
	$q_{e,exp}^b$ (mg/g)	28.80	31.10	31.61

^a Calculated equilibrium uptake of dispersed oil from the kinetic models.

^b Observed equilibrium uptake of dispersed oil.

Table 3-6. Kinetic model parameters for sorption of dispersed oil from DWAO-II by three model activated charcoals.

Models	Parameters	Materials		
		GAC4×12	GAC12×20	PAC100
	$q_{e,cal}^a$ (mg/g)	17.53	23.61	28.83

Pseudo-first-order model	k_1 (h^{-1})	0.64	3.88	5.91
	R^2	0.984	0.991	0.999
Pseudo-second-order model	$q_{e,cal}^a$ (mg/g)	20.39	24.84	29.52
	k_2 (g/(mg·h))	0.04	0.27	0.51
	R^2	0.995	1.000	1.000
	$q_{e,exp}^b$ (mg/g)	17.89	24.58	29.11

^a Calculated equilibrium uptake of dispersed oil from the kinetic models.

^b Observed equilibrium uptake of dispersed oil.

In both cases, the equilibrium uptake (Q_e) followed the same trend as the rate constants, i.e., PAC100 (31.65 mg/g) > GAC12×20 (31.24 mg/g) > GAC4×12 (28.58 mg/g) for DWAO-I; and PAC100 (29.52 mg/g) > GAC12×20 (24.84 mg/g) > GAC4×12 (20.39 mg/g) for DWAO-II (Tables 3-5 and 3-6), and the oil removal percentage: PAC100 (99.6%) > GAC12×20 (98.0%) > GAC4×12 (90.8%) for DWAO-I; PAC100 (91.8%) > GAC12×20 (77.5%) > GAC4×12 (56.4%) for DWAO-II (Fig. 3-6). This can be attributed to the different fundamental properties of ACs, such as particle size (PAC100 < GAC12×20 < GAC4×12), specific surface area, and pore volume (PAC100 > GAC12×20 > GAC4×12) (Table 3-4). In addition, while hydrophobic interaction is considered the dominant mechanism for adsorption of oil hydrocarbons by ACs (Dias et al., 2007; Liu et al., 2016), the presence of the oil dispersants may alter the adsorption mechanisms (see Section 3.3.5).

3.3.4 Sorption isotherms of dispersed oil by ACs

Fig. 3-7 shows the sorption isotherms of dispersed oil in DWAO-I by the three ACs. The classical Freundlich (**Eqn. 3-5**) and Langmuir (**Eqn. 3-6**) isotherm models are used to interpret the experimental data, and **Table 3-7** lists the best-fitted model parameters.

$$q_e = K_F C_e^{1/n} \quad (3-5)$$

$$q_e = \frac{bQ_{max}C_e}{1+bC_e} \quad (3-6)$$

where q_e and C_e are the solid and aqueous phase oil concentrations (mg/g), respectively, at equilibrium, K_F is the Freundlich capacity constant, n is the Freundlich sorption intensity constant, b is the Langmuir affinity coefficient (L/mg) and Q_{max} is the Langmuir maximum sorption capacity (mg/g).

The Freundlich model offered a much better goodness of fitting ($R^2 \geq 0.994$) than the Langmuir model ($R^2 < 0.9$) (not shown). While both GACs showed an unfavorable isotherm profile, PAC100 displayed a favorable adsorption isotherm (**Fig. 3-7**). In accord with the K_F values (**Table 3-7**), PAC100 offered the highest adsorption capacity of the three ACs, which again is consistent with the specific surface area sequence: PAC100 (889 m²/g) > GAC12×20 (539 m²/g) > GAC4×12 (520 m²/g), and the pore volume: PAC100 (0.95 cm³/g), GAC12×20 (0.68 cm³/g) and GAC4×12 (0.54 cm³/g) (**Table 3-4**).

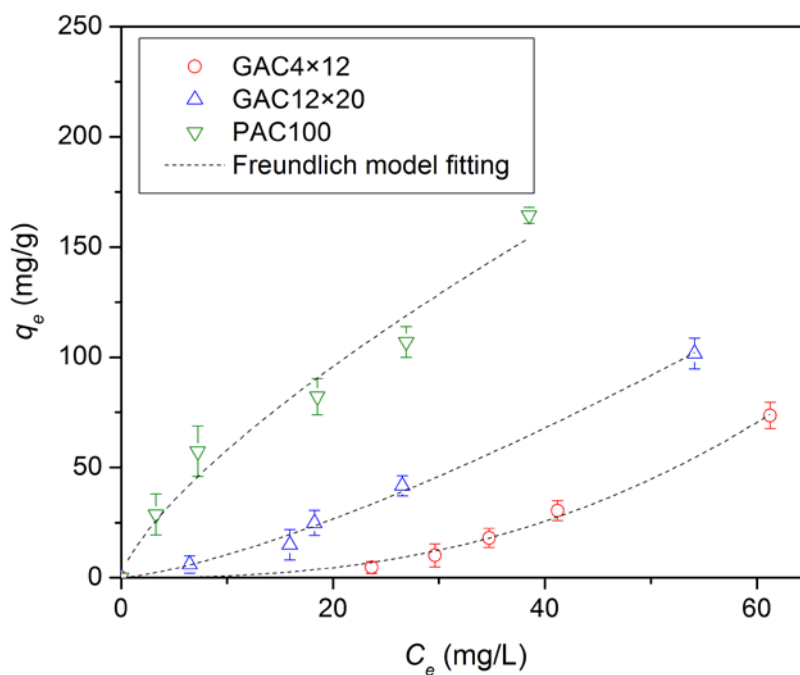


Figure 3-7. Sorption isotherms of dispersed oil in DWAO-I by three activated charcoals.

Experimental conditions: Initial oil content= 79.3 mg/L, volume of solution = 40 mL, mass of sorbent = 0.005-0.5 g, equilibrium time = 24 hours, temperature = 22 ± 1 °C, pH = 8.3 ± 0.1 , salinity = 2 %, and DOM = 2.2 mg/L as TOC.

Table 3-7. Kinetic model parameters for sorption of dispersed oil from DWAO-II by three model activated charcoals.

Isotherm model	Parameters	GAC4x12	GAC12x20	PAC100
Freundlich	R^2	0.994	0.995	0.957
	K_F (mg/g·(L/mg) ^{1/n})	0.003	0.467	10.898
	n	0.401	0.741	1.378

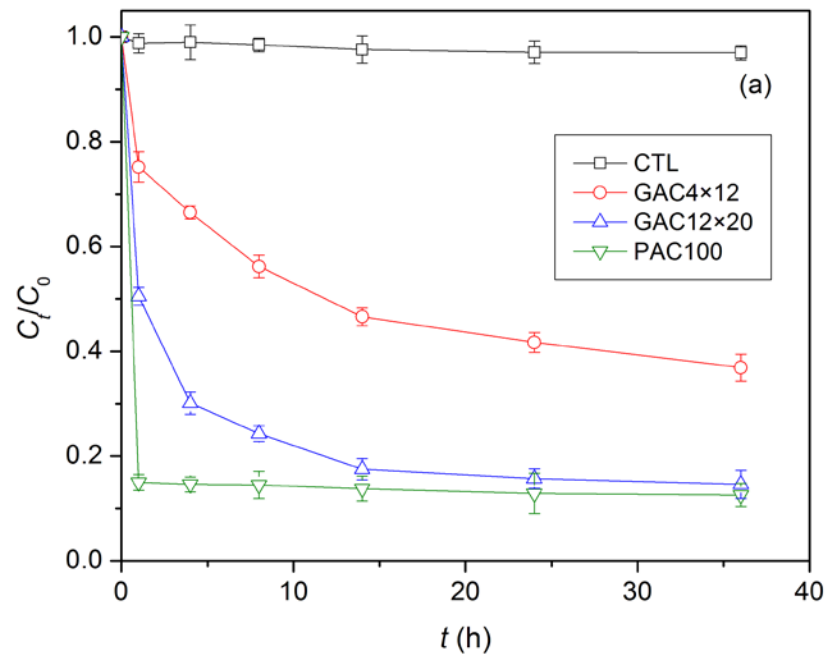
3.3.5 Effects of dispersant on sorption of dispersed oil by ACs

Fig. 3-8a shows the adsorption kinetics of Corexit EC9500A by the three ACs. The pseudo second-order kinetic model was able to interpret the kinetic, and **Table 3-8** lists the best-fitted model parameters. In accord with the oil adsorption data, PAC100 rapidly and completely removed the dispersant within 1 h (the remaining 13% of TOC was attributed to the background TOC in the seawater). In contrast, GAC12×20 removed 83% of TOC, and GAC4×12 removed 64% at 36 h. The equilibrium uptake (Q_e) of Corexit EC9500A followed the order of (mg/g): PAC100 (5.23) > GAC12×20 (5.20) > GAC4×12 (3.90), and in terms of the rate constant k_2 (g/(mg·h)) values: PAC100 (8.94) >> GAC12×20 (0.24) > GAC4×12 (0.09). These results indicate that adsorption of the dispersant is strongly controlled by the particle size, and thus, intraparticle diffusion is likely the rate-limiting step.

When the dispersant adsorption data are compared with the dispersed oil adsorption data (**Fig. 3-6a** and **Fig. 3-8a**), the latter had faster kinetics (i.e., less time to reach equilibrium), though the relative rates for the three ACs showed the same trend. For instance, the k_2 value (8.94 g/(mg·h)) for the dispersant adsorption by PAC100 was 1.17 times higher than that for oil adsorption (7.62 g/(mg·h)), and the difference was even more profound for the GACs (**Tables 3-5 and 3-7**).

The slower adsorption of the dispersant can be attributed to the blocking effect of the dispersant molecules due to the accumulation of the molecules at the pore entrance, and to the slow mass transfer rate of the aggregated dispersant molecules inside the narrow pores. This claim is backed by the findings of Ahn et al. (2007) reported that adsorption of a nonionic surfactant (Triton X-100) may block 80%-90% of the micropores (< 2 nm) and 20%-60% of the mesopores (2-50

nm) in activated carbons, and they attributed the blocking effect to the larger size of the surfactant molecules or their aggregates than the pore size.



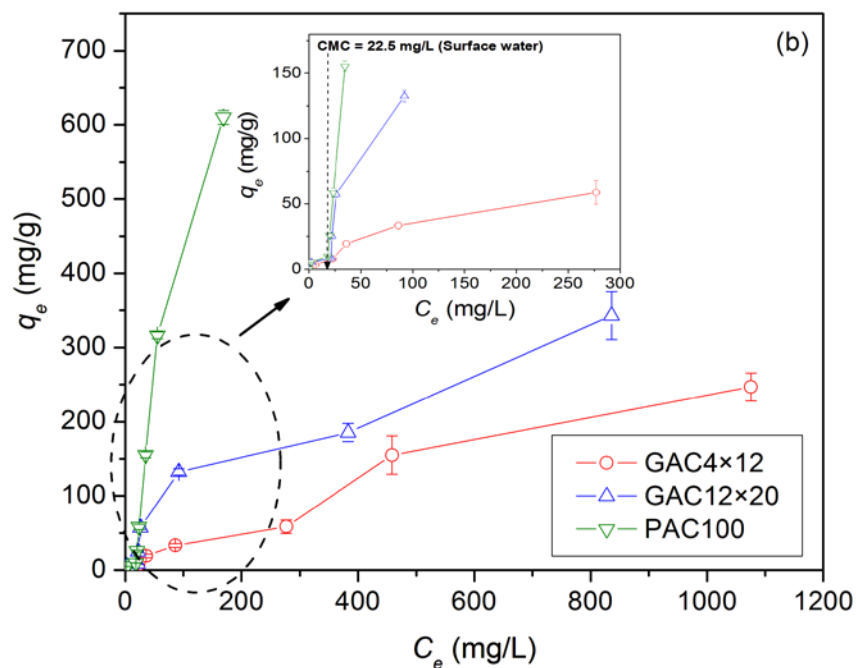


Figure 3-8. Sorption kinetics (a) and isotherms (b) of Corexit EC9500A by three model activated charcoals. Experimental conditions: Initial dispersant concentration for kinetics = 15.1 mg/L as TOC, initial dispersant concentration for isotherms = 15.1 – 1693 mg/L as TOC, volume of solution = 40 mL, mass of sorbent = 0.1 g, equilibrium time = 24 hours, temperature = 22±1 °C, pH = 8.3, salinity = 2 %, and TOC of seawater = 2.2 mg/L.

Table 3-8. Kinetic model parameters for sorption of dispersed oil from DWAO-II by three model activated charcoals.

Model	Parameters	Materials		
		GAC4×12	GAC12×20	PAC100
Corexit EC9500A	$q_{e,cal}^a$ (mg/g)	3.90	5.20	5.23

k_2 (g/(mg·h))	0.09	0.24	8.94
R^2	0.963	0.997	1.000
$q_{e,exp}^b$ (mg/g)	3.81	5.16	5.28

^a Calculated equilibrium uptake of dispersed oil from the kinetic models.

^b Observed equilibrium uptake of dispersed oil.

Corexit EC9500A consists of three neutral surfactants, one anionic surfactant and several organic solvents (**Table 3-1**) (Cai et al., 2017; Gong et al., 2014). The initial dispersant concentration in our case was 20 mg/L, which is close to the apparent CMC value of Corexit EC9500A (22.50 mg/L), and thus some dispersant aggregates are expected at least during the initial stage of the adsorption, which can significantly slow down the mass transfer and intensify the pore-blocking effect, resulting in the observed slow kinetics.

However, the dispersant behavior can be greatly altered in the presence of oil. First, as dispersant molecules are attached to the fine oil droplets, the formation of dispersant micelles or aggregates is deterred, resulting in improved mass transfer rate; and second, the attached dispersant molecules can serve as mass transfer vehicles facilitating the transfer of oil from bulk solution to the adsorption sites. In all cases, dispersed smaller oil components can access smaller pores, whereas larger dispersed oil components take up larger pores. As a result, the adsorption rate for dispersed oil exceeded that for the dispersant only.

At the experimental solution pH (8.3), all of three ACs were negatively charged based on the zeta potential and pH_{pzc} (**Fig. 3-4b** and **Table 3-4**), which are attributed to the ionized functional groups, i.e., C–OH, O–H and C–H groups (**Fig. 3-3**). As a result, the surfactants were adsorbed mainly through the hydrophobic interactions with the AC surface.

Fig. 3-8b shows the adsorption isotherms of Corexit EC9500A by the three ACs. The characteristic S-shaped isotherms are consistent with the previous report by Gong et al. (2014), who studied sorption of Corexit EC9500A onto a sandy loam sediment. Mechanistically, the isotherms may be separated into two regions. In the low concentration region (0-21.1 mg/L), the dispersant is adsorbed as monomeric molecules, resulting in the low uptake, which is consistent with the kinetic results (**Fig. 3-8a**). At dispersant concentrations higher than the CMC (25-150 mg/L), surface hemimicelles are formed due to aggregation/accumulation of the adsorbed surfactant monomers (Ko et al., 1998), resulting in the sharp rise in the dispersant uptake. It should be noted that the mixed solvents, anionic and nonionic surfactants may synergistically facilitate surface aggregation, resulting in larger and denser surfactant layers on the solid surface (Zhao et al., 2005; Gong et al., 2014).

Of the three ACs, PAC100 offered the highest dispersant uptake and a very sharp-rise profile. The uptake of Corexit EC9500A sharply increased from 58.4 to 316.4 mg/g as the equilibrium dispersant concentration increased from 23.3 to 55.5 mg/L (**Fig. 3-8b**). This observation indicates not only the AC's very high sorption capacity. This isotherm profile excludes the single-layer Langmuir adsorption mechanism, rather the sorption may involve surface aggregation and micropore hole filling and capillary effect (Liu et al., 2016), which is consistent with the larger fraction of micropores of PAC100.

In Region III (>150 mg/L), the change in the adsorption for all three ACs became less steep, e.g., the uptake of Corexit EC9500A increased from 58.6 to 246.9 mg/g for GAC4×12 and 132.5 to 342.9 mg/g for GAC12×20 as the equilibrium dispersant concentration increased from 276.8 to 1075.7 mg/L and 92.0 to 835.6 mg/L, respectively. This can be attributed to the elevated

electrostatic repulsion between anionic heads of SDSS, elevated surface coverage, and competitive formation of aqueous-phase micelles (Gong et al., 2014).

Fig. 3-9 compares the equilibrium uptakes of dispersed oil in the presence of various amounts of the dispersant added in DWAO-I. The sorption reached a maximum for all three ACs at the dispersant dosage of 15 mg/L, i.e., 32.4, 36.9 and 39.5 mg/g for GAC4×12, GAC12×20 and PAC100, respectively, representing an increase by 12.5%, 18.6% and 25.0% compared to those without the additional dispersant. When the dispersant dosage was increased to 25 mg/L, the oil uptakes dropped by 8.9%, 13.0% and 9.6%, respectively, compared to the peak values. This observation indicates the additional dispersant at low concentration (in this case, i.e., < 15 mg/L) facilitated the oil uptake through adsolubilization, i.e., the adsorbed dispersant molecules acted as additional sorption sites for taking up more hydrocarbons. This additional sink effect increases with the accumulation of the sorbed dispersant/surfactant monomers, which may aggregate to form hemimicelles/admicelles through the interactions of the hydrophobic tails (Ko et al., 1998). However, as more hemimicelles/admicelles are formed, further adsorption may be subject to elevated electrostatic repulsions between the like-charged head groups, which, along with the formation of aqueous surfactant aggregates and/or micelles, would tend to restrain more oil hydrocarbons in the aqueous phase (Zhao et al., 2016). The results are consistent with those by Zhao et al. (2016), who studied adsorption of dispersed oil by a marine sediment.

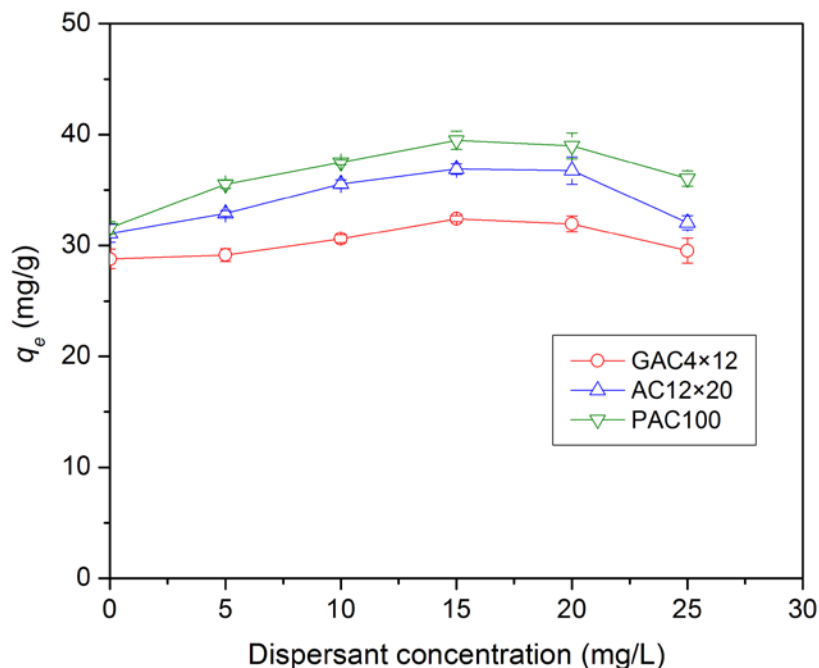


Figure 3-9. Uptake of dispersed oil by three model activated charcoals as a function of additional dispersant (Corexit EC9500A) added in DWAO-I. Experimental conditions: Initial oil content= 79.3 mg/L, volume of solution = 40 mL, mass of sorbent = 0.1 g, equilibrium time = 24 hours, temperature = 22 ± 1 °C, pH = 8.3 ± 0.1 , salinity = 2 %, and DOM = 2.2 mg/L as TOC.

Taken together, **Fig. 3-10** presents a conceptualized depiction on sorption, solubilization and interactions in the dispersant-oil-seawater-AC system. Herein, the surfactant molecules can exist as micelles, monomers, hemimicelles and admicelles, depending on the surfactant concentration. Dispersants can cause two contrasting effects for oil hydrocarbons, i.e., adsolubilization and solubilization effect (Ahn et al., 2007; Ahn et al., 2008; Gong et al., 2014; Zhao et al., 2016).

First, dispersant molecules in the aqueous phase tend to increase the apparent solubility of oil hydrocarbons (Ji et al., 2018), reducing the solid-phase uptake of oil droplets (Duan et al., 2018; Zhao et al., 2015) (**Scenario I**).

Second, the surfactants can be adsorbed by AC through the interactions between the hydrophobic tail of a surfactant monomer and the AC surface probably in the form of a monolayer (**Scenario II** in **Fig. 3-10**). Using atomic force microscopy, Patrick et al. (1997) observed the formation of a monolayer on graphite surface upon adsorption of a series of poly(oxyethylene) *n*-dodecyl ether (C₁₂E_n) nonionic surfactants. The sorption of surfactant monomers is faster than that of the oil droplets due to the smaller size and faster mass transfer rate (Ahn et al., 2007) (**Scenario II** and **III**), which is in accord with PAC100 sorption kinetic data (**Tables 3-5** and **3-8**). However, the different surfactants or components of the dispersant are not equally adsorbed on the surface of AC. For instance, in our case, the AC may take up Tween 85 (neutral surfactant) more preferably than Tween 80 and SDSS (anionic surfactant) due to the stronger van der Waals interactions and less the electrostatic repulsion from the negative surface charge (**Fig. 3-4b** and **Table 3-4**). Fu et al. (2017) reported that the surfactant Span 80, which is sparingly dissolved and dispersed in seawater and with a lower density (0.99 g/mL) than seawater (1.02 g/mL-1.03 g/mL), can facilitate accumulation of more hydrophobic hydrocarbons to the upper layer of the water column, and thus may promote the adsolubilization effect.

Third, the sorbed dispersant molecules may form hemimicelles or admicelles, providing additional partitioning capacity to facilitate surface adsolubilization of the oil components (Ko et al., 1998; Zhao et al., 2015; Zhu et al., 1988) (**Scenario V**). **Fig. 5b** reflects this additional sink effect of the sorbed dispersant for the uptake of oil hydrocarbons. Conversely, the accumulation of dispersant molecules may block some of the entrances of the pores in AC (especially

micropores) (**Fig. 3-8a** and **Table 3-8**) and occupy some surface area (Ahn et al., 2007), resulting in reduced surface area on AC for oil droplets.

Fourth, adsorbed oil hydrocarbons can facilitate sorption of more dispersant molecules by interacting with the lipophilic tails of the surfactants, leaving less dispersant molecules in the aqueous phase (**Scenario IV**).

The interactions between AC and dispersant/oil hydrocarbons can be attributed to hydrophobic interactions and π - π interaction provided by π - π bonds (Garcia et al., 2004; Lin and Xing, 2008).

Based on results from this and prior studies (Zhao et al., 2015), the enhanced adsolubilization effect is likely to prevail at low dispersant concentrations (e.g., < the CMC), while the solubilization effect may outweigh the adsolubilization effect at elevated dispersant concentrations.

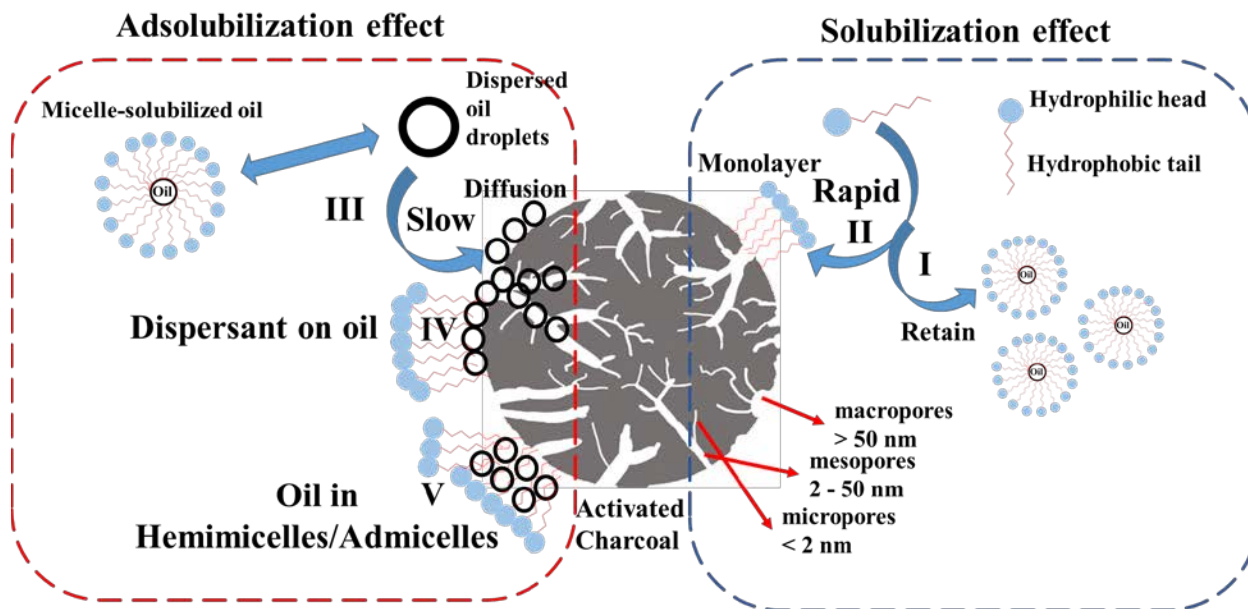


Figure 3-10. The schematic for sorption of dispersed oil in the dispersant-oil-seawater-activated charcoal system.

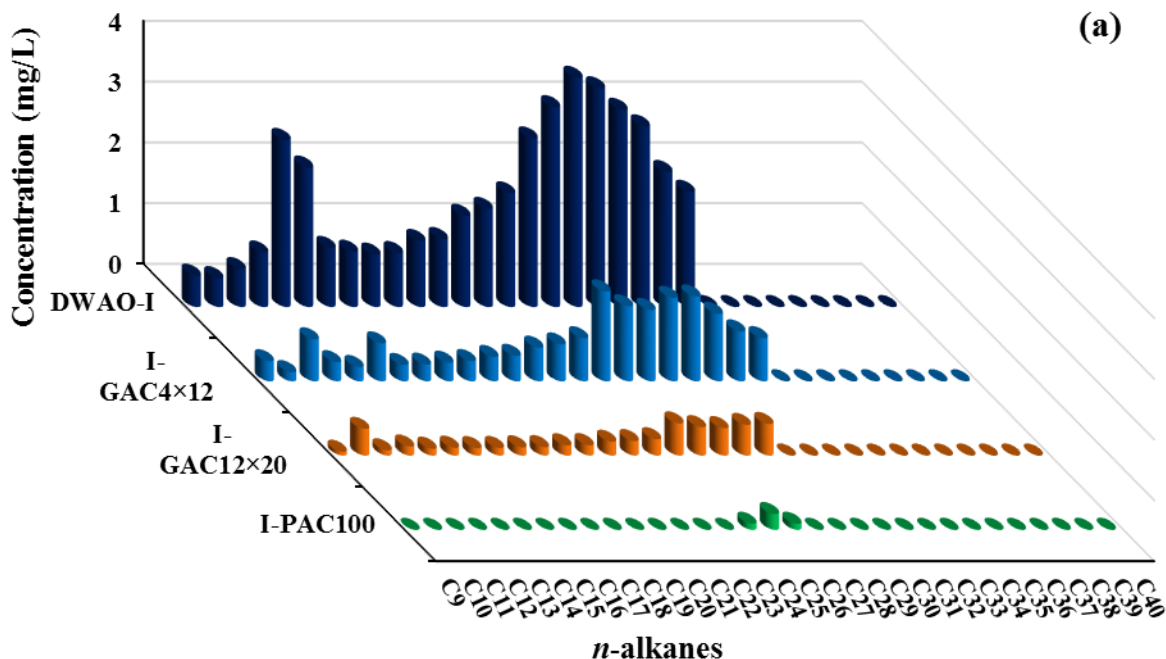
To acquire some deeper insight into the sorption mechanisms, *n*-alkanes and PAHs in the dispersed oil in DWAO-I and DWAO-II before and after the sorption were determined. **Figs. 3-11a** and **3-11b** profile the distribution of *n*-alkanes in DWAO-I and DWAO-II before sorption and after 8 hour's sorption by the three ACs. The results reveal that the two dispersants resulted in quite different compositions of the dispersed oil, i.e., different alkanes were selectively dispersed by the two dispersants, which is consistent with our previous observation (Ji et al., 2018). While the total concentration of *n*-alkanes in both DWAO-I and DWAO-II was the about the same (42-43 mg/L), Corexit EC9500A predominantly dispersed C13 (5.1 mg/L or 12.1% of total *n*-alkanes) and the medium-molecular-weight (i.e., C24-C30) *n*-alkanes, which accounted for 51.9% of total *n*-alkanes (**Fig. 3-11a**), whereas Corexit EC9527A dispersed mainly C10 (9.3 mg/L), which accounted for about ~21.5% of the total *n*-alkanes (**Fig. 3-11b**). In addition, broader distributions of *n*-alkanes were detected in DWAO-I. The results agree with the observation by Zhao et al. (2016). This can be due to the different chemical compositions of the two oil dispersants and their specific affinities to different *n*-alkanes (**Table 3-1** in SM).

Corexit EC9500A is generally considered as newer and enhanced formula than Corexit EC9527A (George-Ares and Clark, 2000) (**Table 3-1**). Theoretically, the better performance of Corexit EC9500A can be contributed to the different formulations (surfactant and solvent type) and the surfactant characteristics (e.g., CMC and hydrophile-lipophile balance (HLB) in **Table 3-1**). Of the two dispersants, Corexit EC9500A contains more solvent DPnB but no solvent DPnB. According to Zhao et al. (2016), these solvents can greatly lower the surface tension due to their low dielectric constants and thus enhance the solubility of the surfactants and facilitate the breakage of oil slicks.

All three ACs can efficiently remove all *n*-alkanes of the broad molecular weight range (Fig. 3-11a and 3-11b). However, for DWAO-I, the lower-molecular-weight (i.e., C9-C15) *n*-alkanes were removed faster than the medium-molecular-weight (i.e., C24-C30) *n*-alkanes, which can be attributed to the slower mass transfer rate of larger *n*-alkanes, which can be further slowed down due to the attachment of the dispersant molecules. This is also consistent with findings by Liyana-Arachchi et al. (2014) that various dispersed *n*-alkanes (C15, C20 and C30) show different thermodynamic preferences to interfaces based on molecular dynamics simulations.

Fig. 3-11c compares the distributions of *n*-alkanes in DWAO-I after the AC adsorption tests for the three ACs in the absence or presence of the additional 15 mg/L of Corexit EC9500A. The presence of the additional dispersant remarkably enhanced the uptake of all detected *n*-alkanes (C9-C40) without a clear pattern of preference towards a specific fraction of *n*-alkanes.

In both DWAO-I and DWAO-II, the removal percentage and rate of *n*-alkanes followed the trend: PAC100 > GAC12×20 > GAC4×12, which agrees with the results for TPH and the dispersant adsorption (Sections 3.3.3 and 3.3.4).



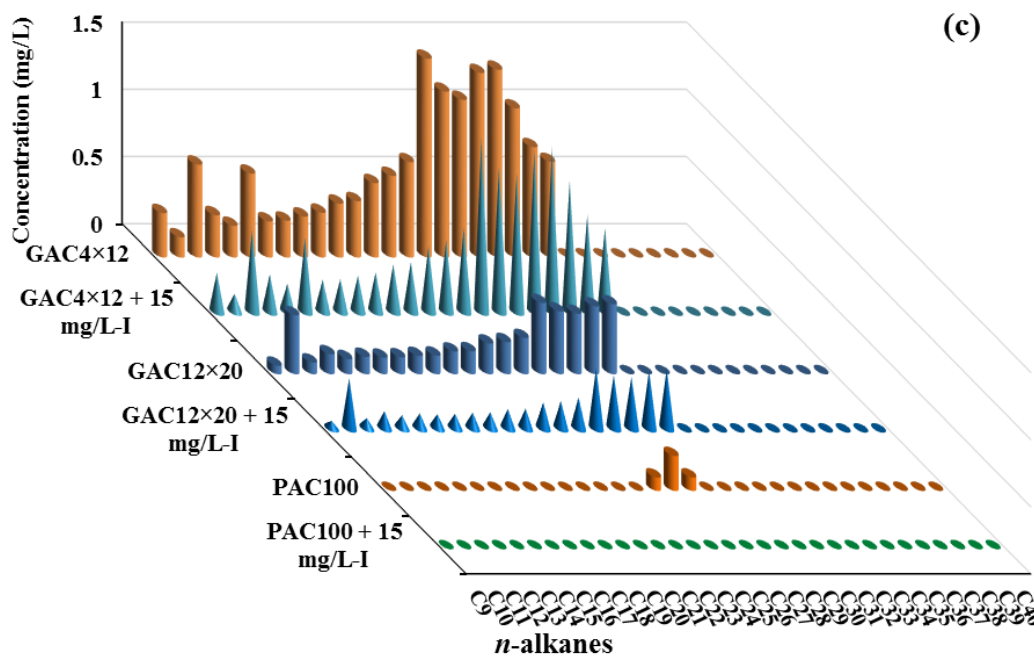
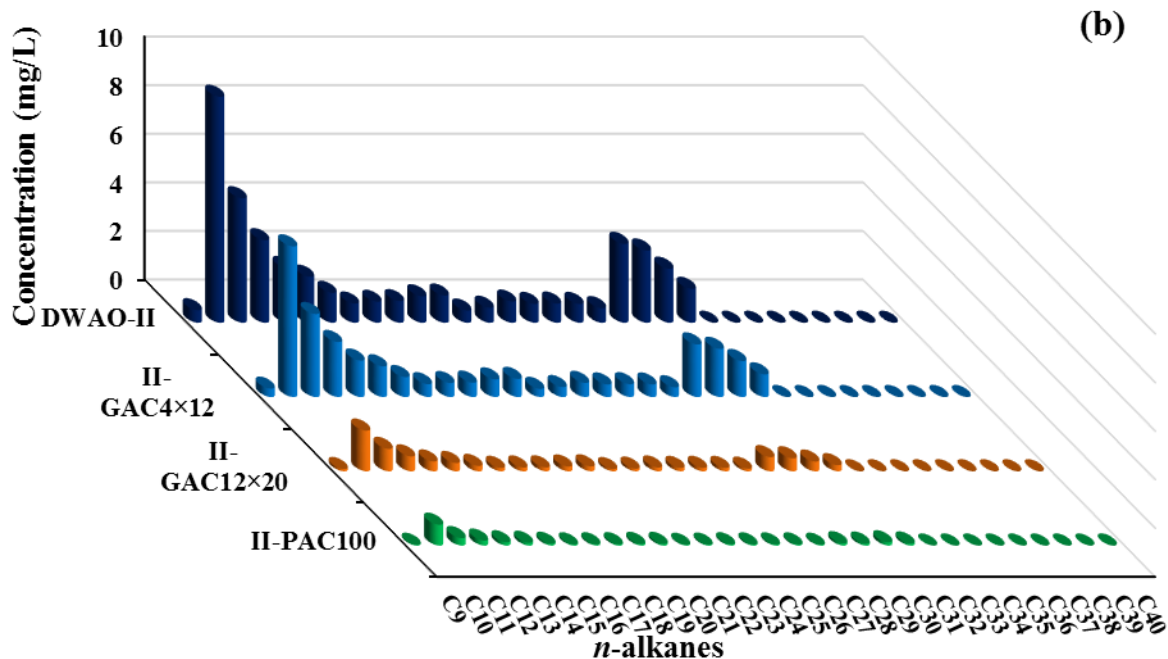
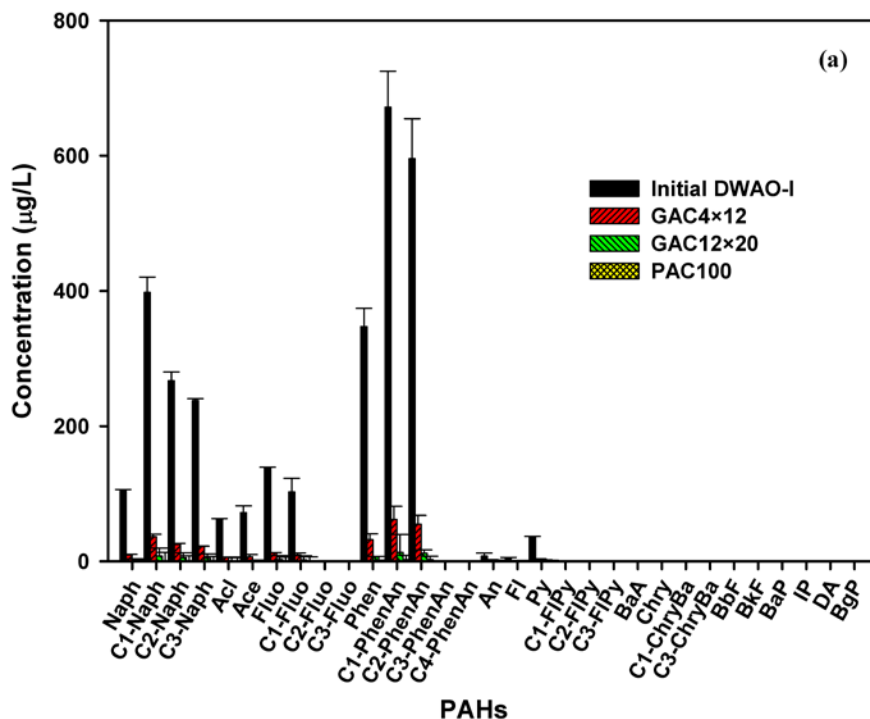


Figure 3-11. Aqueous *n*-alkanes distributions in DWAO-I (a) and DWAO-II (b) before and after 8 hour's sorption by three model activated charcoals, and aqueous *n*-alkanes distributions in DWAO-I in the absence or presence of additional 15 mg/L Corexit EC9500A (c). Experimental conditions: Initial oil content= 79.3 mg/L, initial *n*-alkanes concentration = 42.2

mg/L in DWAO-I or 43.2 mg/L in DWAO-II, volume of solution = 40 mL, mass of sorbent = 0.1 g, temperature = 22 ± 1 °C, pH = 8.3 ± 0.1 , salinity = 2 %, and DOM = 2.2 mg/L as TOC.

Fig. 3-12 displays the distributions of PAHs in DWAO-I and DWAO-II before and after the AC sorption. The PAHs distribution patterns before the sorption are consistent with our previous observation (Ji et al., 2018). The initial concentrations of PAHs were 3.05 and 2.01 mg/L in DWAO-I and DWAO-II, respectively. The 2-ring and 3-ring PAHs and their alkylated PAHs i.e., C1-naphthalene (C1-naph), C2-naphthalene (C2-naph), C3-naphthalene (C3-naph), C1-phenanthrene (C1-Phen) and C2-phenanthrene (C2-Phen)) were preferably dispersed in both DWAOs. Phenanthrene (Phen) was the most abundant parent PAH in both cases, accounting for 11.4% of the total PAHs in DWAO-I, 5.0% in DWAO-II. C1-Phenanthrene (C1-Phen) was the most abundant alkylated PAH, accounting for 22.0% of the total PAHs in DWAO-I, 32.6% in DWAO-II. The concentration of total alkylated PAHs was 3.6 times higher than that of total parent PAHs. Both dispersants are much less effective for solubilizing PAHs and alkylated PAHs than *n*-alkanes, which can be attributed to the competition between the oil hydrocarbons and dispersant micelles (Zhao et al., 2016). Moreover, the oil-dispersant interactions are also associated with the hydrophilic-lipophilic balance (HLB) values of the surfactants. For instance, Diallo et al (1994) reported that the molar solubilization ratio (MSR) for *n*-alkanes decreases with increasing HLB of surfactants, whereas the MSR for PAHs reaches a peak with increasing HLB and then decreases. For Corexit EC9500A and Corexit EC9527A, the HLBs of the surfactants range from 4.3 to 15 as listed in **Table 3-1**, which are more favorable for interacting with *n*-alkanes over PAHs or alkylated PAHs.

Fig. 3-12 shows that PAHs in DWAO-I were sorbed much faster and to a greater extent than those in DWAO-II, especially for 2-ring (Naph) and 3-ring (Phen) PAHs and their alkylated homologs. For example, the 8-h equilibrium removal of Naph and its alkylated homologs (C1-Naph, C-Naph and C3-Naph), and Phen and its alkylated homologs (C1-Phen, C2-Phen and C3-Phen) in DWAO-I by PAC100 reached 99.6%, compared to 91.8% in DWAO-II. This observation indicates that Corexit EC9500A can not only facilitate more effective solubilization of PAHs, but also adsolubilization than EC9527A due to the stronger dispersant-PAH interactions. Similar trend of the dispersant effects was also observed for *n*-alkanes, although the extents differed due to their different molecular characteristics and the AC properties. In all cases, PAC100 showed the highest sorption of PAHs.



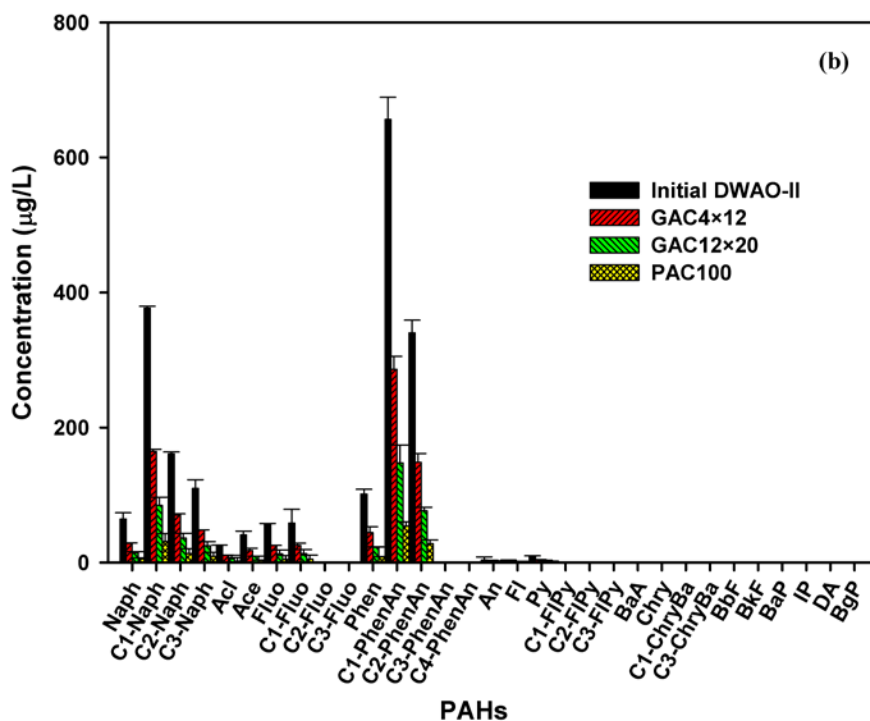
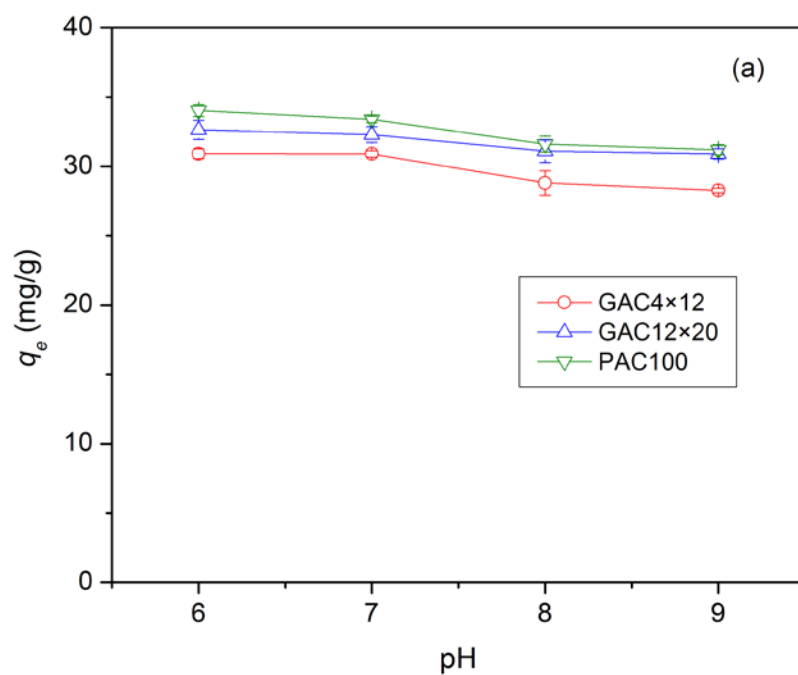


Figure 3-12. Aqueous PAHs distributions in DWAO-I (a) and DWAO-II (b) before and after 8 hour's sorption by three model activated charcoals. Experimental conditions: Initial oil content= 79.3 mg/L, initial PAHs concentration = 3.05 mg/L in DWAO-I or 2.01 mg/L in DWAO-II, volume of solution = 40 mL, mass of sorbent = 0.1 g, temperature = 22 ± 1 °C, pH = 8.3 ± 0.1 , salinity = 2 %, and DOM = 2.2 mg/L as TOC.

3.3.6 Effect of pH

Fig. 3-13a compares the equilibrium uptakes of dispersed oil by the three ACs as a function of solution pH. In all cases, the effect of solution pH appeared quite minor over the pH range of 6-9. Increasing pH from 6.0 to 9.0 lowered the oil uptake by 8.6% for GAC4×12 ($P = 0.202$ at the 0.05 level of significance), 5.3% for GAC12×20 ($P = 0.346$) and 8.3% for PAC100 ($P = 0.184$), respectively. The slight drop in oil uptake can be attributed to the deprotonation of the surface

functional groups of AC such as C-OH as indicated by the zeta potential profile (**Fig. 3-4b**) and FTIR (**Fig. 3-3**). The modest pH effect also confirms that the sorption of dispersed oil hydrocarbons was attributed primarily to hydrophobic interactions.



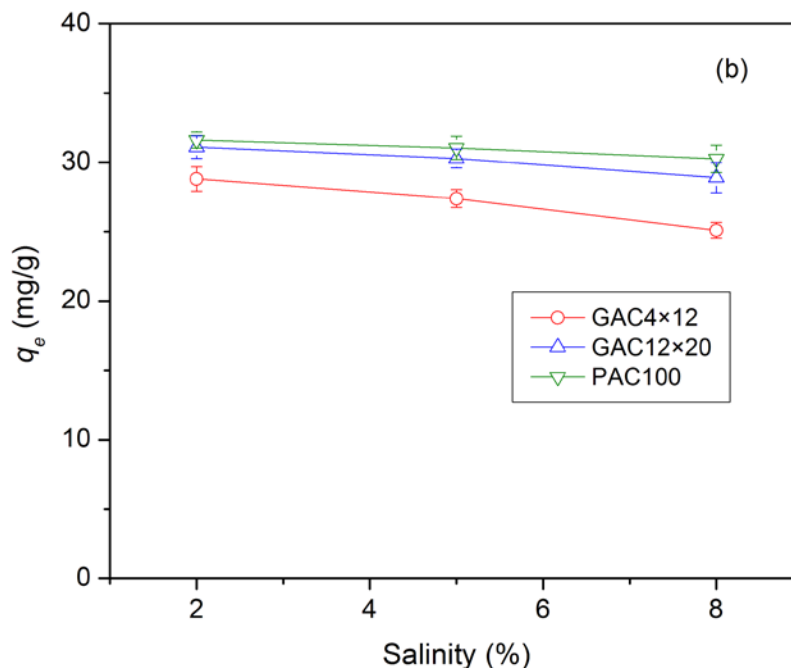


Figure 3-13. Equilibrium uptakes of dispersed oil by three model ACs as a function of solution pH (a) and salinity (b). Experimental conditions: Initial oil content = 79.3 mg/L, volume of solution = 40 mL, mass of adsorbent = 0.1 g, equilibrium time = 24 hours, temperature = 22 ± 1 °C.

3.3.7 Effect of salinity

Fig. 3-13b shows the effect of salinity on the equilibrium uptake of dispersed oil in DWAO-I. Increasing the water salinity from 2 to 8 wt.% decreased the oil uptake by 12.8%, 7.1% and 4.3% for GAC4×12 ($P = 0.120$ at the 0.05 level of significance), GAC12×20 ($P = 0.260$) and PAC100 ($P = 0.440$), respectively. Sorption electrolytes at elevated concentrations may render the AC surface more hydrophilic, resulting in reduced oil uptake. While the “salting out” effect tends to drive more oil hydrocarbons to the sorbent-water interface, the effect is partially offset by the

dispersant due to lowered surface tension and dispersant-facilitated solubilization of the hydrophobic oil hydrocarbons (Gong and Zhao, 2017; Ji et al., 2018). Moreover, high salinity may push more oil compounds into the dispersant/solvent cages (as shown in **Fig. 3-10**), i.e., accumulation of oil hydrocarbons in the micelles or surfactant aggregates, which weakens the thermodynamic driving force for the diffusion and sorption of oil hydrocarbons by AC (Chu and Jia, 2009; Zhang et al., 2011).

3.4 Conclusions

This study investigated the sorption behavior of some prototype activated charcoals for removal of dispersed oil hydrocarbons in seawater and the effects of two model oil dispersants.

The primary findings are summarized as follows:

- 1) All three ACs were able to effectively adsorb oil hydrocarbons dispersed by either Corexit EC9500A or Corexit EC9527A. The sorption capacity far exceeds that of a sample biochar or polypropylene fiber. ACs of smaller particle size, or larger specific surface area, gave greater adsorption capacity.
- 2) The dispersants can not only facilitate selective dispersion of different fractions of *n*-alkanes and PAHs, but adsolubilization of the oil hydrocarbons. Of the two DWAOs, Corexit EC9500A was much more effective in facilitating sorption of dispersed oil hydrocarbons than Corexit EC9527A owing to the different surfactants, solvents, and the surfactant characteristics (i.e., CMC and HLB). However, addition of more dispersant into the dispersed oil may result in contrasting effects on the oil uptake, i.e., the presence of the additional dispersant at lower concentration increases oil adsorption for all three ACs and the maximum effect was observed at the 15 mg/L dispersant concentration (i.e., below the CMC value), but the dispersant decreases the oil adsorption when the concentration exceeds the CMC values due to increased competition of the solubilization effect facilitated by micelles.
- 3) All three ACs displayed rapid adsorption kinetics despite the relatively large size of the dispersant-associated oil droplets, suggesting that other mass transfer mechanisms, such as surface spreading and capillary hole-filling, then diffusion may occur. The smaller particles showed faster adsorption kinetics, with equilibrium time ranging from 1 h to 8 h, indicating the importance of intraparticle mass transfer. The pseudo-second-order kinetic model was able

to fit the sorption kinetic data for sorption of both the dispersant and the dispersed oil. For the three ACs (GAC4×12, GAC12×20, and PAC100), the pseudo second-order rate constant k_2 (g/(mg·h)) was determined to be 0.48, 0.52 and 7.62 in DWAO-I and 0.04, 0.27, and 0.51 in DWAO-II, respectively.

- 4) The Freundlich isotherm model was able to well fit the isotherm data, while the Langmuir model failed to interpret the sorption data. Of the three ACs, PAC100 showed the highest adsorption capacity with a Freundlich K_F value of 10.90 mg/g·(L/mg)^{1/n}, $n = 1.38$) due to the higher specific surface area (889 m²/g) and pore volume (0.95 cm³/g).
- 5) All three ACs were able to adsorb Corexit EC9500A, and PAC100 showed the fastest rate and higher uptake capacity. The pseudo second-order rate constant k_2 (g/(mg·h)) value was determined to be 8.94, 0.24 and 0.09 for PAC100, GAC12×20, and GAC4×12, respectively, and equilibrium uptake 5.23, 5.20, and 3.90 mg/g.
- 6) FTIR spectra indicated the presence of the C–OH groups, the O–H groups, C=C or C=O groups and C–H groups on the surface of the ACs. And zeta potential analyses revealed the pH_{PZC} values were 7.3, 6.8 and 6.1, respectively, for GAC4×12, GAC12×20 and PAC100s.
- 7) All three ACs can efficiently remove all the dispersed *n*-alkanes and PAHs of the broad molecular weight range. However, the lower-molecular-weight (i.e., C9–C15) *n*-alkanes in DWAO-I were removed more preferably than the medium-molecular-weight (i.e., C24–C30) *n*-alkanes. PAHs in DWAO-I were sorbed much faster than those in DWAO-II, especially for 2-ring (Naph) and 3-ring (Phen) PAHs and their alkylated homologs. The dispersant effects on the sorption of PAHs and *n*-alkanes followed a similar trend, although the extent on *n*-alkane far exceeded that on PAHs differed due to their different molecular characteristics, interactions

with the dispersants, and the AC properties. In all cases, PAC100 showed the highest sorption rate and extent for *n*-alkanes and PAHs.

- 8) The solution pH only modestly affected the sorption of dispersed oil, and increasing the solution pH from 6.0 to 9.0 decreased the oil uptake by <9% for all three ACs, resulting from the deprotonation of the surface functional groups of ACs.
- 9) Increasing salinity from 2 wt.% to 8 wt.% decreased the oil uptake by 12.8%, 7.1% and 4.3% for GAC4×12, GAC12×20 and PAC100, respectively, due to more hydrophilic AC surface and solvent cage effect.

The results indicate that commercial activated charcoals appear promising for removal of dispersed oil from contaminated water or saline water, and thus may serve as low-cost and efficient adsorbents for oil spill cleanup.

Chapter 4. Silica aerogel supported titanium dioxide (TiO₂/SiO₂) composites for adsorption and efficient visible light photocatalytic degradation of PAHs

We prepared various silica aerogel supported TiO₂ (TiO₂/SiO₂) composite materials through initial sol-gel method and subsequent calcination, and tested the materials for removal of phenanthrene through adsorption and photocatalysis. Sorption kinetics and isotherms of phenanthrene were conducted. To elucidate the sorption mechanism, various characterizations of TiO₂/SiO₂ were investigated. Furthermore, the photocatalytic activity of TiO₂/SiO₂-800 was studied under the simulated solar light system.

4.1 Introduction

Polycyclic aromatic hydrocarbons (PAHs), consisting of two or more fused aromatic rings, may be produced during incomplete combustion of fossil fuels, and important components of crude oil (Gong et al., 2014; Zhao et al., 2015). Due to their persistence by natural degradation and potential risks to human health, like toxic, mutagenic and carcinogenic properties, PAHs represent a major environmental concern associated with oil spill, seepage and surface run-off, and thus, have been classified as the priority pollutants by US Environmental Protection Agency (USEPA water quality criteria) (Jia et al., 2012; Nam et al., 2008; Wen et al., 2002). Thus, effective removal of PAHs from aqueous phase before their discharge into environment is an urgent research (Sannino et al., 2014; Yang et al.).

Heterogeneous photocatalysis using TiO_2 under UV-irradiation and/or solar light has shown great potential (Grover et al., 2014; Nakata and Fujishima, 2012) and drawn great interest in recent years (Chen and Burda, 2008; Chen and Mao, 2007a; Liu et al., 2013; Pelaez et al., 2012; Tan et al., 2014) for the photocatalytic decomposition and adsorption of organic contaminants due to their low-cost, environmental friendly and high photocatalytic activity (PCA). TiO_2 is a typical *n*-type semiconductor with relatively large band gaps (Pelaez et al., 2012), which can limit its optical absorption in the solar spectrum consisting of UV, visible and infrared (IR) radiations with a relative energy distribution of ~5%, 43% and 55%, respectively (Chen et al., 2015; Shankar et al., 2015). Therefore, a great deal of effort has been devoted to improving the visible light absorption of TiO_2 . Zhao et al. (2016) prepared a new type of photocatalyst, referred to as cobalt-doped titanate nanotubes for catalyzing photodegradation of phenanthrene under solar light, which was about 10 times higher removal efficiency than the original TiO_2 photocatalysts. Pal et al. (Grover et al., 2017) developed the $\text{SiO}_2@ \text{TiO}_2$ nanocomposites for adsorption and photocatalytic degradation of naphthalene and anthracene. The results indicated that the PCA in the presence of SiO_2 was improved.

However, lower specific surface areas of TiO_2 , fewer reacting molecules can adsorb on the surface, which indicates the disadvantage of its PCA. Based on this content, surface modification of TiO_2 through depositing, coating and other ways with inert compounds, especially SiO_2 , has elicited numerous research interest (Chen and Mao, 2007b; Grover et al., 2017; Haghightazadeh et al., 2017; Nussbaum and Paz, 2012). Silica aerogel is an effective adsorbent for oil hydrocarbons (Adebajo et al., 2003; Standeker et al., 2007; Wang et al., 2012), and it can float on water due to its mesoporous structure and low density. Considering the excellent photocatalytic activity of TiO_2 and good adsorptive performance of silica aerogel, depositing nano- TiO_2 onto

silica aerogel may result in a highly efficient supported photocatalyst that can remove TPHs through initial adsorption and subsequent photocatalysis. In this study, a series of new composite materials, namely, silica aerogel supported TiO₂ (denoted as TiO₂/SiO₂), were synthesized through a sol-gel method, and these novel materials were found highly efficient for removing phenanthrene (and possibly other PAHs) via simultaneous adsorption and photocatalysis. Moreover, the synthetic materials can float on the water, which offer great convenience for *in-situ* oil removal from contaminated water.

The overall goal of this work was to develop and test a new type of silica aerogel supported TiO₂ (TiO₂/SiO₂) composite materials for efficient removal of phenanthrene (as a model of PAHs) under solar light. The specific objectives were to: (1) develop an optimized sol-gel-calcination method for preparing the desired catalyst, (2) test the effectiveness of the catalyst for phenanthrene adsorption and photodegradation, and (3) elucidate the mechanisms for adsorption and photocatalysis by characterizing the morphology, crystal phases and compositions of TiO₂/SiO₂.

4.2 Materials and Methods

4.2.1 Chemicals

All chemicals used in this study were of analytical grade or higher. Tetrabutyl titanate (TBOT) was purchased from Degussa Corporation (Germany) and was used as the precursor for nano-TiO₂. Silica aerogel (Enova IC3120, 100 μm–1.2 mm) was obtained from CABOT Corporation (Boston, MA, USA). Chromatographic dichloromethane (DCM), NaOH and NaCl were obtained from Fisher Scientific (Fair lawn, NJ, USA). Methanol (HPLC grade) were obtained from Acros Organics (Fair Lawn, NJ, USA). HCl and HNO₃ was acquired from BDH Aristar (West Chester, PA, USA). Terephthalic acid was purchased from Alfa Aesar (Ward Hill, MA,

USA) for hydroxyl radical detection. Deionized (DI) water (Millipore Co., 18.2 M Ω ·cm) was used to prepare all solutions. Phenanthrene (the model PAH) was purchased from Alfa Aesar (Ward Hill, MA, USA), and was dissolved in methanol to form a stock solution of 2 g L⁻¹.

4.2.2 Synthesis of TiO₂/SiO₂

The TiO₂/SiO₂ composites were synthesized through a sol-gel method using silica aerogel as a support. Specifically, the method included the following steps: 1) 1.17 g of the silica aerogel was dispersed in 100 mL methanol and magnetically stirred for 10 min; 2) 5 mL of tetrabutyl titanate (TBOT, precursor of nano-TiO₂) was added and continuously stirred for another 30 min; 3) Afterwards, a mixture of 0.26 mL DI water and 0.035 mL concentrated HNO₃ was added in the mixture dropwise to start the hydrolysis, which lasted for another 2 h with stirring; 4) following the hydrolysis, the mixture was quickly heated to 265 °C to vent out the solvents; 5) After cooled to room temperature, the resulting material was washed with 40 mL methanol 3 times to remove the residual organic compounds and finally dried at 80 °C for 4 h, the resultant composite material is referred to as TiO₂/SiO₂; and 6) TiO₂/SiO₂ was calcinated at 400, 600 and 800 °C in a muffle furnace under atmospheric conditions, and the resulting materials are designated as TiO₂/SiO₂-400, TiO₂/SiO₂-600 and TiO₂/SiO₂-800, respectively.

4.2.3 Material characterizations

The morphology of material was analyzed using Tecnai30 FEG transmission electron microscopy (TEM, FEI, USA) operated at 300 kV, and energy dispersive spectra (EDS) of the materials were obtained at the same time. The crystal phase of the sample was obtained by means

of a Bruker D2 phaser X-ray diffractometer (XRD, Bruker AXS, Germany) using Cu $K\alpha$ radiation ($\lambda = 1.5418 \text{ \AA}$) at a scan rate (2θ) of $4^\circ/\text{min}$.

EPR spectra of the materials at X-band frequency (9 GHz) were obtained on a Bruker EMX spectrometer fitted with an ER-4119-HS high sensitivity perpendicular-mode cavity, which was operated with center field of 3510G, sweeping width of 100 G, modulation frequency of 100 kHz, and microwave power of 20 mW. Cooling of the sample was performed using a liquid-nitrogen finger Dewar (77 K). Adequate signal to noise ratio was obtained after 5–10 scans.

4.2.4 Experimental methods: adsorption and photocatalysis

Adsorption kinetic tests were carried out in a brown glass bottle with 500 $\mu\text{g/L}$ of phenanthrene (40 mL) and 0.5 g/L of the catalyst. The solution pH was adjusted to 7.0 ± 0.2 using diluted HCl and NaOH, and the mixture was shaken (200 rpm, $25 \pm 0.2 \text{ }^\circ\text{C}$) in dark for 6 h. Samples were taken at the bottom of bottle and filtered through a 0.22 μm PTFE membrane. Water samples (1 mL each) were taken at predetermined times and immediately centrifuged at 8000 rpm (6400 g-force) for 10 min. The supernatant was then mixed with methanol at 1:1 (v/v) ratio, and then analyzed for phenanthrene using an Agilent 1260 Infinity high performance liquid chromatography (HPLC) system equipped with a Poroshell 120 EC-C18 column ($50 \times 4.6 \text{ mm}$, 2.7 μm). The column temperature was held constant at 30 $^\circ\text{C}$, and the mobile phase was comprised of acetonitrile and water at 70:30 (v/v) and at a flow rate of 1 mL min^{-1} in the isocratic mode. The eluate was analyzed with a UV diode array detector at 254 nm. The detection limit for phenanthrene was $\sim 1 \mu\text{g/L}$. Control tests were conducted in the absence of any catalysts but under otherwise identical conditions.

For adsorption isotherms, the initial phenanthrene was varied from 50 to 500 $\mu\text{g/L}$ with a fixed material dosage of 0.5 g/L at $\text{pH } 7.0 \pm 0.2$. After the mixture was shaken for 4 h, samples were taken and the aqueous concentration of phenanthrene was determined after filtration of the samples. Phenanthrene was analyzed.

Kinetic tests were carried out to determine the removal of phenanthrene by the $\text{TiO}_2/\text{SiO}_2$ composites due to adsorption during the initial 4 hours in dark and during the subsequent 6-hours photocatalysis under solar light. The kinetic tests used the experimental setup as in **Fig. 4-1**, which includes a sealed glass photo-reactor (volume = 250 mL) with a quartz cover, an Oriel Sol 1A solar simulator (Newport, USA) with a 450 W xenon lamp, a water circulating system and a magnetic stirrer. The solar irradiation was set at of $85 \pm 0.5 \text{ mW/cm}^2$ (AM 1.5G). The reactor temperature was maintained at $25 \pm 0.2 \text{ }^\circ\text{C}$ through the circulating water. At predetermined time intervals, samples were taken and membrane filtered by $0.22 \text{ }\mu\text{m}$ PTFE membrane to determine the phenanthrene concentration in the aqueous phase. At the same time, the solid particles were extracted using 3 mL of methanol for 24 h to determine the phenanthrene concentration in the solid-phase.

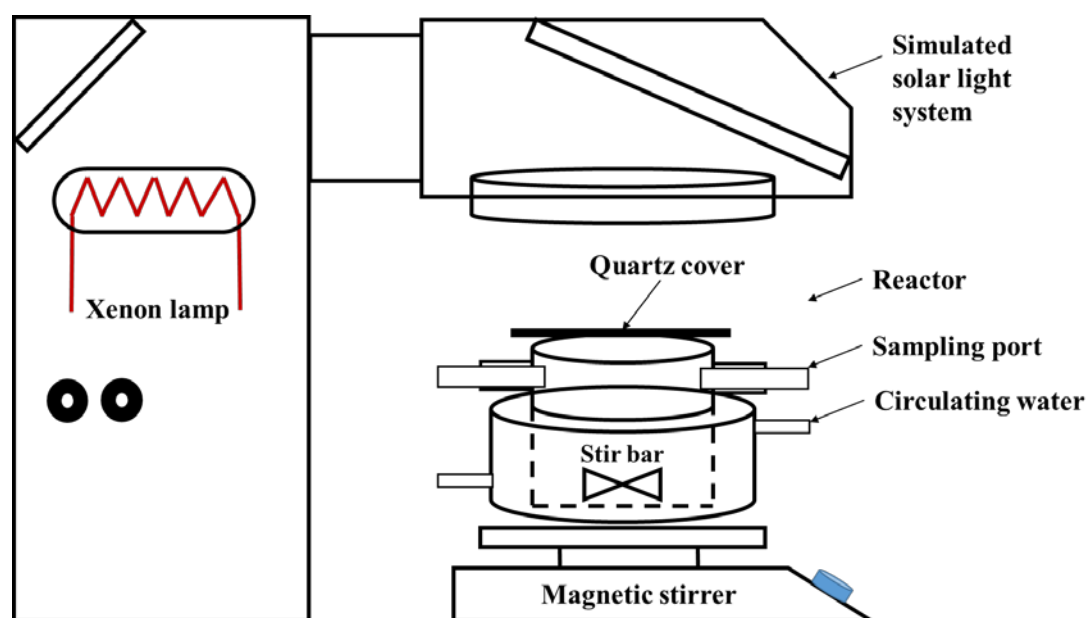


Figure 4-1. Schematic of the experimental set-up for photocatalytic reaction.

To test the photodegradation intermediates, samples (100 mL each) were collected at 1, 3, and 6 h. After centrifugation, each sample was extracted using 10 mL dichloromethane in 125 mL separatory funnels. The organic phase was collected and treated with anhydrous sodium sulfate to remove moisture. Upon filtering through 0.22 μm PTFE membrane, the solvent was analyzed using a GC-MS system (Agilent 7890A GC with 5975C Series mass spectrometry, Agilent Technologies Inc., Santa Clara, CA, USA) equipped with an Agilent DB EUPAH column (30 m \times 180 μm , 0.14 μm film thickness). The GC was operated in the full scan mode. The injection was carried out in the splitless mode (2.0 μL) at 300 $^{\circ}\text{C}$. The oven temperature was programmed as follows: 40 $^{\circ}\text{C}$ (1 min hold) ramped to 300 $^{\circ}\text{C}$ at 8 $^{\circ}\text{C}/\text{min}$ and held for 10 min.

To further investigate the combined ozonation and photodegradation rates and extent of DWAO in the presence of the $\text{TiO}_2/\text{SiO}_2$ -800 composite material. The degradation experiments were carried out in a new glass cylinder reactor that can facilitates both ozonation and photodegradation, and an ozone generator as described in **Section 2.2.2**. In each test, 250 mL of a solution was loaded in the reactor along with a known mass of the photocatalyst under constant magnetic stirring at 400 rpm, resulting in a surface area of 50 cm^2 . For the tests with ozonation only or adsorption, the reactor was kept in dark, while the reactor was exposed simulated solar light for reactions involving both ozonation and photocatalytic mechanisms. At predetermined times, each 20 mL of the solution was sampled and extracted with dichloromethane in three consecutive steps (20 mL solution with 5 mL dichloromethane in each step) according to EPA Method 3510C, and then the extracts were filtered through a glass column packed with 5 g of anhydrous sodium sulfate and concentrated to 4 mL under a gentle nitrogen flow. Then the samples were filtered through a PTFE membrane (0.22 μm) filter and separated to amber glass vials with

equal volumes (labeled as B1 and B2). B1 was analyzed for *n*-alkanes and PAHs using GC-MS, and B2 for TPHs using GC-FID. Specifically, the 16 parent PAHs (as specified in EPA Method 610) and *n*-alkanes (C9–C40) in the DWAO before and after reactions were targeted. More details on the analytical methods can be found in **Section 2.2.5**.

4.2.5 Measurement of hydroxyl radicals

The formation of hydroxyl radicals ($\bullet\text{OH}$) in the presence of various $\text{TiO}_2/\text{SiO}_2$ materials was determined through the photoluminescence (PL) technique using terephthalic acid as the probe molecule, which can react with $\bullet\text{OH}$ to form a highly fluorescent product, i.e. 2-hydroxyterephthalic acid. Thus, the fluorescence intensity is proportional to the concentration of $\bullet\text{OH}$ (Yu et al., 2009). In each test, 0.2 g of a material was dispersed in a mixture of 0.5 mM terephthalic acid and 2 mM NaOH with a total volume of 200 mL in the photo-reactor. After 2-h irradiation under simulated solar light, samples were taken and filtered via 0.22 μm PTFE membrane. And then the PL spectra were obtained on a fluorescence spectrophotometer (SpectraMax M2, Molecular Devices, Sunnyvale, CA, USA) at an excitation wavelength of 425 nm (Cai et al., 2016; Yu et al., 2009; Zhao et al., 2016a).

4.3 Results and Discussions

4.3.1 Characterization of $\text{TiO}_2/\text{SiO}_2$

Fig. 4-2 shows the TEM and high resolution TEM (HRETM) images of $\text{TiO}_2/\text{SiO}_2$ composites synthesized at the same initial Ti/Si weight ratio (1:1) but different calcination temperatures. In all cases, the composite materials appear as aggregated nanoparticles. The uncalcined $\text{TiO}_2/\text{SiO}_2$, appear as scattered aggregates with ambiguous edges, and both SiO_2 and

TiO₂ are amorphous as no crystal lattices were observed in the high resolution TEM (HRTEM) images (**Figs. 4-2a and 4-2b**). In contrast, the crystalline structure of TiO₂ became increasingly evident as the calcination temperature was increased from 400 to 800 °C (**Figs. 4-2d – 4-2h**). For TiO₂/SiO₂-600, the interlayer distance of the formed nanoparticles was determined to be 0.35 nm, which is consistent with the crystal plane of anatase (101) (**Fig. 4-2f**) (Xu et al., 2011; Zhao et al., 2016b). For TiO₂/SiO₂-800, both anatase (101) and rutile (110) crystal structures are observed (**Fig. 1h**) (Xu et al., 2011). The TEM findings are in accordance with the XRD results (**Fig. 4-3**).

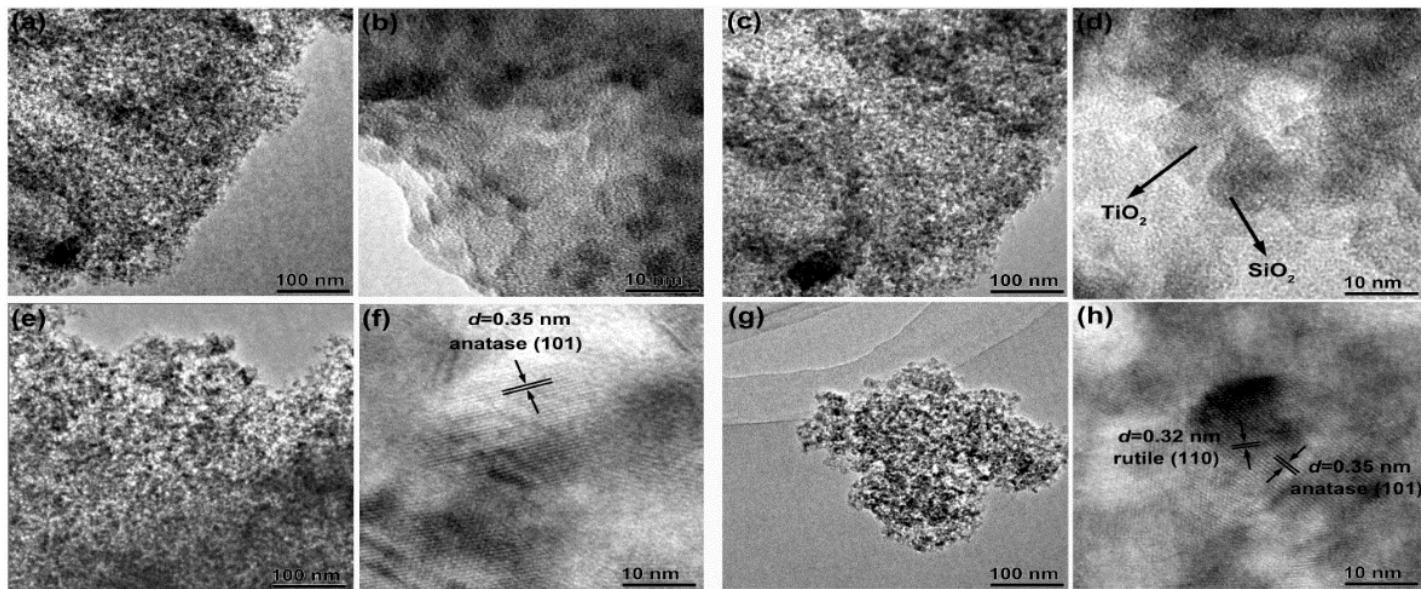


Figure 4-2. TEM and HRTEM images of uncalcined TiO₂/SiO₂ (a, b, c, d), TiO₂/SiO₂-600 (e, f) and TiO₂/SiO₂-800 (g, h).

Fig. 4-3 displays the XRD patterns of these TiO₂/SiO₂ composites. There was no fine crystal phase observed without calcination. However, the crystallinity of TiO₂ became increasingly evident when the material was calcined at 400-800 °C. For TiO₂/SiO₂-400, the peaks at 25.3°, 37.8°, 48.1°, 53.9°, 55.0°, 62.8° and 75.1° are assigned to anatase, especially the crystal plane of A(101) (JCPDS 21-1272) (Hu et al., 2003; Huang et al., 2000). For TiO₂/SiO₂-600, several new peaks at 37.0°, 38.6°, 68.8° and 70.4° were observed, which are also ascribed to anatase (JCPDS 21-1272) and indicate better defined crystalline of anatase (Hu et al., 2003; Huang et al., 2000). For TiO₂/SiO₂-800, the diffraction peak of A(101) became even sharper, and in addition, peaks for rutile phases (R(110), R(101) and R(211)) (JCPDS 21-1276) were observed (Hu et al., 2003; Huang et al., 2000). The enhanced crystallinity of TiO₂ gives improved photocatalytic activity, which agrees with our prior observation that higher calcination temperature gives greater photo-degradation effectiveness of phenanthrene.

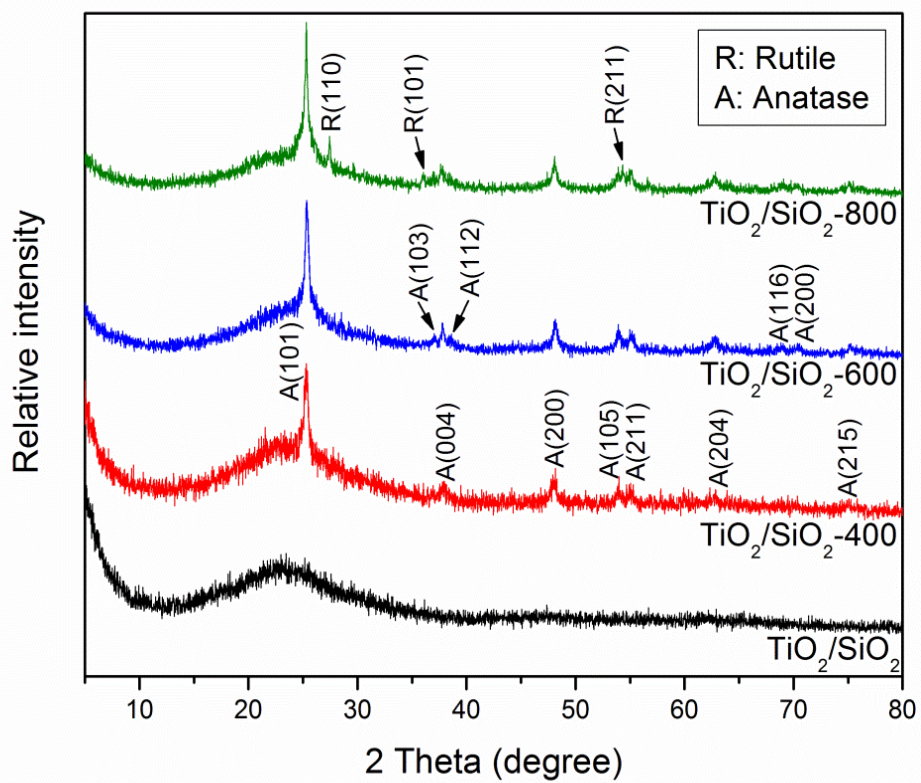


Figure 4-3. XRD patterns of various TiO₂/SiO₂ composites.

4.3.2 Adsorption of phenanthrene by various TiO₂/SiO₂ composite materials

Fig. 4-4 shows the adsorption kinetics of phenanthrene by various TiO₂/SiO₂ composite materials. The pseudo-first-order and pseudo-second-order models are used to interpret the adsorption kinetic data (Ho and McKay, 1998; Ho and McKay, 1999):

$$\text{Pseudo-first-order model: } Q_t = Q_e - Q_e \exp(-k_1 t) \quad (4-1)$$

$$\text{Pseudo-second-order model: } \frac{t}{Q_t} = \frac{1}{k_2 Q_e^2} + \frac{t}{Q_e} \quad (4-2)$$

where Q_t and Q_e ($\mu\text{g/g}$) are the uptake of phenanthrene at time t (min) and equilibrium, respectively, and k_1 (min^{-1}) and k_2 ($\text{g}/(\text{mg}\cdot\text{min})$) are the rate constants of the pseudo-first-order and pseudo-second-order kinetic models, respectively.

Rapid adsorption kinetics was observed for all the materials tested (**Fig. 4-4**). Adsorption equilibrium was reached at 120 min for the plain silica aerogel, and within 180 min for all other TiO₂/SiO₂ composite materials. At an initial phenanthrene concentration of 500 $\mu\text{g/L}$, the equilibrium uptake (Q_e) follows the order of: silica aerogel (719.4 $\mu\text{g/g}$) > TiO₂/SiO₂ (690.6 $\mu\text{g/g}$) > TiO₂/SiO₂-400 (497.8 $\mu\text{g/g}$) > TiO₂/SiO₂-600 (140.5 $\mu\text{g/g}$) > TiO₂/SiO₂-800 (52.2 $\mu\text{g/g}$), and the phenanthrene removal percentage: silica aerogel (71.9%) > TiO₂/SiO₂ (69.1%) > TiO₂/SiO₂-400 (49.7%) > TiO₂/SiO₂-600 (14.1%) > TiO₂/SiO₂-800 (5.2%) (**Table 4-1**). The pseudo-second-order kinetic model better describes the adsorption kinetic data ($R^2 > 0.999$), suggesting that the rate-controlling step for adsorption is likely to be the initial diffusion and then interaction with the adsorbents (Ho and McKay, 1999).

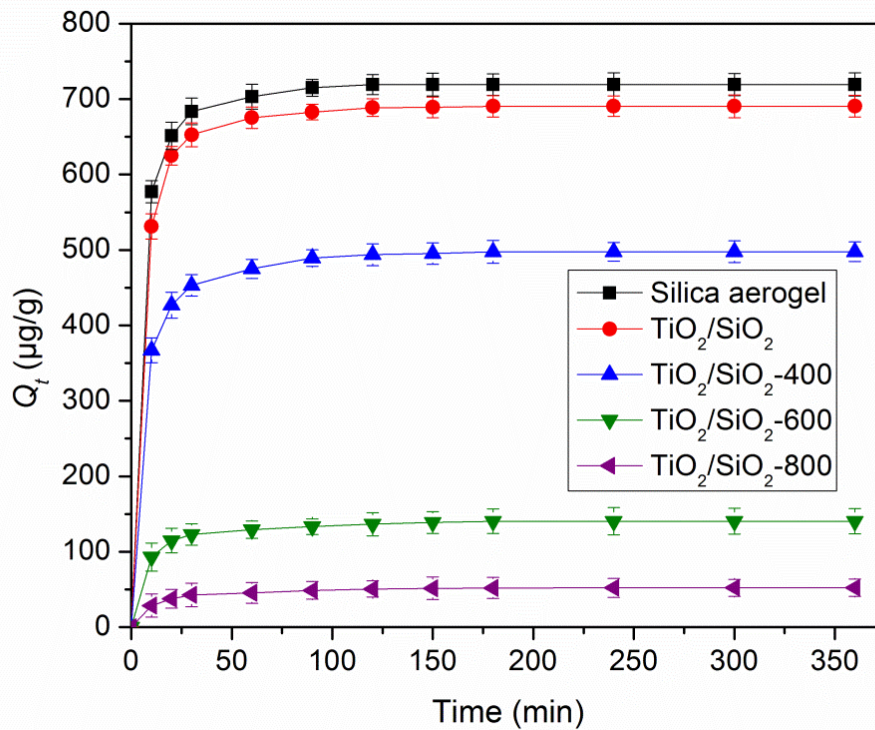


Figure 4-4. Adsorption kinetics of phenanthrene by various TiO₂/SiO₂ composite materials.

Experimental conditions: Initial phenanthrene = 500 µg/L, material dosage = 0.5 g/L, pH = 7.0 ± 0.2, temperature = 25 ± 0.2 °C

Table 4-1. Parameters of Pseudo-first-order and Pseudo-second-order kinetic models for phenanthrene adsorption onto various TiO₂/SiO₂ materials.

kinetic Model	Parameters	Adsorbent				
		SiO ₂ aerogel	TiO ₂ /SiO ₂	TiO ₂ /SiO ₂ -400	TiO ₂ /SiO ₂ -600	TiO ₂ /SiO ₂ -800
Pseudo	$Q_{e,cal}^a$ (µg/g)	61.61	115.57	147.87	55.71	25.16

-first	k_1 (min^{-1})	0.0728	0.0700	0.0723	0.0638	0.0518
-order	R^2	0.7708	0.8656	0.9314	0.8887	0.9775
Pseudo-	$Q_{e,cal}$ ($\mu\text{g/g}$)	724.64	694.44	502.51	143.06	53.71
second	K_2 ($\text{g}/(\text{mg}\cdot\text{min})$)	0.0008	0.0007	0.0007	0.0013	0.0023
-order	R^2	1.0000	1.0000	1.0000	0.9999	0.9998

$Q_{e,cal}$ refers to the equilibrium adsorption calculated from kinetic models.

Fig. 4-5 shows the adsorption isotherms of phenanthrene by various $\text{TiO}_2/\text{SiO}_2$ composite materials. Linear, Langmuir and Freundlich isotherm models are tested to interpret the isotherm data, and **Table 4-2** lists the best-fitted model parameters. Consistent with the kinetic test results, the precursor, silica aerogel showed the highest adsorption capacity ($Q_{max} = 4386.0 \mu\text{g/g}$) for phenanthrene, indicating the great efficiency of silica aerogel for removal of phenanthrene via adsorption. The linear model can well describe the adsorption of phenanthrene by all the materials ($R^2 > 0.98$). Hydrophobic effect is considered the dominant mechanism for phenanthrene adsorption onto these inorganic materials (Fang et al., 2008; Lorphensri et al., 2006; Wang et al., 2001). The non-calcinated $\text{TiO}_2/\text{SiO}_2$ also showed very high adsorption capacity, with a distribution coefficient (K_d) of 4.36 L/g that is only slightly lower than that of silica aerogel (5.28 L/g). However, the adsorption capacity greatly decreased upon calcination, and the higher the calcination temperature, the lower the adsorption ($K_d = 2.09, 0.34$ and 0.12 for $\text{TiO}_2/\text{SiO}_2$ -400, $\text{TiO}_2/\text{SiO}_2$ -600 and $\text{TiO}_2/\text{SiO}_2$ -800, respectively). For $\text{TiO}_2/\text{SiO}_2$ -800, the maximum Langmuir adsorption capacity is $163.9 \mu\text{g/g}$, which is only 3.7% of that for uncalcined $\text{TiO}_2/\text{SiO}_2$. However, as to be shown later on, the photocatalytic activity is enhanced due to the enhanced crystallinity at higher temperatures.

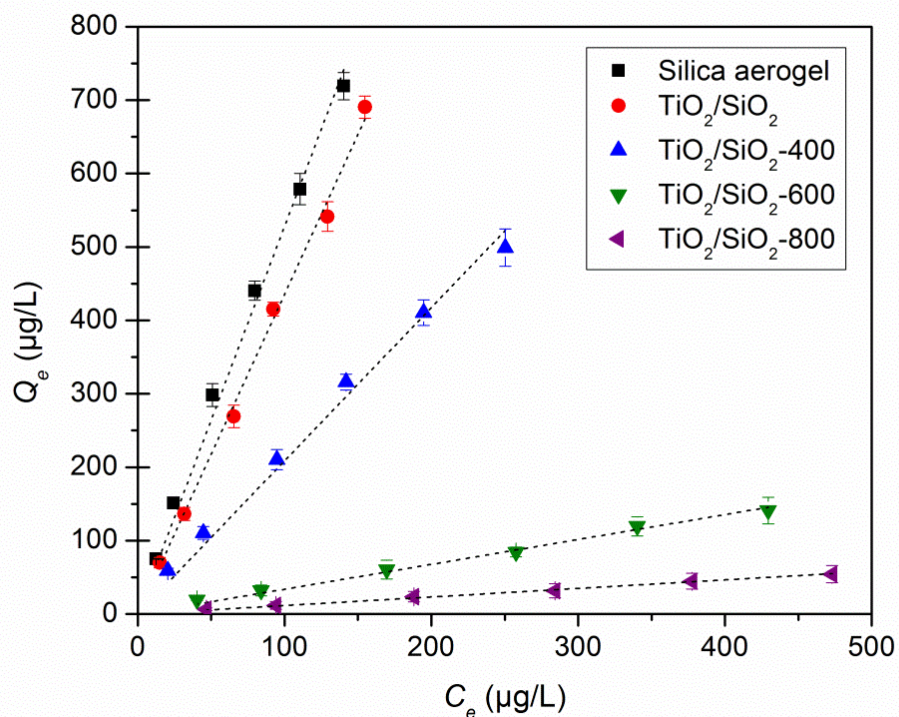


Figure 4-5. Adsorption isotherms of phenanthrene by various $\text{TiO}_2/\text{SiO}_2$ composite materials. Experimental conditions: Initial phenanthrene = 50–500 $\mu\text{g/L}$, material dosage = 0.5 g/L, pH = 7.0 ± 0.2 , temperature = 25 ± 0.2 °C

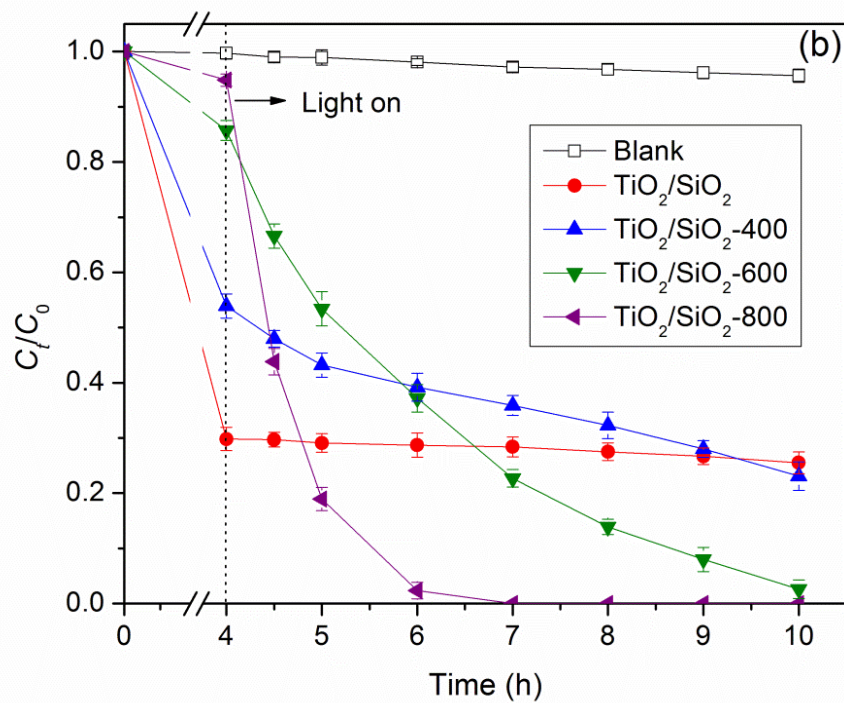
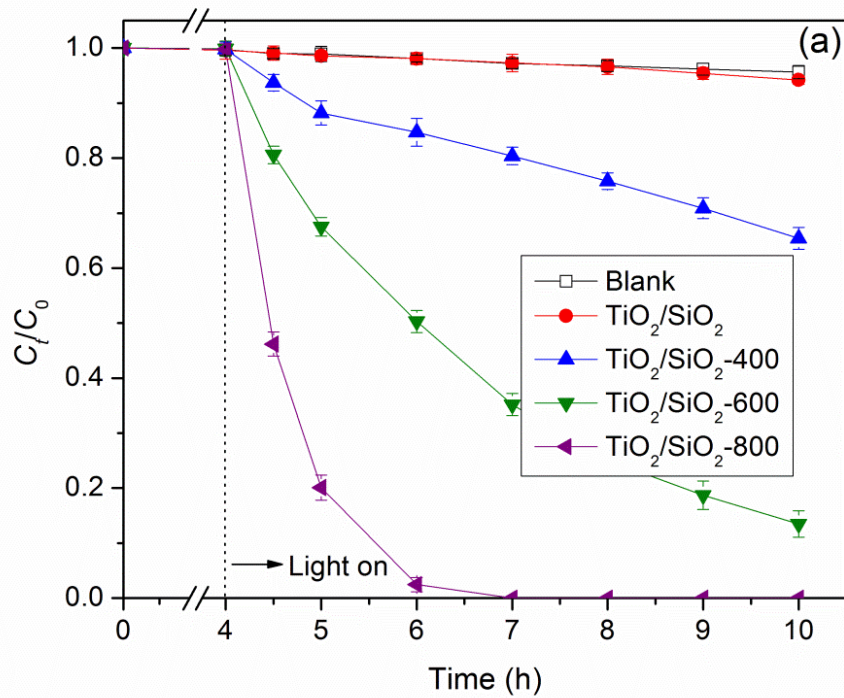
Table 4-2. Parameters of isotherm models for phenanthrene adsorption onto various $\text{TiO}_2/\text{SiO}_2$ materials.

Isotherm Model	Parameters	Adsorbent				
		SiO_2 aerogel	$\text{TiO}_2/\text{SiO}_2$	$\text{TiO}_2/\text{SiO}_2$ -400	$\text{TiO}_2/\text{SiO}_2$ -600	$\text{TiO}_2/\text{SiO}_2$ -800
Linear	K_d (L/g)	5.28	4.36	2.09	0.34	0.12

	R^2	0.9924	0.9959	0.9885	0.9913	0.9950
	Q_{max} ($\mu\text{g/g}$)	4385.97	3816.79	1015.23	256.73	163.94
Langmuir	b ($\text{L}/\mu\text{g}$)	0.0014	0.0012	0.0030	0.0019	0.0009
	R^2	0.9996	0.9987	0.9949	0.9873	0.9963
	K_F ($\mu\text{g/g}\cdot(\text{L}/\mu\text{g})^{1/n}$)	7.74	4.79	4.32	0.76	0.19
Freundlich	n	1.09	1.02	1.16	1.17	1.09
	R^2	0.9988	0.9975	0.9989	0.9953	0.9977

4.3.3 Photocatalysis of phenanthrene by various TiO₂/SiO₂ composite materials

Fig. 4-6a shows that during the photocatalysis process, the total phenanthrene concentration in the reactor system almost did not change in the presence of uncalcined TiO₂/SiO₂, while phenanthrene in the aqueous phase decreased by 70.2%, indicating that all the removal was due to adsorption, i.e. uncalcined TiO₂/SiO₂ did not offer any photocatalytic activity under solar light. In contrast, the total phenanthrene concentration decreased by 35% and 88% in the presence of TiO₂/SiO₂-400 and TiO₂/SiO₂ -600, respectively, in the end of the tests, indicating much enhanced photocatalytic activity due to calcination. However, phenanthrene adsorbed in the solid phase remained about the same, indicating the adsorption inhibited the photodegradation of phenanthrene (**Fig. 4-6c**). The total removal efficiency for the aqueous phenanthrene by TiO₂/SiO₂-600 was 97.4% at 10 h, of which 86.5% was due to photo-degradation and 10.9% to adsorption. TiO₂/SiO₂-800 was most effective (**Fig. 4-6b**), and it was able to completely remove phenanthrene from water within 3 hours of photocatalysis, and the initially adsorbed phenanthrene (5.2% of total phenanthrene) was completely photodegraded after 3 hours of the photocatalysis.



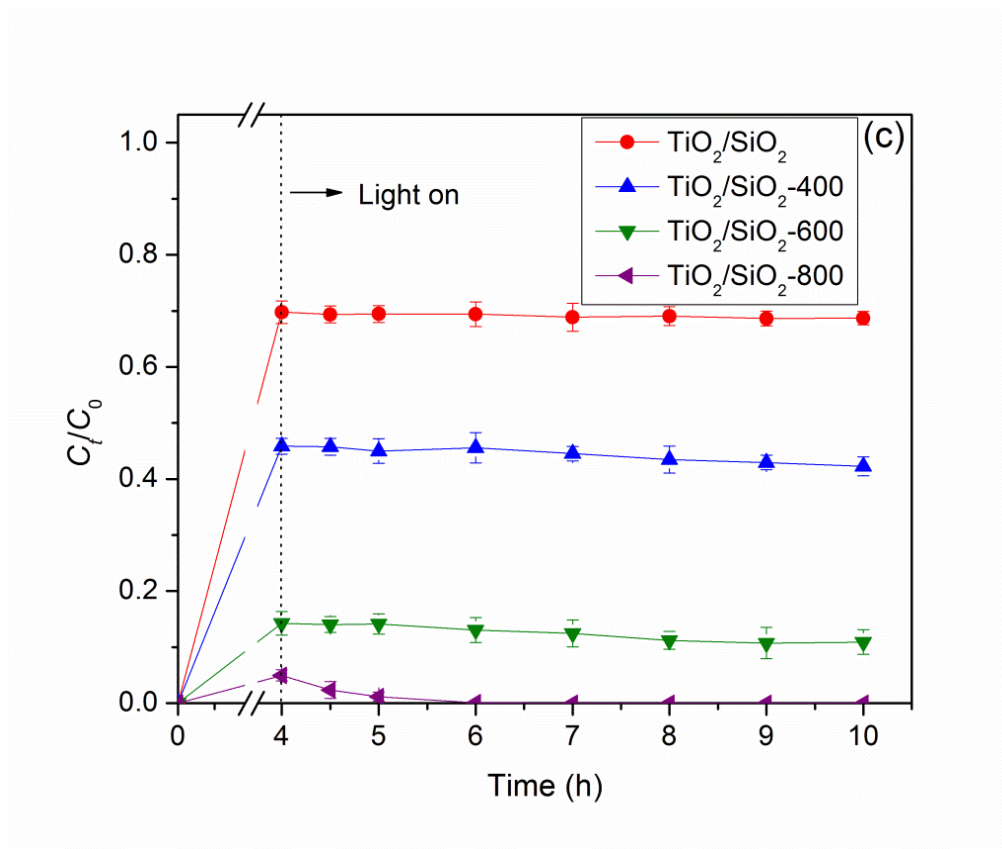


Figure 4-6. Total phenanthrene (a), dissolved phenanthrene (b), and adsorbed phenanthrene (c) in the adsorption-photocatalysis system in the presence of various TiO₂/SiO₂ composite materials. Experimental conditions: Initial phenanthrene = 500 µg/L, material dosage = 0.5 g/L, pH = 7.0 ± 0.2, temperature = 25 ± 0.2 °C

Therefore, the calcination temperature plays a critical role in the photocatalytic activity of the material. Strong adsorption may inhibit the photodegradation process. For the TiO₂/SiO₂-800 composite, both TiO₂ and SiO₂ are important for efficient removal of phenanthrene, where TiO₂ acts as the primary photocatalyst and silica serves as the support for nano-TiO₂. As a weak adsorbent for phenanthrene, the silica support can facilitate the photodegradation by loosely adsorbing phenanthrene from solution to the surface of material.

To test the effect of the initial adsorption phase, the photodegradation tests were also carried out without the initial 4-h adsorption, i.e., the source solar light was turned on immediately after TiO₂/SiO₂-800 was added in the phenanthrene solution. **Fig. 4-7** shows that the pre-adsorption process only slightly enhanced the removal of phenanthrene by TiO₂/SiO₂-800, with a slightly higher apparent rate constant ($k_1 = 0.0298 \text{ min}^{-1}$ or 0.0266 min^{-1} with or without pre-adsorption), and 100% phenanthrene removal was achieved in 140 min with pre-adsorption and in 160 min without pre-adsorption. For both cases, phenanthrene was extracted from the material, and no adsorbed phenanthrene was detected at 140 and 160 min, respectively, indicating complete degradation of phenanthrene was achieved.

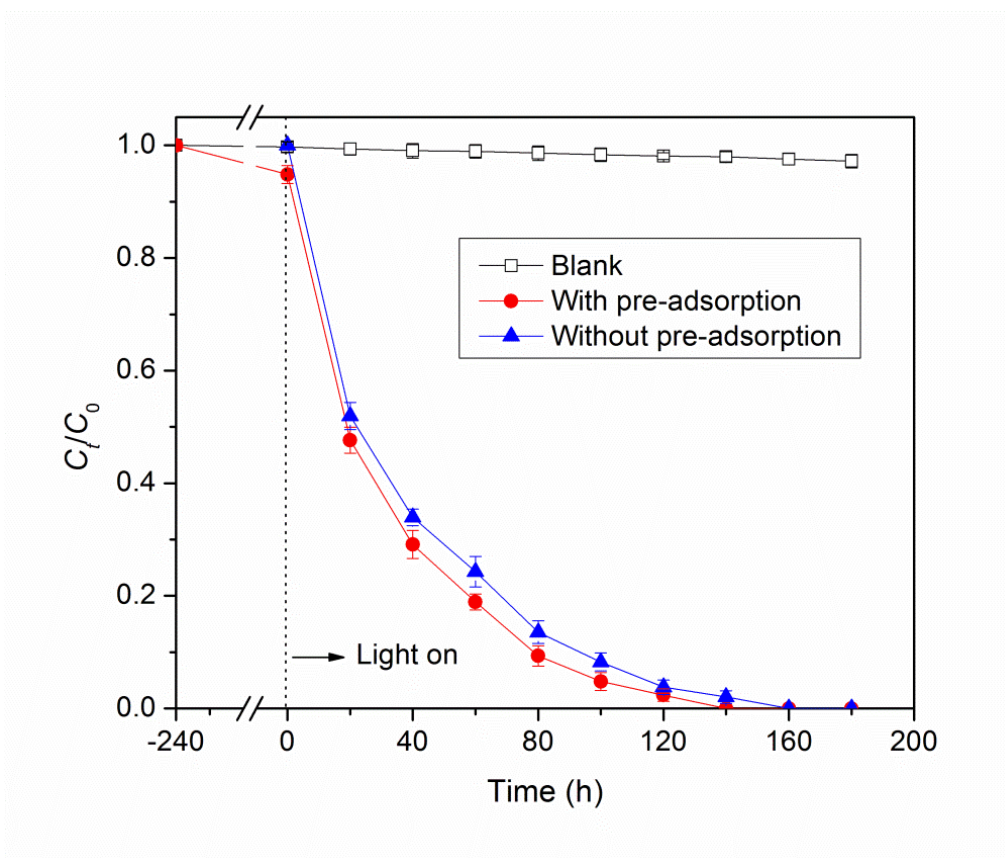


Figure 4-7. Removal of phenanthrene by TiO₂/SiO₂-800 with and without pre-adsorption.

Experimental conditions: Initial phenanthrene = 500 µg/L, material dosage = 0.5 g/L, pH = 7.0 ± 0.2, temperature = 25 ± 0.2 °C.

4.3.4 Mechanisms for enhanced photocatalytic activity of TiO₂/SiO₂-800

Fig. 4-8 shows PL spectra of terephthalic acid, reflecting the production of •OH under solar irradiation. The fluorescence intensity at 425 nm for the materials follows the sequence of: TiO₂/SiO₂-800 > TiO₂/SiO₂-600 > TiO₂/SiO₂-400 > TiO₂/SiO₂, which is consistent with that of the dissolved phenanthrene degradation (Fig. 4-6b). Therefore, enhanced production of the •OH radicals accounts for the enhanced photodegradation of phenanthrene by TiO₂/SiO₂-800.

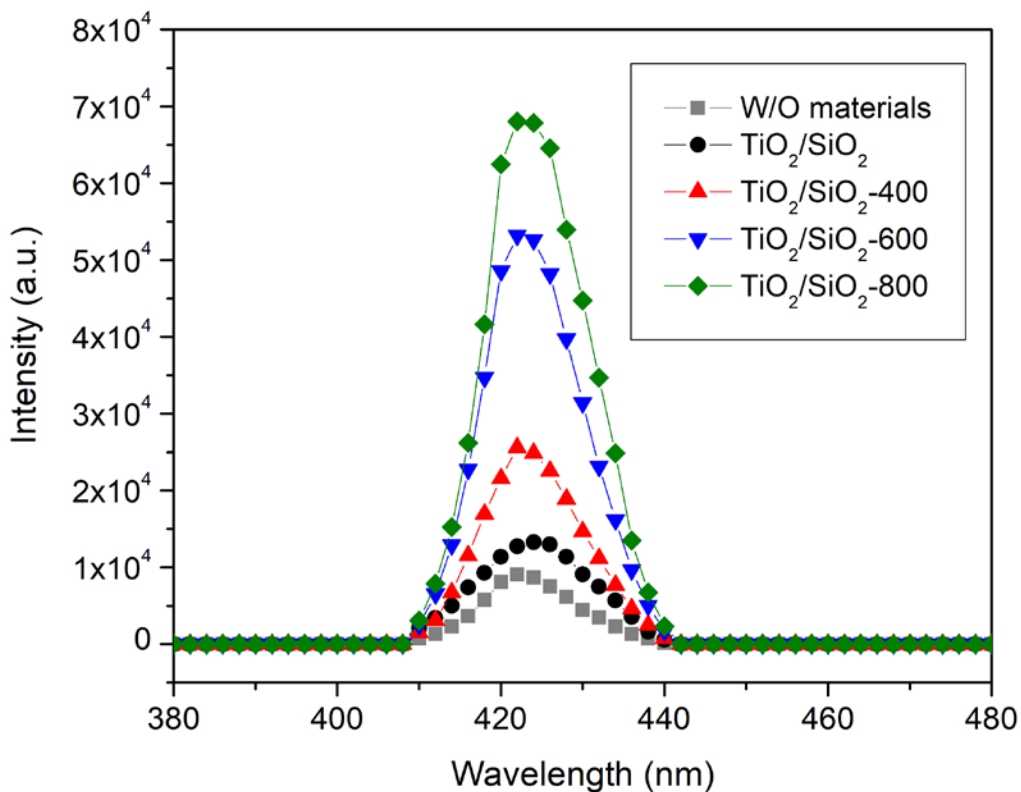


Figure 4-8. PL spectra of various Ti-based materials under solar illumination.

Fig. 4-9 displays EPR spectra for various TiO₂/SiO₂ composites materials. The significant peak was observed, which can be characterized by the set of g value, $g = 2.004$, which is assigned as surface hole centres (Howe and Gratzel, 1987; Micic et al., 1993). And another signal appeared for TiO₂/SiO₂-800, which can be assigned as Ti³⁺ centres (Panarelli et al., 2016). Upon the irradiation (i.e. band gap excitation), the generated electrons and holes are trapped at the surface of TiO₂, forming paramagnetic species representing as Ti³⁺ (Ti⁴⁺ + e⁻ → Ti³⁺, surface trapped electron) and O^{•-} (O²⁻ + h⁺ → O^{•-}, surface trapped holes) stabilized in the charge carriers (i.e. TiO₂) (Nakaoka and Nosaka, 1997; Panarelli et al., 2016), which can be detected by Electron Paramagnetic Resonance spectroscopy (EPR) in the absence of reactive molecules (i.e., under vacuum). Afterwards, Surface trapped electrons and holes can either recombine or be acting as initiators for subsequent process to produce ROS at the composites surface (Schneider et al., 2014). In the presence of reactive molecules (water sorbed at the surface or oxygen), surface trapped electrons and holes can further react with them to form the ROS. In our cases, TiO₂/SiO₂-800 composite shows the highest signal response for the surface trapped centres and appeared the significant Ti³⁺ centres, which can be attributed to the enhanced crystallinity of TiO₂ by the higher calcination temperature.

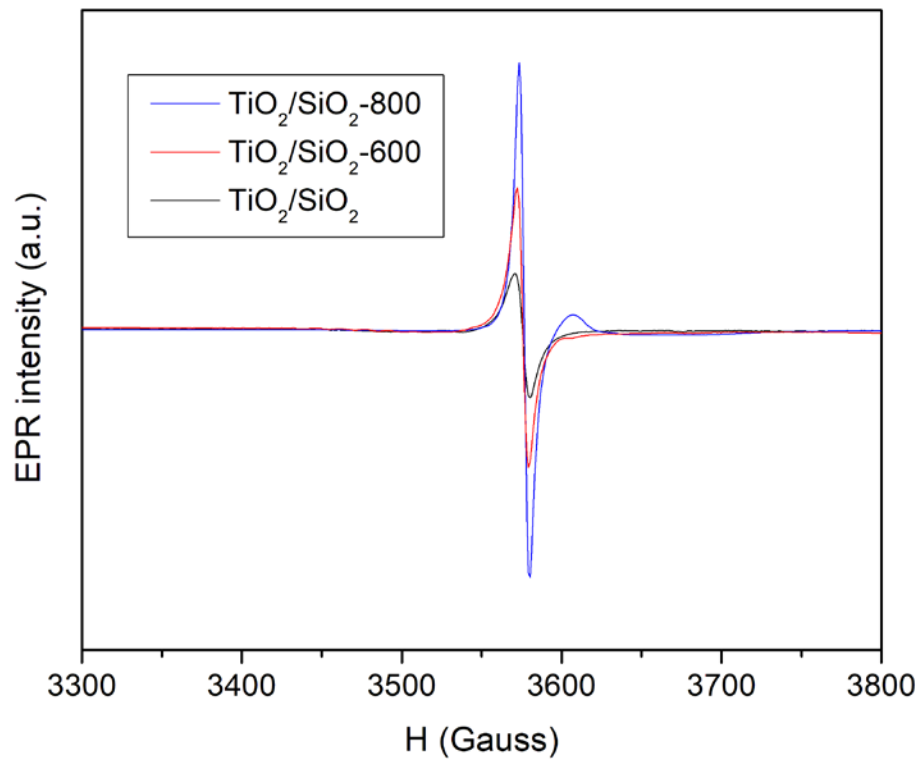
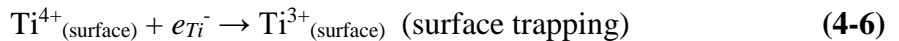
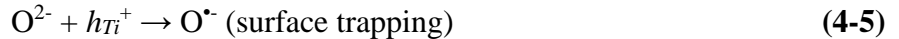
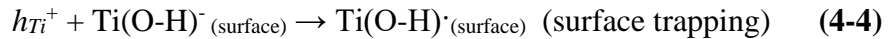
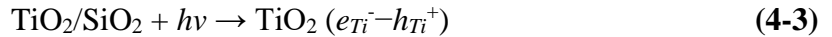


Figure 4-9. EPR spectra for various TiO₂/SiO₂ composites materials.

Fig. 4-10 illustrates the key mechanisms for the enhanced photocatalytic activity of TiO₂/SiO₂-800. Under solar irradiation, anatase (the main one) and rutile all can generate a conduction band (e^- , electrons) and a valence band (h^+ , holes) (**Eqn. 4-3**). In the presence of water and oxygen, the trapped hole (Ti(O-H) \cdot and O \cdot^-) by surface OH $^-$ groups (**Eqn. 4-4**) (**Fig. 4-9**) (Nakaoka and Nosaka, 1997; Panarelli et al., 2016) and oxygen atoms (**Eqn. 4-5**) (Panarelli et al., 2016), respectively, can directly generate the reactive oxygen species (ROS) (mainly \cdot OH). Because the uncalcination TiO₂/SiO₂ are weakly responsive to visible light (**Fig. 4-8** and **Fig. 4-9**), the production of the reactive oxygen species (ROS), e.g. \cdot OH, \cdot O₂ $^-$, HO₂ \cdot , H₂O₂, will be limited. In addition, the excited electron-hole pairs are prone to recombination for TiO₂/SiO₂ due to the loss of the crystalline phases. The electrons and surface trapped electrons (**Eqn. 4-6**) can react with other acceptors, i.e. oxygen, to form superoxide radicals (**Eqn. 4-7**) and hydroxyl radicals (**Eqn. 4-11**), respectively (Cai et al., 2016; Schneider et al., 2014). In addition, the holes can oxidize water molecules (hole transfer to water) into the ROS (mainly \cdot OH), which are responsible for phenanthrene degradation (**Eqn. 4-9**). Meanwhile, phenanthrene can be directly attacked by holes to produce the radicals and further degraded following the **Eqn. 13** (Kou et al., 2009). Equations 4-3 – 4-14 depict the photocatalytic reactions during photodegradation of phenanthrene by TiO₂/SiO₂:



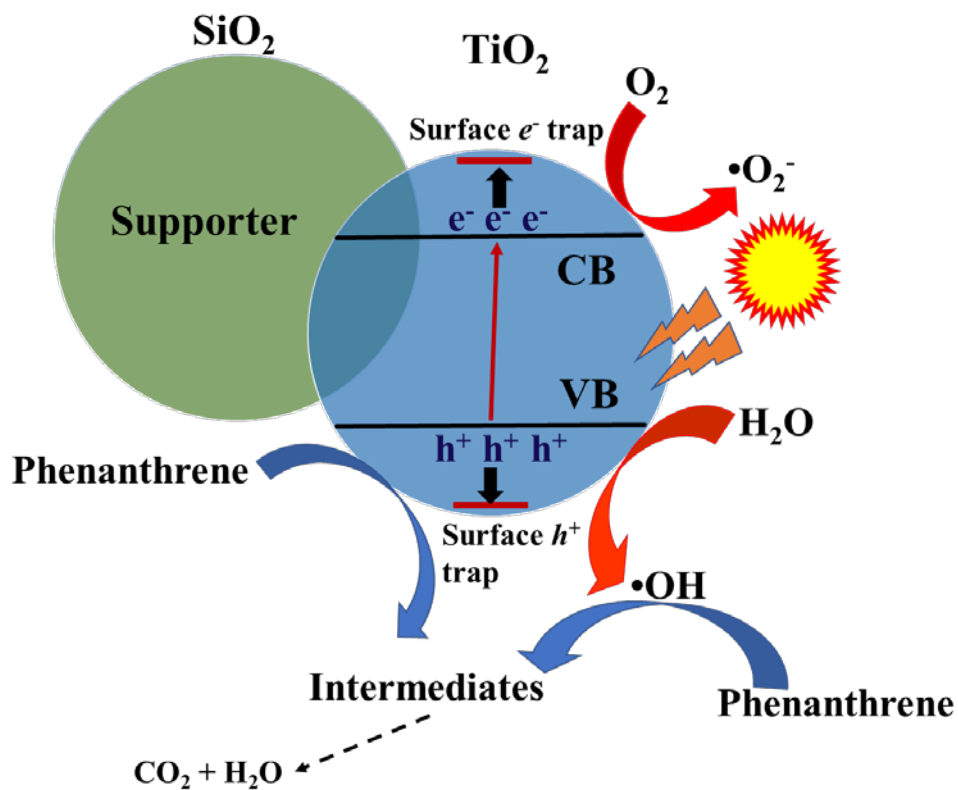
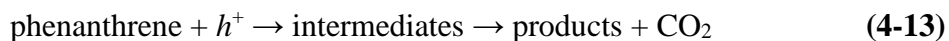
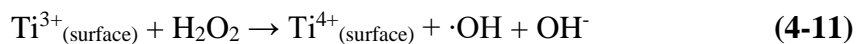


Figure 4-10. Schematic illustration of enhanced photocatalytic activity of TiO₂/SiO₂-800.

Fig. 4-11 demonstrates the proposed phenanthrene photodegradation pathway by TiO₂/SiO₂-800 under solar light. The main intermediates were quantified as 9,10-phenanthrene-9,10-dione (B), (1,1-biphenyl)-2,2-dicarboxaldehyde (C) and bis(2-ethylhexyl) phthalate (D) (**Fig. 4-12** and **4-13**). Following the Step 1 and 2 in **Fig. 4-11**, phenanthrene will form due to ketonization of the hydroxylated benzene ring, and Product C was produced via ring-opening of Product B (Step 3). The results are consistent with other researches (Jia et al., 2012; Kou et al., 2009; Woo et al., 2009). At 3 h (**Fig. 4-12c**), Product B disappeared whereas a new peak assigned to D arose, indicating continued benzene ring opening and subsequent alkylation by some photo-activated alkanes ($\bullet R$) (Steps 3-5) (Jia et al., 2012; Wen et al., 2002). At 6 h (**Fig. 4-12d**), Product D disappeared. Afterwards, the phthalates would be further oxidized into smaller organic compounds, such as cyclohexanols, alkanolic acids, alkenes, alkanes, and alcohols (Step 6) (Jia et al., 2012; Kou et al., 2009), which are then mineralized to CO₂ and H₂O (Step 7).

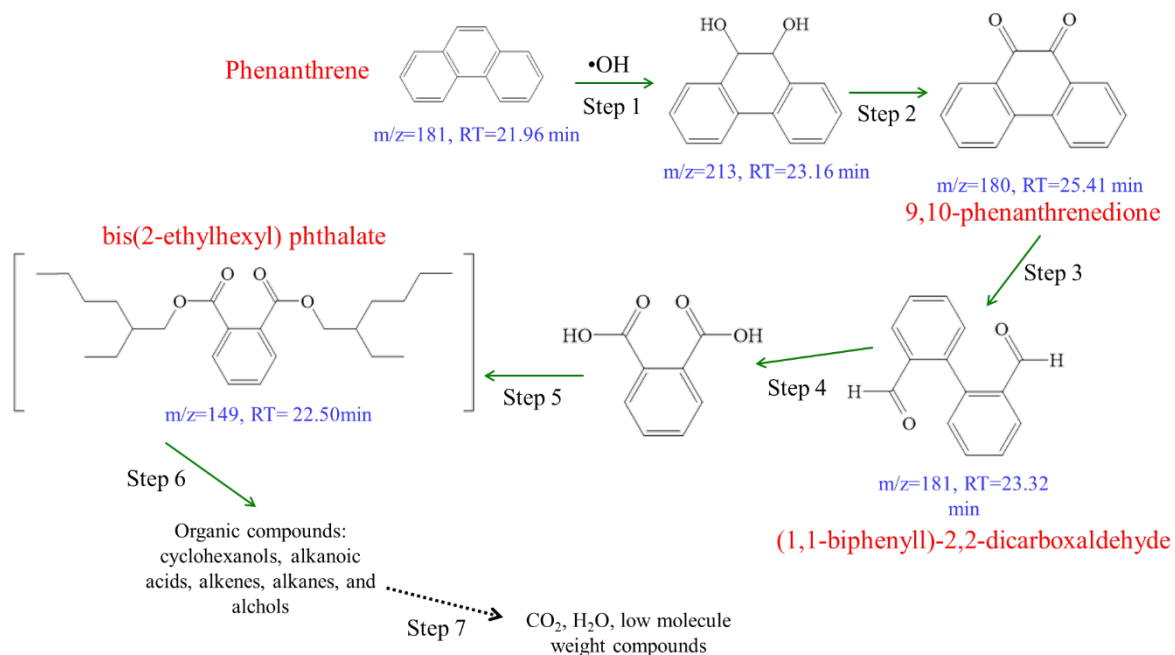
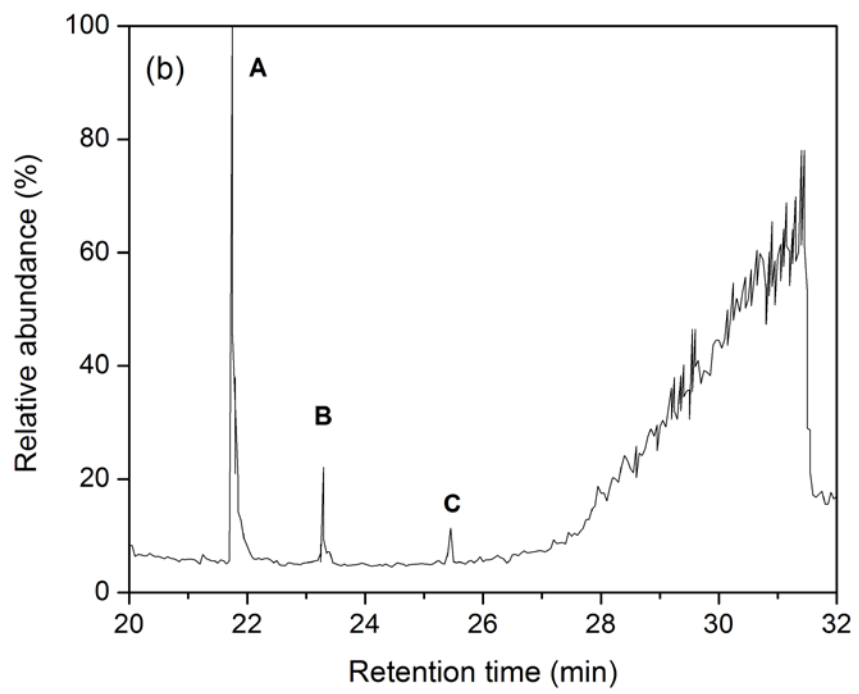
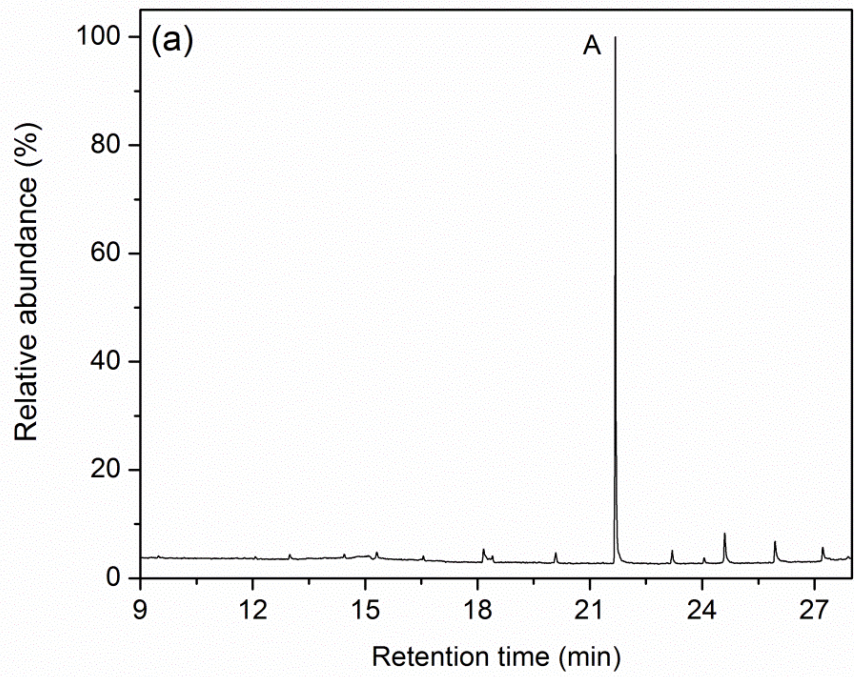


Figure 4-11. Proposed degradation pathway of phenanthrene by TiO_2/SiO_2-800 under solar light.



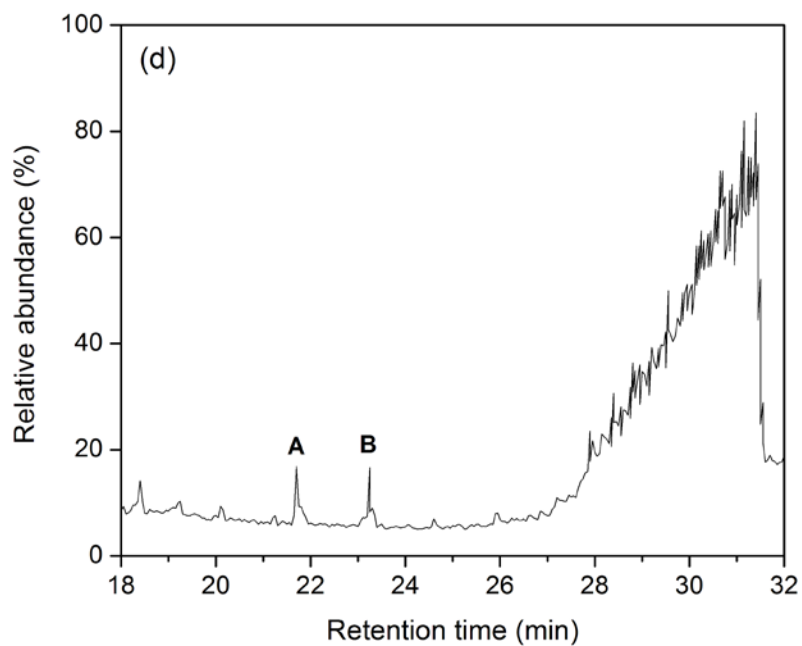
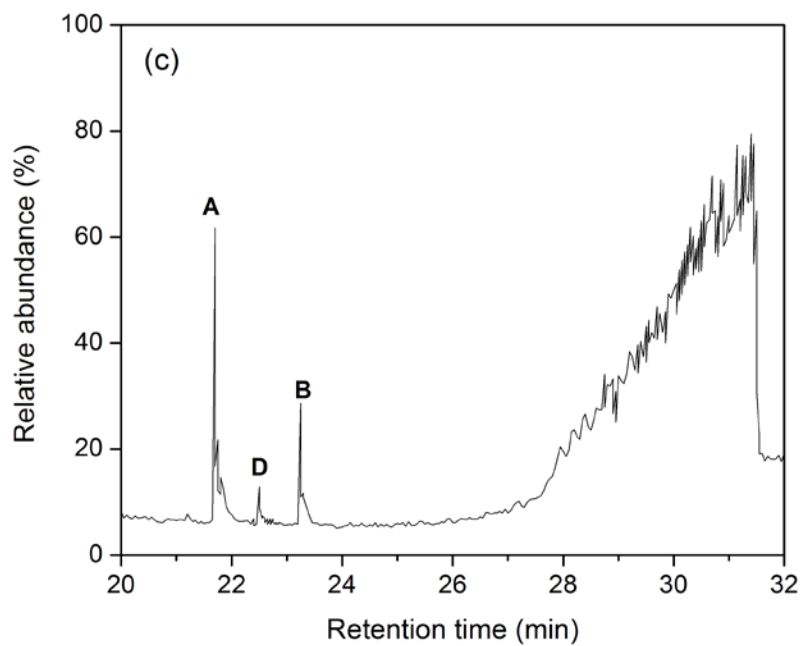
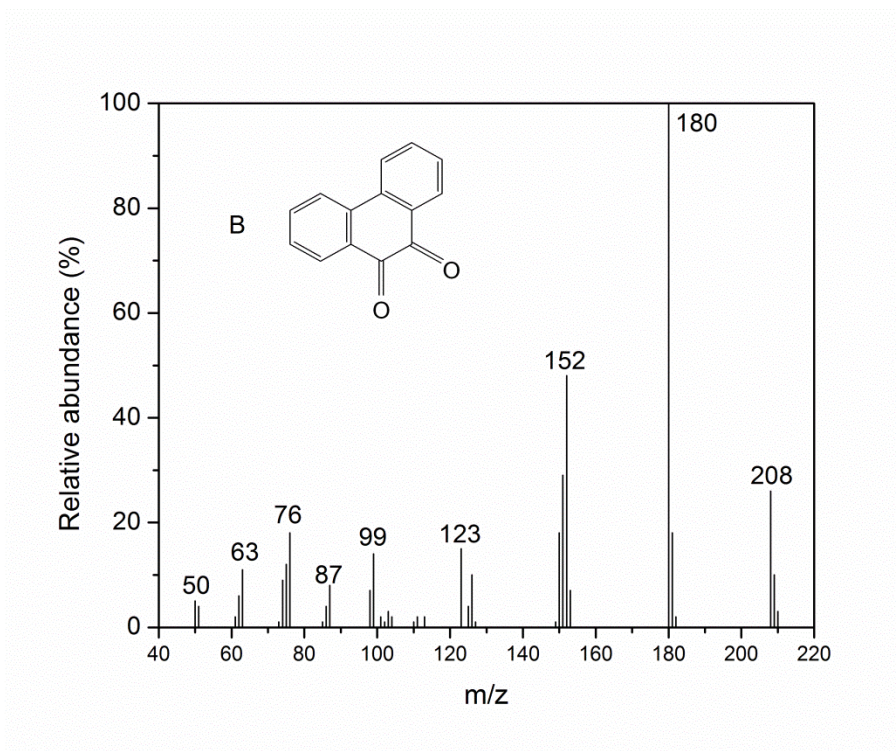
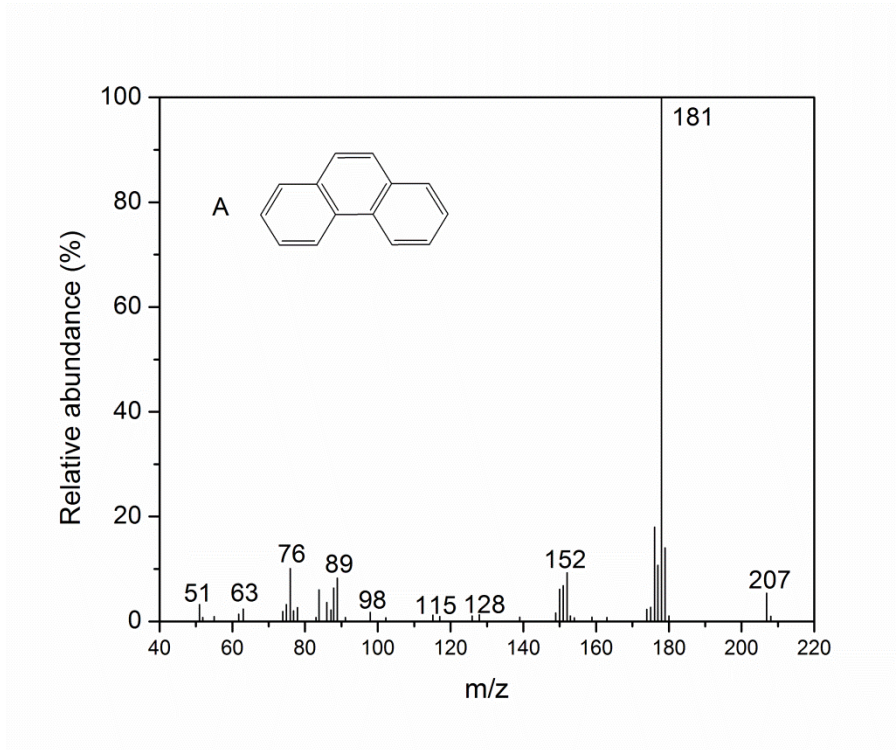


Figure 4-12. Total ion chromatograms of phenanthrene and degradation intermediates at (a) 0, (b) 1, (c) 3, and (d) 6 h of photocatalysis using TiO₂/SiO₂-800. Phenanthrene (A), 9,10-

phenanthrene-1,9-dione (B), (1,1'-biphenyl)-2,2'-dicarboxaldehyde (C) and bis(2-ethylhexyl) phthalate (D)



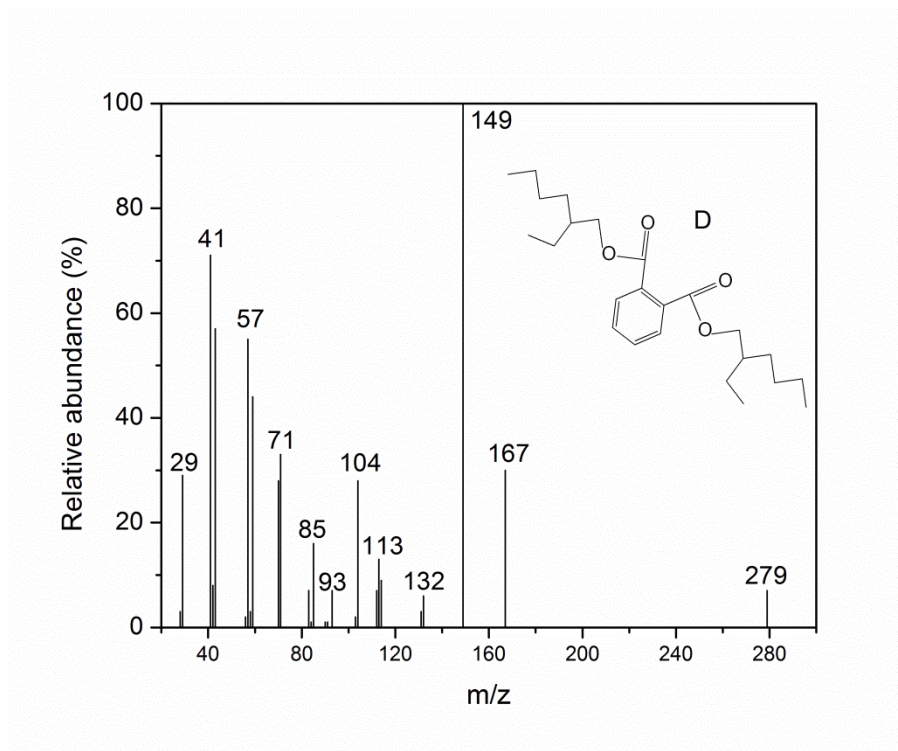
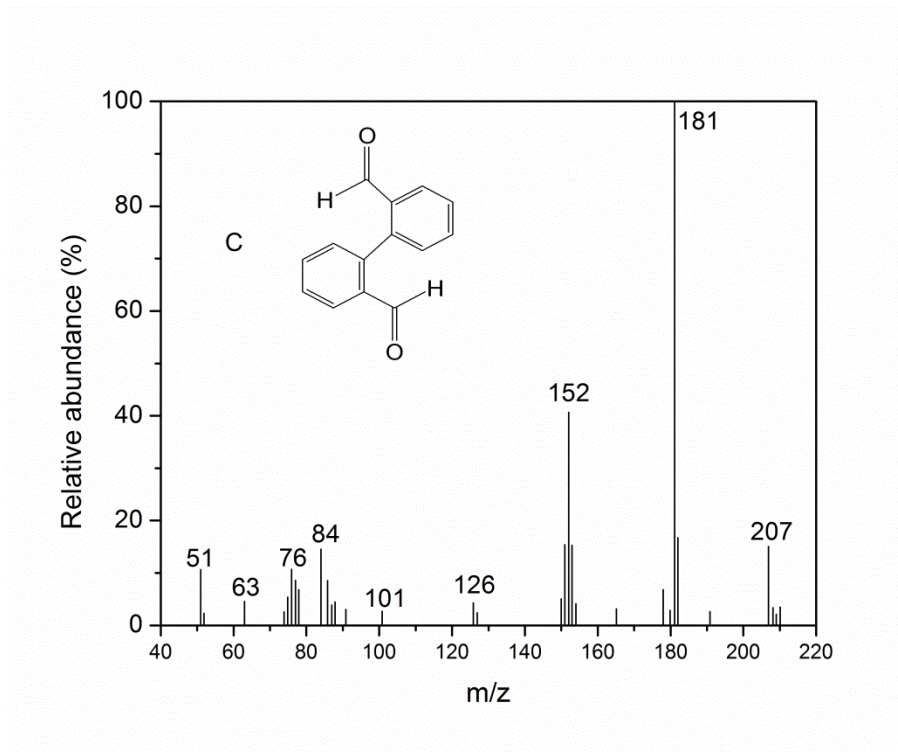


Figure 4-13. Mass spectra of phenanthrene and degradation intermediates in the photocatalysis process by TiO₂/SiO₂-800.

4.3.5 Reusability of TiO₂/SiO₂-800

TiO₂/SiO₂-800 was reused in 5 consecutive cycles for removal of phenanthrene without pre-adsorption (**Fig. 4-14**). The results indicate that 100% of phenanthrene was effectively removed after 5 cycles of repeated uses without significant rate drop, and no phenanthrene was adsorbed on material after extraction in each cycle, indicating the material can be reused in multiple cycles of operations.

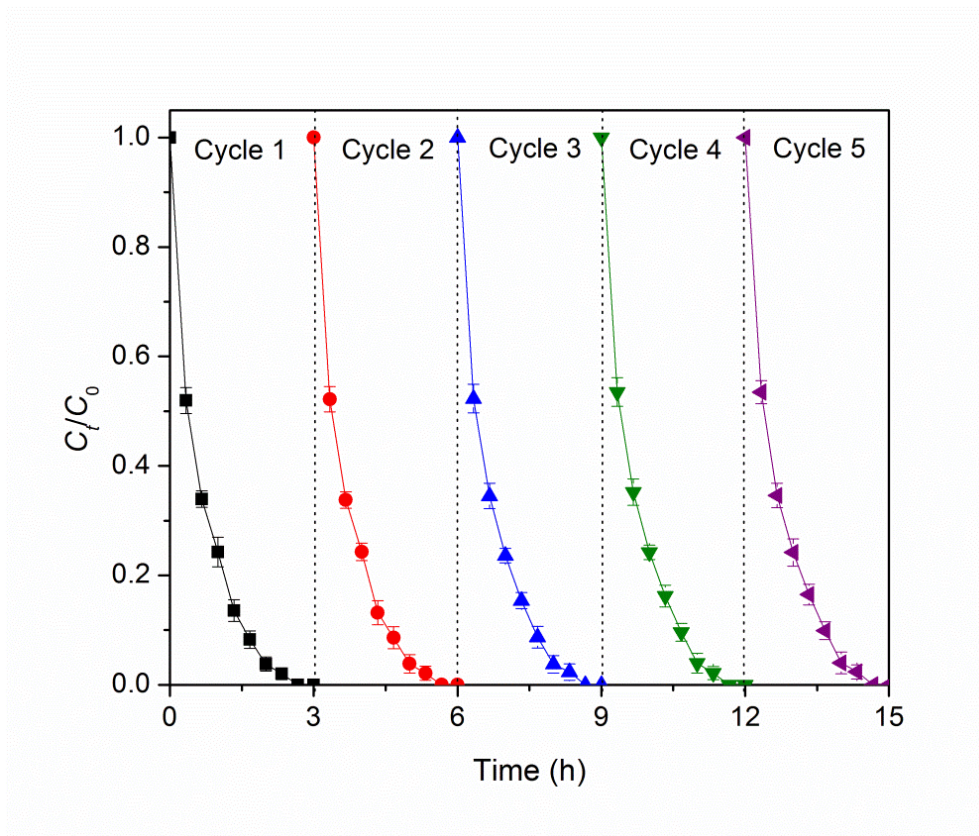


Figure 4-14. PL spectra of various Ti-based materials under solar illumination.

Table 4-3. Phenanthrene removal efficiency (*R*) by TiO₂/SiO₂-800 over 5 cycles of consecutive runs.

Cycles	<i>R</i> (%)
1	100
2	100
3	100
4	100
5	100

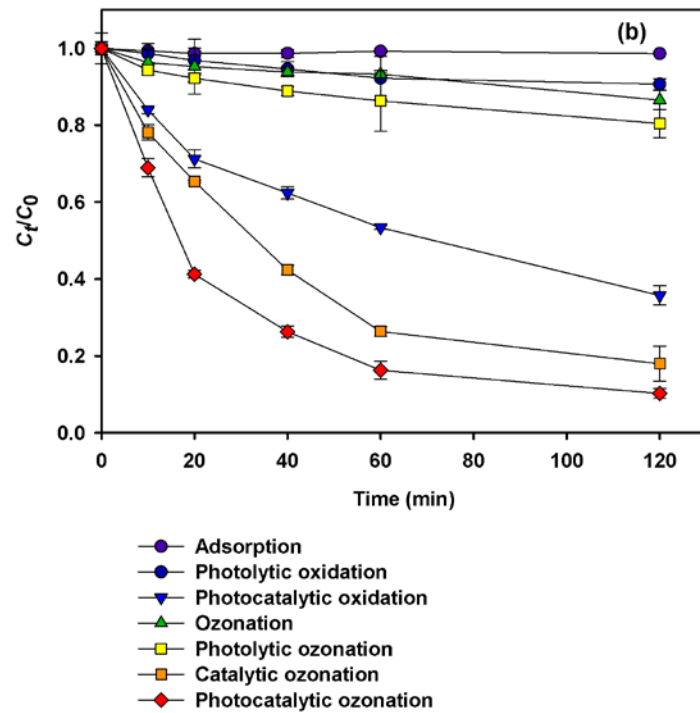
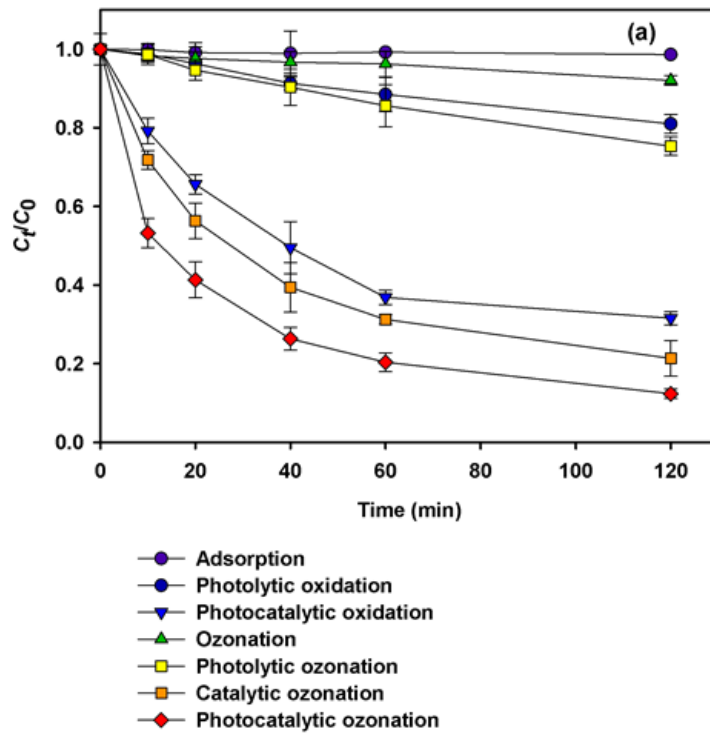
4.3.6 Synergistic effect of ozonation and photodegradation using TiO₂/SiO₂-800

While catalytic photolysis and ozonation can each tackle persistent organic compounds through ROS, the rather different yields and types of ROS generated and the reaction mechanisms enable the two processes to be synergistically supplementary (Agustina et al., 2005), i.e., ROS produced in photolysis may prime persistent oil/PAHs to the active intermediates to ease ozonation, and vice versa. Such synergistic effects can be further augmented in the presence of catalysts and oil dispersants. Since photolysis, ozonation and catalysis are concurrently present in the Gulf Coast ecosystems, it is of pivotal importance to determine the contribution of combined catalytic photolysis and ozonation to the overall weathering of oil/PAHs, which has been largely ignored in the research community.

Studies have reported the synergistic effect of catalytic photolysis and ozonation for degradation of organic compounds. Beltrán et al. (2005) observed that the degradation effectiveness of fluorene follows the sequence of: TiO₂-catalyzed photolysis and ozonation (TiO₂/UVA/O₃) > photolysis and ozonation (UVA/O₃) > ozonation (O₃) ≈ TiO₂-catalyzed ozonation (TiO₂/O₃) ≈ TiO₂-catalyzed photolysis (TiO₂/UVA) > adsorption (TiO₂). Li et al. (2003) found that combined photocatalysis with UV irradiation and ozonation (TiO₂/UV/O₃) considerably increased the removal rate of catechol compared to combined photocatalysis with UV irradiation and oxygen oxidation (TiO₂/UV/O₂), ozonation alone (O₃) process, combined ozonation and UV irradiation (UV/O₃). García-Araya et al. (2010) reported that ozonation alone resulted in incomplete oxidation of diclofenac, while photolytic TiO₂ catalyzed ozonation was more effective in mineralization of diclofenac. Parrino et al. (2014) found that combined photocatalytic ozonation was more efficient for oxidizing organics and reducing hazardous bromate than either photocatalysis or ozonation alone. While the latest science predicts that a combination of catalysis,

photolysis and ozonation will synergistically accelerate weathering of persistent oil/PAHs and while these important abiotic processes are known to take place concomitantly in the Gulf Coast environment, information has been lacking on the roles and mechanisms of such processes and on the roles of oil dispersants and naturally existing catalysts (e.g., metal ions, metal oxides, sulfides and sands) in combined weathering processes.

Fig. 4-15 profiles the adsorption, photolytic oxidation, photocatalytic oxidation, ozonation, photolytic ozonation, catalytic ozonation and photocatalytic ozonation of DWAO in the presence or absence atmospheric ozone and visible light. First-order model is tested to interpret the kinetic data and **Table 4-4** lists the fitted model parameters. Consistent with the kinetics result, the composites showed the highest photocatalytic ozonation rate for dispersed oil hydrocarbons in DWAO, indicating the great efficiency of $\text{TiO}_2/\text{SiO}_2\text{-800}$ for removal of dispersed oil hydrocarbons via combined ozonation and photodegradation. The photocatalytic activity is enhanced by ozone. In the adsorption process, the dispersed oil hydrocarbons (including *n*-alkanes and TPAHs) concentration in the presence of $\text{TiO}_2/\text{SiO}_2\text{-800}$ almost did not change over the time, while dispersed oil hydrocarbons in the aqueous phase decreased by 89.8% and 90.1% in the photocatalysis process, indicating all the removal was due to photocatalytic ozonation (**Fig. 4-15**).



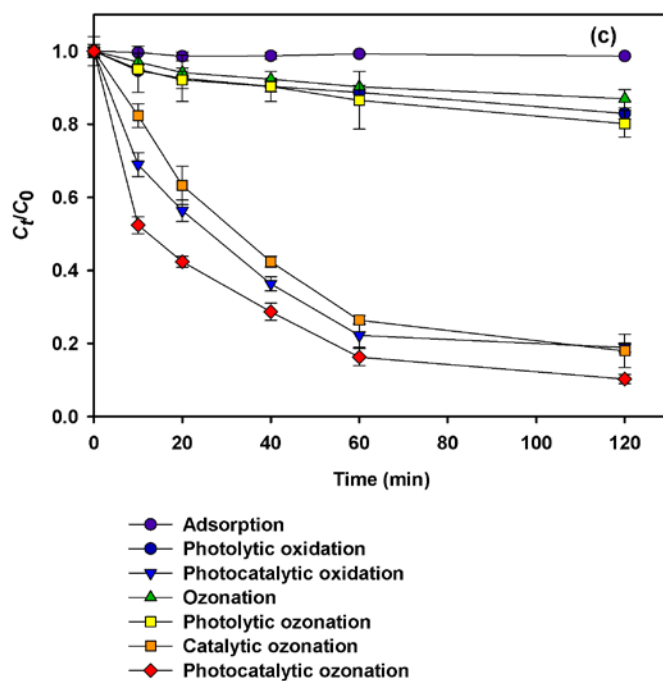


Figure 4-15. Removal of (a) TPHs, (b) *n*-alkanes and (c) Total PAHs in DWAO (Corexit EC9500A) solution by combined ozonation and photodegradation. Experimental conditions: Initial TPHs, *n*-alkanes and TPAHs concentration in DWAO = 149.7, 79.3 and 6.21 mg/L, gas flow rate = 4 mL/min, temperature = 22±1 °C, volume of solution = 250 mL, solution pH = 8.1±1, salinity = 2%, and dissolved organic matter (DOM) = 2.2 mg/L as total organic carbon (TOC). Symbols: experimental data plotted as mean of duplicates; lines linear regressions or First-order-type non-linear fittings; error bars refer to deviation from the mean to indicate data reproducibility.

Table 4-4. First order ozone oxidation rate constants for TPHs, n-alkanes and TPAHs in DWAO for different reactions.

Type	TPHs		<i>n</i> -alkanes		TPAHs	
	k_1 (h ⁻¹)	R^2	k_2 (h ⁻¹)	R^2	k_3 (h ⁻¹)	R^2
Adsorption	0.0001	0.8236	0.0001	0.8236	0.0001	0.8236
Ozonation	0.0006	0.9678	0.0011	0.9400	0.0011	0.8878
Photolytic oxidation	0.0018	0.9833	0.0008	0.8858	0.0014	0.9023
Photolytic ozonation	0.0024	0.9938	0.0017	0.9184	0.0017	0.9420
Photocatalytic oxidation	0.0135	0.9139	0.0092	0.9555	0.0236	0.9487
Catalytic ozonation	0.0192	0.9327	0.020	0.9794	0.0203	0.9791
Photocatalytic ozonation	0.0351	0.9145	0.0351	0.9735	0.0356	0.9307

4.4 Conclusion

This study proposed and tested a new class of silica aerogel supported TiO₂ (TiO₂/SiO₂) composite materials for removal of phenanthrene through adsorption and photocatalysis under solar light. The primary findings are summarized as follows:

- (1) TiO₂/SiO₂ were successfully synthesized through a two-step process, i.e., sol-gel treatment of tetrabutyl titanate (TBOT) as the nano-TiO₂ precursor with silica aerogel followed by calcination at 400, 600 and 800 °C. TEM, HRTEM and XRD characterizations indicate that TiO₂/SiO₂ is a nano-composite consisting of anatase or rutile and SiO₂. Anatase was formed at calcination temperature of 400 and 600 °C, while mixed crystal phases of anatase and rutile were found at 800 °C. EPR spectra confirm the surface trapped holes and electrons centres.
- (2) All the TiO₂/SiO₂ composite materials were able to rapidly adsorb phenanthrene, with equilibrium being reached within 180 min at dosage of 0.5 g/L. The pseudo-second-order kinetic model can better describe the adsorption kinetic data. The equilibrium uptake (Q_e) follows the order of: silica aerogel (719.4 µg/g) > TiO₂/SiO₂ (690.6 µg/g) > TiO₂/SiO₂-400 (497.8 µg/g) > TiO₂/SiO₂-600 (140.5 µg/g) > TiO₂/SiO₂-800 (52.2 µg/g), and the phenanthrene removal percentage: silica aerogel (71.9%) > TiO₂/SiO₂ (69.1%) > TiO₂/SiO₂-400 (49.7%) > TiO₂/SiO₂-600 (14.1%) > TiO₂/SiO₂-800 (5.2%).
- (3) The linear model can fit the adsorption isotherms of phenanthrene by all the materials. Silica aerogel showed the highest adsorption capacity ($Q_{max} = 4386.0$ µg/g) for phenanthrene. For various TiO₂/SiO₂ composites, the adsorption capacity greatly decreased upon calcination, and the higher the calcination temperature, the lower the

adsorption ($K_d = 2.09, 0.34$ and 0.12 for $\text{TiO}_2/\text{SiO}_2$ -400, $\text{TiO}_2/\text{SiO}_2$ -600 and $\text{TiO}_2/\text{SiO}_2$ -800, respectively)

- (4) For the degradation of phenanthrene, the calcination temperature plays a critical role in the photocatalytic activity of the material. Higher calcination temperature resulted in better crystallinity of TiO_2 , higher photocatalytic activity, and reduced the adsorption affinity of the material toward phenanthrene. $\text{TiO}_2/\text{SiO}_2$ -800 showed minimal phenanthrene uptake (only 5.2% of total phenanthrene) but the strongest photocatalytic activity, and it was able to completely degrade phenanthrene within 3 h without any residual in the solid phase.
- (5) The SiO_2 in $\text{TiO}_2/\text{SiO}_2$ -800 can facilitate effective adsorption of phenanthrene, but also serve as a mediator that inhibits recombination of the pairs. Likewise, the anatase crystalline resulting from the calcination process promotes production of more electron-hole pairs and further impedes the electron-hole recombination.
- (6) $\text{TiO}_2/\text{SiO}_2$ -800 can be reused in multiple cycles of operations without significant loss in its photocatalytic activity. Synergistic effect between ozonation and photodegradation of oil hydrocarbons in DWA0 by $\text{TiO}_2/\text{SiO}_2$ -800 was achieved.

Overall, $\text{TiO}_2/\text{SiO}_2$ appears to be an efficient photocatalyst for adsorption and degradation of persistent PAHs under solar light.

Chapter 5. Removal of Oil Components by Activated Charcoal Supported Titanate Nanotubes

A composite material, activated charcoal supported titanate nanotubes (TNTs@AC), was used for efficient adsorption and photodegradation of oil components from (dispersed water accommodated oil) DWAO. TNTs@AC was prepared through a one-step hydrothermal method, and is composed of an activated charcoal core and a shell of carbon-coated titanate nanotubes. Sorption kinetics and isotherms of phenanthrene were conducted. Furthermore, the photocatalytic activity of TNTs@AC was studied under the UV light.

5.1 Introduction

Consider increasing water contamination and growing global energy demand, low-cost and high-efficient water treatment technologies has been the focus of considerable research in the past few decades (Shannon et al., 2008). Among the tremendous treatment methods that have been reported, heterogeneous photocatalysts using solar irradiation has drawn great interest due to their potential to transform various organic pollutants into mineral salts and then final products such as CO₂ and H₂O (Chowdhury and Balasubramanian, 2014; Ibadon and Fitzpatrick, 2013; Schneider et al., 2014; Sud and Kaur, 2012; Wang and Xu, 2012). Traditionally, titanium dioxide (TiO₂)-based photocatalysis has been the most widely used for effective degradation of environmentally related contaminants, such as organic compounds, dyes, pharmaceuticals and so on (Chen and Burda, 2008; Chen and Mao, 2007; Liu et al., 2013; Sampaio et al., 2015; Zhang et al., 2017).

However, the efficiency of degradation of TiO₂ under visible light due to its large band gaps, i.e. 3.2 eV, and recombination rate of charge carriers (Jo and Natarajan, 2015; Zhao et al., 2016). As a result, a great deal of strategies have been reported to enhance its visible light absorption and lifetimes of its charge carriers (Asahi et al., 2001; Jo and Natarajan, 2015; Zhao et al., 2016). However, the removal efficiencies remain unexpected. Therefore, enormous efforts have been devoted to design an efficient visible-light driven photocatalysts.

It is well known that the morphology of TiO₂ has a great effect on its photocatalytic activity. Of various modifications, one-dimensional titanate nanotubes (TNTs) synthesized by hydrothermal treatment of TiO₂ have gained significant attention in recent years (He et al., 2013; Liu et al., 2013a; Liu et al., 2013b). We therefore expect that the synthesis of titanium nanotubes (TNTs) and hybridize with active charcoal to improve the adsorption and photocatalytic activity.

Taking advantage of the high adsorption capacity of AC and photocatalytic activity of TNTs, we conceived a novel composite material, referred to as TNTs@AC, by depositing TNTs onto a common activated charcoal. The newly synthesized TNTs@AC is expected to show the following synergistic effects: 1) the high adsorption capacity of AC will concentrate the target organic pollutants onto the surface of TNTs@AC, facilitating the subsequent photocatalytic degradation; 2) the high photocatalytic activity of TNTs will facilitate effective degradation of the adsorbed pollutants, which also regenerates the spent TNTs@AC; 3) the hydrothermal treatment during the material synthesis may facilitate micro-AC coating on TNTs, and the AC-amended TNTs will enhance both the adsorption capacity and kinetics; and 4) AC on TNTs may serve as the electron shuttles and prevent recombination of the excited holes and electrons, and thus enhance the photodegradation efficacy.

Herein, the overall goal of this section of study was to develop a novel bi-functional material that offers both high adsorption capacity and efficient photodegradation/regeneration for rapid and complete removal of oil components in seawater. This work aimed to: 1) synthesize and the desired TNTs@AC; 2) test the adsorption kinetics and capacity of TNTs@AC using DWAO; 3) evaluate the photo-degradation/regeneration efficiency and material reusability; and 5) elucidate the underlying mechanisms of the reaction of oil components with TNTs@AC.

5.2 Materials and Methods

5.2.1 Chemicals

All chemicals used in this study were of analytical grade or higher. Nano-TiO₂ (P25, 80% anatase and 20% rutile), which were used as the precursor for TNTs, were purchased from Degussa Corporation (Germany). NaOH and methanol (HPLC grade) were obtained from Acros Organics (Fair Lawn, NJ, USA). HCl and absolute ethanol was acquired from BDH Aristar (West Chester, PA, USA). Deionized (DI) water (Millipore Co., 18.2 MΩ·cm) was used to prepare all solutions.

5.2.2 Synthesis of TNTs@AC

TNTs@AC was synthesized through a one-step hydrothermal method based on our previous studies on TNTs preparation (Liu et al., 2016). Typically, 2.4 g of AC and 1.2 g of TiO₂ were mixed with 66.7 mL of a 10 mol/L NaOH solution. After being stirred for 12 h, the mixture was transferred into a Teflon reactor with a stainless steel cover, and then heated at 130 °C for 72 h. The black precipitate (TNTs@AC) was then separated and washed with deionized (DI) water until pH reached ~7.5–8.5, and then dried at 80 °C for 4 h.

5.2.3 Seawater and oil samples

Seawater was collected from the top 30 cm of the water column from Grand Bay, AL, USA (N30.37926/W88.30684). All the detail information about seawater sample was described in **Section 3.2.2**.

A surrogate LSC oil was acquired through courtesy of BP (Houston, TX, USA). According to the supplier, the physical, chemical and toxicological properties of the surrogate oil are similar to those of the Macondo Well crude oil of Mississippi Canyon Block 252. All the detail information and pre-treatment method of oil sample were described in **Section 3.2.2**.

5.2.4 Experimental methods: adsorption and photocatalysis

Water accommodated oil (WAO) and dispersant-facilitated water accommodated oil (DWAO) were prepared with the surrogate oil following a slightly modified protocol by Singer et al. (2000). The preparation details were described by Ji et al. (2018). In this paper, DWAO also refers to dispersed oil. For typographical convenience, DWAO prepared with Corexit EC9500A is referred to as DWAO, respectively.

The oil sorption kinetic tests were conducted at pH 8 with 40 mL of DWAO and TNTs@AC dosage of 0.625 g/L or 0.5g/L in Teflon-lined brown glass vials (43 mL), and then mixing them on an end-to-end rotator at 60 rpm and at room temperature (22±1 °C). At predetermined times, selected vials were centrifuged at 8000 rpm for 5 minutes, and then each 20 mL of the solution sample was extracted with DCM in three consecutive steps (5 mL DCM in each step) according to EPA Method 3510C (EPA, 1996), and then the extracts were combined and filtered through a glass column (L×D = 3×1 cm) packed with 5 g of anhydrous sodium sulfate to remove moisture, and then concentrated to 4 mL under a gentle nitrogen flow. Then, the

concentrated samples were filtered through a polytetrafluoroethylene (PTFE) membrane (0.22 μm) filter to remove residual sodium sulfate, and then filtrates were analyzed for oil content and/or PAHs, *n*-alkanes followed the analytic method described in Section 3.2.5.

The sorption isotherm tests were carried out following similar procedures as for the kinetic tests and by equilibrating the sorption for 24 h. The sorption was initiated by adding 0.005–0.5 g of an adsorbent into 40 mL of DWAO in 43 mL amber glass vials with Teflon-lined caps. Upon equilibrium, the vials were centrifuged, and the samples were extracted and analyzed in the same manner as in the kinetic tests. Control tests were carried in the absence of TNTs@AC, and the results indicated that the loss of TPHs in DWAO was less than 1% in all cases. All experiments were conducted in duplicate, and data reported as mean of duplicates with errors calculated as relative deviation from the means.

The equilibrium oil uptake (q_e , mg/g) and removal efficiency (E , %) are calculated via:

$$q_e = \frac{(C_0 - C_e)V}{m} \quad (5-1)$$

$$E = \frac{(C_0 - C_e)}{C_0} \times 100\% \quad (5-2)$$

where C_0 and C_e are the initial and equilibrium oil concentrations (mg/L) in the aqueous phase, respectively, V is the solution volume (L), and m is the mass of the sorbents.

Regeneration of spent TNTs@AC was performed through photodegradation of oil organics in DWAO adsorbed on TNTs@AC under UV light. Upon adsorption equilibrium using 1.25g/L of TNTs@AC, the mixture was left still for 1 h to achieve the settling of > 99% spent TNTs@AC. After that, ~90% of the supernatant was removed, and the residual solid-liquid mixture was transferred into a glass photo-reactor with a quartz cover, which was then placed under UV light (365 nm, 1.42 mW/cm²) to start photo-degradation. The photo-reaction lasted for 4 hours and samples are taken every 1 hour. To quantify the residual oil components (TPHs, *n*-alkanes and

PAHs) on the material phase after photo-degradation, TNTs@AC was separated and extracted using 10 mL DCM and then concentrated to 4 mL for further measurement.

5.3 Results and Discussions

5.3.1 Adsorption kinetics of oil components in DWAO by TNTs@AC

Fig. 5-1 shows the adsorption kinetics of TPHs, *n*-alkanes and PAHs by TNTs@AC. Evidently, TNTs@AC was able to rapidly remove all the oil components from the DWAO at a low material dosage of 0.625 g/L. In all cases, the adsorption was completed or nearly completed within 4 h. **Fig. 5-1a** shows that the final removal of TPHs, *n*-alkanes and PAHs amounted to 83.4%, 81.6% and 99.4% at 24 h, respectively. When the material dosage was increased to 1.25 g/L, nearly all (> 99.5%) of the oil components were depleted within 24 h (**Fig. 5-1b**), indicating that TNTs@AC have an excellent adsorption affinity for oil hydrocarbons. The pseudo-first order and pseudo-second order models were employed to interpret the adsorption kinetic data (Ho and McKay, 1998), and **Table 5-1** lists the best-fit model parameters. Evidently, the pseudo-second order model was more suitable for simulating the adsorption kinetics ($R^2 \geq 0.9999$), and the model also well simulated the experimental equilibrium uptake (q_e), suggesting that adsorption is likely to be the rate-controlling step (Ho and McKay, 1999).

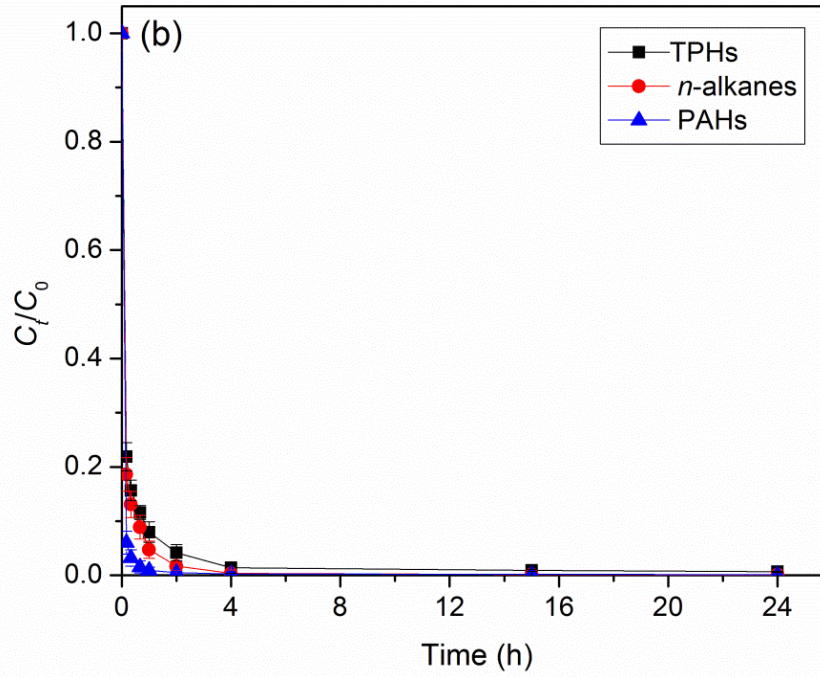
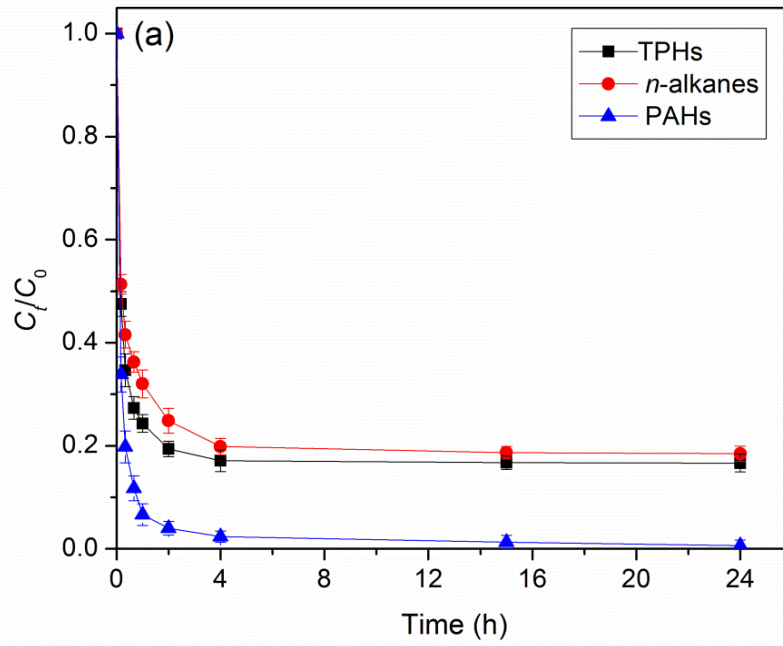


Figure 5-1. Adsorption kinetics of TPHs, n-alkanes and PAHs in DWAO by TNTs@AC (a) with a material dosage of 0.625 g/L, and (b) 1.25 g/L. Experimental conditions: solution pH =8.1, temperature = 22±1 °C, initial salinity = 2 wt.%, and dissolved organic matter (DOM) = 2.2 mg/L as TOC.

Table 5-1. Kinetic parameters for adsorption of TPHs, *n*-alkanes and PAHs in DWAO by TNTs@AC

Kinetic models	Parameters	Material dosage (g/L)					
		0.625			1.25		
		TPHs	<i>n</i> -alkanes	PAHs	TPHs	<i>n</i> -alkanes	PAHs
Pseudo-first order model	k_1 (min ⁻¹)	0.71	2.78	0.82	0.89	0.79	0.69
	q_e (mg/g)	17.63	28.66	0.09	34.49	26.46	0.99
	R^2	0.6765	0.8191	0.7794	0.7460	0.8278	0.8629
Pseudo-second order model	k_2 (g/(mg•min))	0.15	0.47	48.46	0.07	0.08	2.68
	q_e (mg/g)	119.8	57.21	2.70	197.39	93.76	5.39
	R^2	1.0000	1.0000	1.0000	1.0000	0.9999	1.0000

5.3.2 Distribution of oil components in DWAO during adsorption by TNTs@AC

Fig. 5-2 displays the distribution of *n*-alkanes in the aqueous phase during the adsorption process at a material dosage of 0.625 g/L. The targeted *n*-alkanes (C9-C40) were grouped into lower molecular weight hydrocarbons (LMWHs, C9-C20), medium molecular weight hydrocarbons (MMWHs, C21-C30) and higher molecular weight hydrocarbons (HMWHs, C31-C40). The initial total concentration of *n*-alkanes was 71.5 mg/L, and two main peaks were centered in C24-C29 and C11-C13. The concentration of all *n*-alkanes gradually decreased as the adsorption proceeded, and the total *n*-alkanes removal was 49%, 80% and 82% at 10 min, 4 h and 24 h, respectively. However, the removal efficiency of LMWHs, MMWHs and HMWHs at 24 h was 79%, 82% and 91%, respectively, indicating that *n*-alkanes with longer carbon chains are more preferentially adsorbed, which can be attributed to their higher hydrophobicity.

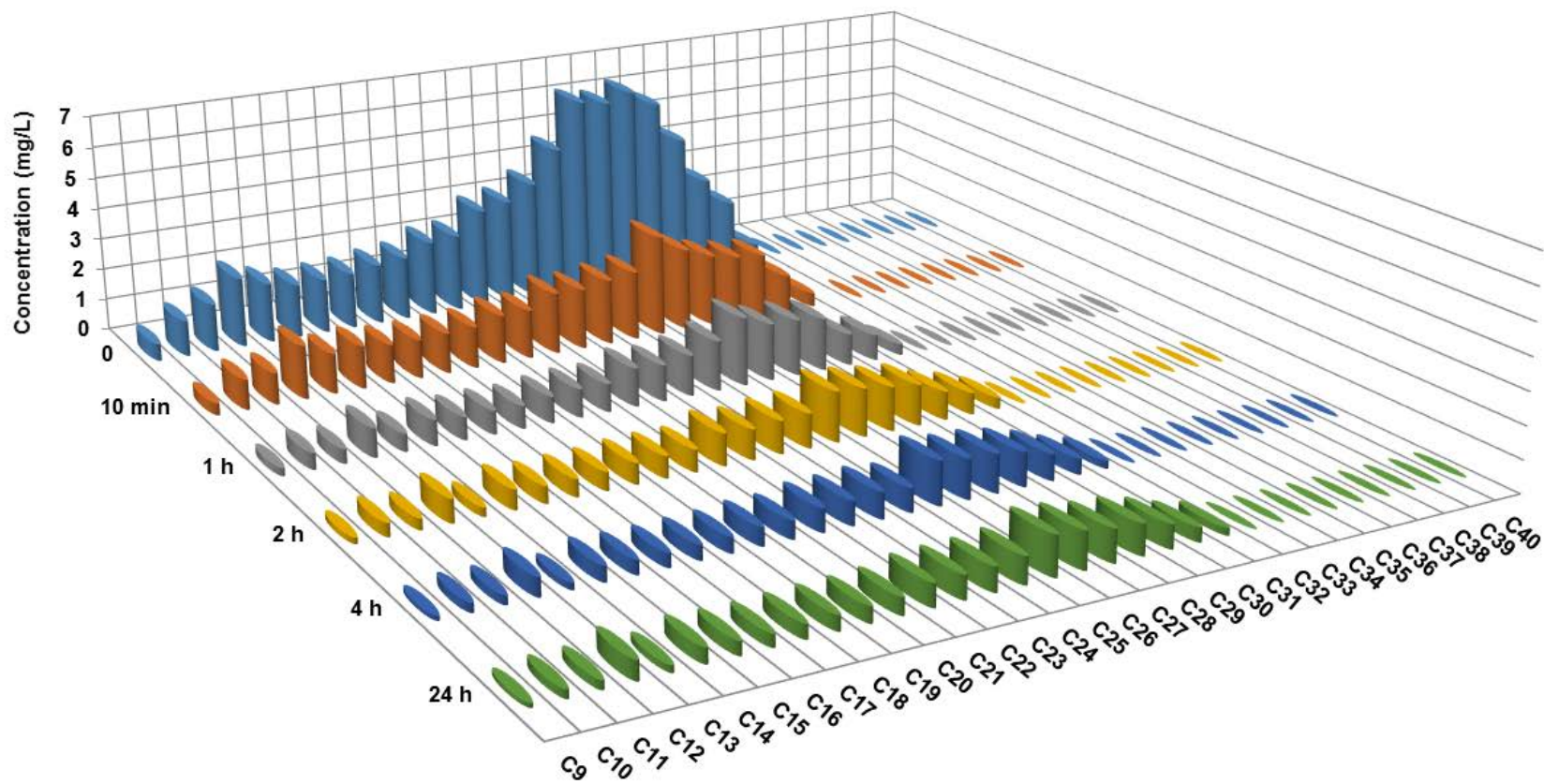


Figure 5-2. Distribution of *n*-alkanes in DWAO during adsorption by TNTs@AC. Experimental conditions: material dosage = 0.625 g/L, solution pH = 8.1, temperature = 22±1 °C, initial salinity = 2 wt.%, and dissolved organic matter (DOM) = 2.2 mg/L as TOC.

Fig. 5-3 shows the distribution of PAHs during the adsorption at a material dosage of 0.625 g/L. The targeted 16 parent PAHs include naphthalene (Naph), acenaphthylene (Acel), acenaphthene (Acen), fluorene (Fluo), phenanthrene (Phen), anthracene (Anth), fluoranthene (Flan), pyrene (Pyre), benzo(a)anthracene (BaA), Chrysene (Chry), benzo(b)fluoranthene (BbF), benzo(k)fluoranthene (BkF), benzo(a)pyrene (BaP), Indeno(1,2,3-cd)pyrene (IP), dibenzo(a,h)anthracene (DA), and benzo(g, hi)perylene (BgP). In addition, primary alkylated PAHs were also targeted, including alkylated-Naph, alkylated-Fluo, alkylated-Phen, alkylated-Anth, alkylated-Flan, and alkylated-Pyre. The initial concentration of the total PAHs was 3.4 mg/L, including 1.0 mg/L of parent PAHs and 2.4 mg/L of alkylated PAHs. The 2-ring (e.g., Naph, Acen and Fluo) and 3-ring (e.g., Phen) PAHs were found to be the main components, while very low concentrations of >5-ring PAHs (< 0.4% of total PAHs) were detected in the DWAO. TNTs@AC were very effective at adsorbing PAHs. More than 90% of PAHs were removed within 1 h, and over 99% of both parent and alkylated PAHs were removed at 24 h, which is much higher than that for THPs (83%) and *n*-alkanes (82%). In addition, TNTs@AC preferred to adsorb parent PAHs over the corresponding alkylated PAHs, for example, 74% of the parent PAHs was adsorbed on TNTs@AC at 10 min compared with 63% for the alkylated PAHs.

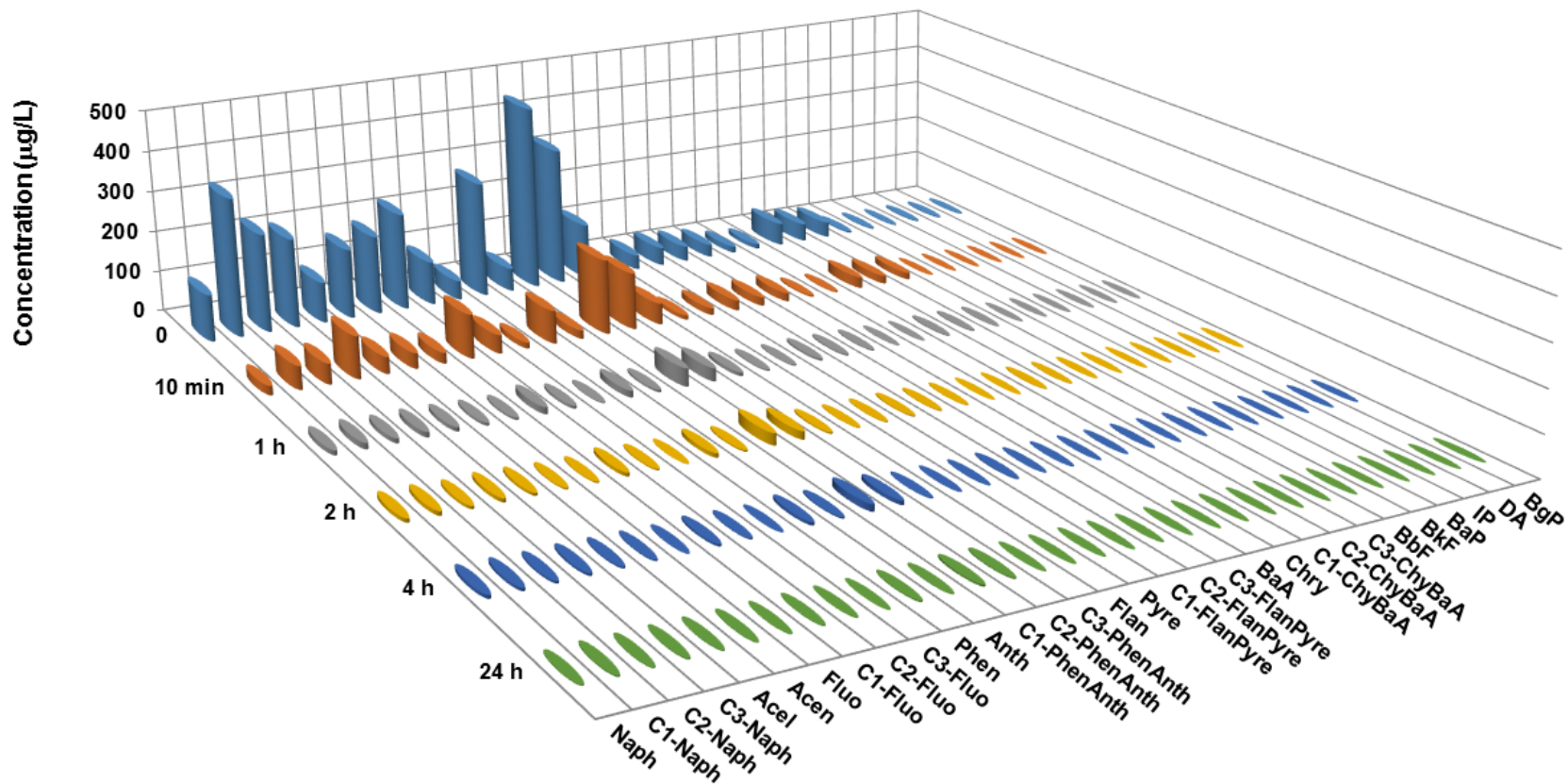


Figure 5-3. Distribution of PAHs in DWAO during adsorption by TNTs@AC. Experimental conditions: material dosage = 0.625 g/L, solution pH = 8.1, temperature = 22±1 °C, initial salinity = 2 wt.%, and dissolved organic matter (DOM) = 2.2 mg/L as TOC.

5.3.3 Adsorption isotherms of oil components in DWAO by TNTs@AC

Fig. 5-4 shows the adsorption isotherms of: (a) TPHs, (b) *n*-alkanes and (c) PAHs by TNTs@AC, and **Table 5-2** lists the best-fitted more parameters. The linear isotherm model was able to adequately interpret the adsorption equilibrium data for TPHs and *n*-alkanes (Figures 4a and 4b), with a distribution coefficient (K_d) of 8.8 and 7.8 L/g, respectively. However, the dual-mode isotherm model (Equation 11) was found more suitable for interpreting the adsorption of PAHs by TNTs@AC ($R^2 > 0.99$). The results indicate that the uptake of PAHs by TNTs@AC was primarily due to partitioning; adsorption plays only a minor role. It is also noteworthy that the K_d values for PAHs are much higher than those for TPHs and *n*-alkanes, indicating TNTs@AC is more favorable toward PAHs than *n*-alkanes.

Linear, Langmuir, Freundlich isotherm and dual-mode models are used to interpret the adsorption isotherm data for TNTs@AC.

The linear isotherm model indicates that adsorption would be linearly proportional to the equilibrium aqueous phase concentration, which can be described as:

$$Q_e = K_d C_e \quad (5-3)$$

The Langmuir isotherm model assumes that the adsorption sites on a monolayer surface are homogeneous and equivalent, and there are no interactions between adsorbate molecules on adjacent sites, which is expressed as (Langmuir, 1918):

$$q_e = \frac{Q_{max} b C_e}{1 + b C_e} \quad (5-4)$$

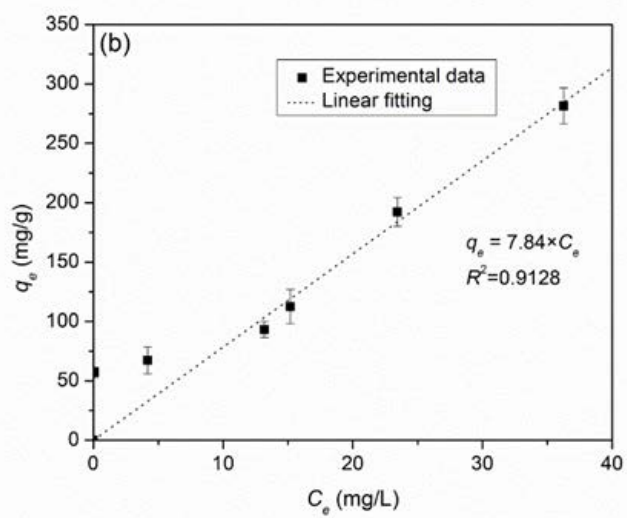
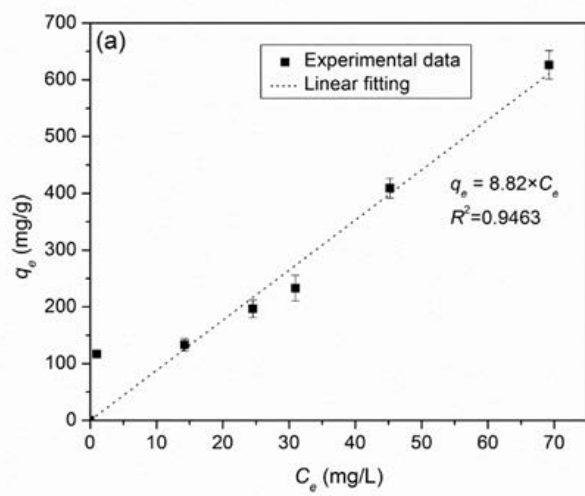
The Freundlich isotherm model is an empirical equation that describes adsorption on an energetically heterogeneous surface, and is expressed as (Freundlich, 1906):

$$q_e = K_F C_e^{1/n} \quad (5-5)$$

The dual-mode model considers the total sorption to adsorbent is the sum of sorption in the dissolution domain (linear distribution) and sorption in the hole-filling domain (Langmuir adsorption), which is expressed as (Zhao et al., 2001; Zhao et al., 2002):

$$Q_e = K_d C_e + \frac{Q_L b C_e}{1 + b C_e} \quad (5-6)$$

where K_d (L/g) is the distribution coefficient; Q_{\max} ($\mu\text{g/g}$) is the maximum adsorption capacity of the adsorbent, and b (L/ μg) is the Langmuir constant related to the affinity of binding sites and is also a measure of free energy of adsorption; K_F ($\mu\text{g/g}\cdot(\text{L}/\mu\text{g})^{1/n}$) is the Freundlich constant related to the adsorption capacity of the adsorbent, and n is the heterogeneity factor indicating the adsorption intensity of the adsorbent; Q_L ($\mu\text{g/g}$) is the Langmuir maximum adsorption capacity.



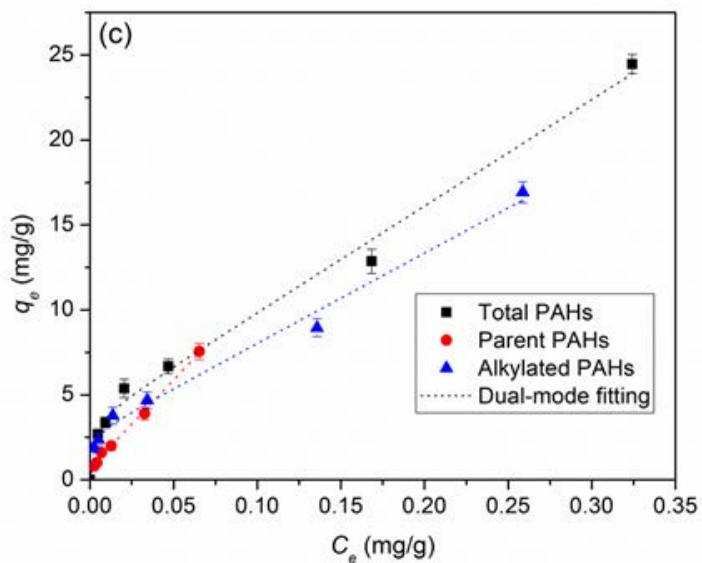


Figure 5-4. Adsorption isotherms of: (a) TPHs, (b) *n*-alkanes and (c) PAHs in DWAO by TNTs@AC. Experimental conditions: solution pH = 8.1, temperature = 22 ± 1 °C, initial salinity = 2 wt.%, and dissolved organic matter (DOM) = 2.2 mg/L as TOC.

Table 5-2. Isotherm parameters for adsorption of TPHs, *n*-alkanes and PAHs in DWAO by TNTs@AC.

Isotherm models	Parameters	TPHs	<i>n</i> -alkanes	PAHs		
				Total	Parent	Alkylated
Linear model	K_d (L/g)	8.82	7.84	77.59	119.02	67.10
	R^2	0.9463	0.9128	0.8936	0.9569	0.8701
Langmuir model	Q_{\max} (mg/g)	657.89	272.48	25.28	9.45	16.76
	b (L/mg)	0.03	0.10	14.59	34.13	23.31
	R^2	0.4591	0.6048	0.8038	0.6617	0.8235
Freundlich model	K_F (mg/g•(L/mg) ^{1/n})	88.78	79.62	35.68	41.41	24.80
	n	2.93	4.99	2.01	1.50	2.26
	R^2	0.6358	0.5855	0.9755	0.9849	0.9690
Dual-Mode model	K_d (L/g)	7.57	6.05	62.53	103.36	52.99
	Q_L (mg/g)	655.43	254.58	3.64	0.72	2.76
	b (L/mg)	0.0031	0.0089	500.24	1964.94	849.94
	R^2	0.9367	0.9034	0.9935	0.9977	0.9925

5.3.4 Photodegradation of adsorbed oil components by TNTs@AC

The highly efficient adsorption of oil components by TNTs@AC and the excellent photochemical activity of the AC-modified TNTs create a favorable condition to rapidly collect dispersed oil from contaminated water and then completely destroy it through subsequent photodegradation. **Fig. 5-5** presents the photo-degradation kinetics of adsorbed TPHs, *n*-alkanes and PAHs on TNTs@AC. **Fig. 5-5a** shows that 98.0%, 94.8% and 98.4% of the pre-concentrated TPHs, *n*-alkanes and PAHs were degraded within 4 h, respectively. **Table 5-3** lists the best-fit model parameters when the pseudo first order model was used to interpret the photocatalytic kinetic data. The apparent rate constant (k_1) follows the sequence of: PAHs (1.01 h^{-1}) > TPHs (0.89 h^{-1}) > *n*-alkanes (0.70 h^{-1}), indicating that PAHs are more prone to the photocatalytic degradation. When PAHs and alkylated PAHs are compared, alkylated PAHs are more preferentially photodegraded (**Figure 5-5b**), with a higher k_1 value of 1.17 h^{-1} . Apparently, the ROS (e.g. $\bullet\text{OH}$, $\bullet\text{O}_2^-$ and $^1\text{O}_2$) produced in the photocatalytic reactions are more likely to attack the alkyl-groups in alkylated PAHs.

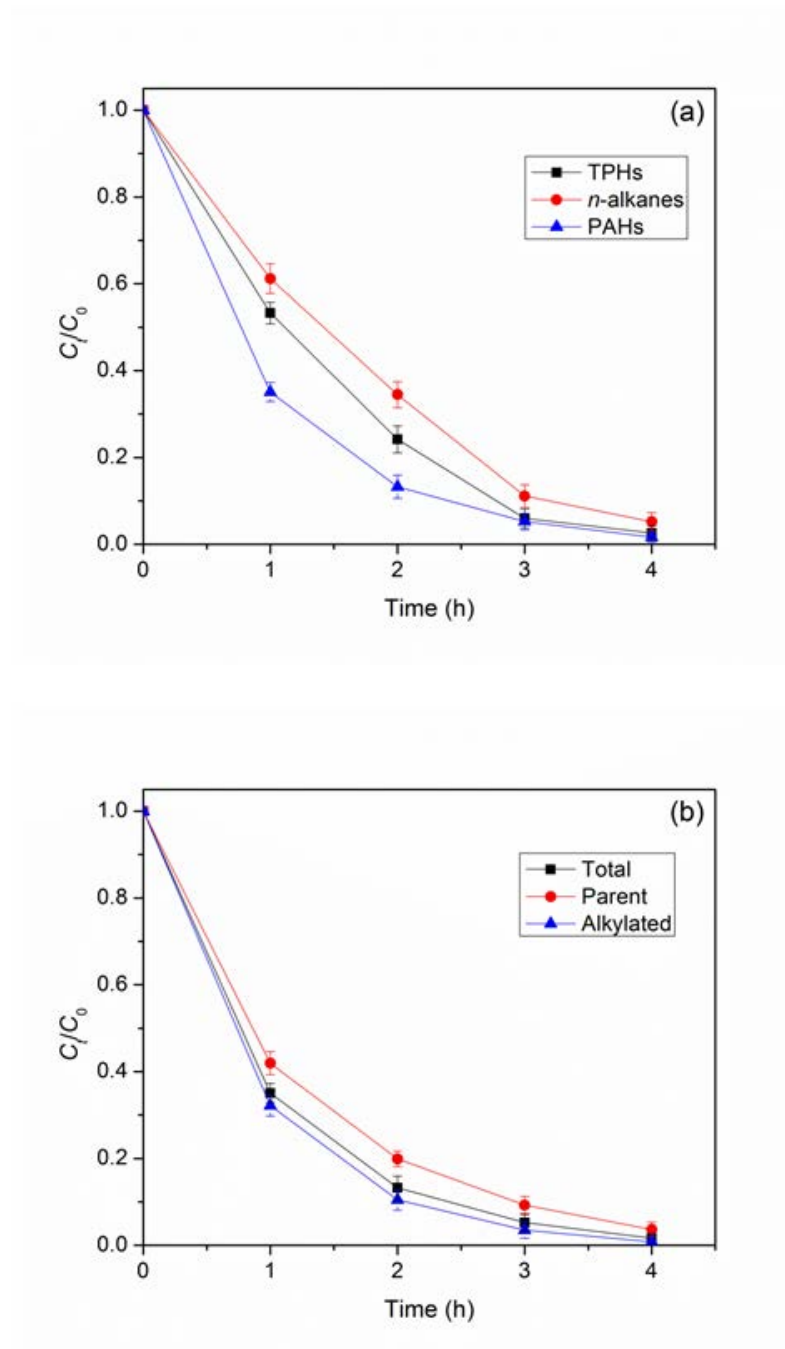


Figure 5-5. Photodegradation kinetics of oil components (a) Photodegradation of various oil components, and (b) various PAHs pre-concentrated on TNTs@AC. Experimental conditions: UV light intensity = 1.4 mW/cm², solution pH = 8.1, temperature = 22±1 °C.

Table 5-3. Parameters of first-order kinetic model for photocatalytic degradation of TPHs, n-alkanes and PAHs by TNTs@AC

Parameters	TPHs	<i>n</i>-alkanes				PAHs		
		Total	LMWHs	MMWHs	HMWHs	Total	Parent	Alkylated
k_1 (h ⁻¹)	0.8852	0.7046	0.6771	0.7237	0.6250	1.0144	0.8168	1.1723
R^2	0.9751	0.9675	0.9543	0.9691	0.9904	0.9986	0.9984	0.9951

5.4 Conclusion

This study proposed and tested a new class of AC supported TNTs (TNTs@AC) composite materials for removal of oil compounds through adsorption and photocatalysis under UV light. The primary findings are summarized as follows:

A novel composite material, TNTs@AC, was synthesized through a simple hydrothermal process based on low-cost commercial AC and TiO₂. TNTs@AC offer not only rapid adsorption, but also high adsorption capacity for oil compounds due to the ink-bottle-shaped pores in the micro-AC modified TNTs and capillary condensation. TNTs@AC displayed superior photocatalytic activity, which allowed for rapid degradation of adsorbed oil compounds. TNTs@AC hold great potential to substantially advance current practices in treating spilled oil from water or seawater. More than 99.5% of TPHs, *n*-alkanes and PAHs could be adsorbed at 1.25 g/L TNTs@AC, and then, 98.0%, 94.8% and 98.4% of the pre-concentrated TPHs, *n*-alkanes and PAHs could be degraded within 4 h under UV irradiation.

Chapter 6. Conclusions and Suggestions for Future Research

6.1 Summary and Conclusions

As dispersants are often used in combination with other clean-up methods (e.g., skimmers, booms, and/or burning) and used to clean or remove oil from wildlife or from beach areas, larger amounts of wastewater with dispersed oil are generated. Chapter 2 is the first systematic investigation on oil weathering under simulated atmospheric ozone, and on the effects of a model oil dispersant on the ozonation rates of various oil components. Corexit EC9500A increased the concentrations of TPHs, *n*-alkanes and PAHs in DWAO by 189, 648 and 12 times, respectively, than in WAO. The dispersant is more effective for *n*-alkanes than PAHs. Meanwhile, Corexit EC9500A accelerates ozonation of TPHs, *n*-alkanes and PAHs in DWAO. In the presence of 238 mg/L of Corexit EC9500A and at a gaseous ozone concentration of 86 ppbv, the pseudo first-order ozonation rate constants of TPHs, *n*-alkanes and total PAHs were 2.2, 1.01 and 1.96 times higher than those in WAO. Alkylated PAHs were more prone to ozonation than parent PAHs in both WAO and DWAO. The ozonation rates for all the oil compounds increased with increasing ozone concentration. The ozonation rates of TPHs, *n*-alkanes and total PAHs were increased by 14.8, 5.1 and 6.3 times when the gaseous ozone concentration was increased from 86 to 300 ppbv. Increasing pH slightly inhibited ozonation, especially for the 2-, 3- and 4-ring PAHs and their homologues in DWAO due to the major loss in the direct ozonation. Elevated humic acid concentrations also inhibited the ozonation reactions, and the inhibitive effect of humic acid is more evident on larger *n*-alkanes, in particular the C24–C30 fraction. Higher salinity enhanced the ozonation of all the dispersed oil components due to reduced solvent cage effect and the salting-

out effect of hydrophobic compounds. Meanwhile, addition of 18 mg/L or 24 mg/L of the dispersant to DWAO accelerated the ozonation of TPHs and *n*-alkanes, but inhibited the ozonation of PAHs due to ozone-facilitated alkylation process and dispersant cage effect. Direct ozonation accounted for 56%, 54% and 45.8% of the overall ozonation of TPHs, *n*-alkanes and PAHs, respectively. The dispersant can increase soluble ozone concentration and enhance the hydroxyl radical generation, but may also compete with oil hydrocarbons for both molecular ozone and free radicals. These contrasting effects result in the different reaction rates for various oil compounds. The results indicate that ozonation may play an important role in oil weathering, and thus should be taken into account in the oil budget estimation and in the related impact assessment.

To obtain the knowledge on the effects of oil dispersants on the sorption of dispersed petroleum hydrocarbons by commercial activated charcoal, we investigated the sorption behavior of some prototype activated charcoals for removal of dispersed oil hydrocarbons from water and the effects of two model oil dispersants. All three ACs, especially the PAC100, were able to effectively sorb oil hydrocarbons that are dispersed by either Corexit EC9500A or Corexit EC9527A. Of the two DWAOs, the sorption was more effective in DWAO-I owing to the different surfactant and solvent type, the surfactant characteristics (i.e., CMC and HLB), and weight percentages. And the sorption equilibrium uptake (Q_e) followed the same trend, i.e., PAC100 (31.65 mg/g) > GAC12×20 (31.24 mg/g) > GAC4×12 (28.58 mg/g) for DWAO-I; and PAC100 (29.52 mg/g) > GAC12×20 (24.84 mg/g) > GAC4×12 (20.39 mg/g) for DWAO-II. Based on the Freundlich isotherm model, PAC100 showed the highest adsorption capacity with a Freundlich K_F value of 10.90 mg/g·(L/mg)^{1/n}, $n = 1.38$) due to the higher specific surface area (889 m²/g for BET surface area and 0.95 cm³/g for total pore volume). While all three ACs were able to adsorb Corexit EC9500A, PAC100 showed much faster and more effective adsorption rate and extent

than the GACs, with a pseudo second-order rate constant k_2 (g/(mg·h)) value of 8.94, 0.24 and 0.09 for PAC100, GAC12×20, and GAC4×12, respectively, and equilibrium uptake 5.23, 5.20, and 3.90 mg/g. The dispersant displayed some contrasting effects on the oil sorption, i.e., adsolubilization effect at lower concentrations of the dispersant, and solubilization effect at higher dispersant concentrations. FTIR spectra indicated the presence of the C–OH groups, the O–H groups, C=C or C=O groups and C–H groups in the surface of ACs. And the pH_{pzc} value of GAC4×12, GAC12×20 and PAC100 as 7.3, 6.8 and 6.1, respectively. XPS spectra of the AC showed the presence of atomic percentile of C associated with the π – π bond (9.9 %) which can be attributed to adsorption of organic compounds through π – π interactions. The solution pH only modestly affected the sorption of dispersed oil, and increasing the solution pH from 6.0 to 9.0 decreased the oil uptake by <8% resulting from the deprotonation of the surface functional groups of ACs. Salinity presents the inhibitive effect for the sorption uptake of oil hydrocarbons, i.e., increasing salinity from 2 to 8 wt.% decreased the oil uptake by 12.8%, 7.1% and 4.3% for GAC4×12, GAC12×20 and PAC100, respectively, due to more hydrophilic AC surface and solvent cage effect. The results indicate that commercial activated charcoals appear promising for removal of dispersed oil from contaminated water, and thus may serve as low-cost and efficient sorbents for oil spill cleanup.

To enhance the adsorption and obtain the photocatalytic ability, we synthesized two types of engineered catalyst. First, we proposed and tested a new class of AC supported TNTs (TNTs@AC) composite materials for removal of oil compounds through adsorption and photocatalysis under UV light. A novel composite material, TNTs@AC, was synthesized through a simple hydrothermal process based on low-cost commercial AC and TiO_2 . TNTs@AC offer not only rapid adsorption, but also high adsorption capacity for oil compounds due to the ink-bottle-

shaped pores in the micro-AC modified TNTs and capillary condensation. TNTs@AC displayed superior photocatalytic activity, which allowed for rapid degradation of adsorbed oil compounds. TNTs@AC hold great potential to substantially advance current practices in treating spilled oil from water or seawater. More than 99.5% of TPHs, *n*-alkanes and PAHs could be adsorbed at 1.25 g/L TNTs@AC, and then, 98.0%, 94.8% and 98.4% of the pre-concentrated TPHs, *n*-alkanes and PAHs could be degraded within 4 h under UV irradiation. In addition, we proposed and tested series of silica aerogel supported TiO₂ (TiO₂/SiO₂) composite materials for removal of phenanthrene through adsorption and photocatalysis under solar light. TiO₂/SiO₂ were successfully synthesized through a two-step process, i.e., sol-gel treatment of tetrabutyl titanate (TBOT) as the nano-TiO₂ precursor with silica aerogel followed by calcination at 400, 600 and 800 °C. TEM, HRTEM and XRD characterizations indicate that TiO₂/SiO₂ is a nano-composite consisting of anatase or rutile and SiO₂. Anatase was formed at calcination temperature of 400 and 600 °C, while mixed crystal phases of anatase and rutile were found at 800 °C. EPR spectra confirm the surface trapped holes and electrons centres. All the TiO₂/SiO₂ composite materials were able to rapidly adsorb phenanthrene, with equilibrium being reached within 180 min at dosage of 0.5 g/L. The pseudo-second-order kinetic model can better describe the adsorption kinetic data. The equilibrium uptake (Q_e) follows the order of: silica aerogel (719.4 µg/g) > TiO₂/SiO₂ (690.6 µg/g) > TiO₂/SiO₂-400 (497.8 µg/g) > TiO₂/SiO₂-600 (140.5 µg/g) > TiO₂/SiO₂-800 (52.2 µg/g), and the phenanthrene removal percentage: silica aerogel (71.9%) > TiO₂/SiO₂ (69.1%) > TiO₂/SiO₂-400 (49.7%) > TiO₂/SiO₂-600 (14.1%) > TiO₂/SiO₂-800 (5.2%). The linear model can fit the adsorption isotherms of phenanthrene by all the materials. Silica aerogel showed the highest adsorption capacity ($Q_{max} = 4386.0$ µg/g) for phenanthrene. For various TiO₂/SiO₂ composites, the adsorption capacity greatly decreased upon calcination, and the higher the

calcination temperature, the lower the adsorption ($K_d = 2.09, 0.34$ and 0.12 for $\text{TiO}_2/\text{SiO}_2$ -400, $\text{TiO}_2/\text{SiO}_2$ -600 and $\text{TiO}_2/\text{SiO}_2$ -800, respectively). For the degradation of phenanthrene, the calcination temperature plays a critical role in the photocatalytic activity of the material. Higher calcination temperature resulted in better crystallinity of TiO_2 , higher photocatalytic activity, and reduced the adsorption affinity of the material toward phenanthrene. $\text{TiO}_2/\text{SiO}_2$ -800 showed minimal phenanthrene uptake (only 5.2% of total phenanthrene) but the strongest photocatalytic activity, and it was able to completely degrade phenanthrene within 3 h without any residual in the solid phase. $\text{TiO}_2/\text{SiO}_2$ -800 can be reused in multiple cycles of operations without significant loss in its photocatalytic activity. Meanwhile, Synergistic effect between ozonation and photodegradation of oil hydrocarbons in DWAO by $\text{TiO}_2/\text{SiO}_2$ -800 was achieved.

6.2 Suggestions for Future Work

The specific recommendations for future work are as follows:

1. Corexit EC9500A and Corexit EC9527A were the complex mixture. The detailed mechanism by various components, i.e. Tween 80, Tween 85, Span 80, SDSS and DPnB, will be considered for the effect of ozonation for oil hydrocarbons in DWAO.

2. To get more insight photodegradation mechanism, Electron Paramagnetic Resonance spectroscopy (EPR) for various radicals during the UV or solar irradiation using two types of engineered catalysts will be tested.

3. In order to gain regulatory and public acceptance for using engineered nanomaterials in environmental remediation, more detailed information on toxicology and fate of engineered nanomaterials is needed. More experiments need to be conducted to investigate the fate and toxicology behaviors of the engineered nanomaterials under different conditions, i.e., leachability, stability in environment, toxicity effect.

4. Based on the computational chemistry, a Quantitative Structure-Photocatalytic Activity Relationship (QSPAR) model will be used to mechanically study the relationship between the molecular structure/property of 16 oil PAHs and their photocatalysis rates, which reveals relationship between the reaction rate constant and the energy of highest occupied molecular orbital (E_{HOMO}) of PAH molecule and its initial concentration in DWAO.

5. To the different approach of treatment and various containments, these two materials will be optimized.

References

- Adebajo MO, Frost RL, Kloprogge JT, Carmody O, Kokot S. Porous materials for oil spill cleanup: A review of synthesis and absorbing properties. *J. Porous Mater.* 2003 10:159-170.
- ADEM, 2016. Alabama 8-Hour Ozone Data. <<http://www.adem.state.al.us/programs/air/airquality/ozone/8HourOzoneData.pdf>> Data accessed on Sep. 8 2016.
- Agustina TE, Ang HM, Vareek VK. A review of synergistic effect of photocatalysis and ozonation on wastewater treatment. *J. Photochem. Photobiol. C.* 2005; 6(4):264-273.
- Ahmad AL, Sumathi S, Hameed BH. Residual oil and suspended solid removal using natural adsorbents chitosan, bentonite and activated carbon: A comparative study. *Chem. Eng. J.* 2005; 108:179-185.
- Ahn CK, Kim YM, Woo SH, Park JM. Selective adsorption of phenanthrene dissolved in surfactant solution using activated carbon. *Chemosphere* 2007; 69: 1681-1688.
- Ahn CK, Woo SH, Park JM. Enhanced sorption of phenanthrene on activated carbon in surfactant solution. *Carbon* 2008; 46: 1401-1410.
- Anderson BS, Arenella-Parkerson D, Phillips BM, Tjeerdema RS, Crane D. Preliminary investigation of the effects of dispersed Prudhoe Bay Crude Oil on developing topsmelt embryos, *Atherinops affinis*. *Environ. Pollut.* 2009; 157: 1058-1061.
- Asahi R, Morikawa T, Ohwaki T, Aoki K, Taga Y. Visible-light photocatalysis in nitrogen-doped titanium oxides. *Science* 2001; 293: 269-271.
- Ayotamuno MJ, Kogbara RB, Ogaji SO, Probert SD. Petroleum contaminated ground-water: Remediation using activated carbon. *Appl. Energy.* 2006 83:1258-1264.
- Bacosa H.P., Erdner D. L., Liu Z.F., 2015. Differentiating the roles of photooxidation and biodegradation in the weathering of Light Louisiana Sweet crude oil in surface water from the Deepwater Horizon site. *Mar. Pollut. Bull.* 95, 265-272
- Bader H., Hoigné J., 1981. Determination of ozone in water by the indigo method. *Water Res.* 15, 449-456.

- Bailey P.S., Batterbee J.E., Lane A.G., 1968. Ozonation of benz[a]anthracene. *J. Am. Chem. Soc.* 90, 1027-1033.
- Baumard P., Budzinski H., Garrigues P., Sorbe J.C., Burgeot T., Bellocq J., 1998. Concentrations of PAHs (polycyclic aromatic hydrocarbons) in various marine organisms in relation to those in sediments and to trophic level. *Mar. Pollut. Bull.* 36, 951-960.
- Bejarano AC, Barron MG. Development and practical application of petroleum and dispersant interspecies correlation models for aquatic species. *Environ. Sci. Technol.* 2014; 48: 4564-4572.
- Beltrán D, Selma MV, Marín A, Gil MI. Ozonated water extends the shelf life of fresh-cut lettuce. *J. Agricul. Food Chem.* 2005; 53(14):5654-5663.
- Beltran F.J., Ovejero G., Encinar J.M., Rivas J., 1995. Oxidation of polynuclear aromatic hydrocarbons in water. 1. Ozonation. *Ind. Eng. Chem. Rev.* 34, 1596-1606.
- Beyer J, Trannum HC, Bakke T, Hodson PV, Collier TK. Environmental effects of the Deepwater Horizon oil spill: A review. *Mar. Pollut. Bull.* 2016; 110:28-51.
- Bianchi TS, Osburn C, Shields MR, Yvon-Lewis S, Young J, Guo L, et al. Deepwater Horizon oil in Gulf of Mexico waters after 2 years: Transformation into the dissolved organic matter pool. *Environ. Sci. Technol.* 2014; 48: 9288-9297.
- Blondina GJ, Singer MM, Lee I, Ouano MT, Hodgins M, Tjeerdema RS, Sowby ML. Influence of salinity on petroleum accommodation by dispersants. *Spill Sci. Technol. Bull.* 1999; 5:127-34.
- Board M., Council N.R., 1989 *Using oil spill dispersants on the sea*: National Academies Press.
- Cai Z., Gong Y., Liu W., Fu J., O'Reilly S.E., Hao X., et al., 2016. A surface tension based method for measuring oil dispersant concentration in seawater. *Mar. Pollut. Bull.* 109, 49-54.
- Cai Z, Fu J, Liu W, Fu K, O'Reilly S, Zhao D. Effects of oil dispersants on settling of marine sediment particles and particle-facilitated distribution and transport of oil components. *Mar. Pollut. Bull.* 2017; 114: 408-418.
- Cai Z, Zhao X, Wang T, Liu W, Zhao D. Reusable platinum-deposited anatase/hexa-titanate nanotubes: roles of reduced and oxidized platinum on enhanced solar-light-driven photocatalytic activity. *ACS Sustain. Chem. Eng.* 2016; 5: 547-555.
- Calcagnile P, Fragouli D, Bayer IS, Anyfantis GC, Martiradonna L, Cozzoli PD, et al. Magnetically driven floating foams for the removal of oil contaminants from water. *ACS nano* 2012; 6: 5413-5419.

- Camilli R., Reddy C.M., Yoerger D.R., Van Mooy B., Jakuba M.V., Kinsey J.C., et al., 2010. Tracking hydrocarbon plume transport and biodegradation at Deepwater Horizon. *Science* 330, 201-204.
- Chelme-Ayala P., El-Din M.G., Smith D.W., Adams C.D., 2011. Oxidation kinetics of two pesticides in natural waters by ozonation and ozone combined with hydrogen peroxide. *Water Res.* 45, 2517-2526.
- Chen X, Burda C. The electronic origin of the visible-light absorption properties of C-, N- and S-doped TiO₂ nanomaterials. *J. Am. Chem. Soc.* 2008; 130: 5018-5019.
- Chen X, Liu L, Huang F. Black titanium dioxide (TiO₂) nanomaterials. *Chem. Soc. Rev.* 2015.
- Chen X, Mao SS. Titanium dioxide nanomaterials: synthesis, properties, modifications, and applications. *Chem. Rev.* 2007; 107: 2891-2959.
- Chin SF, Romainor ANB, Pang SC. Fabrication of hydrophobic and magnetic cellulose aerogel with high oil absorption capacity. *Mater. Letters* 2014; 115: 241-243.
- Chiu C., Chen Y., Huang Y., 2007. Removal of naphthalene in Brij 30-containing solution by ozonation using rotating packed bed. *J. Hazard. Mater.* 147, 732-737.
- Chou M., Huang B., Chang H., 2006. Degradation of gas-phase propylene glycol monomethyl ether acetate by ultraviolet/ozone process: A kinetic study. *J. Air Was. Manage. Assoc.* 56, 767-776.
- Chowdhury S, Balasubramanian R. Graphene/semiconductor nanocomposites (GSNs) for heterogeneous photocatalytic decolorization of wastewaters contaminated with synthetic dyes: a review. *Appl. Catal. B* 2014; 160: 307-324.
- Chu W., Chan K.H., Graham N.J.D., 2006. Enhancement of ozone oxidation and its associated processes in the presence of surfactant: Degradation of atrazine. *Chemosphere* 64, 931-936.
- Chu W, Jia J. The photodegradation and modeling of a typical NAPL, trichloroethene, by monochromatic UV irradiations. *Environ. Sci. Technol.* 2009; 43(5): 1455-1459.
- Chu Y, Pan Q. Three-dimensionally macroporous Fe/C nanocomposites as highly selective oil-absorption materials. *ACS Appl. Mater. Interfaces* 2012; 4: 2420-5.
- Cojocar C, Macoveanu M, Cretescu I. Peat-based sorbents for the removal of oil spills from water surface: application of artificial neural network modeling. *Colloid Surf. A: Physicochem. Eng. Asp.* 2011; 384: 675-684.
- Conmy R.N., Coble P.G., Farr J., Wood A.M., Lee K., Pegau W.S., et al., 2014. Submersible optical sensors exposed to chemically dispersed crude oil: wave tank simulations for improved oil spill monitoring. *Environ. Sci. Technol.* 48, 1803-1810.

- Couillard C.M., Lee K., Légaré B., King T.L., 2005. Effect of dispersant on the composition of the water-accommodated fraction of crude oil and its toxicity to larval marine fish. *Environ. Toxicol. Chem.* 24, 1496-1504.
- Diallo M.S., Abriola L.M., Weber W.J., 1994. Solubilization of nonaqueous phase liquid hydrocarbons in micellar solutions of dodecyl alcohol ethoxylates. *Environ. Sci. Technol.* 28, 1829-1837.
- Dias JM, Alvim-Ferraz MC, Almeida MF, Rivera-Utrilla J, Sánchez-Polo M. Waste materials for activated carbon preparation and its use in aqueous-phase treatment: A review. *J. Environ. Manag.* 2007; 85(4):833-846.
- Duan J, Liu W, Zhao X, Han Y, O'Reilly S, Zhao D. Study of residual oil in Bay Jimmy sediment 5 years after the Deepwater Horizon oil spill: Persistence of sediment retained oil hydrocarbons and effect of dispersants on desorption. *Sci. Total Environ.* 2018; 618: 1244-1253.
- Elovitz M.S., von Gunten U. Hydroxyl radical/ozone ratios during ozonation processes. I. The R_{ct} concept. *Ozone Sci. Eng.* 1999; 21, 239-260.
- Elovitz M.S., von Gunten U., Kaiser H.P. Hydroxyl radical/ozone ratios during ozonation processes. II. The effect of temperature, pH, alkalinity, and DOM properties. *Ozone Sci. Eng.* 2000; 22, 123-150.
- EPA, 1984. EPA Method 610. <https://www.epa.gov/sites/production/files/2015-10/documents/method_610_1984.pdf> Data accessed on Oct. 2015.
- EPA, 1996. EPA 3510C. <<https://www.epa.gov/sites/production/files/2015-12/documents/3510c.pdf>> Data accessed on Dec. 2015.
- Eriksson M., 2005. Ozone chemistry in aqueous solution: ozone decomposition and stabilization. PhD diss., KTH.
- Fang J, Shan X-q, Wen B, Lin J-m, Lu X-c, Liu X-d, et al. Sorption and desorption of phenanthrene onto iron, copper, and silicon dioxide nanoparticles. *Langmuir* 2008; 24: 10929-10935.
- Fakhru'l-Razi A, Pendashteh A, Abdullah LC, Biak DR, Madaeni SS, Abidin ZZ. Review of technologies for oil and gas produced water treatment. *J. Hazar. Mater.* 2009; 170:530-551.
- Faksness, L.G., Brandvik, P.J., Sydnnes, L.K., 2008. Composition of the water accommodated fractions as a function of exposure times and temperatures. *Mar. Pollut. Bull.* 56(10), 1746-1754.
- Forni L., Bahnemann D., Hart E.J., 1982. Mechanism of the hydroxide ion-initiated decomposition of ozone in aqueous solution. *J. Phy. Chem.* 86, 255-259.

- Freundlich, H. Ueber die Adsorption in Lösungen. *Z. Phys.e Chem.* 1906, 57, 385-470.
- Fu J, Cai Z, Gong Y, O'Reilly SE, Hao X, Zhao D. A new technique for determining critical micelle concentrations of surfactants and oil dispersants via UV absorbance of pyrene. *Colloid Surf. A: Physicochem. Eng. Asp.* 2015 484:1-8.
- Fu J., Gong Y., Cai Z., O'Reilly S.E., Zhao D., 2017. Mechanistic investigation into sunlight-facilitated photodegradation of pyrene in seawater with oil dispersants. *Mar. Pollut. Bull.* 114, 751-758.
- Fu J., Gong Y., Zhao X., O'Reilly S.E., Zhao D., 2014. Effects of oil and dispersant on formation of marine oil snow and transport of oil hydrocarbons. *Environ. Sci. Technol.* 48, 14392-14399.
- Fujita H., Izumi J., Sagehashi M., Fujii T., Sakoda A., 2004. Adsorption and decomposition of water-dissolved ozone on high silica zeolites. *Water Res.* 38, 159-165.
- García - Araya JF, Beltrán FJ, Aguinaco A. Diclofenac removal from water by ozone and photolytic TiO₂ catalysed processes. *J. Chem. Technol. Biotechnol.* 2010; 85(6):798-804.
- Garcia T, Murillo R, Cazorla-Amoros D, Mastral A, Linares-Solano A. Role of the activated carbon surface chemistry in the adsorption of phenanthrene. *Carbon* 2004; 42: 1683-1689.
- George-Ares A., Clark J.R. Aquatic toxicity of two Corexit® dispersants. *Chemosphere* 2000; 40, 897-906.
- Glover, C.M., Mezyk, S.P., Linden, K.G., Rosario-Ortiz, F.L. Photochemical degradation of Corexit components in ocean water. *Chemosphere* 2014; 111(0), 596-602.
- Gong Y., Fu J., O'Reilly S.E., Zhao D. Effects of oil dispersants on photodegradation of pyrene in marine water. *J. Hazard. Mater.* 2015; 287, 142-150.
- Gong Y., Zhao D., 2017. Effects of oil dispersant on ozone oxidation of phenanthrene and pyrene in marine water. *Chemosphere* 172, 468-475.
- Gong Y., Zhao X., O'Reilly S.E., Qian T., Zhao D. Effects of oil dispersant and oil on sorption and desorption of phenanthrene with Gulf Coast marine sediments. *Environ. Pollut.* 2014; 185, 240-249.
- Gong Y, Zhao X, Cai Z, O'Reilly S, Hao X, Zhao D. A review of oil, dispersed oil and sediment interactions in the aquatic environment: Influence on the fate, transport and remediation of oil spills. *Mar. Pollut. Bull.* 2014; 79: 16-33.
- Grover IS, Prajapat RC, Singh S, Pal B. SiO₂-coated pure anatase TiO₂ catalysts for enhanced photo-oxidation of naphthalene and anthracene. *Particuology* 2017; 34: 156-161.

- Grover IS, Singh S, Pal B. Stable anatase TiO₂ formed by calcination of rice-like titania nanorod at 800° C exhibits high photocatalytic activity. RSC Advances 2014; 4: 24704-24709.
- Guix M, Orozco J, García M, Gao W, Sattayasamitsathit S, Merkoçi A, et al. Superhydrophobic alkanethiol-coated microsubmarines for effective removal of oil. ACS Nano 2012; 6: 4445-4451.
- Haagen-Smit A.J., Bradley C.E., Fox M.M., 1953. Ozone formation in photochemical oxidation of organic substances. Ind. Eng. Chem. 45(9), 2086-2089.
- Haghighatzadeh A, Mazinani B, Shahedi Asl M, Bakhtiari L. TiO₂ (rutile and anatase) deposited on ordered mesoporous SiO₂: effect of pore size on photocatalytic activity. Desal. Water Treat. 2017; 80: 156-163.
- Hamilton G.A., Ribner B.S., Hellman T.M., 1968. The mechanism of alkane oxidation by ozone. Advances in Chemistry 77.
- He Y, Liu Y, Wu T, Ma J, Wang X, Gong Q, et al. An environmentally friendly method for the fabrication of reduced graphene oxide foam with a super oil absorption capacity. J. Hazard. Mater. 2013; 260: 796-805.
- Hellman T.M., Hamilton G.A., 1974. Mechanism of alkane oxidation by ozone in the presence and absence of iron (III) chloride. J. Am. Chem. Soc. 96, 1530-1535.
- Hemmer M.J., Barron M.G., Greene R.M., 2011. Comparative toxicity of eight oil dispersants, Louisiana sweet crude oil (LSC), and chemically dispersed LSC to two aquatic test species. Environ. Toxicol. Chem. 30, 2244-2252.
- Herndon VA. Literature review of chemical oil spill dispersants and herders in fresh and brackish waters. <https://www.bsee.gov/sites/bsee.gov/files/tap-technical-assessment-program//ab1.pdf>. 2010.
- Ho KA, Patton L, Latimer JS, Pruell RJ, Pelletier M, McKinney R, Jayaraman S. The chemistry and toxicity of sediment affected by oil from the North Cape spilled into Rhode Island Sound. Mar. Pollut. Bull. 1999; 38(4):314-323.
- Ho YS, McKay G. Sorption of dye from aqueous solution by peat. Chem. Eng. J. 1998; 70: 115-124.
- Ho YS, McKay G. Pseudo-second order model for sorption processes. Process Biochem. 1999; 34: 451-465.
- Howe RF, Gratzel M. EPR study of hydrated anatase under UV irradiation. J. Phys. Chem. 1987; 91: 3906-3909.

- Hu Y, Tsai HL, Huang CL. Effect of brookite phase on the anatase-rutile transition in titania nanoparticles. *J. Euro. Ceram. Soc.* 2003; 23: 691-696.
- Huang WP, Tang XH, Wang YQ, Kolytyn Y, Gedanken A. Selective synthesis of anatase and rutile via ultrasound irradiation. *Chem. Comm.* 2000: 1415-1416.
- Ji H, Gong Y, Duan J, Zhao D, Liu W. Degradation of petroleum hydrocarbons in seawater by simulated surface-level atmospheric ozone: Reaction kinetics and effect of oil dispersant. *Mar. Pollut. Bull.* 2018; 135: 427-440.
- Jia H, Zhao J, Fan X, Dilimulati K, Wang C. Photodegradation of phenanthrene on cation-modified clays under visible light. *Appl. Catal. B* 2012; 123-124: 43-51.
- Jo W-K, Natarajan TS. Influence of TiO₂ morphology on the photocatalytic efficiency of direct Z-scheme g-C₃N₄/TiO₂ photocatalysts for isoniazid degradation. *Chem. Eng. J.* 2015; 281: 549-565.
- Jusufi A., Hynninen A.P., Panagiotopoulos A.Z., 2008. Implicit solvent models for micellization of ionic surfactants. *J. Phy. Chem. B* 112, 13783-13792.
- Kasprzyk-Hordern B., Ziolek M., Nawrocki J., 2003. Catalytic ozonation and methods of enhancing molecular ozone reactions in water treatment. *Appl. Catal. B* 46, 639-669.
- Kleindienst S., Paul J.H., Joye S.B. Using dispersants after oil spills: impacts on the composition and activity of microbial communities. *Nature Rev. Microbiol.* 2015; 13: 388.
- Ko SO, Schlautman MA, Carraway ER. Partitioning of hydrophobic organic compounds to sorbed surfactants. 1. Experimental studies. *Environ. Sci. Technol.* 1998; 32: 2769-2775.
- Kou J, Li Z, Yuan Y, Zhang H, Wang Y, Zou Z. Visible-light-induced photocatalytic oxidation of polycyclic aromatic hydrocarbons over tantalum oxynitride photocatalysts. *Environ. Sci. Technol.* 2009; 43: 2919-2924.
- Kover, S.C., Rosario-Ortiz, F.L. Linden, K.G. Photochemical fate of solvent constituents of Corexit oil dispersants. *Water Res.* 2014; 52(0), 101-111.
- Koos, E., Johannsmeier, J., Schwebler, L., Willenbacher, N. Tuning suspension rheology using capillary forces. *Soft Matter* 2012; 8(24), 6620-6628.
- Kujawinski E.B., Kido Soule M.C., Valentine D.L., Boysen A.K. Longnecker K., Redmond M.C. Fate of dispersants associated with the Deepwater Horizon oil spill. *Environ. Sci. Technol.* 2011; 45, 1298-1306.
- Kumagai S, Noguchi Y, Kurimoto Y, Takeda K. Oil adsorbent produced by the carbonization of rice husks. *Waste Manag.* 2007; 27: 554-61.

- Langmuir, I. The adsorption of gases on plane surfaces of glass, mica and platinum. *J. Am. Chem. Soc.* 1918, 40 (9), 1361-1403.
- Lee K, Neff J, (editors). *Produced water: environmental risks and advances in mitigation technologies*. Springer Science & Business Media; 2011.
- Li Z., Lee K., King T., Boufadel M.C., Venosa A.D. Evaluating chemical dispersant efficacy in an experimental wave tank: 2—Significant factors determining in situ oil droplet size distribution. *Environ. Eng. Sci.* 2009; 26, 1407-1418.
- Lima A.L., Farrington J.W., Reddy C.M., 2005. Combustion-derived polycyclic aromatic hydrocarbons in the environment—a review. *Environ. Forensics.* 6(2), 109-131.
- Lin C., Zhang W., Yuan M., Feng C., Ren Y., Wei C., 2014. Degradation of polycyclic aromatic hydrocarbons in a coking wastewater treatment plant residual by an O₃/ultraviolet fluidized bed reactor. *Environ. Sci. Pollut. Res.* 21, 10329-10338.
- Lin D, Xing B. Adsorption of phenolic compounds by carbon nanotubes: Role of aromaticity and substitution of hydroxyl groups. *Environ. Sci. Technol.* 2008; 42: 7254-7259.
- Litter M., Quici N., 2010. Photochemical advanced oxidation processes for water and wastewater treatment. *Recent Patents on Engineering* 4, 217-241.
- Liu J., Bacosa H.P., Liu Z., 2017. Potential environmental factors affecting oil-degrading bacterial populations in deep and surface waters of the northern Gulf of Mexico. *Front. Microbiol.* 10(7): 2131.
- Liu W, Cai Z, Zhao X, Wang T, Li F, Zhao D. High-capacity and photoregenerable composite material for efficient adsorption and degradation of phenanthrene in water. *Environ. Sci. Technol.* 2016; 50: 11174-11183.
- Liu W, Sun W, Borthwick AGL, Ni J. Comparison on aggregation and sedimentation of titanium dioxide, titanate nanotubes and titanate nanotubes-TiO₂: Influence of pH, ionic strength and natural organic matter. *Coll. Surf. A Physicochem. Eng Asp.* 2013; 434: 319-328.
- Liu W, Wang T, Borthwick AGL, Wang Y, Yin X, Li X, et al. Adsorption of Pb²⁺, Cd²⁺, Cu²⁺ and Cr³⁺ onto titanate nanotubes: Competition and effect of inorganic ions. *Sci. Tot. Environ.* 2013; 456: 171-180.
- Liu Y, Ma J, Wu T, Wang X, Huang G, Liu Y, et al. Cost-effective reduced graphene oxide-coated polyurethane sponge as a highly efficient and reusable oil-absorbent. *ACS Appl. Mater. Interfaces* 2013; 5: 10018-26.
- Liu Z., Liu J., Zhu Q., Wu W., 2012. The weathering of oil after the Deepwater Horizon oil spill: insights from the chemical composition of the oil from the sea surface, salt marshes and sediments. *Environ. Res. Lett.* 7, 035302.

- Lorphensri O, Intravijit J, Sabatini DA, Kibbey TCG, Osathaphan K, Saiwan C. Sorption of acetaminophen, 17 alpha-ethynyl estradiol, nalidixic acid, and norfloxacin to silica, alumina, and a hydrophobic medium. *Wat. Res.* 2006; 40: 1481-1491.
- Major D., Zhang Q., Wang G., Wang H., 2012. Oil-dispersant mixtures: understanding chemical composition and its relation to human toxicity. *Toxicol. Environ. Chem.* 94, 1832-1845.
- Masten S.J., Davies S.H., 1994. The use of ozonation to degrade organic contaminants in wastewaters. *Environ. Sci. Technol.* 28, 180A-185A.
- McAuliffe CD. The use of chemical dispersants to control oil spills in shallow nearshore waters. *Oil Dispersants: New Ecological Approaches* 1989; ASTM International.
- Mendoza WG, Riemer DD, Zika RG. Application of fluorescence and PARAFAC to assess vertical distribution of subsurface hydrocarbons and dispersant during the Deepwater Horizon oil spill. *Environ. Sci.: Processes & Impacts* 2013; 15: 1017-1030.
- Micic OI, Zhang Y, Cromack KR, Trifunac AD, Thurnauer MC. Trapped holes on titania colloids studied by electron paramagnetic resonance. *J. Phy. Chem.* 1993; 97: 7277-7283.
- Miller J.S., Olejnik D., 2004. Ozonation of polycyclic aromatic hydrocarbons in water solution. *Ozone Sci. Eng.* 26, 453-464.
- Mitchell FM, Holdway DA. The acute and chronic toxicity of the dispersants Corexit 9527 and 9500, water accommodated fraction (WAF) of crude oil, and dispersant enhanced WAF (DEWAF) to *Hydra viridissima* (green hydra). *Water Res.* 2000; 34: 343-348.
- Muthukumar M., Selvakumar N., 2004. Studies on the effect of inorganic salts on decolouration of acid dye effluents by ozonation. *Dyes and Pigments* 62, 221-228.
- Nadarajah, N., Singh, A., Ward, O.P., 2002 De-emulsification of petroleum oil emulsion by a mixed bacterial culture. *Proc. Biochem.* 37(10), 1135-1141.
- Nguyen HN, Pignatello JJ. Laboratory tests of biochars as absorbents for use in recovery or containment of marine crude oil spills. *Environ. Engin. Sci.* 2013; 30: 374-380.
- Nakaoka Y, Nosaka Y. ESR investigation into the effects of heat treatment and crystal structure on radicals produced over irradiated TiO₂ powder. *J. Photochem. Photobio. A* 1997; 110: 299-305.
- Nakata K, Fujishima A. TiO₂ photocatalysis: design and applications. *J. Photochem. Photobio. C* 2012; 13: 169-189.
- Nam JJ, Thomas GO, Jaward FM, Steinnes E, Gustafsson O, Jones KC. PAHs in background soils from Western Europe: Influence of atmospheric deposition and soil organic matter. *Chemosphere* 2008; 70: 1596-1602.

- Ning X., Shen L., Sun J., Lin C., Zhang Y., Yang Z., et al., 2015 Degradation of polycyclic aromatic hydrocarbons (PAHs) in textile dyeing sludge by O₃/H₂O₂ treatment. *Rsc. Adv.* 5, 38021-38029.
- Nussbaum M, Paz Y. Ultra-thin SiO₂ layers on TiO₂: improved photocatalysis by enhancing products' desorption. *Phy. Chem. Chemical Phy.* 2012; 14: 3392-3399.
- Omotosho, J., Whateley, T., Florence, A., 1989. Methotrexate transport from the internal phase of multiple w/o/w emulsions. *J. Microencapsulation* 6(2), 183-192.
- Panarelli EG, Livraghi S, Maurelli S, Polliotto V, Chiesa M, Giamello E. Role of surface water molecules in stabilizing trapped hole centres in titanium dioxide (anatase) as monitored by electron paramagnetic resonance. *J. Photochem. Photobio. A* 2016; 322: 27-34.
- Parrino F, Camera-Roda G, Loddo V, Palmisano G, Augugliaro V. Combination of ozonation and photocatalysis for purification of aqueous effluents containing formic acid as probe pollutant and bromide ion. *Wat. Res.* 2014; 50:189-99.
- Patrick HN, Warr GG, Manne S, Aksay IA. Self-assembly structures of nonionic surfactants at graphite/solution interfaces. *Langmuir* 1997; 13: 4349-4356.
- Pelaez M, Nolan NT, Pillai SC, Seery MK, Falaras P, Kontos AG, et al. A review on the visible light active titanium dioxide photocatalysts for environmental applications. *Appl. Catal. B* 2012; 125: 331-349.
- Place B., Anderson B., Mekebri A., Furlong E.T., Gray J.L., Tjeerdema R., et al., 2010. A role for analytical chemistry in advancing our understanding of the occurrence, fate, and effects of Corexit oil dispersants. *Environ. Sci. Technol.* 44, 6016-6018.
- Pollard SJ, Fowler GD, Sollars CJ, Perry R. Low-cost adsorbents for waste and wastewater treatment: a review. *Sci. Total Environ.* 1992; 116:31-52.
- Pryor W.A., Giamalva D.H., Church D.F., 1984. Kinetics of ozonation. 2. Amino acids and model compounds in water and comparisons to rates in nonpolar solvents. *J. Am. Chem. Soc.* 106, 7094-7100.
- Pryor W.A., Wu M., 1992. Ozonation of methyl oleate in hexane, in a thin film, in SDS micelles, and in distearoylphosphatidylcholine liposomes: yields and properties of the Criegee ozonide. *Chem. Rev. Toxicol.* 5, 505-511.
- Przepiórski J. Enhanced adsorption of phenol from water by ammonia-treated activated carbon. *J. Hazard. Mater.* 2006; 135: 453-456.
- Quiñones DH, Rey A, Álvarez PM, Beltrán FJ, Plucinski PK. Enhanced activity and reusability of TiO₂ loaded magnetic activated carbon for solar photocatalytic ozonation. *Appl. Catal. B* 2014; 144: 96-106.

- Ramseur J.L., 2010. Deepwater Horizon oil spill: the fate of the oil. Congressional Research Service, Library of Congress Washington, DC.
- Razumovskii S., 2005. Reactions of ozone with aromatic compounds. *Chem. Kinet.* 259.
- Reddy C.M., Arey J.S., Seewald J.S., Sylva S.P., Lemkau K.L., Nelson R.K., et al., 2012. Composition and fate of gas and oil released to the water column during the Deepwater Horizon oil spill. *Proc. Natl. Acad. Sci.* 109, 20229-20234.
- Ryerson TB, Camilli R, Kessler JD, Kujawinski EB, Reddy CM, Valentine DL, et al. Chemical data quantify Deepwater Horizon hydrocarbon flow rate and environmental distribution. *PNAS* 2012; 109: 20246-20253.
- Ringuet J., Albinet A., Leoz-Garziandia E., Budzinski H., Villenave E., 2012. Reactivity of polycyclic aromatic compounds (PAHs, NPAHs and OPAHs) adsorbed on natural aerosol particles exposed to atmospheric oxidants. *Atmospheric Environ.* 61, 15-22.
- Rosenfeldt E.J., Linden K.G., Canonica S., von Gunten U., 2006. Comparison of the efficiency of OH radical formation during ozonation and the advanced oxidation processes O₃/H₂O₂ and UV/H₂O₂. *Water Res.* 40, 3695-3704.
- Rubio-Clemente A., Torres-Palma R.A., Peñuela G.A., 2014. Removal of polycyclic aromatic hydrocarbons in aqueous environment by chemical treatments: A review. *Sci. Total Environ.* 478, 201-225.
- Ryerson T.B., Aikin K.C., Angevine W.M., Atlas E.L., Blake D.R., Brock C.A., et al., 2011. Atmospheric emissions from the Deepwater Horizon spill constrain air-water partitioning, hydrocarbon fate, and leak rate. *Geophys. Res. Lett.* 38, L07803.
- Sammarco P.W., Kolian S.R., Warby R.A., Bouldin J.L., Subra W.A., Porter S.A., 2013. Distribution and concentrations of petroleum hydrocarbons associated with the BP/Deepwater Horizon oil spill, Gulf of Mexico. *Mar. Pollut. Bull.* 73, 129-143.
- Sampaio MJ, Silva CG, Silva AM, Pastrana-Martínez LM, Han C, Morales-Torres S, et al. Carbon-based TiO₂ materials for the degradation of Microcystin-LA. *Appl. Catal. B* 2015; 170: 74-82.
- Sannino F, Pirozzi D, Vitiello G, D'errico G, Aronne A, Fanelli E, et al. Oxidative degradation of phenanthrene in the absence of light irradiation by hybrid ZrO₂-acetylacetonate gel-derived catalyst. *Appl. Catal. B* 2014; 156: 101-107.
- Scelfo G.M., Tjeerdema R.S., 1991. A simple method for determination of Corexit 9527® in natural waters. *Mar. Environ. Res.* 31, 69-78.

- Schneider J, Matsuoka M, Takeuchi M, Zhang J, Horiuchi Y, Anpo M, et al. Understanding TiO₂ photocatalysis: mechanisms and materials. *Chem. Rev.* 2014; 114: 9919-9986.
- Shankar R, Shim WJ, An JG, Yim UH. A practical review on photooxidation of crude oil: Laboratory lamp setup and factors affecting it. *Wat. Res.* 2015; 68: 304-315.
- Shannon MA, Bohn PW, Elimelech M, Georgiadis JG, Mariñas BJ, Mayes AM. Science and technology for water purification in the coming decades. *Nature* 2008; 452: 301-310.
- Short JW. Advances in understanding the fate and effects of oil from accidental spills in the United States beginning with the Exxon Valdez. *Arch. Environ. Contamin. and Toxicol.* 2017; 73:5-11.
- Simpson M.J., Simpson A.J., Hatcher P.G., 2004. Noncovalent interactions between aromatic compounds and dissolved humic acid examined by nuclear magnetic resonance spectroscopy. *Environ. Toxicol. Chem.* 23, 355-362.
- Singer M, George S, Lee I, Jacobson S, Weetman L, Blondina G, et al. Effects of dispersant treatment on the acute aquatic toxicity of petroleum hydrocarbons. *Arch. Environ. Contamin. and Toxicol.* 1998; 34: 177-187.
- Singer M.M., Aurand D., Bragin G.E., Clark J.R., Coelho G.M., Sowby M.L., et al., 2000. Standardization of the preparation and quantitation of water-accommodated fractions of petroleum for toxicity testing. *Mar. Pollut. Bull.* 40, 1007-1016.
- Singer MM, Smalheer DL, Tjeerdema RS, Martin M. Effects of spiked exposure to an oil dispersant on the early life stages of four marine species. *Environ. Toxicol. Chem.* 1991; 10: 1367-1374.
- Smultea MA, Würsig B. Behavioral reactions of bottlenose dolphins to the Mega Borg oil spill, Gulf of Mexico 1990. *Aquat. Mamm.* 1995; 21(3):171-181.
- Sorial G., Chandrasekar S., Weaver J.W., 2004. Characteristics of spilled oils, fuels, and petroleum products: 2a. Dispersant effectiveness data for a suite of environmental conditions - The effects of temperature, volatilization, and energy. EPA/600/R - 04/119. <<http://www.epa.gov/athens/research/projects/eros>> Data accessed on Sep. 8, 2004.
- Staelin J., Hoigne J., 1985. Decomposition of ozone in water in the presence of organic solutes acting as promoters and inhibitors of radical chain reactions. *Environ. Sci Technol.* 19, 1206-1213.
- Standeker S, Novak Z, Knez Z. Adsorption of toxic organic compounds from water with hydrophobic silica aerogels. *J. of Coll. Inter. Sci.* 2007; 310: 362-368.
- Sud D, Kaur P. Heterogeneous photocatalytic degradation of selected organophosphate pesticides: a review. *Crit. Rev. in Environ. Sci. Technol.* 2012; 42: 2365-2407.

- Tan H, Zhao Z, Niu M, Mao C, Cao D, Cheng D, et al. A facile and versatile method for preparation of colored TiO₂ with enhanced solar-driven photocatalytic activity. *Nanoscale* 2014; 6: 10216-10223.
- Tan IA, Hameed BH, Ahmad AL. Equilibrium and kinetic studies on basic dye adsorption by oil palm fibre activated carbon. *Chem. Eng. J.* 2007 127:111-119.
- Terzyk AP. The influence of activated carbon surface chemical composition on the adsorption of acetaminophen (paracetamol) in vitro: Part II. TG, FTIR, and XPS analysis of carbons and the temperature dependence of adsorption kinetics at the neutral pH. *Colloid Surf. A: Physicochem. Eng. Asp.* 2001; 177:23-45.
- Toyoda M, Inagaki M. Sorption and recovery of heavy oils by using exfoliated graphite. *Spill Sci. Technol. Bull.* 2003; 8: 467-474.
- von Gunten U., 2003. Ozonation of drinking water: Part I. Oxidation kinetics and product formation. *Water Res.* 37, 1443-1467.
- Wang D, McLaughlin E, Pfeffer R, Lin YS. Adsorption of oils from pure liquid and oil-water emulsion on hydrophobic silica aerogels. *Separ. Purif. Technol.* 2012; 99: 28-35.
- Wang JL, Xu LJ. Advanced oxidation processes for wastewater treatment: formation of hydroxyl radical and application. *Crit. Rev. in Environ. Sci. Technol.* 2012; 42: 251-325.
- Walter T., Ederer H., Först C., Stieglitz L., 2000. Sorption of selected polycyclic aromatic hydrocarbons on soils in oil-contaminated systems. *Chemosphere* 41, 387-397.
- Wang G, Sun Q, Zhang Y, Fan J, Ma L. Sorption and regeneration of magnetic exfoliated graphite as a new sorbent for oil pollution. *Desalination* 2010; 263: 183-188.
- Wang Z, Friedrich DM, Beversluis MR, Hemmer SL, Joly AG, Huesemann MH, et al. A fluorescence spectroscopic study of phenanthrene sorption on porous silica. *Environ. Sci. Technol.* 2001; 35: 2710-2716.
- Wang, Z., Fingas, M., 1997. Developments in the analysis of petroleum hydrocarbons in oils, petroleum products and oil-spill-related environmental samples by gas chromatography. *J. Chromatogr. A* 774(1), 51-78.
- Wang, Z., Li, K., Lambert, P., Yang, C., 2007. Identification, characterization and quantitation of pyrogenic polycyclic aromatic hydrocarbons and other organic compounds in tire fire products. *Journal of Chromatogr. A* 1139(1), 14-26.
- Wen S, Zhao J, Sheng G, Fu J, Peng Pa. Photocatalytic reactions of phenanthrene at TiO₂/water interfaces. *Chemosphere* 2002; 46: 871-877.

- Woo OT, Chung WK, Wong KH, Chow AT, Wong PK. Photocatalytic oxidation of polycyclic aromatic hydrocarbons: Intermediates identification and toxicity testing. *J. Hazar. Mater.* 2009; 168: 1192-1199.
- Xu QA, Ma Y, Zhang J, Wang XL, Feng ZC, Li C. Enhancing hydrogen production activity and suppressing CO formation from photocatalytic biomass reforming on Pt/TiO₂ by optimizing anatase-rutile phase structure. *J. Catal.* 2011; 278: 329-335.
- Yang X, Cai H, Bao M, Yu J, Lu J, Li Y. Highly Efficient Photocatalytic Remediation of Simulated Polycyclic Aromatic Hydrocarbons (PAHs) Contaminated Wastewater under Visible Light Irradiation by Graphene Oxide Enwrapped Ag₃PO₄ Composite. *Chinese Journal of Chemistry*
- Yin F., John G.F., Hayworth J.S., Clement T.P., 2015. Long-term monitoring data to describe the fate of polycyclic aromatic hydrocarbons in Deepwater Horizon oil submerged off Alabama's beaches. *Sci. Total Environ.* 508, 46-56.
- Yu D.Y., Kang N., Bae W., Banks M.K., 2007. Characteristics in oxidative degradation by ozone for saturated hydrocarbons in soil contaminated with diesel fuel. *Chemosphere* 66, 799-807.
- Yu J, Xiang Q, Zhou M. Preparation, characterization and visible-light-driven photocatalytic activity of Fe-doped titania nanorods and first-principles study for electronic structures. *Appl. Catal. B* 2009; 90: 595-602.
- Yu Q, Tao Y, Huang Y, Lin Z, Zhuang Y, Ge L, et al. Preparation of porous polysulfone microspheres and their application in removal of oil from water. *Ind. Eng. Chem. Res.* 2012; 51: 8117-8122.
- Zhang L, He X, Xu X, Liu C, Duan Y, Hou L, et al. Highly active TiO₂/g-C₃N₄/G photocatalyst with extended spectral response towards selective reduction of nitrobenzene. *Appl. Catal. B* 2017; 203: 1-8.
- Zhang Y., Wong J., Liu P., Yuan M., 2011. Heterogeneous photocatalytic degradation of phenanthrene in surfactant solution containing TiO₂ particles. *J. Hazar. Mater.* 191, 136-143.
- Zhang Y., Zhou L., Zeng C., Wang Q., Wang Z., Gao S., et al., 2013. Photoreactivity of hydroxylated multi-walled carbon nanotubes and its effects on the photodegradation of atenolol in water. *Chemosphere* 93, 1747-1754.
- Zhao, D.; Pignatello, J. J.; White, J. C.; Braida, W.; Ferrandino, F. Dual-mode modeling of competitive and concentration-dependent sorption and desorption kinetics of polycyclic aromatic hydrocarbons in soils. *Water Resour. Res.* 2001, 37 (8), 2205-2212.
- Zhao, D.; Hunter, M.; Pignatello, J. J.; White, J. C. Application of the dual-mode model for predicting competitive sorption equilibria and rates of polycyclic aromatic hydrocarbons in estuarine sediment suspensions. *Environ. Toxicol. Chem.* 2002, 21 (11), 2276-2282.

- Zhao W., Shi H., Wang D., 2004. Ozonation of Cationic Red X-GRL in aqueous solution: degradation and mechanism. *Chemosphere* 57, 1189-1199.
- Zhao W., Liu F., Yang Y., Tan M., Zhao D., 2011. Ozonation of Cationic Red X-GRL in aqueous solution: Kinetics and modeling. *J. Hazard. Mater.* 187, 526-533.
- Zhao X, Cai Z, Wang T, O'Reilly S, Liu W, Zhao D. A new type of cobalt-deposited titanate nanotubes for enhanced photocatalytic degradation of phenanthrene. *Appl. Catal. B* 2016; 187: 134-143.
- Zhao X., Gong Y., O'Reilly S.E., Zhao D. Effects of oil dispersant on solubilization, sorption and desorption of polycyclic aromatic hydrocarbons in sediment-seawater systems. *Mar. Pollut. Bull.* 2015; 92, 160-169.
- Zhao X., Liu W., Fu J., Cai Z., O'Reilly SE, Zhao D. Dispersion, sorption and photodegradation of petroleum hydrocarbons in dispersant-seawater-sediment systems. *Mar. Pollut. Bull.* 2016; 109, 526-538.
- Zhou Z, Guo L. Evolution of the optical properties of seawater influenced by the Deepwater Horizon oil spill in the Gulf of Mexico. *Environ. Res. Letters* 2012; 7: 025301.
- Zhou Z, Guo L, Shiller AM, Lohrenz SE, Asper VL, Osburn CL. Characterization of oil components from the Deepwater Horizon oil spill in the Gulf of Mexico using fluorescence EEM and PARAFAC techniques. *Mar. Chem.* 2013; 148: 10-21.
- Zhu B-Y, Zhao X, Gu T. Surface solubilization. *J. Am. Chem. Soc.* 1988; 84: 3951-3960.
- Zhu H, Qiu S, Jiang W, Wu D, Zhang C. Evaluation of electrospun polyvinyl chloride/polystyrene fibers as sorbent materials for oil spill cleanup. *Environ. Sci. Technol.* 2011; 45: 4527-4531.

Appendix

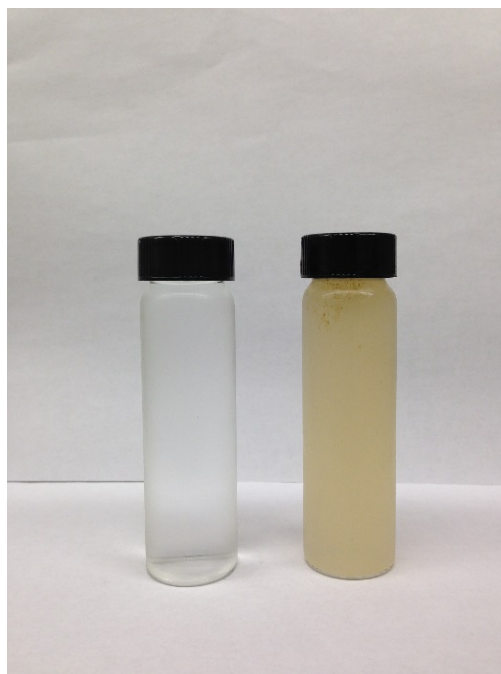
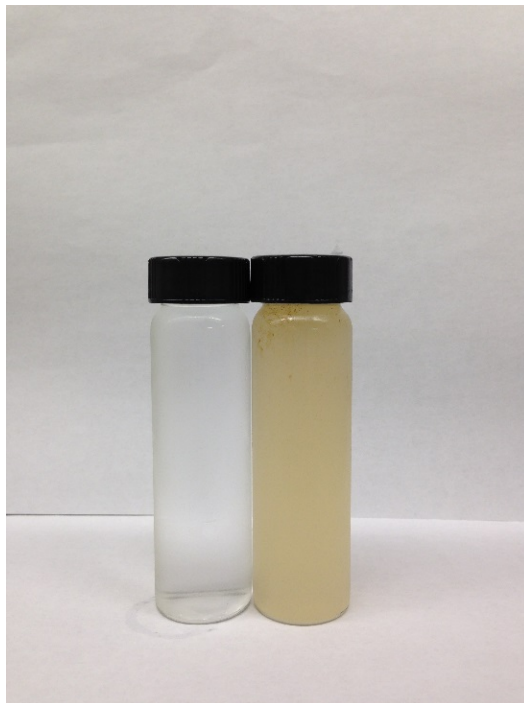


Figure A-1. Left: Oil: Seawater = 1:200 (v/v); Right: Dispersant:Oil:Seawater = 1:20:4000 (v/v/v) Preparation of water accommodated oil (WAO) and dispersant-enhanced WAO.

WAO was prepared at an oil-to-seawater volume ratio of 1:200 resulting in a WAO of 0.4 mg/L as TPHs. DWAO was prepared at a dispersant (Corexit EC9500A)-to-oil-to-seawater volume ratio of 1:20:4000, resulting in a DWAO of 149.7 mg/L as TPHs. Seawater conditions: temperature = 22 ± 1 °C, initial pH = 8.1, salinity = 2%, and initial dissolved organic matter (DOM) = 2.2 mg/L as total organic carbon (TOC).



Figure A-2. A simulated photodegradation system. The arc lamp power supply can supply 450-1000 W power. The light source is a 450 W xenon-zone free short arc lamp with an air mass filter. The optical path area is 4×4 inch.



Figure A-3. Stainless steel jacket with a Teflon reactor for titanate nanotubes synthesis.